

Controlling magnetic domain wall pinning
using atomic force microscope tip-based
nanomachining



Doctor of Philosophy

By

Josh Jones

Cardiff School of Engineering

Cardiff University

Cardiff, Wales

United Kingdom

2019

Abstract

In recent decades, atomic force microscope (AFM) tip-based nanomachining has gained the increased attention of researchers as a technique capable of creating nanoscale features on the surfaces of materials. In principle, it represents a potentially low-cost alternative to other more expensive methods for nanoscale fabrication, particularly at the prototyping stage of device development. However, currently the numbers of practical applications that take advantage of this technique are limited.

At the same time, magnetic domains at nanoscales have also shown to be of interest in recent decades with the potential for use in various applications. An example of which includes racetrack memory, a possible future non-volatile data storage system that would have higher densities and faster read/write speeds [1]. A key issue in successfully developing these systems relates to the ability to accurately control the motion of the magnetic domain boundaries known as domain walls (DWs).

In this context, this thesis presents a study attempting to combine these issues. AFM tip-based nanomachining is used to create vertical nanotrenches cut along the top surface across the width of magnetic nanowires with the intention of pinning DWs at them.

A computational study was conducted focusing on the effects of the shape and geometry of vertical nanotrenches on their pinning strength. This was inspired by the fact that nanotrenches created by AFM tip-based nanomachining have a tendency to be triangular in shape due to the pyramidal tips. Simulations were carried out using the Object-Oriented MicroMagnetic Framework (OOMMF). It was found that triangular nanotrenches pin both transverse and vortex DWs more weakly than their square counterparts. The depth of both shape nanotrenches appear to have approximately linear relationships with the pinning strength. It was found that whilst square nanotrenches retain their pinning strength as their length is increased, triangular nanotrenches reduce in pinning strength beyond a significant length relative to its depth. This was shown to be related to the angle between the triangular nanotrench wall and the x-y plane. It is found that the depinning fields drastically reduce when the angle is reduced below 10° corresponding to relatively shallow and long nanotrenches.

Experiments are carried out to test the viability of AFM tip-based nanomachining for pinning DWs. Anisotropic Magnetoresistance measurements were used to detect the

presence of DWs and measure the resulting depinning fields. In addition to this, magnetic full-field transmission soft x-ray microscopy was utilised to directly image DWs pinned at the created sites. It was found to be a viable option as multiple ferromagnetic nanowires are machined and DWs are pinned at the resulting nanotrenches. Further work was conducted to verify the computational results regarding nanotrench depth and pinning strength. Experimental data gathered agrees with the computational simulations and show an approximately linear increase in depinning fields with an increase in nanotrench depth.

Acknowledgements

First of all, I would like to give huge thanks to my supervisors Dr Emmanuel Brousseau and Dr Dan Read. For giving me the opportunity to attempt a PhD project, but more importantly, it would not have been possible to complete it without the help and support you both have given me over the last four years.

I am very grateful to Dr Kane Esien, who helped me massively during my first year. Showing me how to use all the lab equipment, teaching me the basics of nanomagnetism and domain walls, and providing the foundation that my entire project would become based upon. I also offer thanks to Dr Simon Olivari and Alex Evans for the help and support they provided me in the lab and during trips and experiments conducted at the Advanced Light Source facility.

I would like to thank the staff and scientists, such as beamline scientist Dr Mi-Young Im, who helped me during my trips to the ALS facility and aided in collecting better quality data with my samples.

Throughout my life, my family have been nothing but supportive to me, especially when it has come to my education. I thank every one of you for continuing to encourage and support me so that I have been able to achieve all that I have so far. Special thanks in particular go to my mam (Susan), dad (Anthony), step-dad (Steve), step-mam (Rachel), brother (Rhys) and sisters (Mia and Nikki). I would not be the person I have become without you all. With this I also give thanks to my dogs Reggie and Ronnie who have cheered me up on many days throughout tough times this last year.

Finally, and most importantly, I cannot give enough thanks to my wife-to-be Bethan. You have done nothing but support me for the last nine and half years that we have been together. I know for a fact that I would never have been able to get through this last four years without you there by my side. I am beyond grateful for all the patience you have shown and help you have given me, especially during these last few months.

You have been my rock and I dedicate this thesis to you.

Table of Contents

Abstract.....	III
Acknowledgements.....	V
List of Figures.....	IX
List of Tables.....	XIX
List of Acronyms.....	XX
List of Symbols.....	XXI
1. Introduction.....	1
1.1 Nanomagnetism.....	1
1.1.1 The origin of magnetic moments from electrons.....	1
1.1.2 Magnetic Susceptibility.....	2
1.1.3 Ferromagnetism.....	3
1.1.4 Micromagnetics.....	6
1.1.5 Domains and Domain Walls.....	11
1.1.6 Magnetic Switching.....	14
1.1.7 Domain Walls in small structures.....	16
1.1.8 Domain Wall Pinning.....	21
1.1.9 Magnetisation Dynamics.....	22
1.1.10 Applications to data storage technology.....	24
1.2 The Atomic Force Microscope.....	25
1.2.1 Origin of the Atomic Force Microscope.....	25
1.2.1 Basic Principles of an AFM.....	25
1.2.2 AFM modes of operation.....	29
1.2.4 Introduction to AFM tip-based nano-machining.....	32
2. Literature Review.....	34
2.1 Domain Wall pinning.....	34
2.1.1 Nanowire Design.....	34
2.1.2 Non-topographical methods.....	36
2.1.3 Lateral Changes to magnetic nanowires.....	37
2.1.4 Vertical modifications to nanowires.....	47
2.2 AFM tip-based nanomachining.....	54
2.2.1 AFM as a tool for nanofabrication.....	54
2.2.2 Comparison with other nanofabrication techniques.....	55
2.2.3 Applications of AFM tip-based nanomachining.....	57
2.2.4 AFM nanolithography of ferromagnetic thin films.....	58
2.2.5 Using AFM tip-based nanomachining to pin Domain Walls.....	64

2.3	Knowledge gaps.....	68
3.	Methodology	70
3.1	Sample Fabrication.....	70
3.1.1	Electron Beam Lithography	70
3.1.2	Thin Film Deposition.....	72
3.1.3	AFM nanomachining.....	74
3.1.4	Fabrication process chain.....	77
3.1.5	Permalloy.....	80
3.2	Sample Characterisation.....	80
3.2.1	Scanning Electron Microscopy	80
3.2.2	Magneto-transport measurements.....	82
3.2.3	Full-Field Soft X-ray Microscopy	87
3.3	Micromagnetic Simulations.....	89
4.	Computational Study of the shape influence on pinning strength of vertical nanotrenches.....	91
4.1	Initial prototype model - Phase diagram.....	91
4.2	Inserting nanotrench into computational model	94
4.3	Pinning domain walls with square and triangular vertical nanotrenches....	96
4.3.1	Square Nanotrench.....	96
4.3.2	Triangular nanotrench.....	106
4.3.3	Comparison between square and triangular nanotrenches.....	119
4.3.4	Angular dependence of triangular nanotrenches	124
4.3.5	Trapezoidal nanotrench.....	130
4.4	Summary	136
5.	Implementing AFM nano-machining for magnetic domain wall pinning.....	138
5.1	Initial experiments: AFM machining of a permalloy thin film.....	138
5.2	Pinning of DWs at a nanotrench on a thin permalloy nanowire.....	145
5.3	Pinning of DWs at nanotrenches on thick nanowires	155
5.4	Influence of the nanotrench depth on the DW pinning strength using thick nanowire	160
5.5	Investigation of an alternative sample design for multiple parallel measurements.....	168
5.6	Additional AFM nanomachining experiments for the exploration of future studies.....	175
5.7	Summary	182
6.	Conclusions and Future work.....	184
6.1	Knowledge contributions and key conclusions	184
6.2	Further work	187

References..... 189

List of Figures

Figure 1.1.1: a) and b), schematic of an electron and its associated magnetic moment due to spin. c), schematic of a nucleus and its associated magnetic moment due to the orbiting electron.	2
Figure 1.1.2: An example of a ferromagnetic hysteresis loop, taken from [6].....	6
Figure 1.1.3: Demonstrating the various stages domain creation to reduce stray fields. Dashed arrows represent external stray fields whilst solid arrows represent internal magnetisation of the domain.....	10
Figure 1.1.4: Examples of a 180° DW (a and b) and a 90° DW (c)	12
Figure 1.1.5: Schematic of a) a Bloch wall, and b) a Néel wall [6]	13
Figure 1.1.6: a) Stoner-Wohlfarth ellipsoid, b) Stoner-Wohlfarth astroid. Adapted from [6].....	15
Figure 1.1.7: Examples of how a reversal domain may form and grow. a) Reversal domain nucleates at a crystallographic imperfection or due to thermal fluctuations and grows. b) A previously existing domain may have gotten pinning within the body but can then grow to pass the pinning sites with an applied field. c) Reversal domain nucleates at a surface asperity. Taken from [6].....	16
Figure 1.1.8: Schematic of nanostrip dimensions and angles.....	17
Figure 1.1.9: Simulations showing head-to-head and tail-to-tail examples of transverse, asymmetric transverse and vortex domain walls. Black arrows represent direction of magnetisation for local elements. Red and blue shading represents regions of magnetisation pointing to the right and left respectively.	18
Figure 1.1.10: Different chiralities for transverse and vortex domain walls.	18
Figure 1.1.11: Phase diagram demonstrating which DW type is to be expected depending on the cross-sectional dimensions of a nanostrip. Phase diagram created using numerical simulations. Taken from [24]	20
Figure 1.1.12: a) Micromagnetic simulation of a Landau DW. b) Adjusted phased diagram to include Landau DWs. Images taken from [28]	20
Figure 1.2.1: Graph of atomic force vs distance.....	26
Figure 1.2.2: Schematics of an AFM probe	27
Figure 1.2.3: Schematic of an AFM system	28
Figure 1.2.4: Schematics showing beam positioning for various cantilever deflections	28
Figure 1.2.5: Demonstrating repulsive and attractive regimes.....	29
Figure 1.2.6: Demonstration of differences between constant force and height modes	31
Figure 1.2.7: Schematic of AFM cutting into a sample creating grooves.....	33
Figure 2.1.1: Figure displaying an example of using a curved nanowire in order to create and pin DWs at the corners. Taken from [74].	34
Figure 2.1.2: (a) Schematic diagram, (b) Secondary electron images by focused-ion-beam irradiation of a DW diode structure. Taken from [80].....	35
Figure 2.1.3: Schematic of the Christmas-tree-like spin Hall magnetometer. Taken from [83]	35
Figure 2.1.4: Schematic of device implementing multiple stray field strips to pin DWs. Taken from [91].	37
Figure 2.1.5: Electron image by FIB irradiation of a 200 nm wide Permalloy structure with a T-shaped trap at its middle. Taken from [75].	38

Figure 2.1.6: a) FIB image of triangular notch in a permalloy nanowire. b) Triangular notch schematic. c) Propagation data (\blacktriangle) and depinning data (\circ) for three sets of structures with five different trap sizes. Taken from [94] 39

Figure 2.1.7: a) Switching fields of nanowires containing notches and anti-notches. Squares: nucleation fields HN , triangles: propagation field HP , and open circles: transmission field HT . I DW facing away from notch, II DW points towards notch, III DW points away from anti-notch, and IV DW points towards anti-notch. b) Potential energy profile measurements where H_{pull} is the field required to pull a DW back from a trap and H_{push} is the field required to initially propagate the DW to the trap. Inserts show schematics of nanowire and resulting potential energy landscape. Images taken from [35] 40

Figure 2.1.8: Switching field as a function of wire width of a 5 nm thick Permalloy nanowire. (\blacklozenge) represents magnetization reversal of the nucleation pad, (\blacksquare) represents domain wall injection from the nucleation pad into the wire, and (\bullet) represents domain wall depinning from a triangular notch patterned along one side of the nanowire. Taken from [103]. 41

Figure 2.1.9: a) Four types of transverse domain walls. b) Depinning field strength for different notch configurations and domain walls. Domain walls that passed through the notch were assigned a value of (-)100 Oe which equals to the nucleation field of the domain wall. c) and d) Depinning field strength for a Tail-to-Tail “Down” chirality DW for different notch geometries as a function of; c) notch height whilst the notch width is kept fixed, d) Notch width whilst the notch height is kept fixed. Taken from [105]. 42

Figure 2.1.10: (a) Schematic illustration of the permalloy nanowire with asymmetric notch. (b) SEM image of the fabricated permalloy nanowire with $d = 500$ nm and the enlarged view around the notch. Taken from [100]. 43

Figure 2.1.11: SEM images of (a) Entire permalloy nanowire with one triangular inward notch, and (b) enlarged six types of notch structures. Taken from [106]. ... 44

Figure 2.1.12: Graph of the depinning fields from the constriction, as a function of the pulse amplitude. Each red dot correspond to one half-loop field measurement, for a total of 150 loops. Half-loops during which no pinning occurred are not represented. For a given pulse value, the distribution of depinning field is split in two sub-distributions corresponding to two different micromagnetic configurations of the DW. Taken from [116]. 46

Figure 2.1.13: a) An example of a nanowire constriction/neck. Taken from [115]. b) An example of a set of symmetrical protrusions/anti-notches. Taken from [76]. 46

Figure 2.1.14: Schematic of step-like thickness change in a thin film. Take from [120]. 48

Figure 2.1.15: Dependence of depinning fields for positive and negative magnetic fields, a) for a $0.15 \mu\text{m}$ thick thin film with varying thickness ratio. b) for varying thin film thicknesses with a thickness change ratio of 0.2. Taken from [120]. 49

Figure 2.1.16: Schematic of a groove in a thin film. Taken from [121]. 49

Figure 2.1.17: a) Schematic of nano-oxidation technique using AFM. b) Schematic of cross-section of nanowire with oxide features. Taken from [122]. 50

Figure 2.1.18: a) Schematics of a nanowire with a nanotrench. Simulated b) transverse and c) vortex DW at the nanotrench. Taken from [123]. 50

Figure 2.1.19: Dependence of depinning field with the depth (a) and the length (b) of nanotrench for a transverse wall. (c) and (d) show the dependence of depinning field for vortex walls. Taken from [123]. 51

Figure 2.1.20: Energy profiles with respect to DW position for a transverse (a) and a vortex (b) wall. (c) and (d) show the total energy for transverse and vortex walls for various lengths of nanotrenches. The drop in the energy profile (ΔE_{Tot}) is plotted in the insets for respective DW types. Taken from [123].	52
Figure 2.1.21: (a) Scanning electron micrograph image of the device with the measurement schematics. (b) The histogram plot of the generated DW resistance. (c) A typical depinning profile of a DW from a pinning site. (d) The histogram plot of depinning fields. Taken from [123].	54
Figure 2.2.1: Equipment cost, patterning speed, and minimum resolution of AFM lithography compared with other methods for nanofabrication. (EUV = extreme UV lithography, DUV = deep UV lithography, EBL = electron-beam lithography, NIL = nanoimprint lithography, STM = scanning tunnelling microscopy). Taken from [150].	56
Figure 2.2.2: Example of an application of AFM nanomachining. Periodic hole arrays with a period of 55 nm in an InAs-ALsB surface quantum well created by direct lithography of the InAs top layer. Taken from [154].	58
Figure 2.2.3: AFM scratched groove on NiFe thin film surface using 9 μN applied force: (a) AFM image of groove along scan direction and (b) cross-sectional profiles at ten different groove locations. Taken from [158].	59
Figure 2.2.4: Correlation of depth (d) and width (w_f) of scratched groove with normal applied force F_n for NiFe thin film. Taken from [158].	59
Figure 2.2.5: a) and b) AFM images, c) and d) Geometric profiles of NiFe nanowires before (a and c) and after (b and d) the creation of the nanoconstriction. Images taken from [158]	60
Figure 2.2.6: Correlation of depth (d) and width (w_f) of groove machined on NiFe surface with number of machining cycle (N_0). Image taken from [159].	61
Figure 2.2.7: Si probe with diamond-coated pyramidal tip: (a) schematic of rectangular microcantilever with triangular pyramid tip, (b) SEM image of tip top view, (c) SEM image of tip side view. Taken from [160]	61
Figure 2.2.8: AFM image of grooves scratched by a normal force of 9 μN on $\text{Ni}_{80}\text{Fe}_{20}$ surfaces at four directions: (a) upward, (b) forward, (c) downward, (d) backward. Taken from [160].	63
Figure 2.2.9: AFM-measured cross-sectional profiles of four grooves scratched by a normal force of 9 μN on 30 nm thick $\text{Ni}_{80}\text{Fe}_{20}$ thin films on a SiO_2/Si substrate at 10 different groove locations along: (a) upward direction, (b) forward direction, (c) downward direction, (d) backward direction. Taken from [160].	63
Figure 2.2.10: AFM fabricated nanostructures: (a) hole in the centre of Hall cross ($t_{\text{Co}} = 0.5$ nm). Applied force: $F_{\text{app}} = 14$ μN . (b) Groove across a wire ($t_{\text{Co}} = 1$ nm), $F_{\text{app}} = 30$ μN . Taken from [161]	65
Figure 2.2.11: A) Magnetization reversal process in Pt/Co/Pt Hall crosses ($t_{\text{Co}} = 0.5$ nm). (a) EHE voltage as a function of time, curve 1: defect-free cross; curve 2: device having an AFM machined hole in the cross centre. i)-iv) Kerr images of the DW propagation in the cross with the centre defect. B) Inhibited DW propagation in a Pt/Co/Pt wire ($t_{\text{Co}} = 1$ nm) by an AFM fabricated groove. First reversed domain (dark gray) coming from the upper left. Images taken from [162].	66
Figure 2.2.12: Pinning and depinning of a DW at a shallow inclined trench (at dashed line in (a)). Applied field is 46 Oe. Total time of field application is marked. Taken from [162].	67

Figure 2.2.13: Creation of artificial domains by AFM lithography. DW propagation into the area defined by the AFM fabricated groove (black line in (a)) is inhibited. Applied field is 66 Oe. Taken from [162].	67
Figure 3.1.1: Schematic of interaction between electron beam and an electrically sensitive resist.	72
Figure 3.1.2: Schematic of an evaporation chamber	74
Figure 3.1.3: Photo of the AFM system used in this study.	75
Figure 3.1.4: Schematic of optical lever technique for detecting deformation of the AFM cantilever	76
Figure 3.1.5: Schematic of process chain used in sample fabrication	79
Figure 3.2.1: Photo of SEM system used in this thesis	81
Figure 3.2.2: Diagram displaying defining the relative angle between the magnetisation and current vectors, θ	83
Figure 3.2.3: AMR data for 20 nm thick permalloy thin film. Blue curve shows data from negative to positive fields, red shows the reverse procedure. Blue and red arrows help guide the eye of the direction the magnetisation is changing. Insert demonstrates the thin film with the directions of current and magnetisation.	83
Figure 3.2.4: AMR data for a 20 nm thick, 200 nm wide permalloy nanowire. Blue curve shows data from negative to positive fields, red shows the reverse procedure. Blue and red arrows help guide the eye of the direction the magnetisation is changing. Insert demonstrates the nanowire with the directions of current and magnetisation.	84
Figure 3.2.5: SEM images of an example device. Displaying the larger permalloy pads used to connect to gold wires via silver paint for electrical measurements. The sets of four terminals are shown with annotations of V+, V-, I+ and I-. Lighter grey regions represent permalloy structures.	85
Figure 3.2.6: Schematics of the optical setup of the full field soft X-ray transmission microscope XM-1 located at beamline 6.1.2 at the ALS. Taken from [183].	88
Figure 4.1.1: Initial magnetic state of nanowire before relaxation for creation of phase diagram	92
Figure 4.1.2: Phase diagram of domain wall type for varying nanowire dimensions. Blue line is to help guide the eye to the approximate boundary between transverse and asymmetric-transverse DWs. Black line is to help guide the eye to the approximate boundary between asymmetric-transverse and vortex DWs.	92
Figure 4.2.1: Cross-sectional view of a square nanotrench used in simulations.	94
Figure 4.2.2: Initial simulation set-up for nanotrench	95
Figure 4.2.3: Results of 100 nm wide 10 nm thick nanowire with a cell size of 5 nm x 5 nm x 2 nm. a) Depinning field against depth of nanotrench for various nanotrench lengths. b) Depinning field against length of nanotrench for various nanotrench depths. Lines are to guide the eye.	96
Figure 4.3.1: Square nanotrenches in 100 nm wide, 25 nm thick nanowire - Plot of depinning field against nanotrench length (nm) for various nanotrench depths.	97
Figure 4.3.2: Square nanotrenches in 100 nm wide, 25 nm thick nanowire - Plot of depinning field against nanotrench depth (nm) for various nanotrench lengths. Lines are to guide the eye.	97
Figure 4.3.3: a) Plot of energy contributions over simulated time, b) Plot of approximate DW position for reference with plot in a). Blue shaded region represents the location of the nanotrench. Plots made for a 100 nm wide, 25 nm thick nanowire containing a 20 nm deep, 200 nm long square nanotrench. The figure	

focuses on the simulated time over which the DW depins and propagates through the nanowire.....	98
Figure 4.3.4: Energy plot of the exchange and demagnetisation energies for a 100 nm wide, 25 nm thick nanowire containing a 20 nm deep, 200 nm long square nanotrench. The red shaded region represents the location of the nanotrench.	99
Figure 4.3.5: Square nanotrenches in 50 nm wide, 10 nm thick nanowire - Plot of depinning field against nanotrench width (nm) for various nanotrench depths.....	99
Figure 4.3.6: Square nanotrenches in 50 nm wide, 10 nm thick nanowire - Plot of depinning field against nanotrench depth (nm) for various nanotrench widths. Lines are to guide the eye.	100
Figure 4.3.7: Energy plots showing exchange and demagnetisation energy against DW position. Plots for a 50 nm wide, 10 nm thick nanowire containing; a) 9 nm deep, 200 nm long square nanotrench. b) 9 nm deep, 500 nm long square nanotrench. c) 9 nm deep, 1000 nm long square nanotrench. and d) 9 nm deep, 2150 nm long square nanotrench. Red shaded regioned represent location of nanotrench.	101
Figure 4.3.8: Square nanotrenches in 200 nm wide, 50 nm thick nanowire - Plot of depinning field against nanotrench width (nm) for various nanotrench depths.....	102
Figure 4.3.9: Square nanotrenches in 200 nm wide, 50 nm thick nanowire - Plot of depinning field against nanotrench depth (nm) for various nanotrench lengths. Lines are to guide the eye.	102
Figure 4.3.10: Energy plot of the exchange and demagnetisation energies for a 200 nm wide, 50 nm thick nanowire containing a 35 nm deep, 200 nm long square nanotrench. The red shaded region represents the location of the nanotrench....	103
Figure 4.3.11: Cross-sectional schematic of a triangular nanotrench	107
Figure 4.3.12: Triangular nanotrenches in 100 nm wide, 25 nm thick nanowire - Plot of depinning field against nanotrench length at the surface (nm) for various nanotrench depths.	107
Figure 4.3.13: Triangular nanotrenches in 100 nm wide, 25 nm thick nanowire - Plot of depinning field against nanotrench depth (nm) for various nanotrench lengths. Lines are to guide the eye.	108
Figure 4.3.14: Plot of depinning field against length at the surface for triangular nanotrenches for different x cell sizes. Results found for 10 nm deep nanotrench in a 100 nm wide, 25 nm thick nanowire.....	109
Figure 4.3.15: Plot of depinning field against length at the surface for triangular nanotrenches for different z cell sizes. Results found for 10 nm deep nanotrench in a 100 nm wide, 25 nm thick nanowire.....	109
Figure 4.3.16: Energy plot of the exchange and demagnetisation energies for a 100 nm wide, 25 nm thick nanowire containing a 17.5 nm deep, 200 nm long triangular nanotrench. The red shaded region represents the location of the nanotrench. ...	110
Figure 4.3.17: Triangular nanotrenches in 50 nm wide, 10 nm thick nanowire - Plot of depinning field against nanotrench depth (nm) for various nanotrench lengths. Lines are to guide the eye.	111
Figure 4.3.18: Triangular nanotrenches in 50 nm wide, 10 nm thick nanowire - Plot of depinning field against nanotrench length at the surface (nm) for various nanotrench depths.	111
Figure 4.3.19: Energy plots of the exchange and demagnetisation energies for a 50 nm wide, 10 nm thick nanowire containing; a) a 9 nm deep, 50 nm long triangular nanotrench. b) a 9 nm deep, 110 nm long triangular nanotrench. c) a 9 nm deep, 310 nm long triangular nanotrench. The red shaded region represents the location of the nanotrench.	112

Figure 4.3.20: Results of 22.5 nm deep triangular nanotrenches in 100 nm wide, 25 nm thick nanowire..... 113

Figure 4.3.21: Energy plots of the exchange and demagnetisation energies for a 100 nm wide, 25 nm thick nanowire containing; a) a 22.5 nm deep, 100 nm long triangular nanotrench. b) a 22.5 nm deep, 300 nm long triangular nanotrench. c) a 22.5 nm deep, 1000 nm long triangular nanotrench. d) a 22.5 nm deep, 4000 nm long triangular nanotrench. The red shaded region represents the location of the nanotrench. 114

Figure 4.3.22: Triangular nanotrenches in 200 nm wide, 50 nm thick nanowire - Plot of depinning field against nanotrench depth (nm) for various nanotrench lengths. Lines are to guide the eye. 114

Figure 4.3.23: Triangular nanotrenches in 200 nm wide, 50 nm thick nanowire - Plot of depinning field against nanotrench length at the surface (nm) for various nanotrench depths. Data points within the blue circle indicate instances where metastable asymmetric transverse DWs are present. 115

Figure 4.3.24: Example of asymmetric transverse DW occurring beneath a 45 nm deep, 700 nm long triangular nanotrench in a 200 nm wide, 50 nm thick nanowire. 116

Figure 4.3.25: Energy plots of the exchange and demagnetisation energies for a 200 nm wide, 50 nm thick nanowire containing; a) a 35 nm deep, 200 nm long triangular nanotrench. b) a 35 nm deep, 700 nm long triangular nanotrench. c) a 35 nm deep, 2000 nm long triangular nanotrench. The red shaded region represents the location of the nanotrench. 118

Figure 4.3.26: Depinning field against length of nanotrench for various nanotrench depths for transverse DWs found in a 100 nm wide, 25 nm thick nanowire - Square markers indicate square nanotrench. Triangle markers indicate triangular nanotrench. Markers of the same colour represent nanotrenches of the same depth. 120

Figure 4.3.27: Depinning field against length of nanotrench for various nanotrench depths for transverse DWs found in a 50 nm wide, 10 nm thick nanowire - Square markers indicate square nanotrench. Triangle markers indicate triangular nanotrench. Markers of the same colour represent nanotrenches of the same depth. 121

Figure 4.3.28: Depinning field against length of nanotrench for various nanotrench depths for vortex DWs found in a 200 nm wide, 50 nm thick nanowire - Square markers indicate square nanotrench. Triangle markers indicate triangular nanotrench. Markers of the same colour represent nanotrenches of the same depth. 122

Figure 4.3.29: Cross-sectional area comparison of nanotrenches in a 100 nm wide, 25 nm thick nanowire. Square nanotrenches represented by \square with triangular nanotrenches are represented by Δ . Trends of the same colour correspond to nanotrenches of the same depth. 122

Figure 4.3.30: Cross-sectional area comparison of nanotrenches in a 50 nm wide, 10 nm thick nanowire. Square nanotrenches represented by \square with triangular nanotrenches are represented by Δ . Trends of the same colour correspond to nanotrenches of the same depth. 123

Figure 4.3.31: Cross-sectional area comparison of nanotrenches in a 200 nm wide, 50 nm thick nanowire. Square nanotrenches represented by \square with triangular nanotrenches are represented by Δ . Trends of the same colour correspond to nanotrenches of the same depth. 123

Figure 4.3.32: Triangular nanotrenches in 100 nm wide, 25 nm thick nanowire - Plot of depinning field against angle of nanotrench wall for various nanotrench depths.	126
Figure 4.3.33: Plot of depinning field against nanotrench length at the surface (nm) for a 22.5 nm deep triangular nanotrench in a 100 nm wide, 25 nm thick nanowire.	126
Figure 4.3.34: Triangular nanotrenches in 50 nm wide, 10 nm thick nanowire - Plot of depinning field against angle of nanotrench wall for various nanotrench depths.	127
Figure 4.3.35: Triangular nanotrenches in 200 nm wide, 50 nm thick nanowire - Plot of depinning field against angle of nanotrench wall for various nanotrench depths.	127
Figure 4.3.36: Triangular nanotrenches in 100 nm wide, 25 nm thick nanowire - Plot of depinning field against depth of nanotrench wall for various nanotrench wall angles. Lines are to guide the eye.	129
Figure 4.3.37: Triangular nanotrenches in 50 nm wide, 10 nm thick nanowire - Plot of depinning field against depth of nanotrench wall for various nanotrench wall angles. Lines are to guide the eye.	129
Figure 4.3.38: Triangular nanotrenches in 200 nm wide, 50 nm thick nanowire - Plot of depinning field against depth of nanotrench wall for various nanotrench wall angles. Lines are to guide the eye.	130
Figure 4.3.39: Schematic demonstrating dimensions associated with a trapezoidal nanotrench	131
Figure 4.3.40: Trapezoidal nanotrench in a 50 nm wide, 10 nm thick nanowire. Central section of the nanotrench measures 150 nm long, 9 nm deep. This is the 0 nm length data point in both cases - Depinning field against length of nanotrench sidewall. Lines are to guide the eye.	132
Figure 4.3.41: Trapezoidal nanotrench in a 50 nm wide, 10 nm thick nanowire. Central section of the nanotrench measures 150 nm long, 9 nm deep. This is the 0 nm length data point in both cases - Depinning field against angle of nanotrench sidewall.	132
Figure 4.3.42: Energy plots showing exchange and demagnetisation energies for DW position in a a 50 nm wide, 10 thick nanowire containing; a) trapezoidal nanotrench, 9 nm deep with a central length of 150 nm and a slope length of 50nm. b) trapezoidal nanotrench, 9 nm deep with a central length of 150 nm and a slope length of 200nm. c) trapezoidal nanotrench, 9 nm deep with a central length of 150 nm and a slope length of 1000nm. Blue shaded regions represent location of trapezoidal base, whilst red regions represent location of trapezoidal slopes.	134
Figure 4.3.43: Trapezoidal nanotrench in a 200 nm wide, 50 nm thick nanowire. Central section of the nanotrench measures 500 nm long, 30 nm deep. a) Depinning field against length of nanotrench sidewall. b) Depinning field against angle of nanotrench sidewall.	134
Figure 4.3.44: Energy plots showing exchange and demagnetisation energies for DW position in a a 200 nm wide, 50 thick nanowire containing; a) trapezoidal nanotrench, 30 nm deep with a central length of 500 nm and a slope length of 20nm. b) trapezoidal nanotrench, 30 nm deep with a central length of 500 nm and a slope length of 60nm. c) trapezoidal nanotrench, 30 nm deep with a central length of 500 nm and a slope length of 70nm. d) trapezoidal nanotrench, 30 nm deep with a central length of 500 nm and a slope length of 200nm. e) trapezoidal nanotrench, 30 nm deep with a central length of 500 nm and a slope length of 500nm. Blue shaded	

regions represent location of trapezoidal base, whilst red regions represent location of trapezoidal slopes..... 136

Figure 5.1.1: AFM images showing 1 μm long sections of grooves scratched in the "backward" direction implementing various quantities of 5 μN scratches on a 10 nm thick permalloy thin film..... 139

Figure 5.1.2: AFM images showing 1 μm sections of grooves created scratching in the "forward" direction implementing various quantities of 5 μN scratches on a 10 nm thick permalloy thin film..... 140

Figure 5.1.3: AFM images showing 1 μm sections of grooves created scratching in the "upward" direction implementing various quantities of 5 μN scratches on a 10 nm thick permalloy thin film..... 141

Figure 5.1.4: Plots displaying the height of pile-up formed on either side of the grooves generated using a) "backward", b) "forward" and c) "upward" cutting directions implementing various quantities of 5 μN scratches on a 10 nm thick permalloy thin film. Errorbars represent the standard deviation from multiple measurements. 142

Figure 5.1.5: Plots of average a) depth and b) width of the resulting grooves for "forward", "backward" and "upward" cutting directions implementing various quantities of 5 μN scratches on a 10 nm thick permalloy thin film. Errorbars represent the standard deviation from multiple measurements. 143

Figure 5.1.6: SEM image of area containing grooves generated by horizontal scratches of varying force..... 144

Figure 5.1.7: Plots of a) average depth and b) average width for scratches made in the "upward" direction with various applied forces. 144

Figure 5.2.1: Linescan of the 685 nm wide, 11.5 nm thick nanowire including an AFM image of the central 5 μm region. 145

Figure 5.2.2: Example of the raw AMR data for the 685 nm wide, 11.5 nm thick permalloy nanowire before AFM machining. This data contains two hysteresis loops starting in negative fields (shown in the black circle), increasing through 0 field to positive. Trends of different colours represent individual hysteresis loops. 146

Figure 5.2.3: Examples of the AMR data shown in figure 5.2.2 focusing on when the nanowire switches magnetisation. Left plots show the field transitioning from positive to negative fields. Right plots show the field transitioning from negative to positive fields. 147

Figure 5.2.4: AFM image of the resulting nanotrench produced by a 2 μN scratch along the width of the 685 nm wide, 11.5 nm thick nanowire..... 147

Figure 5.2.5: Average linescan of the profile of the nanotrench generated by a 2 μN scratch along the width of the 685 nm wide, 11.5 nm thick nanowire. 148

Figure 5.2.6: Example hysteresis loop of AMR data taken for the 685 nm wide, 11.5 nm thick nanowire with a 3.9 nm deep nanotrench. 149

Figure 5.2.7: AFM image of the nanotrench after the second 1 μN scratch along the width of the 685 nm wide, 11.5 nm thick nanowire..... 149

Figure 5.2.8: Average linescan of the profile of the nanotrench after the second 1 μN scratch along the width of the 685 nm wide, 11.5 nm thick nanowire. 150

Figure 5.2.9: Example of AMR data taken for the 685 nm wide, 11.5 nm thick nanowire with a 4.46 nm deep nanotrench..... 151

Figure 5.2.10: AFM image of the remaining material from the 685 nm wide, 11.5 nm thick nanowire following rupture. 152

Figure 5.2.11: SEM image of the 685 nm wide, 11.5 nm thick nanowire following rupture..... 153

Figure 5.2.12: Examples of AMR data for each step relating to the 685 nm wide, 11.5 nm thick nanowire. The resistance has been converted to arbitrary units, with each dataset offset in order to aid visual comparison.	153
Figure 5.2.13: Plot of depinning field against nanotrench depth for the 685 nm wide, 11.5 nm thick nanowire. Errorbars in this plot represent the standard error on the mean. Data point at 0 nm is actually an injection field but included as a point of reference.	154
Figure 5.3.1: AFM images of the nanotrenches created in ALS wires A, B and C. ..	156
Figure 5.3.2: Top down M-TXM divided images taken at the ALS facility of DWs pinned at the fabricated nanotrench in ALS wire A. Each image shows the DW pinned during independent hysteresis loops.	157
Figure 5.3.3: M-TXM images taken at the ALS facility of DWs pinning and depinning from the fabricated nanotrench in ALS wire A. a) raw unprocessed image to demonstrate nanotrench position. b), c) and d) divided images showing DW pinned and then propagated within a single hysteresis loop. e) and f) divided images showing DW pinned and propagated in a single hysteresis loop.	158
Figure 5.3.4: M-TXM images taken at the ALS facility of DWs pinning and depinning from the fabricated nanotrench in ALS wire B. a) raw unprocessed image to demonstrate nanotrench position. b) and c) divided images showing DW pinned and then propagated within a single hysteresis loop. d) and e) divided images showing DW pinned and propagated in a single hysteresis loop.	158
Figure 5.3.5: M-TXM images taken at the ALS facility of DWs pinning and depinning from the fabricated nanotrench in ALS wire C. a) raw unprocessed image to demonstrate nanotrench position. b) and c) divided images showing DW pinned and then propagated within a single hysteresis loop. d) and e) divided images showing DW pinned and propagated in a single hysteresis loop.	159
Figure 5.4.1: a) AFM image, b) Linescan showing the cross-section of 320 nm wide, 56 nm thick nanowir.	160
Figure 5.4.2: AFM images of the five distinct nanotrenches measured in the 320 nm wide, 56 nm thick permalloy nanowire. a) shows an 18 nm deep nanotrench resulting from a 4.5 μN and four 4 μN scratches. b) a 25 nm deep nanotrench from a further two 4 μN scratches. c) a 30 nm deep nanotrench from a further four 4 μN scratches. d) a 34 nm deep nanotrench from a further three 4 μN scratches. e) a 41 nm deep nanotrench following a further seven 4 μN scratches.....	162
Figure 5.4.3: SEM image of the broken 320 nm wide, 56 nm thick nanowire	163
Figure 5.4.4: Examples of AMR data taken for the 320 nm wide, 56 nm thick nanowire for various nanotrench depths.....	164
Figure 5.4.5: Plot of depinning field against nanotrench depth for the 320 nm wide, 56 nm thick nanowire. Error bars represent the standard error on the mean. Data point at 0 nm indicates the switching field before the presence of a nanotrench and is included as a reference.....	166
Figure 5.4.6: Experimental and computational results for the 320 nm wide, 56 nm thick nanowire.	166
Figure 5.5.1: SEM image of the newer device design.	168
Figure 5.5.2: SEM images of the four nanowires within the new design.	169
Figure 5.5.3: Example of AMR data for wire A in the new device. a) shows the field passing from positive into negative field values, whilst b) shows the opposite. In both plots, the left y-axis represents the resistance before the introduction of a nanotrench, the right y-axis shows the resistance after.	170

Figure 5.5.4: Example of AMR data for wire B in the new device. a) shows the field passing from positive into negative field values, whilst b) shows the opposite. In both plots, the left y-axis represents the resistance before the introduction of a nanotrench, the right y-axis shows the resistance after..... 170

Figure 5.5.5: Example of AMR data for wire C in the new device. a) shows the field passing from positive into negative field values, whilst b) shows the opposite. In both plots, the left y-axis represents the resistance before the introduction of a nanotrench, the right y-axis shows the resistance after..... 171

Figure 5.5.6: Example of AMR data for wire D in the new device. a) shows the field passing from positive into negative field values, whilst b) shows the opposite. In both plots, the left y-axis represents the resistance before the introduction of a nanotrench, the right y-axis shows the resistance after..... 172

Figure 5.5.7: AFM images of the generated nanotrenches in all four nanowires of the new sample design. 173

Figure 5.5.8: AFM image of nanowires D (left) and C (right) following wire D breaking..... 174

Figure 5.6.1: AFM image of extended nanotrench created in a 445 nm wide, 42 nm thick nanowire. 176

Figure 5.6.2: Average linescan of extended nanotrench created in a 445 nm wide, 42 nm thick nanowire..... 177

Figure 5.6.3: M-TXM images taken at the ALS facility of DWs pinned at the fabricated extended nanotrench in a 445 nm wide, 42 nm thick nanowire. Each row of images are taken from separate hysteresis loops. a) raw unprocessed image to demonstrate nanotrench position. b) and c), d) and e), f) and g) are pairs of divided images showing DW pinned and then propagated within separate hysteresis loops. 177

Figure 5.6.4: AFM images a) side-view, b) top-down view of L-shaped feature created within a 570 nm wide, 57 nm thick nanowire. White outlines to guide the eye to the overall shape of the feature. 178

Figure 5.6.5: Plot of linescan across the width of the 570 nm wide, 57 nm thick nanowire displaying the thickness change across the L-shaped nanotrench..... 179

Figure 5.6.6: M-TXM images taken at the ALS facility of DWs pinned at the fabricated L-shaped nanotrench in a 570 nm wide, 57 nm thick nanowire. Each row of images are taken from separate hysteresis loops. a) raw unprocessed image to demonstrate nanotrench position. b) and c), d) and e), f) and g) are pairs of divided images showing DW pinned and then propagated within separate hysteresis loops. 180

Figure 5.6.7: AFM images showing a) and b) side-views, c) top-down view of the alternating indentations created along a 560 nm wide, 50 nm thick nanowire. The green circles are to guide the eye to highlight the features..... 180

Figure 5.6.8: M-TXM divided images taken at the ALS facility of DWs moving between alternating indentations a 560 nm wide, 50 nm thick nanowire. a), b) and c), d), e) and f) are sets of images showing DW pinned and then propagated within separate hysteresis loops. 181

List of Tables

Table 1.1: Energies contributions in a ferromagnet, values from [5]	7
Table 3.1: Material parameters of permalloy used in OOMMF simulations	90
Table 4.1: Results of Chirality test for square nanotrench. Transverse DWs produced in 50 nm wide, 10 nm thick nanowire. Vortex DWs produced in 200 nm wide, 50 nm thick nanowire. Depinning fields given in Oe.	106
Table 4.2: Results of Chirality test for a triangular nanotrench. Transverse DWs produced in 50 nm wide, 10 nm thick nanowire. Vortex DWs produced in 200 nm wide, 50 nm thick nanowire. In the vortex cases, the first values correspond to the 100 nm long nanotrench whilst the second are the results of the 200 nm long nanotrench. Depinning fields given in Oe.....	119
Table 5.1.1: Details of experimental ALS nanowires A, B and C.....	155
Table 5.2: Summary of depinning field results for the 320 nm wide, 56 nm thick permalloy nanowire.....	165

List of Acronyms

AFM	Atomic Force Microscope
ALS	Advanced Light Source
AMR	Anisotropic Magnetoresistance
ATDW	Asymmetric Transverse Domain Wall
CCD	Charge-coupled device
DW	Domain Wall
EBL	Electron Beam Lithography
EUV	Extreme Ultra-Violet
FFM	Friction Force Microscope
FIB	Focused Ion Beam
FMOKE	Focused Magneto-Optical Kerr Effect
FZP	Fresnel Zone Plate
HDD	Hard Drive Disk
HtH	Head-to-Head
LDW	Landau Domain Wall
LL	Landau-Lifshitz
LLG	Landau-Lifshitz-Gilbert
MOKE	Magneto-Optical Kerr Effect
MRAM	Magnetoresistive Random-Access Memory
M-TXM	Magnetic Transmission X-Ray Microscopy
MZP	Micro Zone Plate
OOMMF	Object Orientated MicroMagnetic Framework
PMMA	Polymethyl methacrylate
PSPD	Photo-Sensitive Photo Diode
RKKY	Ruderman-Kittel-Kasuya-Yosida interaction
SEM	Scanning Electron Microscope
SSD	Solid State Drive
STM	Scanning Tunnelling Microscope
TDW	Transverse Domain Wall
TtT	Tail-to-Tail
UV	Ultra-Violet
VDW	Vortex Domain Wall
XMCD	X-ray magnetic circular dichroism

List of Symbols

The following symbols are presented in the order they appear within this thesis. Bold symbols represent vector quantities whilst other are scalar values.

$\boldsymbol{\mu}$	Magnetic moment
I	Current
\boldsymbol{S}	Area
γ	Gyromagnetic ratio
\boldsymbol{L}	Angular momentum
\boldsymbol{M}	Magnetisation
\boldsymbol{H}	Magnetic field strength
μ_0	Permeability of free space
χ	Magnetic susceptibility
μ	Magnetic permeability of a material
μ_r	Relative permeability
$\hat{\mathcal{H}}$	Heisenberg Hamiltonian
J_{ij}	Exchange constant
\boldsymbol{S}	Spin
g	Landé factor
μ_B	Bohr Magneton
e	Charge of an electron
\hbar	Planck's constant over 2π
m_e	Mass of an electron
c	Speed of light
T_c	Curie point
T	Temperature
C	Curie constant
M_s	Saturation magnetisation
M_r	Remanence field
H_c	Coercive field
\boldsymbol{m}	Unit vector for the atom's magnetisation
ε_{tot}	Total free energy of a ferromagnet
ε_{ex}	Exchange energy
ε_{an}	Anisotropy energy
ε_d	Demagnetisation energy
ε_z	Zeeman energy

ε_{stress}	External stress energy
ε_{ms}	Magnetostrictive energy
A	Exchange stiffness
n	Number of atoms per unit cell
a	Lattice constant
K_1 & K_2	Anisotropy constants
K_s	Surface anisotropy constant
\mathbf{n}	Unit vector parallel to the normal pointing out of the surface
\mathbf{H}_d	Demagnetising field
l_{ex}	Exchange length
V	Volume
α	Angle of the applied field from the easy-axis
θ	Angle of the magnetisation from the easy-axis
$U(x)$	One-dimensional potential energy
H_{depin}	Depinning field
\mathbf{H}_{eff}	Effective field
α_G	Gilbert damping parameter
γ_G	Gilbert gyromagnetic ratio
α_{LL}	Landau-Lifshitz damping parameter
γ_{LL}	Landau-Lifshitz gyromagnetic ratio
F_n	Normal force
k	Normal spring constant of the cantilever
δ_n	Vertical deflection at the free end of the cantilever
V_{A-B}	Output voltage
S_n	Normal sensitivity of the PSPD
R	Resistance
ρ	Material resistivity
L	Length of the current path

1. Introduction

1.1 Nanomagnetism

1.1.1 The origin of magnetic moments from electrons

Magnetism effects many areas of science as fundamentally all materials are magnetic. This can be attributed to the electromagnetic nature of atoms and their orbiting electrons. In classic electromagnetism, it is found that an electric current generates a magnetic field. If a current, I is following around an elementary oriented loop of area $|dS|$, the magnetic moment $d\mu$ produced by this elementary current loop is $d\mu = IdS$ and will have the units A m². Integrating over the area of the finite current loop gives the magnetic moment as[2]:

$$\mu = I \int dS \quad (1.1)$$

For an individual atom, the magnetic moment can be calculated from three key components. The first is associated with the orbiting electron. This can be considered an accelerating charge and so produces a magnetic field and an associated magnetic moment due to its circular motion implying constant acceleration. The magnetic moment lies along the same direction as the angular momentum, L . The magnetic moment is found to be proportional to the angular momentum and is given by[2]:

$$\mu = \gamma L \quad (1.2)$$

where γ is the gyromagnetic ratio. Another contribution to the total magnetic moment of an atom is due to the spin of the electron. Electron spin is complex in nature due to its quantum mechanical properties, but can be quantised as two defined states of spin up and spin down. The final component is due to the intrinsic spin associated with the nucleus of the atom. This is similar to that of the electron; however this contribution is approximately three orders of magnitude smaller than the contribution of the electron. As such, it is often neglected in calculations of the total magnetic moment of an atom.

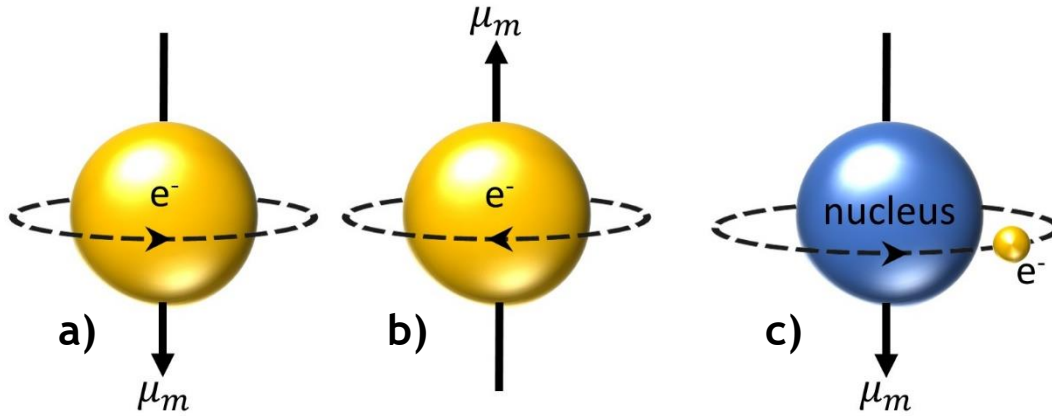


Figure 1.1.1: a) and b), schematic of an electron and its associated magnetic moment due to spin. c), schematic of a nucleus and its associated magnetic moment due to the orbiting electron.

The magnetisation, \mathbf{M} of a material is defined as the magnetic moment per unit volume. The magnetisation in bulk is the combination of all the individual magnetic moments. However, \mathbf{M} is treated as a smooth vector field throughout the material, except for at its edges. Historically the magnetic field vector has been referred to in two ways. \mathbf{B} is known as the magnetic induction or magnetic flux density and is typically used with the units of Tesla, T, whereas \mathbf{H} is referred to as the magnetic field strength and is measured in A m^{-1} . In a vacuum, these two quantities are related to each other by, $\mathbf{B} = \mu_0 \mathbf{H}$ where μ_0 is the permeability of free space. In solids this is extended to:

$$\mathbf{B} = \mu_0 (\mathbf{H} + \mathbf{M}) \quad (1.3)$$

1.1.2 Magnetic Susceptibility

There are a number of different types of magnetic materials and each respond to magnetic fields differently. The key categories of magnetism are paramagnetism, diamagnetism, ferromagnetism, antiferromagnetism, ferrimagnetism and superparamagnetism. The magnetic properties of a material can be distinguished using two parameters known as the magnetic susceptibility, χ and the relative permeability, μ_r . The magnetic susceptibility is defined as the ratio between the material's induced magnetisation and the externally applied magnetic field:

$$\chi = \frac{M}{H} \quad (1.4)$$

The magnetisation, M and the applied field, H both have the units A m^{-1} , therefore the susceptibility, χ is a dimensionless quantity. χ can be positive or negative and

can give an indication of the properties of the material. For example, if χ is negative, then the material is dominated by diamagnetism, whereas a positive χ indicates the material is dominated by another form of magnetism such as paramagnetism, ferromagnetism or ferrimagnetism.

As well as the magnetic susceptibility, the magnetic permeability, μ can be used to define a magnetic material. The magnetic permeability of a material is given by:

$$\mu = \mu_0 \mu_r \quad (1.5)$$

Where μ_0 is the permeability of free space again, and μ_r is the relative permeability of the material. The relative permeability of a material is related to the magnetic susceptibility and is defined by:

$$\mu_r = 1 + \chi \quad (1.6)$$

This thesis concentrates on phenomena that occur in ferromagnetic materials and only includes experiments conducted on ferromagnetic materials. Therefore no further detail shall be given on the other categories of magnetic materials. However, the next section will go into further detail of ferromagnetism.

1.1.3 Ferromagnetism

Ferromagnetic materials differ from diamagnetic and paramagnetic materials such that they are able to maintain magnetisation in the absence of an externally applied field. This occurs due to quantum mechanical interactions between the atomic spins, that overlap in wavefunction, known as exchange interactions. Further detail about exchange energies will be discussed later in this chapter. It is a short range interaction that only effects nearest neighbours. In ferromagnetic materials, the moments have preference to align with one another. The exchange energy between a pair of spins is proportional to $\mathbf{S}_i \cdot \mathbf{S}_j$ where \mathbf{S}_i and \mathbf{S}_j are the spins of the i^{th} and j^{th} spins in the ensemble. For a large ensemble of spins in an applied magnetic field \mathbf{H} , the energy of the system is given by the Heisenberg Hamiltonian [2]:

$$\hat{\mathcal{H}} = - \sum_{i \neq j} J_{ij} \mathbf{S}_i \cdot \mathbf{S}_j + g \mu_B \sum_j \mathbf{S}_j \cdot \mathbf{H} \quad (1.7)$$

Where J_{ij} is the exchange constant, \mathbf{S}_i and \mathbf{S}_j are the i^{th} and j^{th} spins in the ensemble respectively, g is the so-called ‘‘Landé factor’’ and μ_B is the Bohr magneton (defined as $\mu_B = \frac{|e|\hbar}{2m_e c}$). The exchange constants define how neighbouring spins will interact with each other. A positive J_{ij} will have preference to align neighbouring spins with each other (as in ferromagnetism), whereas negative J_{ij} will cause spins to align

anti-parallel with one another (as in antiferromagnetism). There are other forms of J_{ij} that result in other forms of interactions, such as RKKY interactions (indirect exchange that occurs in metals between magnetic ions mediated by conduction electrons) [2] but are not needed for this thesis. The first term in the Hamiltonian is known as the Heisenberg exchange energy, and the second term is known as the Zeeman energy. The Zeeman energy will be discussed further later in this chapter. In addition to these terms, another contribution from magnetocrystalline anisotropy can be considered. Energy contributions related to this will be discussed further later in this chapter. However, the structures created for this thesis consist of permalloy ($\text{Ni}_{81}\text{Fe}_{19}$) which is a soft ferromagnetic material that has negligible anisotropic effects when in crystalline form[3]. Therefore, contributions from anisotropy will not be considered at this stage.

To try and explain these interactions in 1907, Pierre-Ernest Weiss proposed the existence of an internal molecular field in ferromagnetic materials [4]. He proposed that the molecular field was responsible for attempting to align the magnetic dipoles of atoms against thermal fluctuations due to the dominant exchange interactions being positive. Thermal fluctuations have a preference towards complete disorder of the magnetic dipoles resulting in a zero magnetic field within the material without the presence of an externally applied field. As the temperature increases, the thermal fluctuations work to destroy the magnetic ordering within a material. At a critical temperature, known as the Curie point T_c , all magnetic ordering is destroyed and a ferromagnetic material becomes paramagnetic and so cannot hold magnetisation in a zero field. In this regime, the thermal fluctuations are strong enough to completely overcome the exchange interactions between spins. This gives rise to the Curie-Weiss law, which gives the magnetic susceptibility for a ferromagnetic in temperatures about the Curie point [5]:

$$\chi = \frac{C}{T - T_c} \quad (1.8)$$

where C is the Curie constant of the material, T is the temperature, and T_c is the Curie point. The Curie point for ferromagnetic materials is are typically in the order of $T_c \sim 10^3 K$, however some ferromagnets are known to have a T_c much lower, some even below room temperature[2].

The Weiss field explains the temperature dependence and the resulting paramagnetism at high temperatures, but the model leads to there being constant magnetisation for ferromagnets below the Curie point. To try and explain the

unusual field dependence that occurs within ferromagnets, Weiss assumed that the materials were made up of many domains. A domain is referred to as a small region of a material within which all of the local dipoles are aligned. However, not all regions (domains) within the material are aligned with one another. These magnetic domains contribute to magnetic hysteresis, in which the magnetisation of the material is dependent on the history of the externally applied field.

To further understand why hysteresis occurs within ferromagnets, the behaviour of magnetic domains within the material needs to be discussed. If a ferromagnetic alloy is mixed and cooled in zero applied field, the resulting ferromagnet will produce no net external magnetic field. This is due to the presence of many domains all with their magnetisation pointing in random directions as shown in figure 1.1.2. Opposing domains of similar size cancel each other out and so random domain formations produce no net magnetisation. When an external field is applied, this causes the domains most closely aligned with it to grow in size. Within the boundaries of the domains (known as domain walls, and will be discussed in further detail later in this chapter) the spins rotate to align with the external field. As these domains grow, they start to produce a stronger field than the domains opposing them, therefore creating an overall net magnetisation. If the external field grows in strength, this will cause the domains to continue to grow until the entire sample becomes magnetised in the same direction. This is known as magnetic saturation and the field produced by the sample is known as the saturation magnetisation, M_s . Reducing the applied field to zero results in various responses depending on the properties of the ferromagnet. Removing the applied field from a hard magnetic material will result in a minimal change in its magnetisation, providing a square hysteresis loop. However in the case of soft magnetic materials, the magnetisation can be reduced significantly when the applied field is removed[6]. The remaining magnetic field produced by the material once the applied field is reduced to zero is known as the remanence field, M_r . To remove this magnetisation, a field must now be applied in the opposite direction. This will cause spins within domains to begin to rotate to align in the new direction. The value of the applied field needed to reduce the net magnetisation of a sample to zero is known as the coercive field, H_c . Increasing the strength of the applied field will result in magnetic saturation of the sample in the opposite direction but with the same absolute value of M_s . Increasing the applied field back through to positive values will produce the same results as when reversing the field previously. A plot of this phenomenon can be seen in figure 1.1.2 and is known as a hysteresis loop. The area enclosed within the loop can be related to the

amount of energy that is lost from the system during the whole cycle, primarily as heat. A ferromagnet may be return to true zero field with random domains by heating it beyond the Curie point such that it returns to a paramagnet and then cooling it in a zero field.

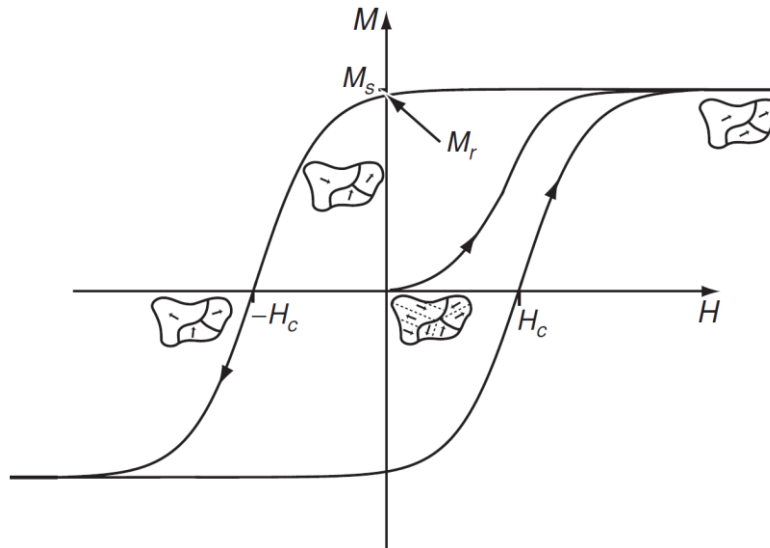


Figure 1.1.2: An example of a ferromagnetic hysteresis loop, taken from [6]

1.1.4 Micromagnetics

Micromagnetism, termed by W. Brown in 1940, is the attempt to describe what is happening within ferromagnetic materials at sub-micron scales. When attempting to do this, challenges such as the Heisenberg Hamiltonian cannot be solved quantum mechanically. Even if the energy terms are disregarded in an attempt to simplify the scenario. As such, until another theory can be developed, the only way to attempt to explain micromagnetic behaviour is to not consider quantum mechanics by ignoring the atomic nature of matter and use classical physics within a continuous medium. This research began in 1935 in a paper published by Landau and Lifshitz [7] that studied the structure of the wall between two anti-parallel domains. Brown then further this work in 1940-1 with several works being published [8]. This classical approach replaces the spins with classical vectors. More specifically, the moments of the atoms are described using a varying vector field of magnetisation, defined by:

$$\mathbf{m} = \frac{\mathbf{M}}{M_s} \quad (1.9)$$

\mathbf{m} is the unit vector for the atom's magnetisation, where \mathbf{M} is the magnetisation and M_s is the saturation magnetisation. To calculate the domain structure within ferromagnets, it is necessary to find the minimum energy state of the system. The

micromagnetic equations are derived from minimisation of the total free energy with respect to \mathbf{m} as done by Brown [8]. The total free energy of a ferromagnet is made up of six competing energy terms [6]:

$$\varepsilon_{tot} = \varepsilon_{ex} + \varepsilon_{an} + \varepsilon_d + \varepsilon_z + \varepsilon_{stress} + \varepsilon_{ms} \quad (1.10)$$

where ε_{tot} is the total energy and the six key terms on the right hand side of equation 1.10 are the exchange ε_{ex} , anisotropy ε_{an} , demagnetisation ε_d , Zeeman ε_z , stress ε_{stress} and magnetostrictive ε_{ms} energy components. The first three terms on the right hand side of equation 1.10 are always present to an extent in ferromagnets. The Zeeman energy is a result of an externally applied field and is responsible for defining the magnetisation process and the corresponding hysteresis loop. The final two terms are caused by externally applying stress and magnetostriction, these two terms are typically ignored during numerical calculations as their associated energies are small in comparison to the contributions of the other energy terms (see table 1.1). This leaves four key energy terms that contribute to the total free energy of a ferromagnet, each will be discussed in turn as follows.

Table 1.1: Energies contributions in a ferromagnet, values from [5]

Energy term	Energy density, in kJ m^{-3}
Exchange, ε_{ex}	$10^3 - 10^5$
Anisotropy, ε_{an}	$10^{-1} - 10^4$
Demagnetisation, ε_d	$0 - 2 \times 10^3$
External field energy (in 1 T), ε_z	$10^2 - 10^3$
External stress energy (in 1 GPa), ε_{stress}	$1 - 10^2$
Magnetostrictive, ε_{ms}	$0 - 1$

The exchange energy is related to the interactions between spins and so has quantum mechanical origins. As previously discussed, in ferromagnets spins have a preference to align with one another. Therefore any deviations from the ideal case costs energy. If it is assumed that the angles between neighbouring spins are small, a Taylor expansion can be made around the neighbouring spin. This is then summed over all neighbouring sites from equation 1.7 and then divided by the unit cell volume. This gives the exchange energy expression as:

$$\varepsilon_{ex} = \int_V A(\nabla\mathbf{m})^2 dV \quad (1.11)$$

The integral is conducted over the whole volume of the ferromagnet. Where $\nabla \mathbf{m}$ is the gradient of \mathbf{m} , i.e. $(\nabla \mathbf{m})^2 = |\nabla m_x|^2 + |\nabla m_y|^2 + |\nabla m_z|^2$, \mathbf{m} is the unit vector magnetisation defined in equation 1.9 and A is a material dependent “exchange stiffness”. This exchange stiffness has units of J/m and can be related to the exchange constant J that appears in equation 1.7:

$$A = \frac{JS^2n}{a} \quad (1.12)$$

where S is the spin of the atoms, a is the lattice constant and n is the number of atoms per unit cell, i.e. 1 in a cubic lattice, 2 for a body centred cubic or 4 in a face centred cubic. The value of A in permalloy (~80% Ni, ~20% Fe) is found to be 1.3×10^{-11} J/m[9].

The second term found on the right hand side of equation 1.10 is the anisotropy energy. Magnetocrystalline anisotropy arises from spin-orbit interactions where there is partial quenching of the angular momentum. The electron orbits are linked to the crystallographic structure, and so the interactions result in crystals having magnetic easy and hard axes. This means that it is easier to magnetise the crystal in particular directions than others. So it costs energy to move the magnetisation away from the direction of the energetically favourable easy axis. The magnetocrystalline energy is usually small in comparison to the exchange energy. In the case of uniaxial anisotropy, the additional energy is in the form:

$$\varepsilon_{an} = K_1 \sin^2 \theta + K_2 \sin^4 \theta \quad (1.13)$$

where θ is the relative angle between the magnetisation and the easy axis and K_1 and K_2 are anisotropy constants that have units of energy/volume. These constants can be found experimentally and the values for Ni, Fe and permalloy can be found in table 1.2. In a cubic system the form of the anisotropy changes to:

$$\varepsilon_{an} = K_1(m_x^2 m_y^2 + m_y^2 m_z^2 + m_z^2 m_x^2) + K_2 m_x^2 m_y^2 m_z^2 \quad (1.14)$$

Where $\mathbf{m} = (m_x, m_y, m_z) = \mathbf{M}/|\mathbf{M}|$.

Table 1.2: Anisotropy constants for Nickel, Iron and Permalloy (NiFe). Values taken from [9] for Ni and Fe and [10] for NiFe.

Material	K_1 (J/m ³)	K_2 (J/m ³)
Ni	$\sim 4.5 \times 10^3$	2.5×10^3
Fe	4.8×10^4	1×10^4
Permalloy (NiFe)	$\sim 10^{-3}$	$\sim 10^{-3}$

There are other forms of anisotropy that occur as a result of other forms of asymmetry. At the edges of the material there is surface anisotropy. In 1954, Néel [10] noted the importance of the reduced symmetry the surface of ferromagnets. This is due to the spins only having neighbours on one side and so the exchange energy cannot be the same as within the bulk. There will be a tendency for spins to align parallel or perpendicular to the surface. This leads to a first-order approximation of the energy term to be[5]:

$$\varepsilon_s = \frac{1}{2}K_s \int (\mathbf{n} \cdot \mathbf{m})^2 dS \quad (1.15)$$

where \mathbf{n} is a unit vector parallel to the normal pointing out of the surface and K_s is the coefficient for surface anisotropy. The integral is done over the surface of the ferromagnet. The form of equation 1.15 makes the assumption that the surface anisotropy is a geometrical feature that depends on the shape of the surface alone.

The fourth and final term to be discussed of equation 1.10 is the demagnetisation energy. This can also be called the stray field energy or the magnetostatic energy. It is connected to the magnetic field that is produced by the dipole-dipole interactions of individual magnetic moments. As regions of the magnetic body align with one another, this will create a larger net magnetisation and will result in magnetic fields being produced outside of the body. This makes it very dependent on the distribution of magnetisation throughout the body. The demagnetisation energy works over larger scale distances than the exchange energy as all moments may affect one another. The demagnetisation energy is given in the form:

$$\varepsilon_d = \frac{\mu_0}{2} \int_{all\ space} \mathbf{H}_d^2 dV = -\frac{\mu_0}{2} \int_{sample} \mathbf{H}_d \cdot \mathbf{M} dV \quad (1.16)$$

where ε_d is the demagnetisation energy, μ_0 is again the permeability of free space and \mathbf{H}_d is the demagnetising field. The factors of 2 are there to avoid double counting the interactions between dipoles. The first integral is carried out over all space and shows that the energy is always positive, and so the only way to obtain zero demagnetisation energy is to produce no demagnetising field. The second integral in equation is done over the volume of the sample and is usually easier to evaluate. In order to reduce the demagnetisation energy, the sample will attempt to arrange the internal magnetisation such that it produces a weaker stray fields. This involves splitting the sample up into a number of magnetic domains. Figure 1.1.3 demonstrates how this can help in the reduction of stray fields.

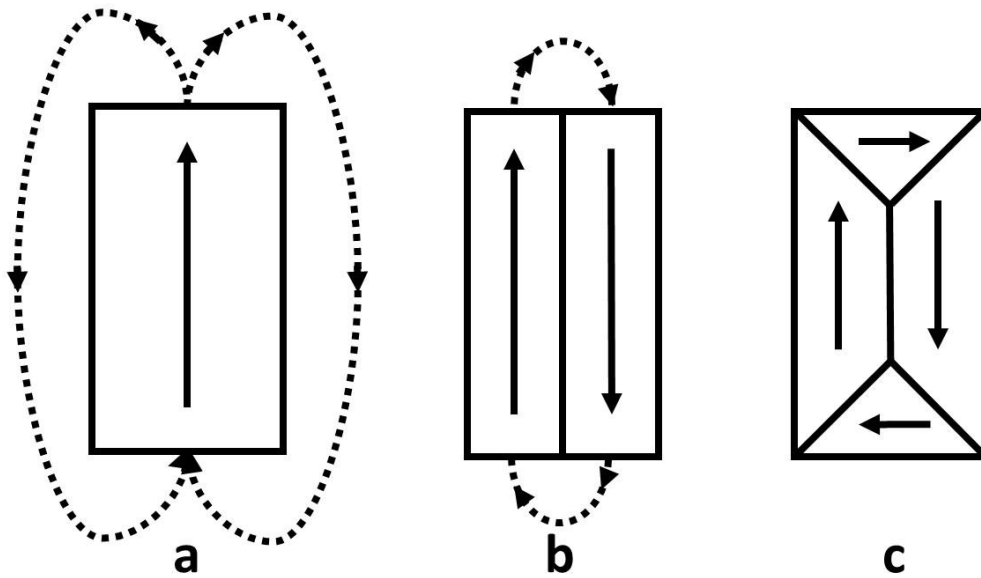


Figure 1.1.3: Demonstrating the various stages domain creation to reduce stray fields. Dashed arrows represent external stray fields whilst solid arrows represent internal magnetisation of the domain.

Figure 1.1.3a demonstrates a uniformly magnetised sample and the resulting stray field. As there are no opposing magnetic moments, a large stray field is created by magnetic moments at the surface external to the magnetic body. If the sample was to split itself into two anti-parallel domains (as in figure 1.1.3b), the opposing magnetic moments reduce the net magnetisation greatly, also reducing the effects of the surface moments by a considerable amount. This results in a far weaker stray field. If the magnetic body was to split into further domains (shown in figure 1.1.3c), then the stray field can be eliminated altogether. When the stray field is reduced to zero, as in figure 1.1.3c, it is known as a flux closure state, with the smaller edge domains known as flux closure domains. In order to reduce the demagnetisation energy, the body will continue to split into smaller domains until the energy cost of creating the domain becomes larger than the resulting reduction in energy. These domains are separated by boundaries known as domain walls (DWs). These DWs have been very significant in technological research in recent years and will be the key focus of this thesis. The next section will discuss DWs in more detail.

Another result of the demagnetising field is shape anisotropy. It occurs in a similar way to surface anisotropy. At reduced dimensions the shape of the material can influence the energetically favourable directions for magnetisation. Shape

anisotropy in thin films leads to an energetic saving if the magnetisation stays within the plane of the film.

Within magnetic bodies there are competing energy terms. As previously discussed, the exchange energy has the preference to align spins with one another and attempts to do this over the whole sample. However, the magnetocrystalline anisotropy and the demagnetising field tries to align spins relative to favoured crystallographic axes and contours of the sample shape. These competing energies result in a term known as the exchange length [11], [12]. The exchange length is the distance within the magnetic body in which the magnetisation is approximately constant. This exchange length is defined as [13]:

$$l_{ex} = \sqrt{\frac{2A}{\mu_0 M_s^2}} \quad (1.17)$$

where A is the exchange constant, μ_0 the permeability of free space and M_s the saturation magnetisation. This form of the exchange length does not consider contributions from magnetocrystalline anisotropy. As discussed earlier, as the structures in this thesis consist of permalloy, this form of the exchange length is acceptable for us to consider. The relevant parameter values for Ni, Fe and permalloy can be found in table 1.3.

Table 1.3: Material parameters for Nickel, Iron and permalloy. Values taken from [8]

Material	A , (J/m)	M_s , (A/m)	l_{ex} , (m)
Fe	10^{-11}	17×10^5	$\sim 2.3 \times 10^{-9}$
Ni	10^{-11}	4.82×10^5	$\sim 20.7 \times 10^{-9}$
Permalloy (NiFe)	1.3×10^{-11}	8×10^5	$\sim 5.7 \times 10^{-9}$

1.1.5 Domains and Domain Walls

As discussed earlier, Weiss first proposed that a ferromagnetic material consists of many regions known as domains [4]. These domains may not be aligned with one another and can have opposing magnetisations resulting in a small or even zero net magnetisation for the whole body. The creation of domains is due to the competition between the exchange interactions and the demagnetising field. The anisotropy does not influence the resulting magnetisation direction of domains once created due to the fact if a direction, $+x$ is a crystallographic easy axis, then so is the $-x$ direction. Therefore there is no anisotropy energy difference in the domains being parallel or anti-parallel to one another.

Separating the magnetisation into multiple domains does work against the exchange interactions, which prefer spins to be aligned. Even very rough estimations show that the loss of exchange energy is much larger than the gained magnetostatic energy. Following this logic, a system consisting of two anti-parallel domains will have a larger energy than a system of uniform magnetisation. So the system would naturally prefer to be uniformly magnetised.

However, magnetostatic forces work over a very long range and so have the ability to control behaviour over larger distances. This is very different to the exchange interactions that only work over very short distances (nearest neighbour). Due to these opposing behaviours, a compromise can be made between the two. With the preference to align, a large exchange energy occurs when there is an abrupt change in spin angles. However, if a wall was placed between the two domains, within which the angles between neighbouring spins is small, then this reduces the exchange energy greatly. This results in a finite wall where spins gradually rotate from $\phi = 0 \rightarrow \pi$ as opposed to the previously considered case where the direction of spins changed abruptly.

These regions or boundaries between domains within which the spins rotate are known as Domain walls (DWs). DWs can be defined relevant to the change in magnetisation across them. For example, if the magnetisation either side of the wall is anti-parallel, then the wall is labelled a 180° wall. If the magnetisation changes by an angle of 90° , then it is labelled a 90° wall. Examples of these are shown in figure 1.1.4 to help visualise these. Due to the size and shape of the devices used for experimentation in this thesis, we will only be discussing 180° walls.

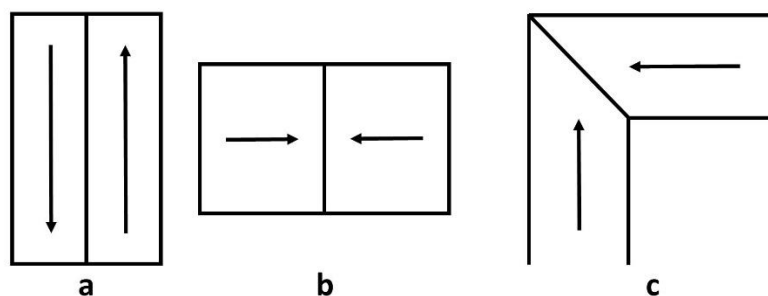


Figure 1.1.4: Examples of a 180° DW (a and b) and a 90° DW (c)

There are various DW structures that can occur, each depend on the energy contributions and how they can each be minimised. The two most common DW structures known and studies are the Bloch DW and the Néel DW. The key difference

between the two structures concerns the rotation axis of the spins as they turn relative to the spin directions. Bloch walls are most common with the spins rotating in the plane of the wall. For example, if the DW extends through the xz plane, then the magnetisation varies only along the y axis, as demonstrated in figure 1.1.5a. This is the most common DW structure and occur in larger bulk materials.

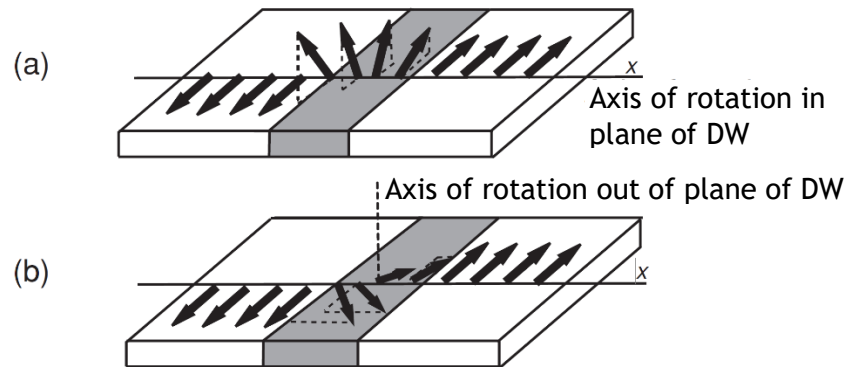


Figure 1.1.5: Schematic of a) a Bloch wall, and b) a Néel wall [6]

In a finite crystal, along the surface any wall structure will contain a non-zero normal component due to surface charges. This needs to be taken into account. In 1955, Néel recognised that this surface charge energy can become too large in very thin films due to them having a larger surface than volume. He suggested a new structure of DW where the surface charge is replaced by a volume charge, showing that the total energy could be reduced by such a transformation. As the film thickness increases, the presence of Bloch walls take over as the energy of the body's surface charge becomes smaller than the volume charge. Therefore Néel DWs occur more commonly in thin films and bodies of smaller dimensions. They may be present in larger bulk materials but would occur close to the surface. This is due to the increase in anisotropy (due to magnetocrystalline or shape) creating a secondary easy axis perpendicular to the DW plane. Therefore it becomes energetically favourable to rotate the spins perpendicular to the DW plane (seen in figure 1.1.5b). Various 1D models conclude that there should be a sharp transition from Bloch to Néel DWs as the size of the sample varies[5]. This is not the case in practice. Experiments have shown the presence of a third type of DW at the boundary between the two cases. The wall structures alternate between Bloch and Néel walls creating a so-called cross-tie wall [14]. These structures are very complicated and cannot be one-dimensional due to a periodicity in the z -direction [5]. As of yet, a theoretical model of the cross-tie wall has not been established.

1.1.6 Magnetic Switching

Energy minimisation of a ferromagnet using equation 1.10 can be used to try and understand the mechanisms of magnetisation reversal. Magnetic reversal can be spontaneous due to thermal fluctuations, or due to the presence of an applied field[6]. The exact process of how the magnetisation switches is due to various factors, including the current micromagnetic configuration. Generally there are three key ways in which magnetic switching occurs. These are coherent rotation, curling and domain wall propagation. As previously discussed, Brown pioneered the use of micromagnetic equations and used them to study magnetic reversal [15]-[17]. These studies resulted in the “linearised Brown’s equations”. The solutions to these equations provide information on the reversal modes. Two analytic solutions could be written for the cases of a sphere and an infinite circular cylinder. One could then be generalised to any ellipsoid whilst the other to an ellipsoid of revolution. These solutions provided two eigenfunction each referring to a different mode of reversal [5].

The first and simplest eigenfunction is coherent rotation and is the basis and a key assumption of the well-known Stoner-Wohlfarth model[18]. This model is based on the Stoner-Wohlfarth particle, a uniformly magnetised ellipsoid that has no crystalline or uniaxial anisotropy but does have shape induced anisotropy. As such the easy axis of the particle is along the long-axis of the ellipsoid. Uniform magnetisation results in zero exchange energy, so the total energy of the particle becomes a summation of the anisotropy and Zeeman energies:

$$\varepsilon = K_1 V \sin^2 \theta - \mu_0 M_s V H \cos(\alpha - \theta) \quad (1.18)$$

where V is the volume, H is the applied field, α and θ are the angles of the applied field and magnetisation from the easy axis respectively. These angles are demonstrated in figure 1.1.6a. Equation 1.18 can be used to find the equilibrium solutions for θ using the requirement that $\partial\varepsilon/\partial\theta = 0$. To establish stable equilibrium points, there is the extra requirement that $\partial^2\varepsilon/\partial\theta^2 > 0$, with $\partial^2\varepsilon/\partial\theta^2 = 0$ giving the boundary between stable and unstable solutions. This boundary gives the critical switching field H_{switch} and is defined by parametric equations made up of the components parallel, H_{\parallel} and perpendicular, H_{\perp} to the easy axis. Plotting H_{\perp} vs H_{\parallel} gives the well-known Stoner-Wohlfarth astroid shown in figure 1.1.6b. External fields with values above H_{switch} lie outside of the astroid and lead to a single stable state. Meaning that any field above H_{switch} will caused the magnetisation within the ellipsoid to rotate and align to a single stable direction regardless of its initial

orientation. However within the astroid, there are two locally stable states with an energy barrier separating them. Magnetisation switching cannot occur within the astroid, only on its surface. The astroid can be used to determine the direction of magnetisation in a given field H . As demonstrated in figure 1.1.6b, from a field point, H , tangents are drawn to the astroid. The resulting angles made with the easy-axis give two possible values for θ . One of these angles $\theta = \beta$ represents the stable energy minimum. The other, $\theta = \beta'$ gives a metastable state that can either be a minimum or a maximum [6].

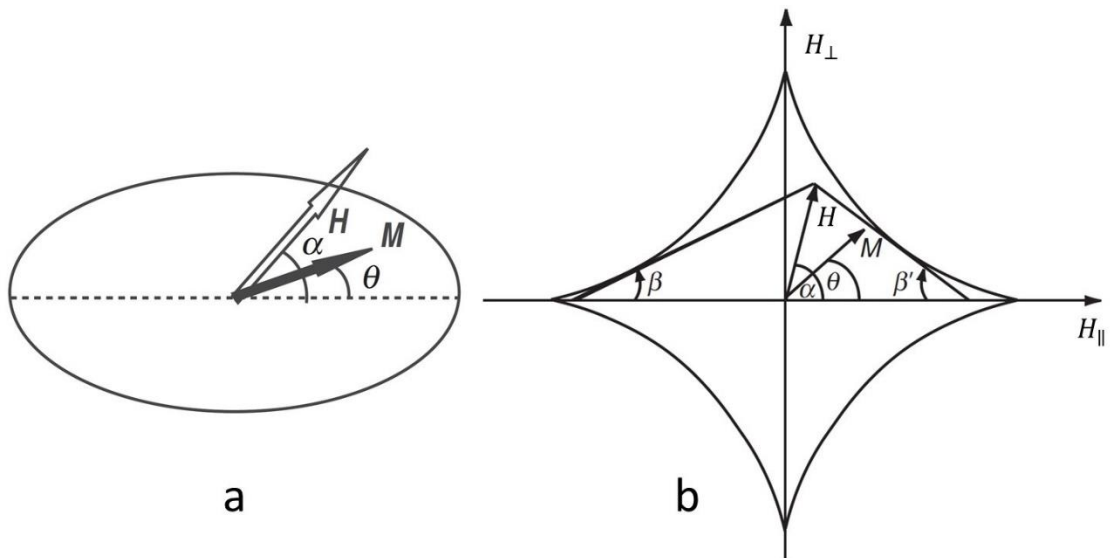


Figure 1.1.6: a) Stoner-Wohlfarth ellipsoid, b) Stoner-Wohlfarth astroid. Adapted from [6]

The other eigenfunction is known as magnetisation curling. Discovered by Brown [15]. This solution of the linearised equations has so far only been applied to an ellipsoid of revolution. Curling is different to coherent rotation as the magnetisation becomes non-uniform and rotates remaining tangential to the surface in order to avoid magnetostatic charges [19]. When coherent rotation occurs, it is due to the exchange energy being too large to overcome. Therefore when curling occurs, it is due to the magnetostatic energy becoming dominant within the magnetic body. This leads to the preference that coherent rotation occurs in smaller bodies, whilst curling is preferred in larger ferromagnets [20].

However, coherent rotation and curling do not tend to occur in real larger ferromagnetic bodies. It has been found that domains with reversed magnetisation may nucleate within the body [12]. This reversed domain can then grow and the magnetisation of the whole body is reversed via DW propagation. These reversal

domains can nucleate at sites within the bodies where an impurity or imperfection is present[6]. This may be a surface asperity, or some crystallographic defect within the lattice. Thermal fluctuations may also result in some spins locally reversing, leading to the growth of a reversed domain[6]. Reversal due to DW propagation is usually the cause of magnetisation reversal if there are already multiple domains present within the system. Figure 1.1.7 shows schematically how nucleation and growth of a reversed domain may occur.

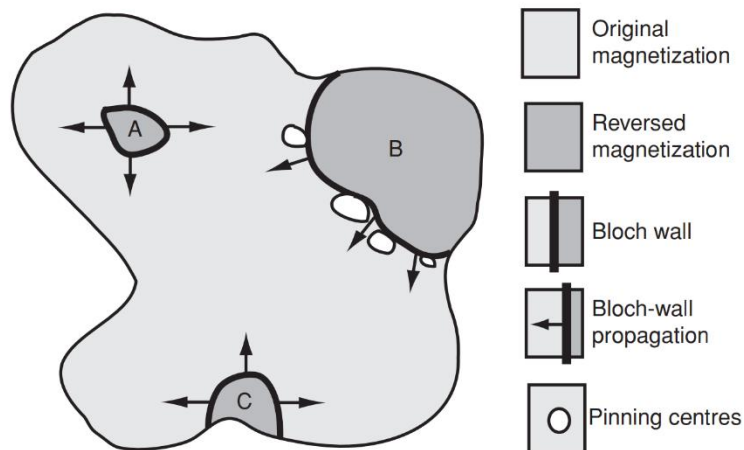


Figure 1.1.7: Examples of how a reversal domain may form and grow. a) Reversal domain nucleates at a crystallographic imperfection or due to thermal fluctuations and grows. b) A previously existing domain may have gotten pinning within the body but can then grow to pass the pinning sites with an applied field. c) Reversal domain nucleates at a surface asperity. Taken from [6]

In very small elements, such as nanowires, the magnetisation is reversed via DW propagation[6]. The presence of a DW within a nanowire has a great influence on how the magnetisation reverses [21], [22]. This is significant for the contents of this thesis, where permalloy nanowires containing single DWs have been studied.

1.1.7 Domain Walls in small structures

In the previous sections, DWs have been discussed for the general case of ferromagnets of all sizes. This section will focus on the structure and dynamics of DWs within small structures, in particular nanowires as these are the subject of this thesis. In some of the literature, these are referred to as nanostrips. These nanostrips are nanowires where their thickness is smaller than the width. Within this thesis, the largest thickness of nanostrip discussed will be ~60nm and all widths will be in the order of 100s of nm.

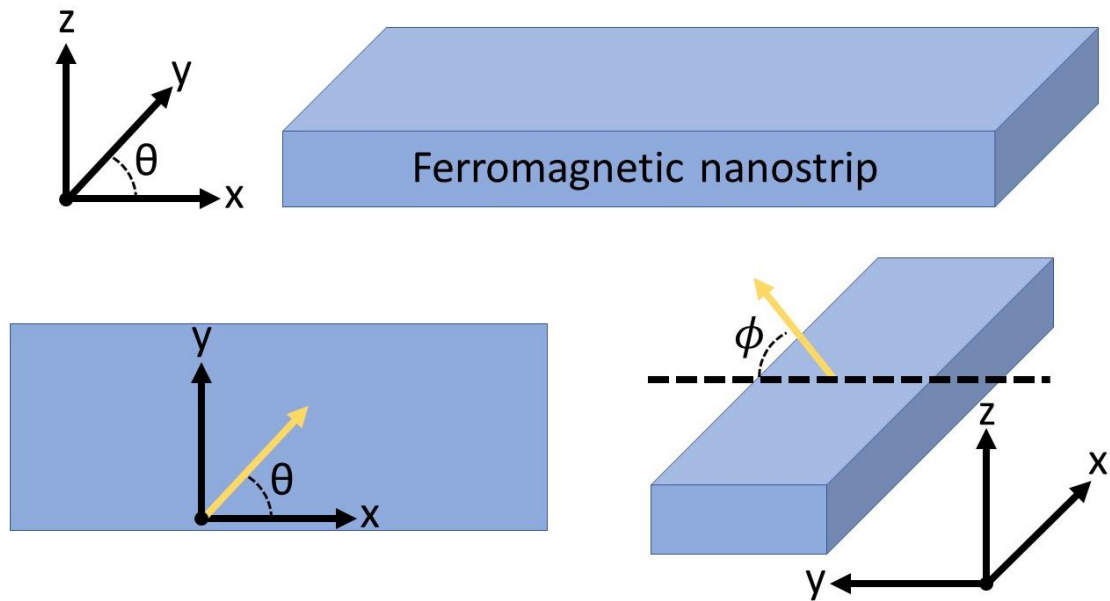


Figure 1.1.8: Schematic of nanostrip dimensions and angles

Due to their reduced size and the strength of the exchange over short length scales, numerical studies of DW micromagnetic configurations within nanowires are achievable [23]-[25]. These numerical studies involve minimising equation 1.10. These studies have shown there are two principle DW structures that occur [24], [25]. These DW structures are spatially different to Bloch and Néel walls found in bulk. Figure 1.1.8 demonstrates the dimensions and co-ordinates that will be used in this discussion. Due to the shape anisotropy of the nanowires, the magnetisation is forced to remain within the x - y plane, with the primary easy-axis being along the x direction. Therefore the different domain structures occur within the x - y plane. These structures are known as “transverse” (TDW) and “vortex” (VDW) domain walls and are both found experimentally and computationally. Simulation results of each are shown in figure 1.1.9. The same wall structures can occur despite the directions of the magnetisation within the opposing domains. DWs where the magnetisations are pointing towards one another are known as head-to-head (HtH) DWs, whilst cases where the magnetisation aims away from one another are known as tail-to-tail (TtT) DWs. The difference is shown in figure 1.1.9 for clarity. Each DW has an associated charge; this is positive in the case of a HtH DW and negative for a TtT DW.

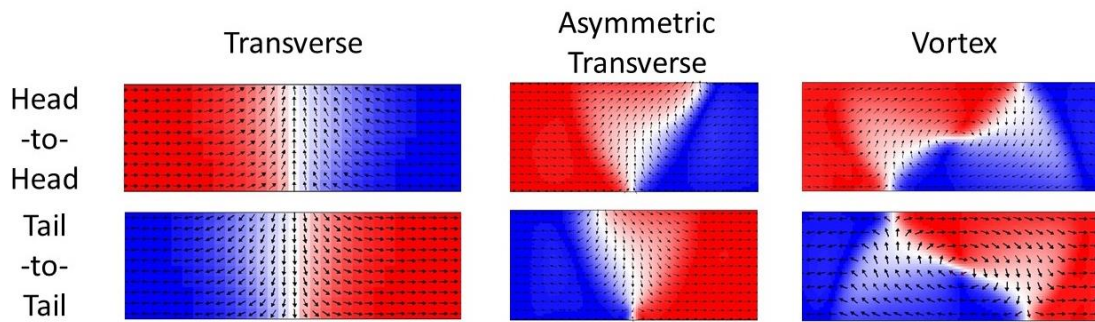


Figure 1.1.9: Simulations showing head-to-head and tail-to-tail examples of transverse, asymmetric transverse and vortex domain walls. Black arrows represent direction of magnetisation for local elements. Red and blue shading represents regions of magnetisation pointing to the right and left respectively.

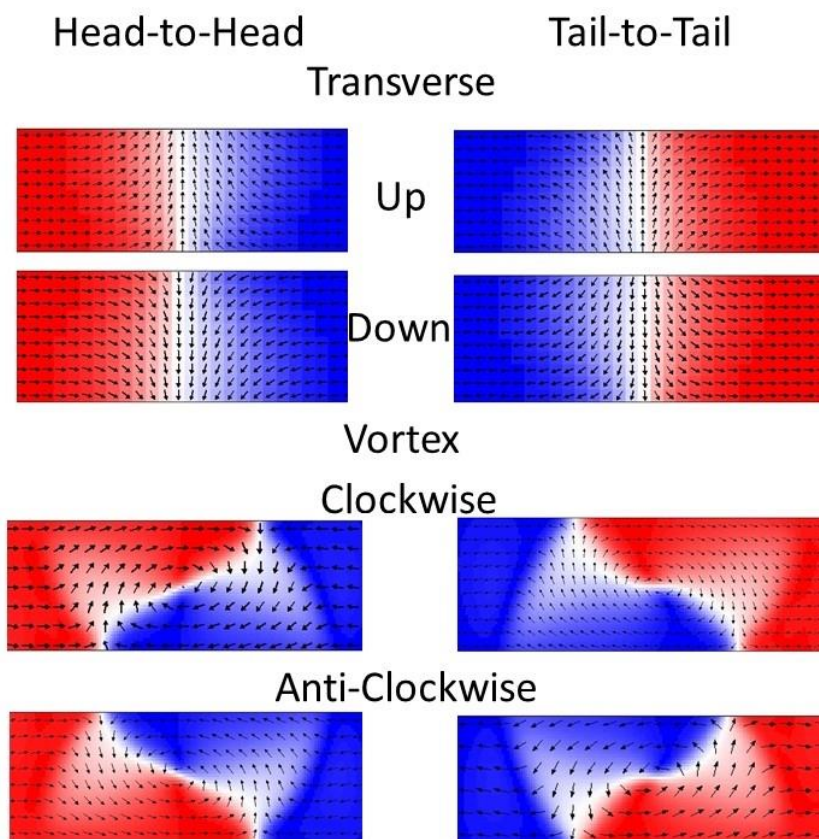


Figure 1.1.10: Different chiralities for transverse and vortex domain walls.

The key difference between the two structures is the overall shape of the DW and how the magnetisation varies within it. TDWs resembles the original 180° Néel wall but has a non-form triangular structure, within which the magnetisation rotates more coherently. VDWs have a spiral-like structure within which the magnetisation curls around a core where the magnetisation actually aligns out of the x - y plane and

along the z -axis. Within each DW there is a degree of freedom that relates to how the magnetisation rotates within it, this is known as the chirality of the DW. For TDWs, the central core can have the magnetisation points either way in the y -direction. The two possible cases are known as up (U) or down (D) TDWs. Similarly, in VDWs the magnetisation can rotate about the core in either a clockwise (C) or anti-clockwise (AC) direction. VDWs have an additional degree of freedom relative to TDWs due to the core magnetisation pointing out of the x - y plane and so can point towards $+z$ or $-z$. Examples of each of these cases can be seen in figure 1.1.10. Note that the central core of the vortex DW cases may point in or out of the page but the image within figure 1.1.10 will appear the same. The lengths of the DWs are comparable to the widths of the nanostrip.

The variation in DW types is due to demagnetising energy, which is dependent on the dimensions of the nanowire cross-section. A special case can be seen when the cross-section is square, i.e. the nanowire has equal width and thickness and is known as the Bloch point [23]. However all nanowires discussed in this thesis will have a width larger than the thickness. Numerical studies have been used in order to find the boundary in nanowire dimensions where TDWs and VDWs occur [24]-[26]. Phase diagrams have been plotted for straight nanostrips and ferromagnetic nano-rings of varying thicknesses and widths. This thesis focuses on straight nanowires and so will not discuss the ring case further. Figure 1.1.11 shows a phase diagram created using a numerical study of permalloy nanostrips. It is shown that TDWs occur in smaller nanostrips, where VDWs take over in thicker and/or wider nanostrips. The boundary between the two cases is not a sharp transition. In this region, DW structures known as asymmetric transverse walls (ATDW) occur. These have a general structure very similar to a TDW but the central core is offset and does not go straight across the wire in the centre of the DW but closer to the edge of it. A ATDW is demonstrated in figure 1.1.9. Nakatani *et al.* [24] found that the transitions from TDW to ATDW and ATDW to VDW are second and first order phase transitions respectively. Meaning that TDWs may occur and be metastable in the VDW region, however they cannot be stable in the ATDW region.

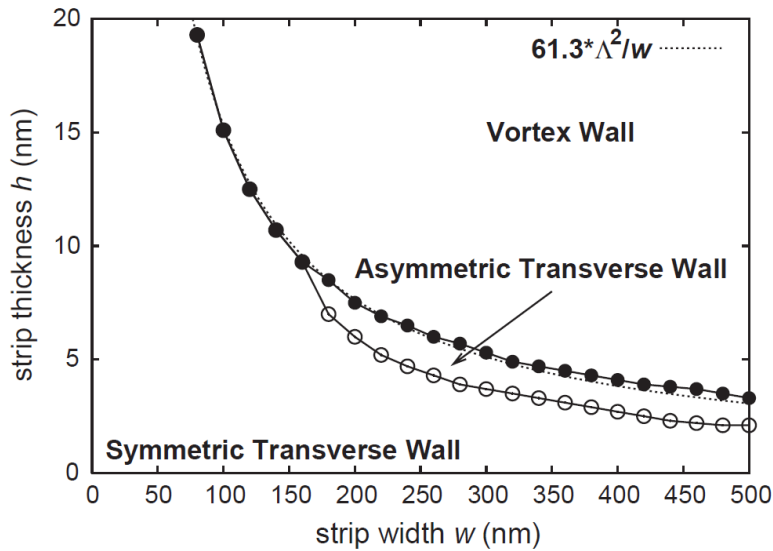


Figure 1.1.11: Phase diagram demonstrating which DW type is to be expected depending on the cross-sectional dimensions of a nanostrip. Phase diagram created using numerical simulations. Taken from [24]

More complex DW structures may occur at larger dimensions, however they are generally seen to be made up of multiple TDW or VDW connected together[27]. In 2015, Nguyen *et al.* [28] suggested the existence of a third type of DW named the “Landau” DW (LDW). The LDW has an appearance similar to the VDW but is elongated and has a much larger length along the nanostrip. LDWs occur at nanostrips typically much thicker than the boundary established between TDWs and VDWs ($\sim 50\text{-}60$ nm and above compared to $\sim 10\text{nm}$ or less). Images of a LDW and the adjusted phase diagram of their occurrence are shown in figure 1.1.12.

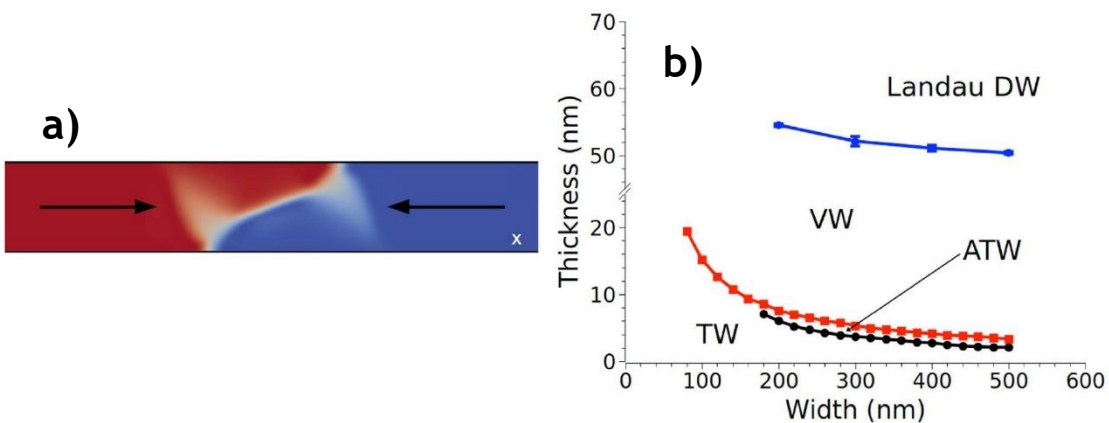


Figure 1.1.12: a) Micromagnetic simulation of a Landau DW. b) Adjusted phased diagram to include Landau DWs. Images taken from [28]

1.1.8 Domain Wall Pinning

In an ideal ferromagnetic material with no imperfections on the surface or within the crystal lattice, DWs may move freely under the influence of any magnetic field [29]. However in real systems, such imperfections are almost impossible to eradicate. How strongly a DW gets pinned to a site can depend on the size or type of imperfection. As DWs propagate through a sample under the influence of a low field, they do so via a series of stochastic positional jumps known as Barkhausen jumps [30]. These jumps are done between small localised pinning sites [31]-[34]. These mechanisms are present when a DW propagates through a nanowire due to intrinsic defects created during the fabrication process. Minimisation of such defects is important as it reduces the strength of any unintentional pinning sites. As discussed in section 1.1.7, nanowire dimensions influence the structure and size of any DWs present. This can be extended such that variations in size or shape of such nanowires can be used to pin DWs at a specific location.

DW pinning in general is due to exchange and magnetostatic effects. These effects generate a potential energy which interacts and effects DW motion. DW pinning occurs when there is a positional dependence of the DW energy. Due to this, the potential energy linked with DW pinning can be described as being one-dimensional, i.e. $U(x)$. With the assumption that changes in the DW structure are negligible, and so the Zeeman energy is only dependent on the DW position, the total energy under an applied field, H becomes the sum of the Zeeman and potential energies:

$$\varepsilon = \varepsilon_z + U(x) = -2\mu_0 M_s S H x + U(x) \quad (1.19)$$

where S is the cross-sectional area of the nanowire. For a DW to move from the site and depin, the net potential gradient everywhere is required to be less than or equal to zero (at zero temperature), i.e. $\partial\varepsilon/\partial x \leq 0$. From this condition the field required to depin a DW can be obtained:

$$\left(\frac{\partial U}{\partial x}\right)_{max} = 2\mu_0 M_s S H_{depin} \quad (1.20)$$

Where H_{depin} is known as the depinning field.

The creation of a pinning site changes the potential energy landscape seen by the DW. DWs can be pinned due to a potential well being created and so the DW will get stuck in the energy well [35]. Alternatively a potential energy barrier may be created, causing the DW to be unable to pass the pinning site until a sufficiently large field is applied. This field causes the Zeeman energy to increase to the point where it can overcome the potential barrier [36]. Whilst the most common method of

pinning DWs involves altering the geometry of a nanowire, there are other methods of creating a pinning site. Observing equation 1.20 shows that altering the saturation magnetisation can also effect the required depinning field. This can be done via methods such as ion implantation, causing properties to be locally altered within a section of a nanowire and therefore will create a pinning site [37].

Further details of case studies and methods used to pin DWs will be discussed in greater depth in section 2.1.

1.1.9 Magnetisation Dynamics

Finding the equilibrium state in a ferromagnetic body requires the energy minimisation using equation 1.10. Brown attempted to find analytic solutions to this using appropriate boundary conditions [5]. Within the magnetic body, there is the presence of not only any externally applied field, but also a field caused by all other atoms within it. These fields combined create an effective field, H_{eff} given in the form:

$$\mathbf{H}_{eff} = -\frac{1}{\mu_0 M_s} \frac{\partial \varepsilon}{\partial \mathbf{m}} \quad (1.21)$$

where $\mathbf{m} = \mathbf{M}/M_s$. Brown stated that the total energy change within a body should be zero at equilibrium when the magnetisation is perturbed by any arbitrary small amount. The magnetisation precesses around the effective field due to a torque given by:

$$\frac{\partial \mathbf{m}}{\partial t} = \gamma_0 (\mathbf{m} \times \mathbf{H}_{eff}) \quad (1.22)$$

where γ_0 is the gyromagnetic ratio. As the effective field produces a torque on the magnetisation, for the system to be in equilibrium, this torque must be zero. So a stability condition was formed that every point within the body must obey:

$$\mathbf{m} \times \mathbf{H}_{eff} = 0 \quad (1.23)$$

for equilibrium. So the energy extrema occurs with the magnetisation aligns parallel to the effective field. Equations 1.21 and 1.23 are termed Brown's static equations. These equations are completed by imposing the boundary condition at the surface of the body to be:

$$\mathbf{m} \times \frac{\partial \mathbf{m}}{\partial n} = 0 \quad (1.24)$$

where $\partial/\partial n$ denotes the derivative in the outside direction normal to the body surface. This may be simplified to the form $\partial \mathbf{m}/\partial n = 0$.

However, equation 1.22 describes a precession where the angle between the two values never changes and so the magnetisation may never align with the effective field. This is an unexpected feature in real systems as no losses have been taken into account. In real systems losses have many origins including eddy currents, macroscopic discontinuities known as Barkhasuen jumps, lattice defects causing diffusion and reorientation and spin-scattering mechanisms [11].

Brown's equations also have the issue of not addressing two important aspects. The equilibrium conditions are stated but do not explain how the system will approach equilibrium if not initially in equilibrium. They also do not describe how the magnetisation may reacts in a time-varying applied field [12].

All damping contributions can be treated using a local dissipative term. This method is used in the Landau-Lifshitz-Gilbert (LLG) equation [11]:

$$\frac{\partial \mathbf{m}}{\partial t} = -\gamma_G \mathbf{m} \times \mathbf{H}_{eff} - \alpha_G \mathbf{m} \times \frac{\partial \mathbf{m}}{\partial t} \quad (1.25)$$

where α_G is the Gilbert damping parameter and γ_G the Gilbert gyromagnetic ratio. The added damping term now allows the magnetisation to turn towards the effective field such that it may align with it to give the stable static solution. It also provides the time evolution of the magnetisation under the effective field. Equation 1.25 can also be referred to as the Gilbert equation as it is a variant of the original Landau-Lifshitz (LL) equation [11]:

$$\frac{\partial \mathbf{m}}{\partial t} = -\gamma_{LL} \mathbf{m} \times \mathbf{H}_{eff} + \alpha_{LL} \mathbf{m} \times (\mathbf{m} \times \mathbf{H}_{eff}) \quad (1.26)$$

where α_{LL} is the LL damping parameter and γ_{LL} is the LL gyromagnetic ratio. Equations 1.25 and 1.26 are mathematically equivalent and can be converted into one another by inserting equation 1.26 into equation 1.25 and comparing coefficients of the vector quantities. This leads to the relations [11]:

$$\gamma_{LL} = \frac{\gamma_G}{1 + \alpha_G^2} \quad (1.27)$$

$$\alpha_{LL} = \frac{\alpha_G \gamma_G}{1 + \alpha_G^2}$$

From this, in zero damping $\alpha_{LL} = \alpha_G = 0$ and so $\gamma_{LL} = \gamma_G = \gamma$, where $\gamma = \mu_0 g e / 2m_e$ with m_e being the mass of an electron, e the charge of an electron and g is the Landé factor which has values close to 2 for many ferromagnetic materials [11].

The choice between using the LLG or LL equations is usually due to mathematical convenience.

1.1.10 Applications to data storage technology

Recent decades have seen an enormous increase in information and technology. The introduction of high performance computing, mobile devices such as phones and tablets, has seen vast amounts of data being produced and required to be stored. Following this there have been a growing demand for cloud data storage with some estimates showing about 3 exabytes (3 billion GB) of data was produced every day in 2017 [38].

Hard Drives Discs (HDD) have been used for over 50 years and continue to dominate the market. HDDs are approaching a limit in areal density and so the market has been shrinking since 2010 [38]. HDDs are being replaced with other technologies such as solid state drives (SSD) and flash memory.

In addition to these, magnetic random access memories (MRAM) have been intensively researched as a non-volatile alternative with the potential for lower power and instant-on capability [39]. The principle of MRAM is based on using magnetic anisotropy energy to retain information whilst utilising magnetoresistance to retrieve it [40].

Other storage schemes being researched includes domain wall (DW) memory. Parkin *et al.* proposed a technology known as racetrack memory [1]. Racetrack memory has the potential to deliver systems capable of higher densities and faster read/write speeds. This system consists of ferromagnetic nanowires containing domains of opposing magnetisations. The direction of magnetisation can be considered as 1s and 0s representing a single bit. The string of domains is propagated along the nanowires passed a read-write head. As the application of an external magnetic field causes domain growth and potential domain annihilation, the domains would need to be current driven. Current driven motion of DWs in ferromagnets have been demonstrated by many independent researchers [41]-[43].

One of the key issues in racetrack memory is the ability to reliably control the DW motion and position within the nanowires. As the domains are moved via short pulses of spin polarised currents, this causes the wire temperature to increase. This causes increases in thermal fluctuations and so features are required to create pinning sites capable of holding the DWs in place during these fluctuations. Domain wall memory

is still growing and evolving with many groups researching methods to make the systems more efficient for real world applications.

The emergence of skyrmions has given rise to their potential application in memory. Skyrmions were theoretically proposed in 1974 [44] but were not experimentally observed until 2009 [45], [46]. They are topological objects consisting of swirling spins structures similar to a vortex. Proposed memory devices consist of skyrmions on a racetrack with the presence or absence of a skyrmion being comparable to binary 1s and 0s [47]. Skyrmion racetracks are still in their infancy however an early problem identified relates to the skyrmion Hall effect. This effect causes the skyrmion to move away from the centre of the racetrack whilst a current is applied [48]. This issues results in the skyrmions annihilating at the walls during high-speed operations [49], [50].

1.2 The Atomic Force Microscope

1.2.1 Origin of the Atomic Force Microscope

The Scanning Tunnelling Microscope (STM) was the predecessor to the Atomic Force Microscope (AFM). An STM is a very powerful tool for obtaining three-dimensional scans of the topography of surfaces with nanoscale resolution. It was invented in 1981 by Binnig and co-workers [51] and utilises the ability of electrons to quantum mechanically tunnel from the surface of a material to a sharp metal tip positioned close to the surface. However the key drawbacks associated with the STM are its requirements for the sample to be placed in an ultra-high vacuum as well as having a conducting surface. These limitations were overcome with the invention of the AFM a few years later [52]. Not only does the AFM not require a conductive surface, but it can also be used in a variety of environmental conditions, not just in a vacuum [53]. AFM instruments can operate in standard atmospheric conditions [54], as well as in liquid solutions [55].

The primary purpose of the AFM is to scan the topography of sample surfaces with nanoscale resolution. Over the last 30 years the AFM has become a key research tool capable of being used in a widespread range of applications. It can be applied for material characterisation and also in other fields of nanotechnology such as in nanotribology investigations and in nano-manufacturing [56].

1.2.1 Basic Principles of an AFM

An atomic force microscope can extract the topography of a surface by sensing the attractive and repulsive inter-atomic forces, hence the given name. The basic

sensing principle of an AFM relies on positioning an extremely sharp tip very close to the sample surface and on the monitoring of how a cantilever on which the tip is mounted, deforms due to these inter-atomic forces. The variation of these force with the tip-specimen distance is shown in figure 1.2.1. The regime under which an AFM operates, i.e. repulsive or attractive, depends on the scanning mode being used. More details on these operational modes will be given in section 1.2.3.

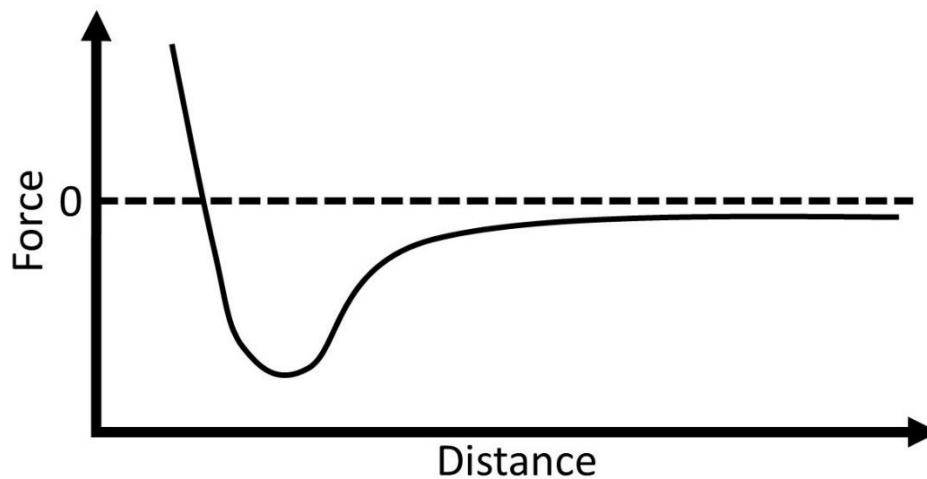


Figure 1.2.1: Graph of atomic force vs distance

An AFM instrument consists of three main components. These three components are force sensing, actuation and feedback control. Each component will now be discussed in turn.

Force sensing: this component of the AFM is directly involved in recording the surface topography. The force sensing itself consists of two key elements. These are the AFM probe and the instrumentation used to monitor and detect any deformation of the probe. The probe is made up of a tip, a cantilever and a chip, see figure 1.2.2. The tip is commonly pyramidal in shape and micro-fabricated to be ultra-sharp at its end. The tip is typically made of silicon or silicon nitride, however tips can be made of other materials such as tungsten, diamond, iron, cobalt-samarium, permanent magnets. A tip can also be coated with polycrystalline diamond in order to make it tougher and more resistant to wear [57]. The tip is mounted on the end of a cantilever. The cantilever is also usually made of silicon or silicon nitride and can be triangular/V-shaped or rectangular. The cantilever is then attached to a much larger chip simply to make manual mounting of the tip and cantilever into the AFM much easier. The cantilever possesses a very low spring constant, k which allows it to bend and deform easily. This is key to how an AFM measures the

interaction force with a surface [58]. This low spring constant allows the cantilever to detect forces as low as $\sim 10^{-9}\text{N}$ [59].

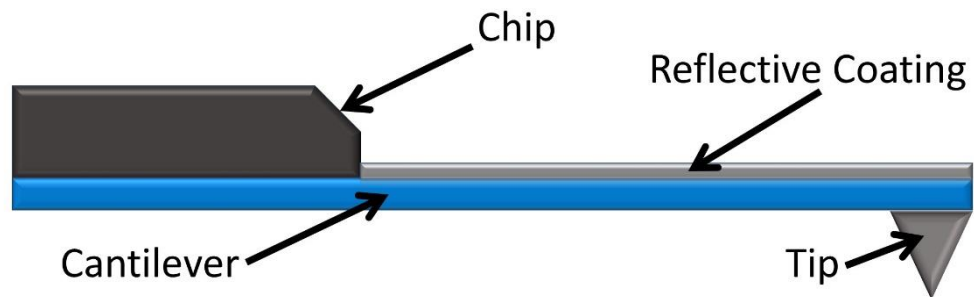


Figure 1.2.2: Schematics of an AFM probe

In most AFM systems, the optical lever method is used to detect the deflection of the cantilever and hence, the force acting between the tip and the surface of a sample. This method involves pointing a laser beam onto the cantilever. The laser then reflects off the cantilever onto a photodetector. An example of this is shown in figure 1.2.3. In order to increase the intensity of the laser light reaching the photodetector, the back side of the cantilever is usually coated with a thin layer of highly reflective metal such as gold or aluminium. The photodetector can be considered a position sensitive photodiode (PSPD). PSPDs are semiconductor devices that convert the laser beam intensity into a voltage signal. In order to accurately monitor the deflection of the cantilever, the PSPD is usually split into four quadrants labelled A, B, C and D, as demonstrated in figure 1.2.3. This enables both the vertical and torsional deflections of the cantilever to be monitored by calculating the difference in voltage outputs between the relevant pairs of quadrants. More specifically, $(A+B)-(C+D)$ is used for the vertical deflection whilst $(A+C)-(B+D)$ is used to monitor the torsional deflection. The vertical deflection signal is employed to monitor the height of the surface topography, whilst the torsional deflection signal is normally analysed to study friction between the surface and the tip. The latter is typically referred to as friction force microscopy (FFM) [60]-[62]. Figure 1.2.4 shows the difference between vertical and torsional deflection.

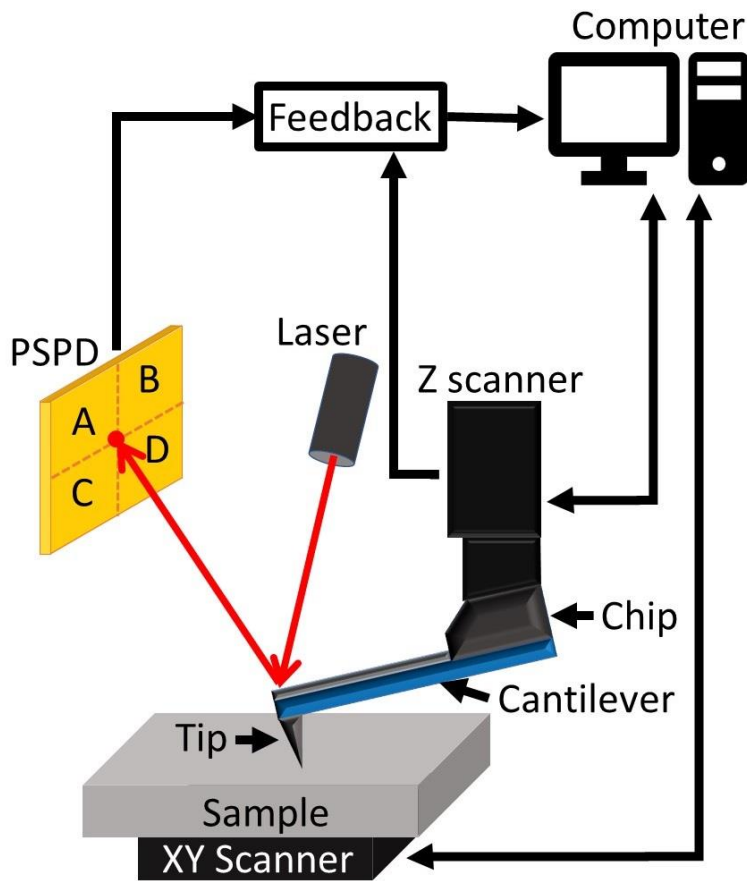


Figure 1.2.3: Schematic of an AFM system

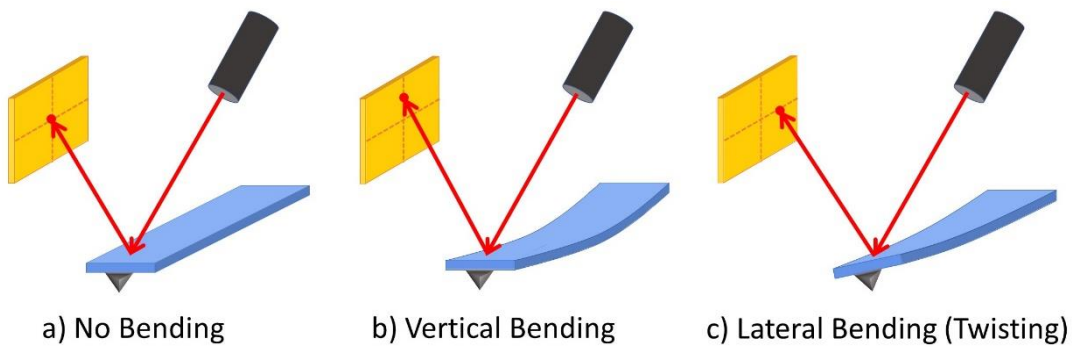


Figure 1.2.4: Schematics showing beam positioning for various cantilever deflections

The second main component of an AFM system is the actuation. The actuators are responsible for the movement between the tip and the surface. These actuators are most commonly made of piezoelectric materials. Piezoelectric materials change dimensions with the introduction of an applied voltage. This enables them to expand or contract depending on the input signal. The movement on the X-Y plane is

controlled by an “X-Y scanner” and can either consist of a single piezoelectric tube, or two separate linear actuators, each acting in one dimension. The vertical displacement of the probe is always controlled by a separate independent actuator known as the “Z-scanner”. The Z-scanner is normally integrated into the head of the AFM system as shown in figure 1.2.3.

The third and final main component of an AFM is the feedback control. This element combines the two previously discussed components. Feedback control consists of a software as opposed to a piece of hardware within the set-up. It is needed to control and maintain a set value for the interaction force between the tip and the sample as it scans along a surface. The feedback control relies on a control loop algorithm within which the signal from the PSPD is used to determine how the Z-scanner should alter the height of the probe as it traverses the surface of a sample. In other words, the signal from the PSPD dictates the applied voltage needed to actuate the Z-scanner in order to modify the height of the tip.

1.2.2 AFM modes of operation

In order to obtain surface topography data, an AFM can operate under three different basic modes of operation. Each of these modes involves the atomic interaction force being utilised in a different way.

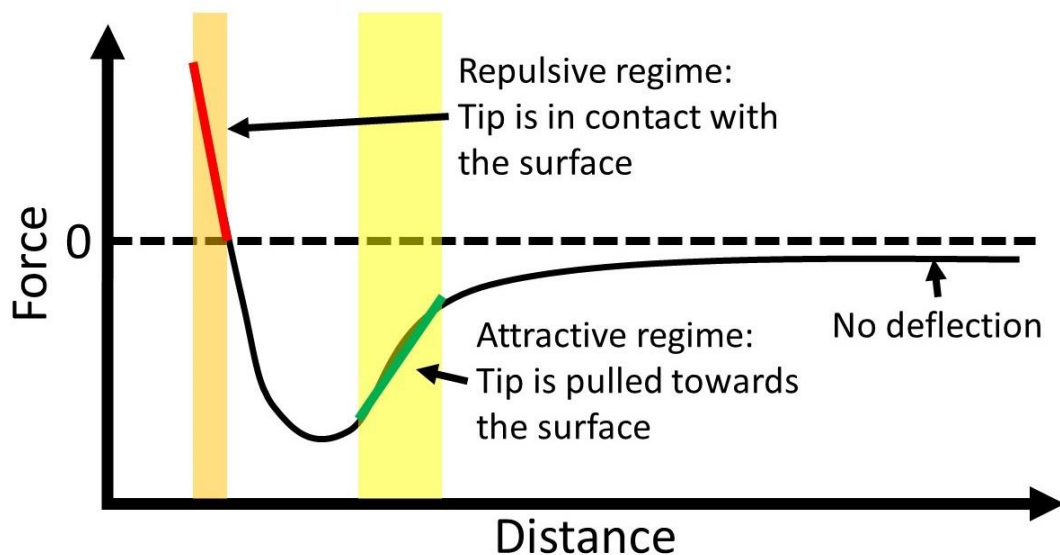


Figure 1.2.5: Demonstrating repulsive and attractive regimes

The three modes of operation are known as contact mode, non-contact mode and tapping mode. Each of these will be briefly discussed in turn. The provision of elaborated details on these modes are beyond the scope of this thesis. Further in-

depth discussions can be found in a number of state-of-the-art reviews such as [63]-[66].

The first mode that will be discussed is contact mode as it was the first method invented. As the name suggests, in contact mode the tip is brought into close contact with the surface. Due to the extremely small distance between the tip and the sample surface, the AFM operates into the repulsive regime in this case. In contact mode, the cantilever deflection can be said to be quasi-static in the sense that it is not subjected to dynamic excitation. There are two ways in which contact mode may be implemented - constant-height mode or constant-force mode. In constant height mode, the feedback loop is turned off and so the height of the Z-scanner does not change. This means the system only detects a change in the cantilever deflection and so topography is measured using the PSPD readout. This mode is useful for small area, high-speed scans with atomic resolution. The drawback to this method however is that there is a relatively large risk of damaging the tip due to the interaction force between the tip and the surface not being constant. The alternative approach is constant-force mode. As the name implies, it is effectively the reverse of constant-height mode in that the force is monitored so it remains constant. To achieve this, the feedback loop is used to alter the height of the Z-scanner in order to keep the interaction force between the tip and surface constant. The topography is then recorded using the changing height of the Z-scanner as opposed to the PSPD signal. This method does allow for higher resolution but it is limited by the response time of the feedback loop of the system. The system detector signals for both of these methods are demonstrated in figure 1.2.6 to help with clarity. The constant-force mode was the original mode developed for AFM operations.

The non-contact mode was invented in 1987 by Martin and colleagues [67] and, as suggested, operates with the tip a set distance from the surface. The tip is placed 30-150 Å above the surface [67] such that it is within the attractive atomic force regime. At this distance, the Van der Waals forces interact with the tip. Non-contact mode is a dynamics process for which the tip is oscillated at its resonant frequency. The action of the attractive forces affect the oscillations by altering both the amplitude or phase of the vibrations. This can be used in two ways. Amplitude modulation AFM, known as (AM-AFM), oscillates the cantilever at a frequency slightly off resonance. Force interactions with the surface causes a change in frequency resulting in a change in amplitude. These changes in amplitude are used in feedback

loop. The alternative approach is to keep only the amplitude fixed and vary the frequency, known as frequency modulation AFM (FM-AFM). AM-AFM can provide near atomic resolution whilst FM-AFM is able to provide atomic resolution [57]. Non-contact AFM provides unique advantages over other AFM and STM techniques. It allows soft samples to be scanned as the repulsive force is absent whereas very strong repulsive force would appear during contact between tip and sample. It also still does not require a conducting surface as STM does.

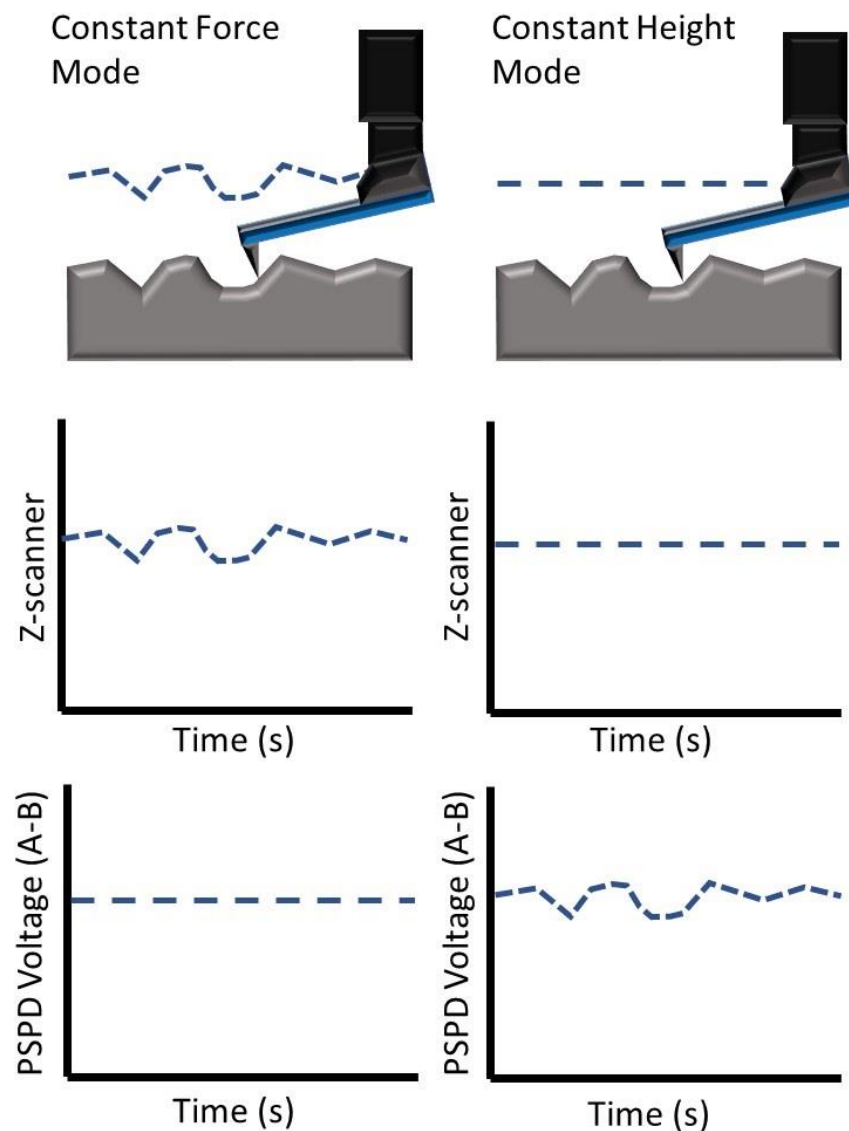


Figure 1.2.6: Demonstration of differences between constant force and height modes

Zhong and co-workers proposed the third mode of operation in 1993 [68]. This was suggested in an attempt to overcome issues occurring in contact and non-contact modes where the tip may stick to the surface. This may occur if the Z-scanner does not perform to a high enough standard and so causes the feedback loop to move the tip further from the surface to compensate. This leads to a significant reduction in lateral resolution. Other issues that may occur involve resulting friction, adhesion and electrostatic forces as the tip moves along the surface. The proposed mode was named "Tapping mode". Tapping mode is also a dynamic mode where the tip is oscillated with a large amplitude. This is done further away from the surface. The tip is then lowered and brought gradually towards the sample until the tip lightly touches or taps the surface. When the tip comes into contact with the surface, energy is lost and so the oscillations must be decreased. This is used to characterise the features of the surface. Tapping the surface in this way reduces the chances of the tip sticking to the surface. The resolution of tapping mode is limited only by the size of the tip being used. One drawback of this method compared with non-contact mode is accelerated wear of the tip due to the tip touching the surface with every oscillation.

1.2.4 Introduction to AFM tip-based nano-machining

Not long after the AFM was invented, researchers began testing if they could modify the surface of a substrate using the probe tip. It was found that by purposely increasing the applied load through the tip whilst moving along the surface, the force became large enough to deform the surface permanently. When this occurs, the tip effectively cuts into the surface and removes or displaces material resulting in a groove. An example of such operation is shown in figure 1.2.7. Throughout the literature this process is referred to by a number of names including scribing, scratching and machining. Reports emerged in the early 1990s showing researchers implementing such AFM tip-based nanomachining operations [69]-[71]. Many studies have been published since which involve the implementation and application of this process.

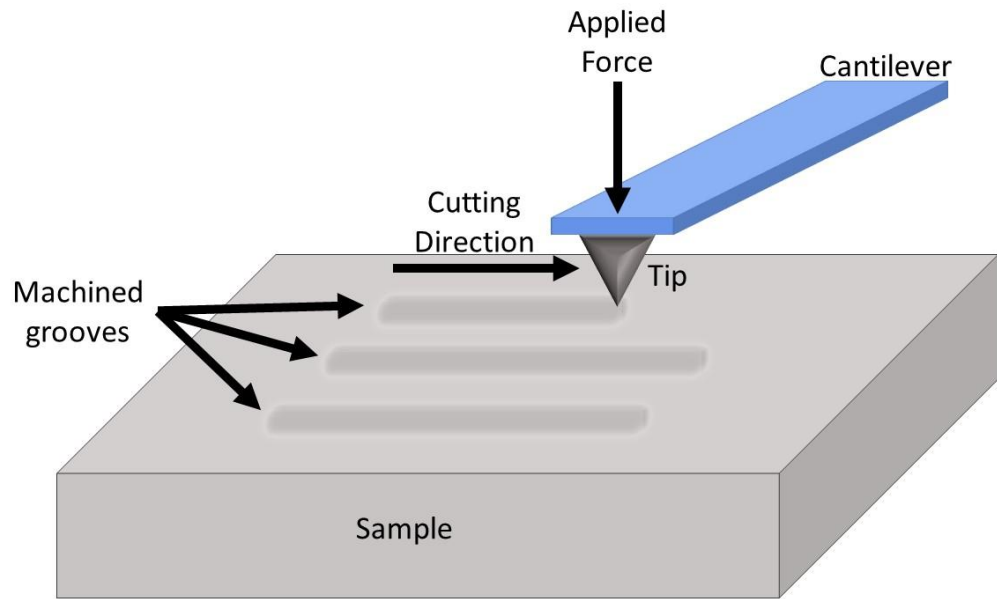


Figure 1.2.7: Schematic of AFM cutting into a sample creating grooves

An overview of AFM tip-based nano-machining and its potential applications will be discussed further in chapter 2.2 as this forms a vital portion of this thesis.

2. Literature Review

2.1 Domain Wall pinning

In section 1.1.10, the applications of magnetic domain walls were briefly discussed. In order to utilise this phenomenon there is a need to be able to reliably and accurately control the motion of DWs. Over the last few decades there have been many studies focused on this area. Most of which involve creating a site at which DWs would be attracted to or pinned at. This would make it easier to know where DWs are likely to be given environmental conditions. Creating multiple of these sites would give the ability to move such DWs between various points within the devices, giving further control over DW motion. This chapter will discuss the various methods researched have used to pin DWs.

2.1.1 Nanowire Design

The most basic method that can be used to create or pin a DW at a specified location in the overall nanowire design. For example, creating a nanowire that contains a significant curve or sharp change of direction [72]-[75], such as in figure 2.1.1. Features such as these in a nanowire provide prime locations for DW creation. Applying an external magnetic field at an angle into the corner or curve of a uniformly magnetised nanowire will create a DW at the centre of the curve or at the corner. Whilst this method of pinning DWs is a simple one, it is not often used as the primary technique for pinning DWs and controlling their motion. Rather it is often used as a method of creating DWs in a specified place to then move for researching other methods of DW pinning or measuring propagation speeds [75]-[79].

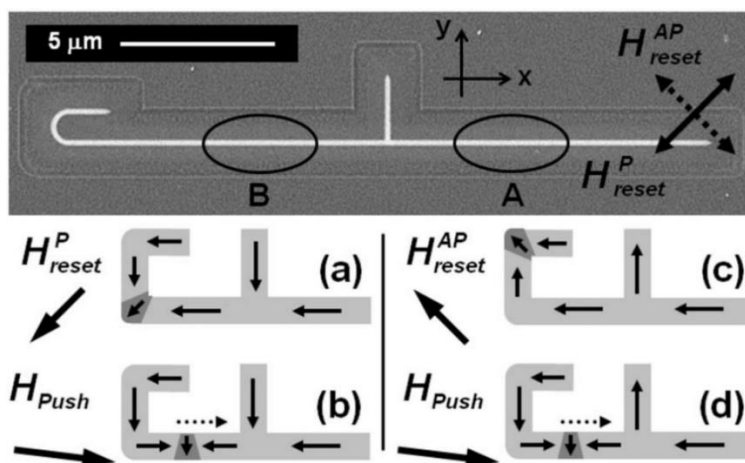


Figure 2.1.1: Figure displaying an example of using a curved nanowire in order to create and pin DWs at the corners. Taken from [74].

Studies have found that nanowires can also be designed such that the DW propagation will have a favoured direction. Allwood and co-workers in 2004 designed a so-called DW diode [80]. A nanowire was designed such that the width of it changed halfway through its length. An additional feature was also added at the change in width such that there was a localised triangular shape as shown in figure 2.1.2. The device was named a diode as this design allowed DWs to propagate much easier in one direction than the other. Thus, representing a possible design to ensure DWs only propagate in one desired direction within a system.

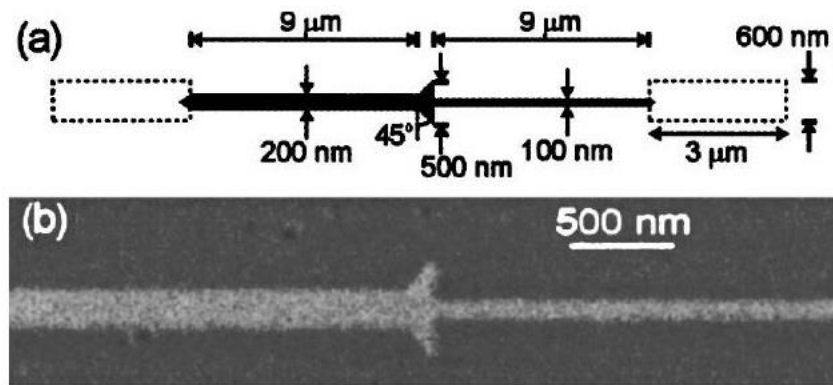


Figure 2.1.2: (a) Schematic diagram, (b) Secondary electron images by focused-ion-beam irradiation of a DW diode structure. Taken from [80].

Utilising a similar methodology, other studies have designed nanowires with a succession of “asymmetric notches” along the side of the wire [81], [82]. Resulting in a so-called Christmas-tree like structure [83]. An example of these structures is shown in figure 2.1.3. As similar to the Allwood and co-workers study in 2004, the resulting designs allow DWs to propagate through the nanowires in one direction much easier than the other, providing direction dependent devices.

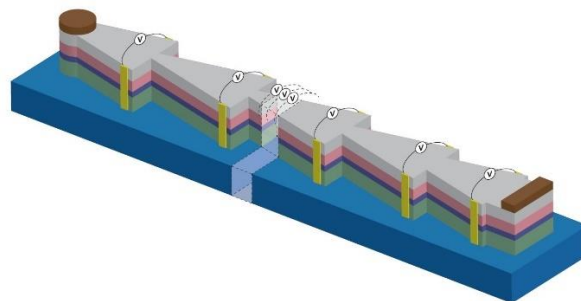


Figure 2.1.3: Schematic of the Christmas-tree-like spin Hall magnetometer. Taken from [83]

2.1.2 Non-topographical methods

Methods have been found to pin DWs that do not involve physically altering the shape or design of magnetic nanowires. Some of which involve locally changing the magnetic properties via ion implantation, other methods pin or distort DWs by utilising stray fields produced by nearby unconnected nanowires.

In the early 2000s, ion implantation to alter properties of magnetic films and multilayers had become of increased interest with the potential applications in small magnetic devices. Two papers published in 2002 focused on effecting such magnetic properties within permalloy thin films. Ozkaya and co-workers [84] implanted $10\ \mu\text{m} \times 10\ \mu\text{m}$ squares with Ga^+ ions into a 30 nm thick permalloy film. The Ga^+ ions had the effect of locally increasing the coercivity of the material. This resulted in the irradiated areas requiring larger applied fields to reverse the magnetisation. It was shown that DW pinning was the major mechanism for the increased coercivity. Another study in 2002 by Woods and co-workers [85] used Ar^+ ion implantation on 5 nm thick permalloy thin films whilst applying a saturating magnetic field. This was shown to be a method of altering the local direction and angular anisotropy in soft magnetic films.

Since these initial reports, there have been further studies employing this method to create pinning sites within nanowires as opposed to thin films. Implanting different ions can have different effects on the magnetic material. Vogel and co-workers use chromium ions in permalloy nanowires in order to locally reduce the saturation magnetisation, creating a pinning site [86], [87]. Ga^+ ions were again used on another study [37], where the multilayer structure Cr/Py/Cr was used to study the influence of ion dose on the pinning strength of the pinning site. It was seen that the pinning strength increased with the ion dose used.

In 2011 Basith and co-workers conducted a study on permalloy nanowires with lateral anti-notches[88]. The nanowires were created using electron beam lithography (EBL) and focused ion beam milling (FIB) to compare the two methods in order to find any differences between them. The devices created were nominally identical with only the method of creation varying between them. DW pinning via lateral notches and anti-notches will be discussed further later in this chapter. In this study DWs were pinned in the anti-notches of both sets of devices, however the pinning strength of the devices created using FIB were lower than those fabricated using EBL. Simulation investigations indicated that this difference in the pinning strengths could be due to ion implantation in the remaining material causing a

reduction in saturation magnetisation. This could create problems for potential memory or logic devices created using FIB. This also could indicate potential problems of unreliability of any pinning sites created using ion implantation as they may prove to be more unpredictable in pinning strength when compared to other methods of DW pinning.

Another method of pinning and influencing DWs involves the near-field interaction of close-by nanowires [89]-[92]. Another nanowire, which can be extremely short, can be placed perpendicularly near the main device. The stray field produced by this smaller piece of magnetic material interacts with the close-by section of the main nanowire such that it can pin DWs. It was also shown that a DW passing by a near perpendicular nanowire can reverse the magnetisation of it [92]. This induced switching could potentially be used for magnetic random access memory applications. Another study showed that multiple small ferromagnetic strips placed adjacently to a nanowire may be used to tune the pinning strength of such features, as shown in figure 2.1.4 [91].

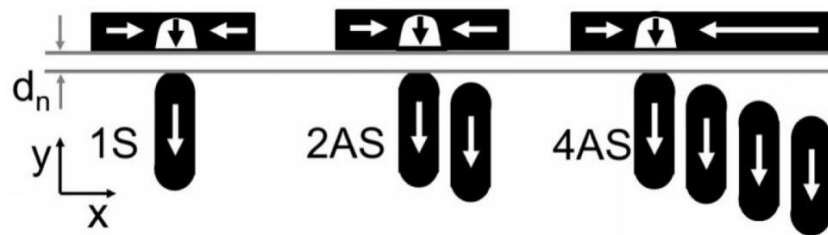


Figure 2.1.4: Schematic of device implementing multiple stray field strips to pin DWs. Taken from [91].

2.1.3 Lateral Changes to magnetic nanowires

The most common method used to pin DWs involves locally changing the lateral or planar dimensions of a nanowire, i.e. changing its width by narrowing it using a notch or widening it using a so-called anti-notch. There have been many studies investigating this area, some of which will be discussed as follows.

The more extreme case of effectively using an anti-notch to pin DWs is the presence of a T-junction between two straight nanowires [75], [93]. A study conducted by Petit and co-workers [75] investigated the potential energy profiles and pinning strength of such a set-up, shown in figure 2.1.5. Only transverse DWs were investigated in this study and it was found that the chirality of the DW effected both. More specifically, it was found that higher switching fields occurred when the

DW core was anti-parallel with the magnetisation of the arm. These results had good agreement both experimentally and computationally.

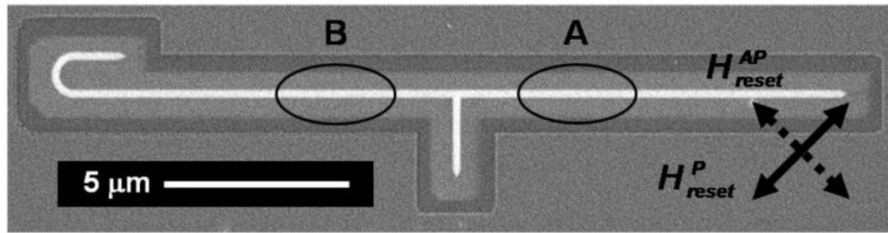


Figure 2.1.5: Electron image by FIB irradiation of a 200 nm wide Permalloy structure with a T-shaped trap at its middle. Taken from [75].

Many studies have investigated pinning DWs using a single notch cut out of the side of a nanowire [35], [36], [94]-[100]. Some studies have focused on the relationship by the feature size and its pinning strength. Faulkner *et al.* [94] created permalloy nanowires with a triangular notch, demonstrated in figure 2.1.6. The dimensions of the notch, i.e. the width and depth, were increased and the resulting depinning fields were measured, these are presented in figure 2.1.6. It was seen that the depinning field did increase with the trap depth. A similar experiment was also conducted by Im *et al.* [101]. However, in these studies, both the depth and width of the triangular notch was changed at every iteration, keeping the same overall triangular shape. This does mean that although the depth was increased, so was the width and so the plot presenting a comparison of depth versus depinning field is not a completely true comparison as it would be expected that the width increasing would also have an effect on the depinning field even if the depth was kept constant. Despite this, the general relationship that the overall size of the notch increasing gives a stronger pinning site is still valid.

Another key area of study focuses on the effects of DW chirality on a site's pinning strength [35], [95], [96], [98], [102]. Atkinson and co-workers [96] conducted computational and experimental studies investigating how the spin direction within a DW structure can affect the pinning strength of lateral notches. Observing transverse DWs, it was found that the pinning strength was higher when the magnetisation of the central spine of the TDW was pointing towards the notch. Experimental and computational results had good agreement. This result provides another degree of freedom to consider when pinning DWs.

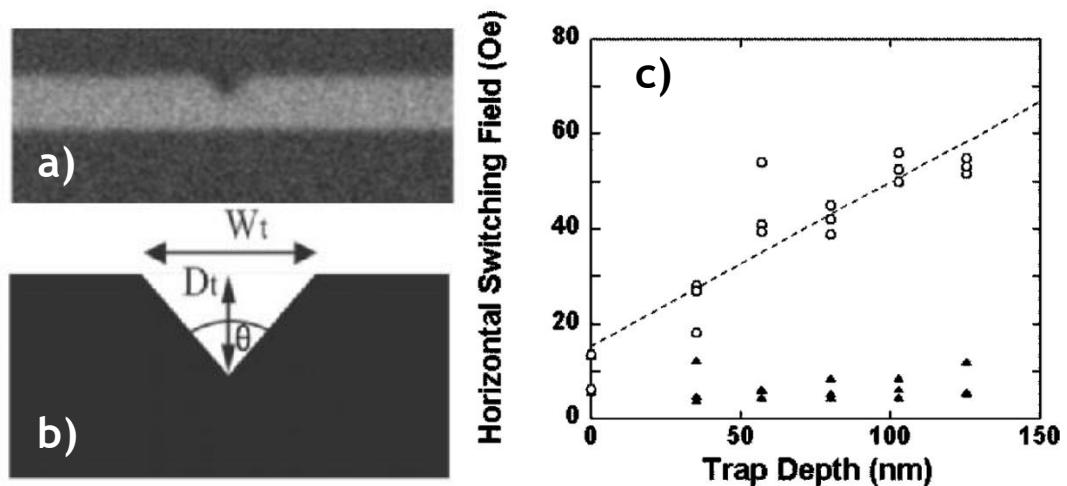


Figure 2.1.6: a) FIB image of triangular notch in a permalloy nanowire. b) Triangular notch schematic. c) Propagation data (▲) and depinning data (○) for three sets of structures with five different trap sizes. Taken from [94]

The way in which DWs interact with pinning sites can be described by the potential energy profile due to the site. Petit and co-workers conducted experimental and computational studies in order to understand further the potential energy profiles produced by round notches and anti-notches for TDWs [35] and ATDWs [98]. It was found that the potential energy profile depended on whether the pinning site was a notch or an anti-notch, but also on the relative chirality of the interacting DW. Data from the TDW study can be seen in figure 2.1.7, along with visual representation of the potential energy profiles found. In summary, If the TDW core magnetisation was pointing towards the notch, the potential energy was found to be a simple singular barrier. In both cases of the TDW core aiming away from the notch and towards an anti-notch, the profile proved to give a potential well with small potential energy barriers situated either side of the well. The data presented for the case where the TDW core aimed away from an anti-notch did not give a clear indication as to how the potential energy profile would form. As such, no obvious conclusion could be made for this case. In a similar study, Zeng *et al.* [102] found that the probability of DW depinning depended on the DW configuration on approach to the pinning site.

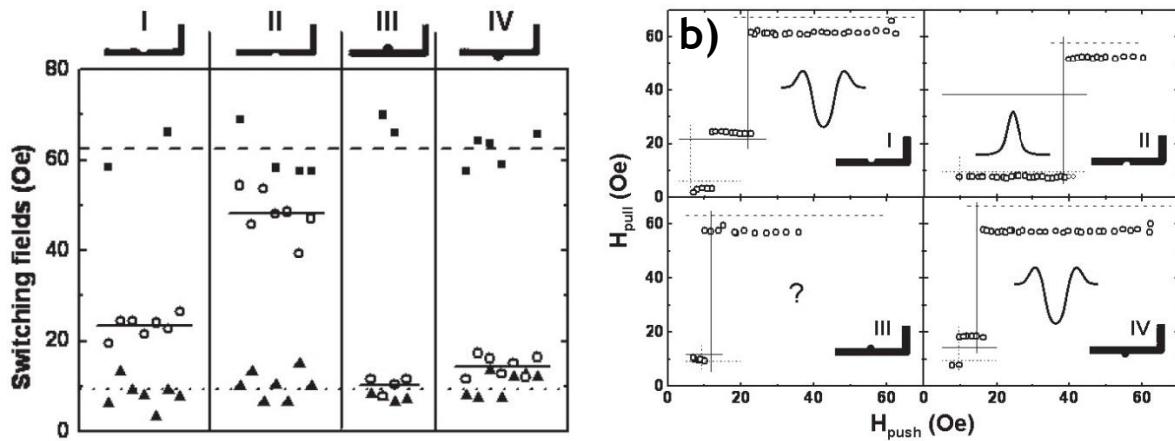


Figure 2.1.7: a) Switching fields of nanowires containing notches and anti-notches.

Squares: nucleation fields H_N , triangles: propagation field H_P , and open circles: transmission field H_T . I DW facing away from notch, II DW points towards notch, III DW points away from anti-notch, and IV DW points towards anti-notch. b) Potential energy profile measurements where H_{pull} is the field required to pull a DW back from a trap and H_{push} is the field required to initially propagate the DW to the trap.

Inserts show schematics of nanowire and resulting potential energy landscape.

Images taken from [35]

The most common lateral notch shapes that have been studied are square/rectangular and triangular. Bogart *et al.* [36] investigated DWs may interact with each of these notch geometries differently. The study included both computational and experimental work and found that the depinning were relatively insensitive to the difference in notch geometry. However, it was found that the depinning fields were highly sensitive to the DW type and chirality. Both variations of pinning site present interactions indicating they act as a potential well or a barrier depending on the micromagnetic structure of the DW.

Whilst discussing the effects of chirality on DW pinning, it is worth discussing how these compare with the effects of the nanowires structures. Other studies [103], [104] compared the size of the injection fields for various width nanowires and compared them with depinning fields for a lateral notch. Injection fields were taken to be the required applied magnetic field to propagate a DW from a nucleation pad into the nanowire. It was observed that decreasing the wire width, especially below 400 nm, had a large influence over the size of the injection fields [103], [104]. This is demonstrated in figure 2.1.8. This is an important aspect to consider when it comes to practical applications. Both studies show the overall nanowire size has a larger influence over injection and resulting depinning fields when compared with notch

size. They also show the geometrical shapes of the notches to not have as significance of an influence over depinning fields as the chirality of the incoming DW. It was found that chirality dependence occurs for both vortex [103] and transverse [104] DWs. Further to the nanowire width, where an inverse relationship was observed between the width and injection fields, it was found that increasing the thickness for the same nanowire width had the effect of increasing the injection fields [104]. It was also found that the injection fields resulting from the nanowire width were chirality independent, this is due to the symmetry within the structure observed by the DW [103]-[105].

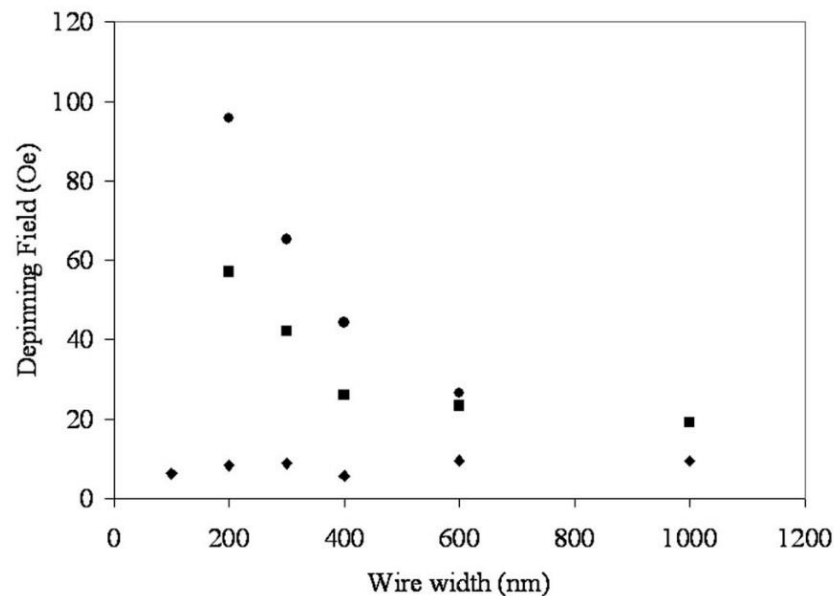


Figure 2.1.8: Switching field as a function of wire width of a 5 nm thick Permalloy nanowire. (◆) represents magnetization reversal of the nucleation pad, (■) represents domain wall injection from the nucleation pad into the wire, and (●) represents domain wall depinning from a triangular notch patterned along one side of the nanowire. Taken from [103].

The work by Goolaup and co-workers [105] focused on the influence of the DW spin structure and notch geometry on the depinning field. Their numerical study used lateral notches of varying sizes and shapes, the effects of both, along with chirality were observed. Nanowire dimensions were used such that transverse DWs were the subject of the study. The first part of the study utilised triangular lateral notches placed on the top, bottom and both edges of the nanowire. For all three of these cases, transverse DWs of various chiralities were tested altering the HtH and TtT configurations along with “up” and “down” chirality. As in previous studies, the up and down chirality were shown to significantly affect the depinning field from the notch. The case of the double notch, creating a central neck, showed no chirality

dependence on depinning field, will all cases depinning at the same applied field. These results are shown in figure 2.1.9(a). This was attributed to the symmetrical nature of the pinning site, as the DW in that instance does not face a spatially asymmetric obstacle in the x-y plane and so it does not affect the potential energy landscape observed for different chiralities.

The second part of the study focused on varying the notch geometry to observe any effects on the depinning field. The notch geometries used were trapezoidal, rectangular, semi-circular and a triangular. The depth of the notch along with the width as the nanowire edge were kept the same for all cases for comparison. It was found that the geometries did have a significant influence over the pinning strength. The trapezoidal the weakest site, with a depinning field of 212.5 Oe, whilst the triangular case proved to pin the strongest with a depinning field of 228 Oe[105].

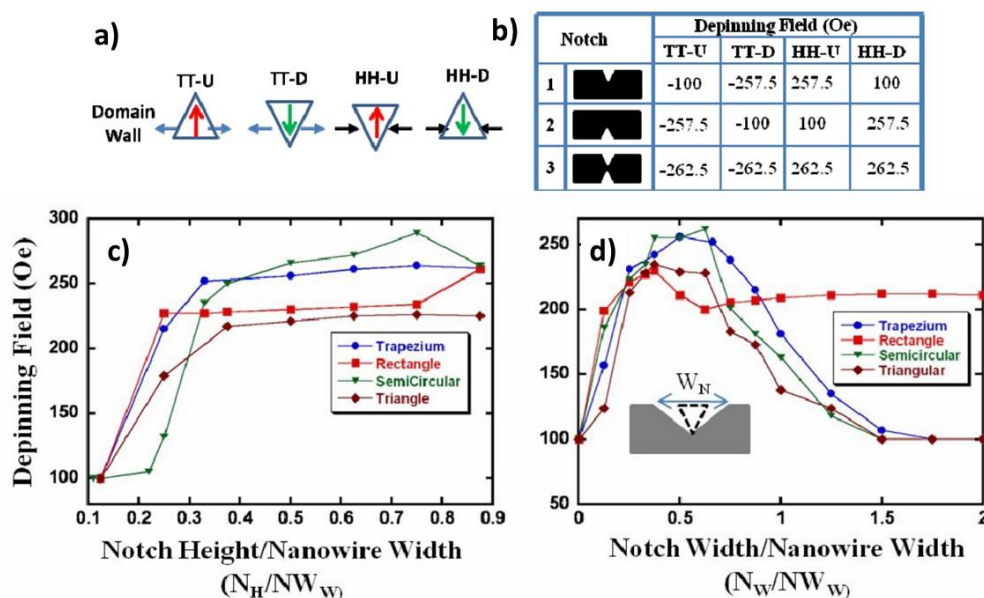


Figure 2.1.9: a) Four types of transverse domain walls. b) Depinning field strength for different notch configurations and domain walls. Domain walls that passed through the notch were assigned a value of (-)100 Oe which equals to the nucleation field of the domain wall. c) and d) Depinning field strength for a Tail-to-Tail “Down” chirality DW for different notch geometries as a function of; c) notch height whilst the notch width is kept fixed, d) Notch width whilst the notch height is kept fixed. Taken from [105].

The final part of the study focused on varying the size of the various notch geometries and observing the effects on the depinning fields. The results of this study can be seen in figure 2.1.9(b). Plots are shown for depinning field against the notch height for fixed widths and against notch width for fixed heights. It was found that the depinning fields initially grew before saturating when increasing the height

of the notches. However, when increasing the notch width, the initial increase in the depinning fields was followed by a fall in field values as the widths grew. This was observed in all notch geometries apart from the rectangular case, where the depinning fields saturated as in the notch height case[105]. This was explained by considering the potential energy landscape along the nanowire. All of the notch geometries considered, apart from the rectangular case, the edges of the notch were at an angle. As the height of the notch remains the same, increasing the width creates a shallower angle of the notch along the nanowire. In the narrow notch cases, the potential energy barrier is also narrower and so provides a sharper. More abrupt change in energies. As the width increases, the depth of the barrier remains the same whilst the change in energies changes more gradually over space. This provides a smoother change in energies along the nanowire, which is easier for the DW to overcome. The exception in this study was the rectangular case. The depinning field values remain constant as the width increases. This matches the explanation given as the angle made by the notch walls remains the same, providing a sharp energetic transition at the edges of the notch regardless of how wide it is[105].

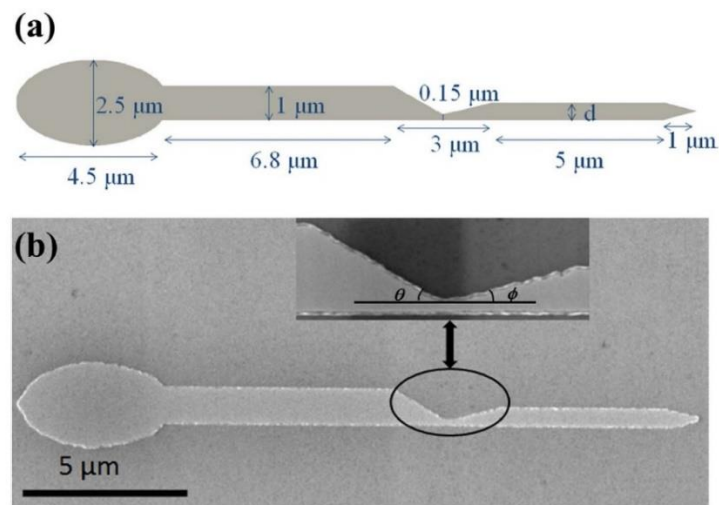


Figure 2.1.10: (a) Schematic illustration of the permalloy nanowire with asymmetric notch. (b) SEM image of the fabricated permalloy nanowire with $d = 500$ nm and the enlarged view around the notch. Taken from [100].

In an attempt to add a further complexity to a pinning site, Gao *et al.* [100] studied the effects of a so-called asymmetric notch. In this case, a triangular notch is placed in the plane of the wire, however the wire is narrower on one side of the notch than the other, as shown in figure 2.1.10. The study reported that as DWs propagated through this feature they had the potential to change their chirality whilst moving

through the notch. This led to there being two possible depinning fields, each having the opposite nanowire width dependencies.

Stochasticity of DW interactions presents a potentially big problem for practical applications. Gao and co-workers researched further complex notch shapes in an attempt to suppress DW depinning stochasticity [106], [107]. Experimental methods to do so were focused magneto-optical Kerr effect (FMOKE) magnetometer and MFM [106] and later longitudinal magnetoresistance (LMR)[107]. Following from the previous idea of using asymmetric notches, these studies researched up to six notch geometries located at a transition in wire width. Each of these are shown in figure 2.1.11. Three of the features studied involved one notch whilst the other three had the same features but placed on both sides of the wire. It was found that the singular larger features provided better reproducibility than the smaller but double sites. In terms of notch shape, there was little difference between the triangular and square notches, as seen previously in the Bogart *et al.* study [36]. It was observed that the DWs increased in size with a reduction in the asymmetry of the notches. This also corresponded to a reduction in DW depinning stochasticity. From the notch shapes studied, it was concluded that using a single triangular notch or a singular trapezoidal notch suppressed the stochasticity the most and so would be the best choice for use in devices.

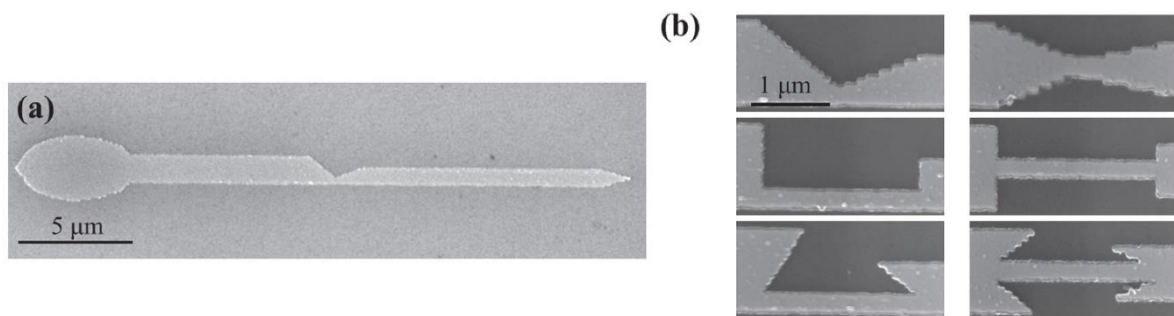


Figure 2.1.11: SEM images of (a) Entire permalloy nanowire with one triangular inward notch, and (b) enlarged six types of notch structures. Taken from [106].

Extending the application of single lateral notches, there have been studies employing a series of notches in order to affect DW motion over a larger range of a nanowire [108], [109]. Kunz and Priem [108] conducted a computational study researching the effects of a series of alternating notches and anti-notches. Comparisons were made of the pinning strengths of both features relative to the chirality for dynamic and static fields. It was observed that if the DWs passed by a pinning site, it did so without any change to its structure. However if a DW was

pinned at the site, the applied field would cause the DW to stretch and grow in size before suddenly shrinking back to the site. It was also observed that notch site pinned DWs stronger than anti-notches for all chirality cases for the equivalent feature size. Another application of series of notches was explored by Chen and co-workers [109]. Computational and experimental work was conducted on nanowires with a series of notches, it was found that in these scenarios DWs do not always form at the ends of a nanowire and can be created at a notch. Symmetrical dumbbell nanowires were created with a series of notches along the central wire with the intention of propagating a DW from either end such that they would meet in the middle to form a 360° DW.

Another popular method for creating pinning sites involves the application of a notch on both sides of the nanowire to create a central constriction, also known as a neck [82], [110]-[116]. The reverse can also be done by adding two anti-notches at the same point of a wire to create a DW pinning site [76], [102]. An example of each of these is shown in figure 2.1.12. It has been found that such “necks” can pin DWs and the strength of the required depinning field increased with a reduced size of the constriction [110], [112]. Other studies have involved propagating DWs using current pulses and observing the corresponding current densities relative to the neck size [115]. Another study in this area propagated DWs initially using an external field to find that the depinning was largely stochastic [116]. The stochasticity had two peaks corresponding to two types of DWs but also had a spread that was too large for any practical applications, as shown in figure 2.1.12. In an attempt to suppress the stochasticity, the DW injection was done using a local pulsed Oersted field, this allowed a reduced injection field. With these lower injection fields, the pinning rate increased to 100%. However the depinning fields decreased with an increased amplitude in the pulse voltage.

In the case of utilising a symmetrical protrusion, it has been seen that DWs can be pinned in front of, partially within or completely inside such a trap depended on the geometry of the protrusions and the chirality of the DW [76]. In the case of transverse DWs, it has been shown that the potential energy profile of such a pinning site acts as a potential well that has small energy barriers on either side [102].

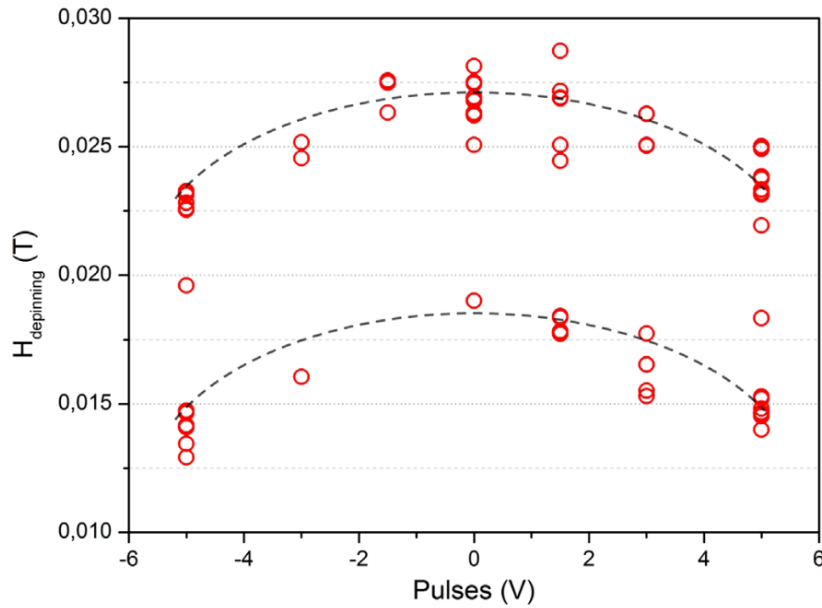


Figure 2.1.12: Graph of the depinning fields from the constriction, as a function of the pulse amplitude. Each red dot correspond to one half-loop field measurement, for a total of 150 loops. Half-loops during which no pinning occurred are not represented. For a given pulse value, the distribution of depinning field is split in two sub-distributions corresponding to two different micromagnetic configurations of the DW. Taken from [116].

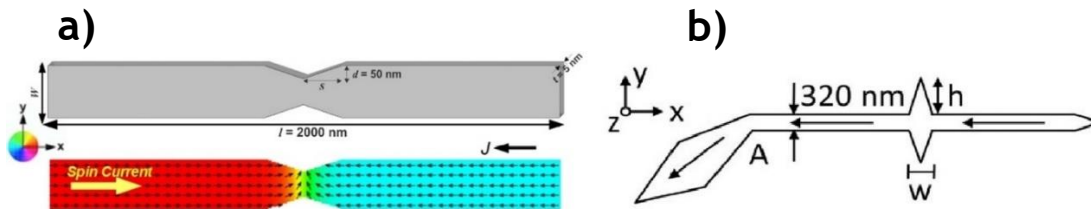


Figure 2.1.13: a) An example of a nanowire constriction/neck. Taken from [115]. b) An example of a set of symmetrical protrusions/anti-notches. Taken from [76].

As done with individual notches, researchers have studied the potential use of a series of constrictions. A series of constrictions was put along a nanowire in an attempt to replicate conditions required for a racetrack memory scenario computationally [113] and experimentally [114]. The study concentrated on varying the distance between constrictions in order to find the optimal separation for information storage.

As discussed in chapter 1.1, magnetisation switching and so DW pinning and depinning can be thermally activated processes. It is important to study how these thermal processes can effect the strength of pinning sites at various temperature

ranges in order to create reliable devices. The stochasticity of DW pinning and depinning at temperatures in the 5 - 50 K range was the focus of an experimental study conducted by Wuth and co-workers [117]. Within this temperature range it was found that the stochasticity reduced with an increase in temperature. At the higher temperatures there were distinct peaks of pinning and depinning fields with a reduced spread. As the temperature was reduced, the spread increased across a wider range of values and the size of any peaks reduced until no distinct peaks could be observed. A computational study conducted by Hayward [118] also focused on the stochastic nature of DW pinning in nanowires. The conducted simulations indicated that stochastic pinning is an intrinsic feature of DW behaviour at finite temperatures. Such features originate from the delicate interplay between thermal perturbations and the complex magnetisation dynamics exhibited by DWs. These results imply that any stochastic effects in DW devices would not be suppressed even if initial DW states and operating parameters could be perfectly defined.

Other studies conducted by Himeno and co-workers have focused on the effects of temperature on DW propagation velocity [111] and the magnitude of DW depinning fields [119]. The DW propagation velocity was investigated over a temperature range of 4.2 to 200 K and was found not to change across this range of temperatures. The velocities also stayed constant over a distance of 2 mm [111]. Studying the temperature dependence on depinning fields found that the required fields reduced as the temperature increased. It was reported that the depinning field values reduced by 40-60% as the temperature increased from 4.2 K to 300K [119].

2.1.4 Vertical modifications to nanowires

The final method of pinning DWs to be discussed in this chapter involved variations in the thickness of thin films and nanowires. This is an area of DW pinning that has not been previously researched in detail and so has not produced much published work. This method of DW pinning is the most relevant technique studied as the main subject of this thesis.

Initial works in this area were conducted by Asada and co-workers [120], [121]. These works were computational studies focused on the use of step changes in the thickness of thin films to pin DWs. The first of these studies [120] studied the effects of a single step change in thickness within an infinite thin film, with the applied boundary conditions. The step change was made such that the thickness changed whilst moving along one direction, as demonstrated in figure 2.1.14. The films used in this study are still relatively thick as the larger section of the film ranged from

0.15 to 0.5 μm , however results are quoted as ratio step changes as opposed to absolute step changes. Before introducing a step change, the DW energy was studied as a function of film thickness. It was seen that the wall energy increased as the thickness decreased, where the exchange energy takes over and becomes dominant. With the introduction of a thickness step change, the total energy increased as the ratio of thickness change increased. This is attributed to an increase in demagnetisation energy with the presence of a step. As the thickness ratio increased it was observed that the required depinning fields also increased. An additional feature was found regarding the DW depinning relative to field direction, shown in figure 2.1.15. It was found that larger depinning fields were required to propagate DWs with negative field values. This is explained by the wall energy per unit length being larger within the thinner region of the film. Finally the the depinning field strength as a function of film thickness was studied. As the film thickness increased, the depinning field sizes decreased. These fields decrease such that they become less than 0.4 Oe when the film thickness is increased to 0.5 μm . This trend is similar to that shown with the exchange energy and can be seen in figure 2.1.15.

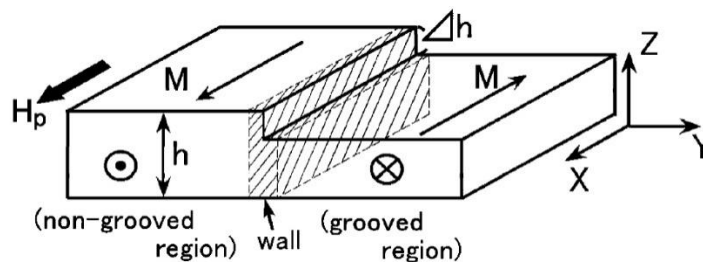


Figure 2.1.14: Schematic of step-like thickness change in a thin film. Take from [120].

Following the previous work, Asada and co-workers investigated the presence of a vertical groove placed within a thin film[121]. The computational model was constructed such that the groove would be placed along the entire y-direction and the thickness change occurred in the x direction, demonstrated in figure 2.1.16. Both directions have boundary conditions in place to assume an infinite film. Similar data sets were taken as done in the previous step change study. As before, it was found that the depinning fields reduces as the film thickness increased. The effects of the groove width on the depinning fields was studied. For a fixed thickness change ratio, the width of the groove was increased from around 100 \AA to 1200 \AA . It was found that the groove width did not have any influence on the depinning fields. This result indicates that the DW pinning is dominated by the magnetisation state in

the vicinity of the step change. However whilst the groove width was studied, the depth of the groove relative to the thickness was not as the thickness change ratio is kept at 0.2 for the whole study.

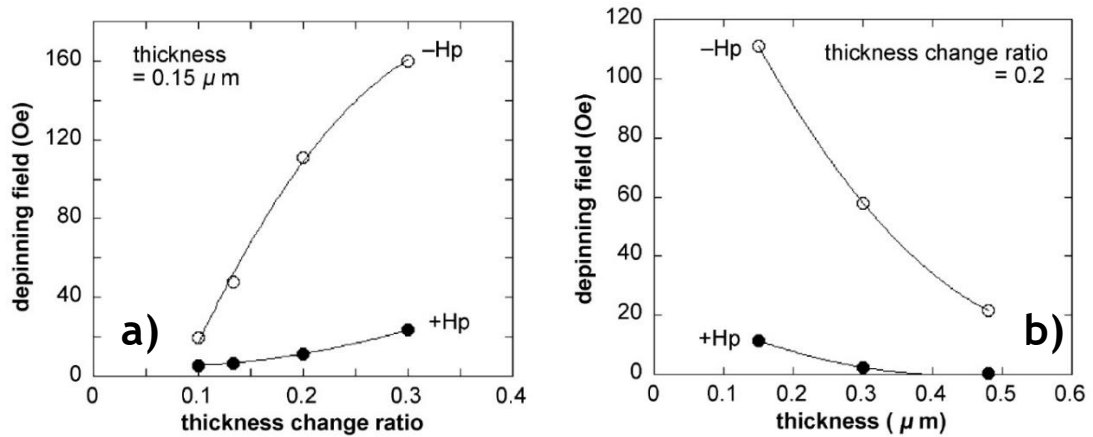


Figure 2.1.15: Dependence of depinning fields for positive and negative magnetic fields, a) for a $0.15 \mu\text{m}$ thick thin film with varying thickness ratio. b) for varying thin film thicknesses with a thickness change ratio of 0.2. Taken from [120].

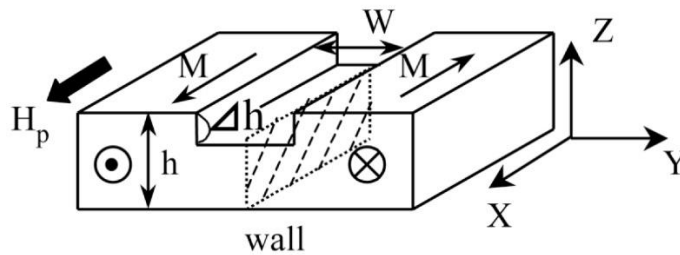


Figure 2.1.16: Schematic of a groove in a thin film. Taken from [121].

With the intention of creating vertical features within nanowires, Watanabe and co-workers utilised an AFM oxidation technique in order to generate pinning sites [122]. NiFe oxide features were generated across the whole width along the top surface of NiFe nanowires using an AFM with an applied voltage to the cantilever. A schematic of this technique is shown in figure 2.1.17. The widths of these nanowires varied between $2\text{-}4 \mu\text{m}$ with the thickness of the films ranging from 15 nm to 30 nm . As shown in figure 2.1.17, the oxide features created penetrate the surface of the nanowire, whilst also creating a protrusion above the top surface. The depth of these features are “considered” to be equal to the size of the features above the surface, and so these heights are used to estimate the depths of the oxide sites. These oxide features were shown to pin DWs. The pinning strengths of these features were reported to pin stronger with a larger ratio of oxide depth. However, there is no replication of oxide depths for the same dimensions of nanowires. As discussed

previously, different dimensions of nanowires produce different switching fields and so distinct conclusions of oxide depths relative to pinning strength would need further research comparing at least similar dimension wires with varying feature sizes.

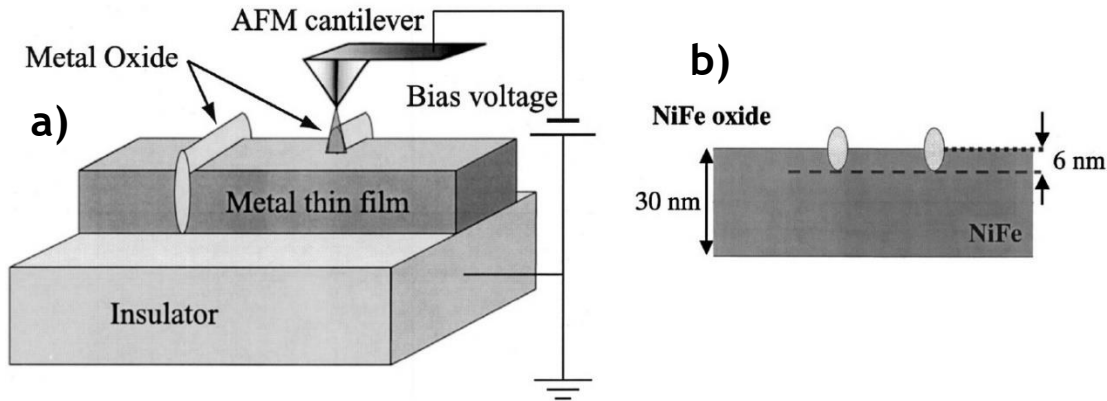


Figure 2.1.17: a) Schematic of nano-oxidation technique using AFM. b) Schematic of cross-section of nanowire with oxide features. Taken from [122].

The final key study that will be discussed in this section is that of Narayanapillai and Yang [123]. This study focuses on vertically etched nanotrenches to pins DWs in nanowires. The majority of this study is computational with a small experimental example at the end. The computational part of the study consists of two nanowires of dimensions of widths and thicknesses of 100 x 10 nm and 200 x 40 nm. Each of these dimensions are chosen to study transverse and vortex DWs respectively. In each case, the dimensions of the vertical nanotrench is varied and the depinning fields are recorded. A schematic of the dimensions defined and examples of the DWs relative to the nanotrench are shown in figure 2.1.18.

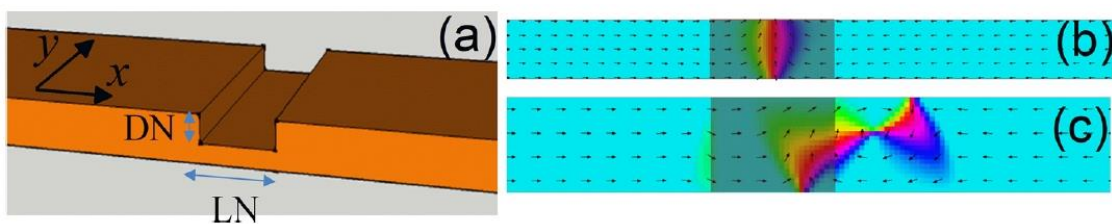


Figure 2.1.18: a) Schematics of a nanowire with a nanotrench. Simulated b) transverse and c) vortex DW at the nanotrench. Taken from [123].

The generated results from this computational study are shown in figure 2.1.19. To sum up the results, it can be seen on both the transverse and vortex DW cases that the quoted “length” of the notch is not as influential to the pinning strength of the

nanotrench. In both cases the depinning field increases up to a length of around 100 nm, beyond which the trend flattens and increases only slightly as the length is increased further. The depth of the nanotrench however appears to be much more influential. In both cases the trend between depinning field and depth of notch increases approximately linearly in all cases and combinations of notch lengths. However it is key to point out that these trends only go as far as creating nanotrenches as deep as 60% of the nanowire thickness and so it is unclear as to whether or not these linear trends would continue as more of the nanowire is removed. Another note to be made on the absolute values of the depinning fields concerns the difference between the two nanowire sizes. The depinning fields quoted for the smaller nanowire, corresponding to the transverse DW, are approximately a factor of two larger than those of the vortex DW case.

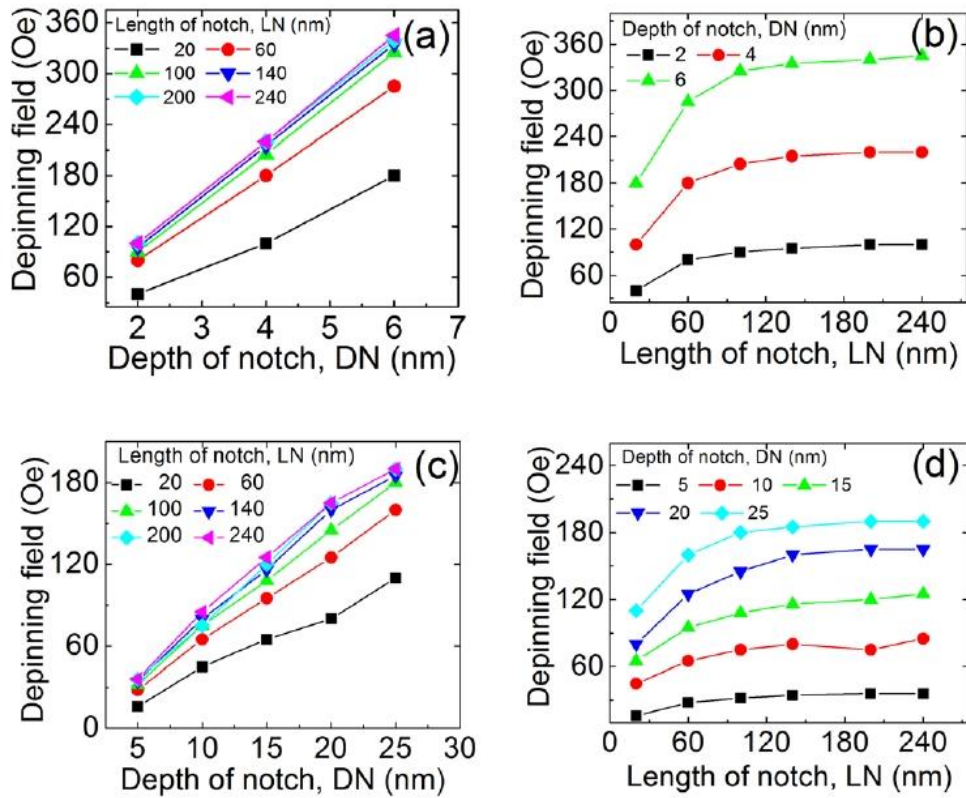


Figure 2.1.19: Dependence of depinning field with the depth (a) and the length (b) of nanotrench for a transverse wall. (c) and (d) show the dependence of depinning field for vortex walls. Taken from [123].

In order to further understand what the driving mechanism is behind these interactions, energy profiles are plotted with respect to DW position. These energy profiles are shown in figure 2.1.20. In all cases the total energy reduces as the DW is in the vicinity of the nanotrench. It is also shown that whilst the exchange energy

does change and reduce slightly, it is always the demagnetisation energy that dominates the change in energy at these scales. This agrees with what was discussed by Asada and co-workers [120], [121]. The DW type also makes a difference in the energy profiles. The transverse DWs interact with the nanotrench such that it creates a simple energy well. However whilst the vortex walls do provide a reduction in energy, there is a relative increase in energy that almost completely restores back to the highest value when the DW is positioned at the centre of the nanotrench. These energy profiles correspond to transverse DWs becoming stable and pinned at the centre of the nanotrench, whilst the larger vortex DW structures have a preference to place themselves at the edge of the nanotrench. This agreed with phenomena observed in other constriction type notches where vortex DWs need to realign their spin structures at the expense of increasing energy terms whilst passing through a notch [36].

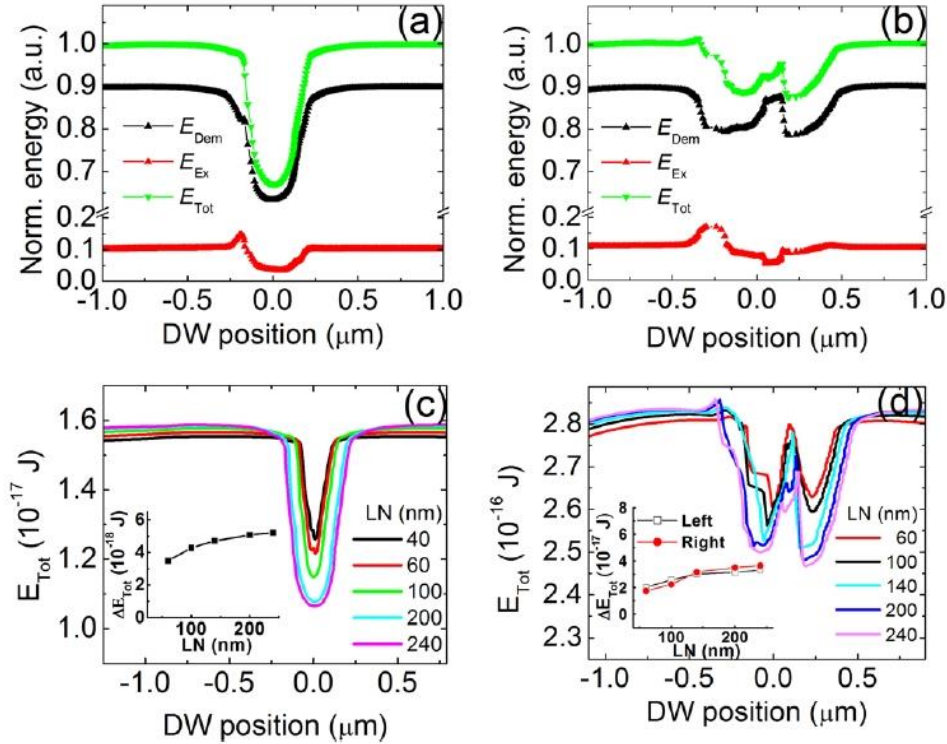


Figure 2.1.20: Energy profiles with respect to DW position for a transverse (a) and a vortex (b) wall. (c) and (d) show the total energy for transverse and vortex walls for various lengths of nanotrenches. The drop in the energy profile (ΔE_{Tot}) is plotted in the insets for respective DW types. Taken from [123].

In an attempt to experimentally demonstrate the results found in the computational part of the study, a nanowire was created consisting of a substrate/Ta (3 nm)/Ni₈₁Fe₁₉ (30 nm)/Ta (3 nm)/Ru (2 nm) stack structure. The nanowire was

measured to have a width of 650nm and a length of 12 μm . A nanotrench was created in the centre of this nanowire using Ar ion milling, the dimensions of which are not stated in the publication. Anisotropic magnetoresistance (AMR) measurements are conducted to detect the presence of DWs and find the corresponding depinning fields. These results are shown in figure 2.1.21. A histogram of the DW resistance measurements show two distinct peaks with an additional smaller peak, indicating the presence of potentially three types of DW occurring within the wire. These are attributed to the presence of transverse, clockwise and anti-clockwise vortex DWs. There is a stochastic spread within the values of the depinning fields that appear to have multiple peaks, but the corresponding number of events do not appear to match the resistance data for reliable relationships to be made between the two. Whilst this experimental work provides an example that a vertically etched nanotrench has the potential to pin DWs, it does not show much further insight than that. The fact that no nanotrench dimensions are quoted within the publication fail to provide any indication as to how much magnetic material was removed and if the found depinning fields agree qualitatively at all. There also appears to be a lack of comparison made with measurements made before the nanotrench was created. Therefore DWs may be pinned at another pinning site generated by a fabrication impurity or nanowire imperfection rather than the nanotrench itself. This could also provide another explanation not considered by the authors for the various depinning fields found. It also does not provide any further insight based on the computational work carried out regarding how the feature size may influence the pinning sites strength. The experimental relationship may prove to differ from the computational results due to simulations being carried out at zero temperature as opposed to temperatures comparable to the experimental work.

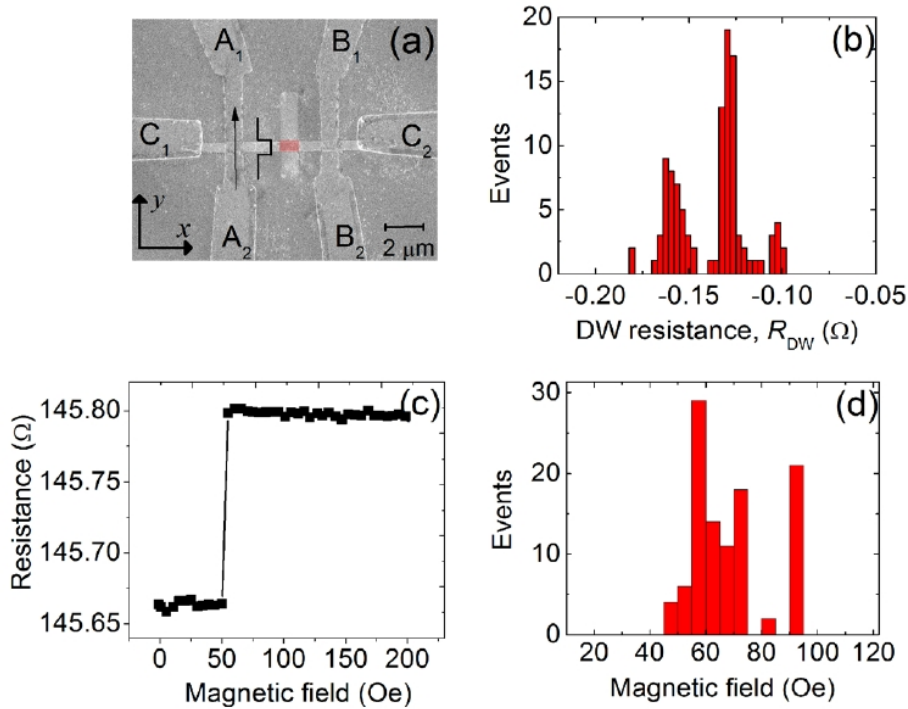


Figure 2.1.21: (a) Scanning electron micrograph image of the device with the measurement schematics. (b) The histogram plot of the generated DW resistance. (c) A typical depinning profile of a DW from a pinning site. (d) The histogram plot of depinning fields. Taken from [123].

2.2 AFM tip-based nanomachining

2.2.1 AFM as a tool for nanofabrication

As introduced in chapter 1.2.4, the tip of an AFM can be used as a nanomachining tool to cut into the surface of a sample. Since original experiments in the early 1990s[69]-[71], there have been many studies testing how materials may be modified via AFM tip-based nanomachining. Such materials include various polymers [124]-[128], silicon [129], [130], metals [131]-[134], oxides [135], semiconductors [136], [137] and biomaterials [138], [139]. Different tip materials have also been employed, including silicon tips [127], [140], [141] silicon nitride tips [56], [69] as well as diamond [142]and diamond-coated tips [143].

As any features created using this process involves direct contact between the tip and the sample, it follows that the quality and accuracy of any machined grooves will depend on the geometry and durability of the tip. Due to these factors, both silicon and silicon nitride tips have limitations resulting from tip wear. Both materials have relatively quick wear rates and so leads to a decrease in quality of produced grooves. It also makes reproducibility very difficult as the wear on the tip

changes its geometry between machining cycles. This influences groove depths and shapes due to variations in stress distribution along the contact surface of the tip for the same given applied force [144], [145]. One possible solution to increase the tip lifespan is to coat these tips with hard materials such as diamond [136] or diamond-like carbon [146].

As a result of the numerous studies conducted over the last few decades in AFM tip-based nanomachining, a few state-of-the-art reviews have been published recently [147]-[149]. Given that the main focus of this thesis is on the application of AFM tip-based nanomachining and not of the process itself, it is not in the scope of this thesis to provide another such review.

2.2.2 Comparison with other nanofabrication techniques

Since AFM tip-based nanomachining has gradually become more researched as a potential nanofabrication process in its own right, it is useful to see how this method compares with other nanolithographic techniques. Figure 2.2.1 provides such a comparison including traditional resist-based lithography methods. The figure illustrates differences in capital cost for the equipment required, minimum resolution and patterning speed. It is seen that AFM lithography is a relatively low-cost process when compared to other methods. Its capital cost is in the region of \$100,000 whilst many others including electron beam lithography (EBL) and other forms of UV lithography require equipment costing over \$1,000,000. The cheaper cost of an AFM means that more organisations and smaller research groups are likely to be able to afford such equipment in order to conduct further research or make use of its potential nanofabrication applications.

AFM lithography also compares extremely well to other techniques for the achieved resolution. As shown in figure 2.2.1, only STM provides a smaller resolution than AFM. AFM lithography actually provides better resolution than multiple techniques that are much more expensive. An increased resolution allows the creation of smaller features, down to the nanometre scale. AFM lithography can therefore be used when dealing with nanoscale components. This is ideal for research into potential downsizing of technology.

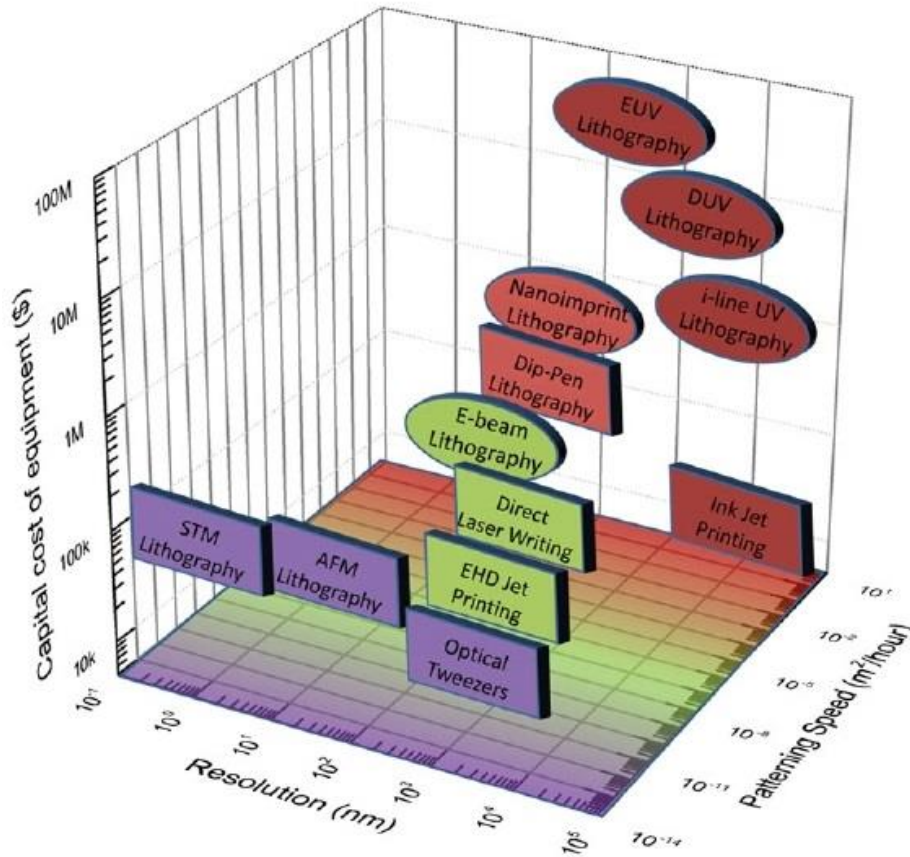


Figure 2.2.1: Equipment cost, patterning speed, and minimum resolution of AFM lithography compared with other methods for nanofabrication. (EUV = extreme UV lithography, DUV = deep UV lithography, EBL = electron-beam lithography, NIL = nanoimprint lithography, STM = scanning tunnelling microscopy). Taken from [150].

The final parameter used for benchmarking in figure 2.2.1 is patterning speed, measured in area per time. AFM lithography does compare rather poorly in this case as only STM is slower. However, this does not necessarily represent the time taken to complete a full process when fabricating a given feature. In particular, AFM lithography is a one-stage process, meaning that the lithography is done in one relatively simple step. In the case of nanomachining, the AFM tip is used to cut into the surface and directly create the desired topography and so does not require any prior surface preparation or subsequent development of the sample to obtain the final feature. However, a multi-step approach is found in resist-based lithography, where the design is first patterned onto a resist prior to subsequent developments through wet or dry etching. Thus, one should keep this in mind when considering the comparison of processes illustrated with figure 2.2.1. AFM machining can also be conducted on any material providing that the tip is hard enough to cut into it. The technique also has the ability to be performed in atmospheric conditions and so does

not need a vacuum environment, such as is the case for EBL for example. A combination of all of these advantages means that whilst the direct patterning speed may not be as high as other techniques, the overall lithography process speed is still competitive.

It is worth noting that with respect to the relatively slow throughput, a number of researchers have tried to improve the patterning speed. Such methods typically involve retrofitting a piezoelectric actuators-based solution onto the stage of AFM systems such that the cutting velocity at the interface between the tip and a sample can be increased [128], [151], [152].

2.2.3 Applications of AFM tip-based nanomachining

A number of research investigations have been published in which AFM tip-based nanomachining was implemented as part of a semiconductor-based process chain to develop devices for specific applications. Of particular interest with such studies is the fact that nanoscale physical phenomena, associated with the features cut with an AFM tip, were also characterised. For example, the fabrication of a single electron transistor on a GaAs/AlGaAs layered structure and its transport properties have been reported by Schumacher and co-workers [153]. In another study, Cortes Rosa *et al.* fabricated an antidot array directly on InAs-AlSb surface quantum wells using an oscillating tip to observe the magnetoresistivity of such structures [154]. Wang *et al.* machined a nanochannel with an AFM tip to connect two microscale reservoirs for studying the flow of fluids and nanobeads through the channel [155].

AFM nanolithography was used to manufacture a Ti nanowire by Hong and co-workers [156]. In this case, AFM tip-based nanomachining was not employed as a direct-write operation but rather as a patterning step prior to a lift-off process, which subsequently revealed the nanowire. Further fabrication and characterisation steps were conducted in this study to demonstrate the fabrication of a functional single titanium oxide nanodot for ultraviolet sensing. Finally, AFM nanolithography was implemented in a different way, compared to pure mechanical machining, i.e. with heated tips, by Vettiger *et al.* [157]. This study employed an array of such tips to modify the topography of various polymer substrates with a view of developing a high-density storage system, coined the “Millipede”.

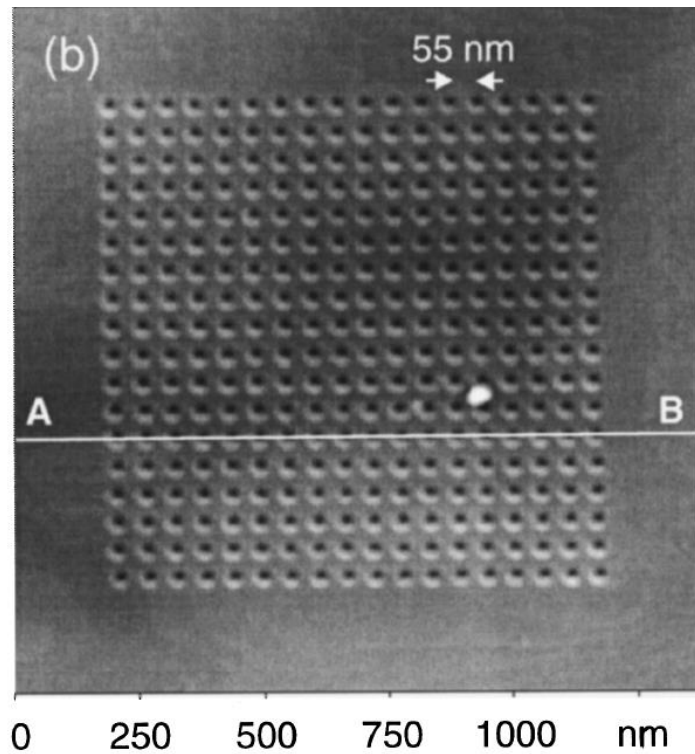


Figure 2.2.2: Example of an application of AFM nanomachining. Periodic hole arrays with a period of 55 nm in an InAs-*AlSb* surface quantum well created by direct lithography of the InAs top layer. Taken from [154].

2.2.4 AFM nanolithography of ferromagnetic thin films

Any application of AFM tip-based nanomachining would require reliable control of the created features. This means that relationships between applied tip loads and size of generated nanogrooves should be established first. Among others, Tseng has conducted a number of studies into this area. The work of Tseng has an increased relevance to this thesis as the primary material used in his experiments was permalloy. Permalloy (NiFe) is a ferromagnetic material consisting of approximately 80% nickel and 20% iron, and as will be explained in the next chapter, it will be the material of choice for the studies in this thesis.

In the first study from Tseng that is summarised here, the relationship between the applied load and the groove dimensions was studied for both silicon and permalloy thin films [158]. Scratches were performed varying the applied load from 1 to 9 μN . An image and examples of the cross-sectional scan of a produced groove can be seen in figure 2.2.3. It was found that both the depth and width of the resulting grooves had a logarithmic correlation with the normal force applied. This was the case for both silicon and permalloy. However, grooves machined in permalloy were

approximately seven times deeper and twice as wide than those obtained in silicon. The plot of the resulting data is shown in figure 2.2.4.

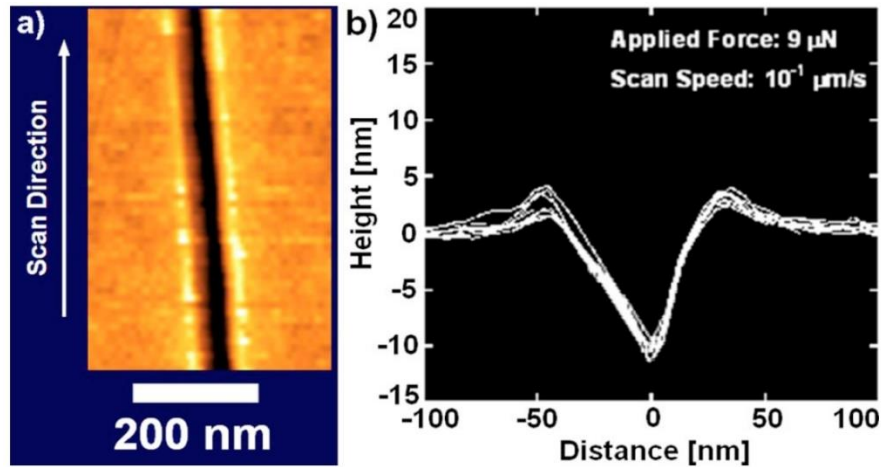


Figure 2.2.3: AFM scratched groove on NiFe thin film surface using 9 μN applied force: (a) AFM image of groove along scan direction and (b) cross-sectional profiles at ten different groove locations. Taken from [158].

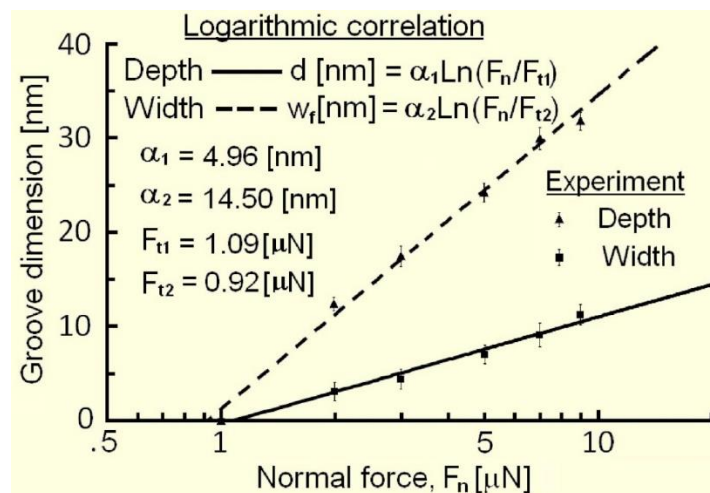


Figure 2.2.4: Correlation of depth (d) and width (w_f) of scratched groove with normal applied force F_n for NiFe thin film. Taken from [158].

The effects of the tip speed during machining was also investigated. The tip speed was varied from 10 to 10,000 nm/s using a constant force of 9 μN. It was found that the size of the resulting nano-grooves did not vary significantly and no distinct trend could be identified. Therefore, any changes due to the scratching speed can be neglected.

The final part of this particular study involved an attempted application of the AFM nano-machining process. A permalloy nanowire was fabricated and then, an AFM tip

was used to scratch away a portion of the nanowire. The vast majority of the wire was removed during this scratch leaving very little material as shown in figure 2.2.5. This was used as a nanoconstriction for potential utilisation for devices to control extremely small currents on the fA scale. It is worth noting that, despite working with NiFe, Tseng did not attempt to study nanomagnetic phenomena within the machined nanowire.

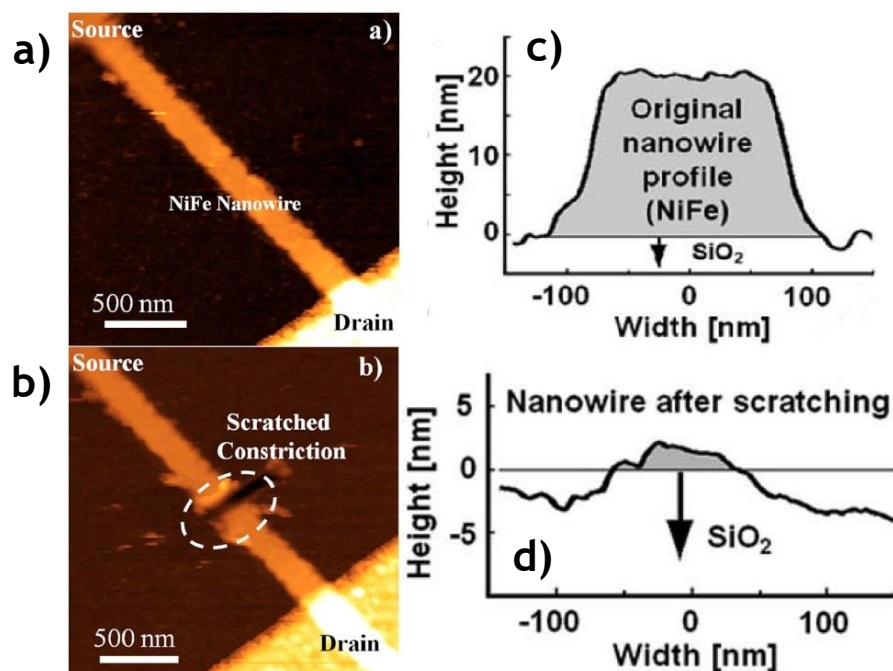


Figure 2.2.5: a) and b) AFM images, c) and d) Geometric profiles of NiFe nanowires before (a and c) and after (b and d) the creation of the nanoconstriction. Images taken from [158]

The second study from Tseng which is discussed here focused on the relationship between the dimensions of a nano-groove and the number of repeated AFM tip scratches used to create it [159]. The applied force was kept constant at 9 μN during all scratches, while the number of scratches was changed from 1 to 9 in increments of 2. A power law was also found to fit the data well in this case as shown in figure 2.2.6.

The third and final study of Tseng that is reported here focused on the influence of the cutting direction relative to the tip shape. The experiments were conducted using permalloy thin films with a nominal thickness of 30 nm deposited onto a SiO₂/Si substrate. A three-sided diamond-coated pyramidal tip was used to perform the scratches [160]. As a result, there were three main distinct directions in the tip could be oriented when cutting into the surface, each of these presenting a

different contact face, also known as the rake face in conventional machining. These directions are illustrated in figure 2.2.7. It should be noted that the figure shows four directions for the tip motion, rather than three. However, the “upward” and “downward” directions are simply mirror images of one another for the purpose of machining.

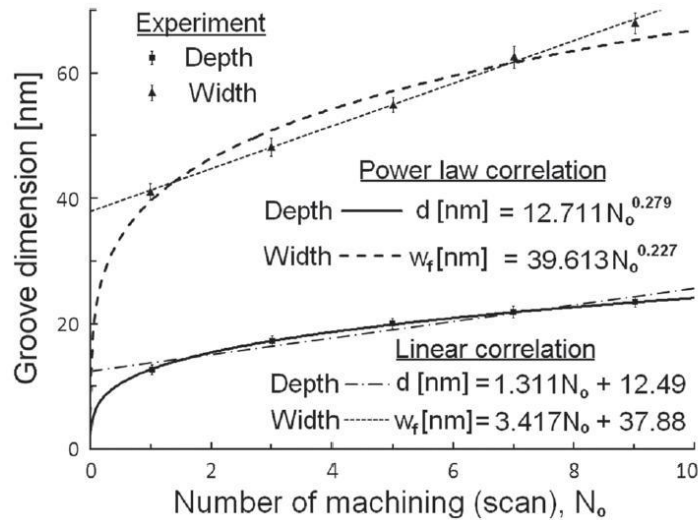


Figure 2.2.6: Correlation of depth (d) and width (w_f) of groove machined on NiFe surface with number of machining cycle (N_0). Image taken from [159].

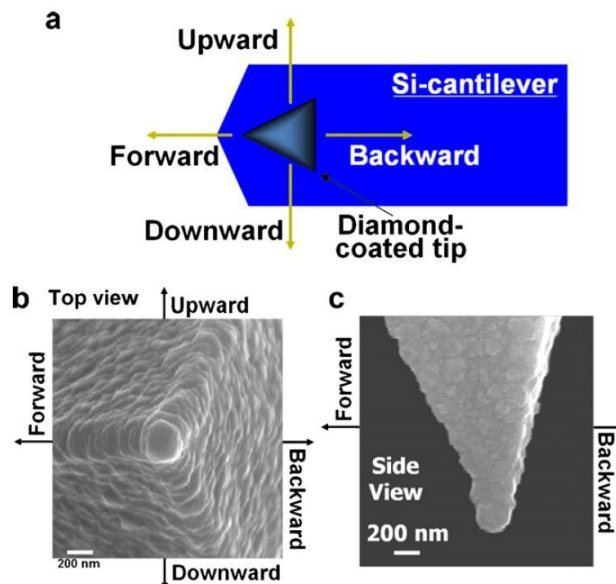


Figure 2.2.7: Si probe with diamond-coated pyramidal tip: (a) schematic of rectangular microcantilever with triangular pyramidal tip, (b) SEM image of tip top view, (c) SEM image of tip side view. Taken from [160]

AFM images and the resulting line scans of each nano-groove are shown in figures 2.2.8 and 2.2.9 respectively. Whilst the shape of the nano-groove itself did not change vastly, there was a noticeable difference in the amount of material piled up at the sides of the groove. The “upward” and “downward” directions resulted in the same groove and pile-up dimensions, with the only difference being that the pile-up was on the opposite side to one another. In each case, pile-up is seen only on one side of the groove. The height of the pile-up is significant and measures at a height comparable to the depth of the groove. Pile-up on one side is expected as the tip-face cutting into the material is at an angle to the direction of motion. The sharpest point is at one edge of the face which will be the primary point where cutting occurs. The sloped face then channels the material across to the opposite side, hence the pile-up only occurring on that side. In the so-called “forward” direction, the dimensions of the groove are still comparable to those generated during the “upward” and “downward” directions. However, there is significant pile-up occurring on both sides of the generated groove, albeit that both are not as high as in the other two cases. This is due to the sharpest cutting point of this direction being in the centre of the tip. This cuts into the material and then moves an equal amount of material either side of this point, thus creating two pile-ups rather than just one. As approximately the same amount of material is still being removed, the resulting pile-up on each side is smaller than for the other two cases where only one-sided pile-up occurred. The final direction studied was the so-called “backward” direction. It differs from the other three cases as it does not result in sharp edge along the cutting face. Therefore, there is effectively a single rake face used to cut into the material as opposed to a sharp edge slicing into the material. In this case, the overall size of the groove, both depth and width, is smaller than in the other three cases. However, whilst there is still pile-up occurring on both sides of the groove, it is vastly reduced in size. The scaling of the pile-up dimensions does not appear to be equal to the relative loss in groove dimensions, and so this direction produces a relatively smoother feature in the thin film.

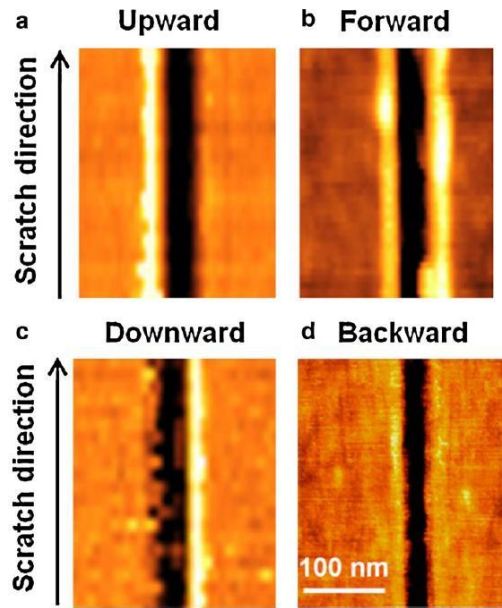


Figure 2.2.8: AFM image of grooves scratched by a normal force of $9 \mu\text{N}$ on $\text{Ni}_{80}\text{Fe}_{20}$ surfaces at four directions: (a) upward, (b) forward, (c) downward, (d) backward.

Taken from [160]

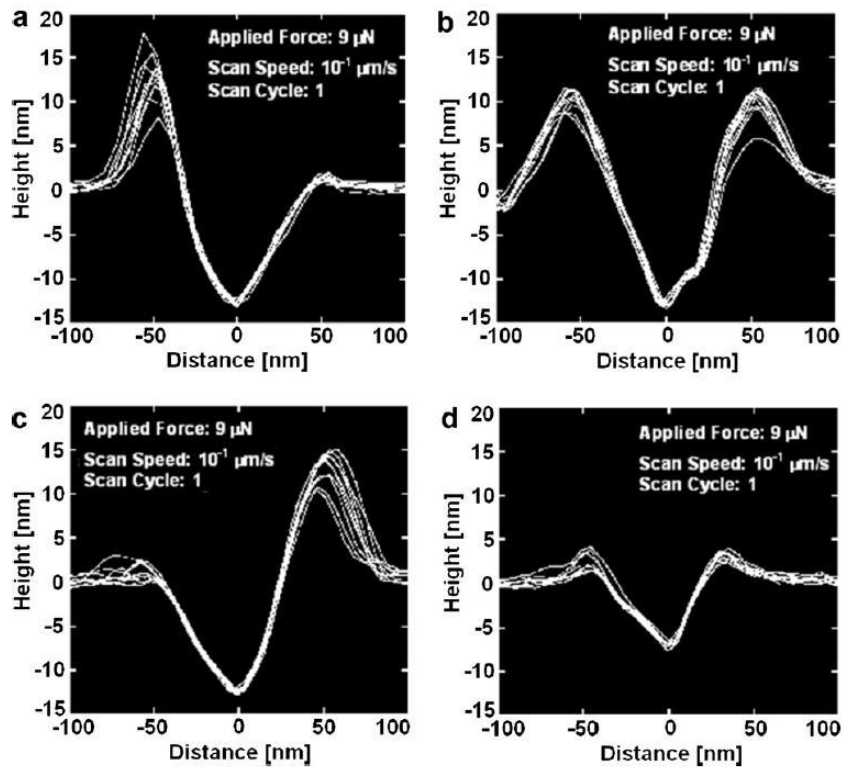


Figure 2.2.9: AFM-measured cross-sectional profiles of four grooves scratched by a normal force of $9 \mu\text{N}$ on 30 nm thick $\text{Ni}_{80}\text{Fe}_{20}$ thin films on a SiO_2/Si substrate at 10 different groove locations along: (a) upward direction, (b) forward direction, (c) downward direction, (d) backward direction. Taken from [160]

2.2.5 Using AFM tip-based nanomachining to pin Domain Walls

As discussed in section 2.2.3, the development of AFM tip-based nanomachining has led to research into different possible applications of this method. So far, it is fair to say that there has not been many such applications reported, with the relatively few exceptions briefly discussed in section 2.2.3. Importantly, there has yet to be any detailed investigations into the potential application of AFM tip-based nanomachining for in the study of nanomagnetic devices. Such devices have a vast range of possible applications, some of which have been discussed in section 1.1.10. These devices would require control of magnetic DW motion. Various methods studied to pin DWs have been discussed in section 2.1, with many of them involving changing the local dimensions of a nanodevice. In this PhD research, it is identified that AFM tip-based nanomachining represents a potentially attractive solutions to create such constrictions that could pin DWs.

To the best knowledge of the author, there have been two studies published in 2001 and 2002, by the same research group, who had the idea to pin DWs using AFM nanomachining [161], [162]. In both studies, Pt/Co/Pt ultrathin film devices were used. The outer layers of Pt are quoted to be 3.4 nm and 4.5 nm with the central magnetic Co layer measuring between 0.5 and 1 nm in thickness, referred to as t_{Co} in figures 2.2.10 and 2.2.11 captions. It is also worth noting that the magnetisation of these thin films was out-of-plane.

In the first study [161] Schumacher and co-workers created two devices, a long nanostrip with a width of 4 μm and a cross junction of nanostrips where the central square measured 2 μm x 2 μm . These are shown in figure 2.2.10. In the cross-junction case, a single nano-indent was created with the AFM tip in the centre of the square. As the magnetic domains propagate through the strips, the DW reaches the central square and interacts with the created indent. The resulting hysteresis loop and Kerr images of this experiment can be found in figure 2.2.11.

The magnetisation switching within the cross junction containing a nanoindentation can be seen in figure 2.2.11. Image i shows a DW entering the structure from the bottom nanostrip. As the applied field is increased, the DW enters the central junction and interacts with the nanoindentation. This is shown in image ii as the DW is angled across the junction as opposed to filling the whole region. Image iii shows more of the material switching magnetisation whilst the region on the other side of the nanoindentation remains unswitched. Finally image iv shows the magnetisation completely switching along the side nanostrips, but not yet along the top nanostrip.

This series demonstrates the nanoindentation interacting and affecting the DW propagation within the magnetic material.

In the wide nanostrip case, a single groove measuring 100 nm wide and 5 nm deep was fabricated along the width of the nanostrip. The depth of the groove indicates that the magnetic Co layer was completely cut through. When reversing the externally applied magnetic field, figure 2.2.11 shows that the left side of the nanostrip reverses magnetisation but then stops at the fabricated groove. This indicates that magnetic DWs can be pinned at features created using AFM nanomachining. However, there is an important caveat to this statement as explained below. Figure 2.2.11 shows the series of images representing the magnetic domains during the reversal process. Image b in the right half of figure 2.2.11 shows that the wire to the left of the groove has reversed its magnetisation, with the DW at the groove. Image c then shows the nanowire reversing its magnetisation from the right, leaving a section unchanged between the notch and the newly reversed region. This indicates that the DW still remains at the groove and therefore does not propagate beyond the machined constriction. This can be explained by the fact that the entire thickness of magnetic layer has been cut, leaving no magnetic material underneath the pinning site that the DW would be able to move through. Due to this key difference, control of DW motion is not achieved in the strict sense of the term and thus, the method reported in this paper cannot necessarily be compared to other methods of DW pinning discussed in section 2.1.

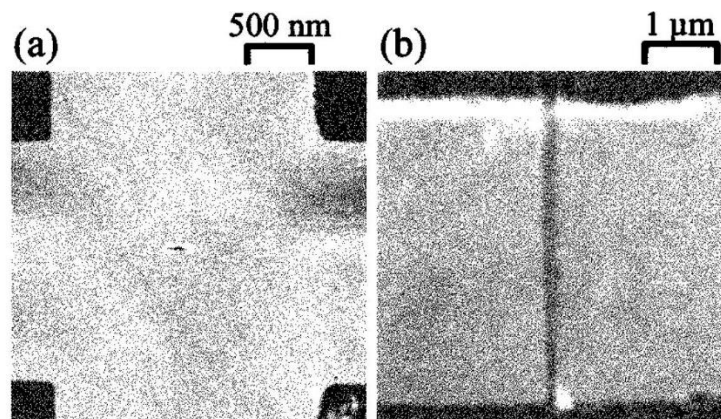


Figure 2.2.10: AFM fabricated nanostructures: (a) hole in the centre of Hall cross ($t_{Co} = 0.5$ nm). Applied force: $F_{app} = 14$ μN. (b) Groove across a wire ($t_{Co} = 1$ nm), $F_{app} = 30$ μN. Taken from [161]

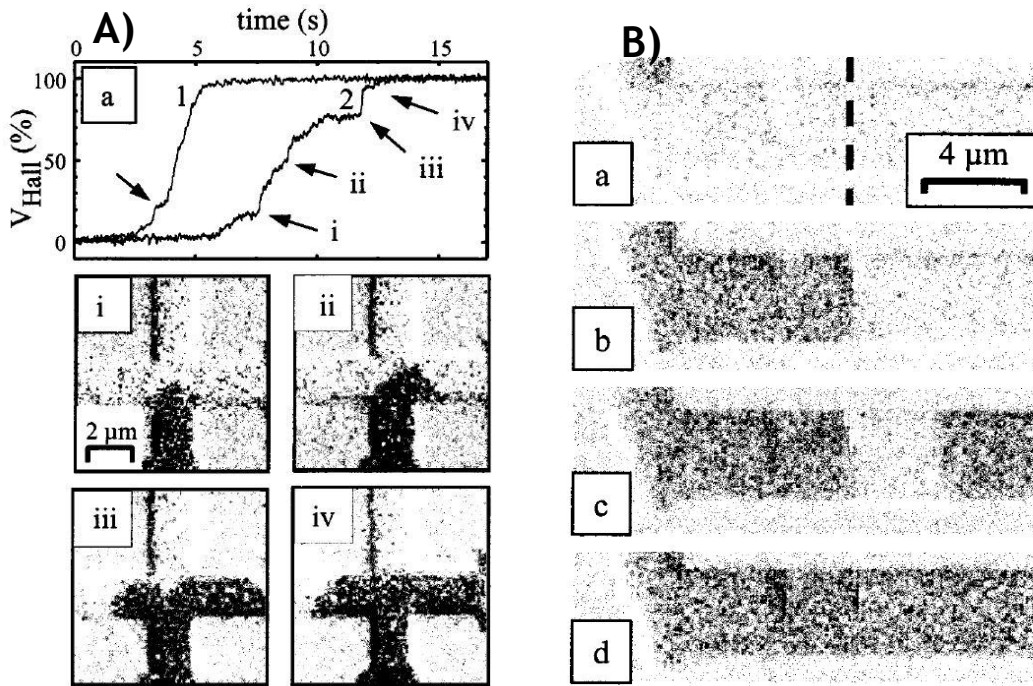


Figure 2.2.11: A) Magnetization reversal process in Pt/Co/Pt Hall crosses ($t_{Co} = 0.5$ nm). (a) EHE voltage as a function of time, curve 1: defect-free cross; curve 2: device having an AFM machined hole in the cross centre. i)-iv) Kerr images of the DW propagation in the cross with the centre defect. B) Inhibited DW propagation in a Pt/Co/Pt wire ($t_{Co} = 1$ nm) by an AFM fabricated groove. First reversed domain (dark gray) coming from the upper left. Images taken from [162].

The second of these two studies [162] replicated the work done in the first one, with some extra features added. The cross-junction work was very similar and as such provides results agreeing with what was previously found. An alteration was made to the single groove experiment as this time, the new groove was created at an angle along the width of the nanostrip as opposed to perpendicularly across. This resulted had a very similar effect as in the previous study although with the small difference that the DW positions itself along the diagonal groove. Figure 2.2.12 demonstrates these results.

The main difference to this study compared to the first one is that AFM nanomachining was also employed to cut a series of connected grooves to create a rectangular shape into the side of the nanostrip as shown in Figure 2.2.13. These grooves measure 100 nm wide and 6 nm deep, indicating that the magnetic Co layer is completely cut through. Therefore, the generated grooves acted to isolate the rectangular section of the magnetic layer of the nanostrip measuring at $1 \mu\text{m} \times 2 \mu\text{m}$. Figure 2.2.13 shows that this is the case as the rest of the nanostrip switches

magnetisation whilst the isolated section remains magnetised in the same direction and so does not switch as easily.

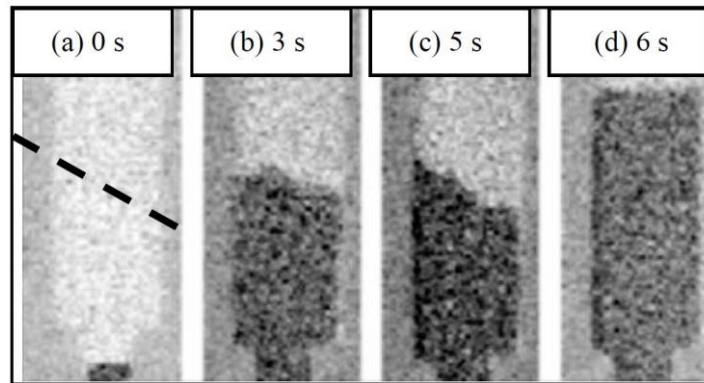


Figure 2.2.12: Pinning and depinning of a DW at a shallow inclined trench (at dashed line in (a)). Applied field is 46 Oe. Total time of field application is marked. Taken from [162].

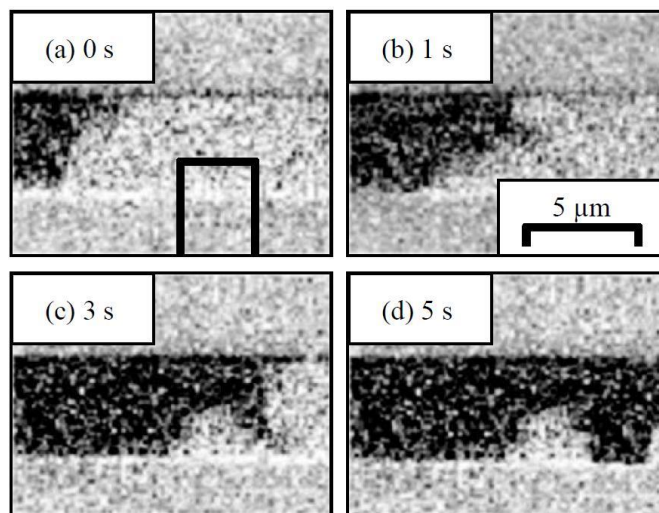


Figure 2.2.13: Creation of artificial domains by AFM lithography. DW propagation into the area defined by the AFM fabricated groove (black line in (a)) is inhibited. Applied field is 66 Oe. Taken from [162].

These studies show that magnetic DWs can potentially be controlled using vertical features created using AFM tip-based nanomachining. However in these two studies, as previously alluded to, using the definition of pinning DWs may not be strictly accurate. This is due to the fact that all of the magnetic material was cut through and so this did not leave any material left for the DW to propagate through. With the whole thickness of the magnetic material removed, the DW did not become pinned as such. Instead it simply reached the end of the connected nanowire. Even if this

method is to be considered pinning a DW, whilst the principle may have been demonstrated, there has not been any characterisation work conducted to investigate how the size of these AFM-machined vertical features influence their interaction with DWs. In particular, it is still unclear whether the DW pinning strength of such features varies with their size or shape. In addition, none of the experimental studies reported above considered the size of the nanowire as a variable parameter when investigating the pinning of DWs although it is known that the type of DWs (i.e. transverse, vortex or Landau) depends on the dimension of the nanowire along which it travels. In particular, it could be reasonably expected that features (i.e. pinning sites), created using AFM tip-based nanomachining, may interact with various types of DWs in different ways. However, this is not a question that has been the focus of previous studies where pinning sites are machined vertically across the width of a nanowire. Besides, in practice, it is likely that any possible devices that would implement such DW pinning phenomena would use nanowires with sub-micron width. These are also likely to be unstacked nanowires using a single material with thicknesses larger than 1 nm. This opens the door to research investigations that explore how the removal of a given percentage (or proportion) of the nanowire material may affect the interaction of the pinning site with the DWs rather than a scenario in which the whole magnetic layer is removed at once as is the case in the studies from Schumacher and co-workers.

The creation of devices that implement technology such as racetrack memory requires all of these issues to be investigated and characterised in order to accurately and reliably control the motion of magnetic DWs.

2.3 Knowledge gaps

As discussed in section 1.1.10, there are a number of potentially important applications that depend on DW motion. These applications rely on the ability to accurately and reliably control the positioning and movement of DWs. There have been many studies based on pinning DWs as discussed in section 2.1, however some research gaps still remain. These gaps primarily concern the use of vertical constrictions in magnetic nanowires as opposed to lateral constrictions. Sections 1.2 and 2.2 discussed the advancement and implementation of AFM tip-based nanomachining. Whilst the technique itself has become well established, practical applications of this methodology have so far been limited, particularly in the area of nanomagnetism, as discussed in section 2.2.3. With this in mind, the specific

knowledge gaps that have been identified in the context of this research are as follows:

- Investigation on the interaction between different types of DWs and the specific geometry of vertical nanotrenches. Features created using AFM tip-based nanomachining have a tendency to be triangular in shape. This is due to the tip being pyramidal in shape. As all previous studies have assumed rectangularly shaped nanotrenches, the influence of nanotrench shape on pinning strength must also be considered. A computational study comparing the DW interactions with rectangular and triangular nanotrenches forms the key focus of chapter 4.
- Demonstration that AFM-tip based nanomachining can be used to create artificial pinning sites for DWs. The type of features that can be created using AFM tip-based nanomachining are such that the technique appears to be an ideal candidate technology to create the vertical nanotrenches discussed in the previous knowledge gap. This presents an opportunity to investigate a new application for AFM tip-based nanomachining that has previously not been considered. This is the technique that has been implemented for creating nanotrenches in magnetic nanowires in chapter 5.
- Experimental confirmation that vertical features can be used to pin DWs and in particular, that the pinning strength increases with the depth of such features. Whilst lateral constrictions in nanowires to pin DWs has been studied extensively, there has been very little research into the potential use of vertical features to control DW motion. The limited number of studies conducted in this area so far have consisted almost entirely of computational models as opposed to experimental trials. This leaves the gap for experimental confirmation of pinning DWs using a vertically placed nanotrench. Experimental work pinning DWs by creating vertical nanotrench within a magnetic nanowire will be discussed in chapter 5.

3. Methodology

This chapter covers all of the techniques that have been used in this study. Section 3.1 will focus on the methods used during the fabrication process of the nanowires created and used for experimental work during the study. Section 3.2 takes a look at all of the experimental techniques used to characterise these fabricated samples. Finally 3.3 goes into further details of the computational model used for the micromagnetic simulations conducted in this thesis.

3.1 Sample Fabrication

This section focuses on the processes utilised for the creation of samples for the experimental portion of this thesis. The first two sections of this chapter contain discussions of the key techniques used during the fabrication process. These techniques are electron beam lithography (EBL) for the pattern design and thermal evaporation is used for material deposition. The third section of this chapter will explain the specific details of how vertical nanotrenches are created within nanowires using AFM tip-based nanolithography. The final section addresses how all of these techniques are implemented as part of a process chain to fabricate samples.

3.1.1 Electron Beam Lithography

There are numerous methods that can be used for creating patterns for micron to nano scale devices. Many involve exposing a material, usually some form of polymer, in order to alter its properties such that it can be later processed further. Examples of such techniques include Photolithography, focused ion beam lithography (FIB) and electron beam lithography (EBL). Each method has its own advantages and disadvantages.

Photolithography exposes a photosensitive resists to light produce micro/nanostructures. It is the standard technique used in industry due to its ability to expose multiple structures in parallel, reducing time and costs. It is also a relatively cheap method that does not require vacuum conditions. The resolution of photolithography is governed by the wavelength of the light used in exposure. Due to the diffractive nature of light, there is a limit as to how small features can be created. With the wavelength reduction to deep UV light and using advanced optics in the system, it is possible to achieve resolution down to 32nm [163]. More recently a method utilising shorter wavelength UV light known as extreme ultraviolet (EUV) lithography has been shown to achieve resolutions sub 8 nm [164].

FIB is another method used to create micro/nanoscale devices however it is an inherently destructive technique. Here the surface is directly bombarded with an incident ion beam in order to remove sections of the material leaving the required design. It typically is not able to achieve the same resolution as EBL whilst it can often take longer to write the pattern due to longer exposure time that may be needed. Also ions can be left implanted in the remaining material which can cause the material properties to change, as demonstrated by Basith and co-workers [88].

In this thesis EBL is used to fabricate the nanodevices to be experimented on. In this study a Raith e-Line system is used during the fabrication process. EBL can produce features in the order of 10 nm whilst causing minimal damage to the substrate [165]. However, the limitation of resolution to 10 nm is due to the resist rather than the electron optics system used, which is capable of reaching 0.1 nm resolution [166]. This will be discussed further shortly. The narrowest nanowire used in this study is in the region of 100 nm and so the resist limitations have not been an issue to consider further.

In this method, a focussed beam of electrons is accelerated towards a resist material in order to alter the material properties for further development. Resists used are known as positive or negative depending on how they interact with the incident electrons. Within a positive resist, the electrons interact and break up the polymer chains within the material. This has the effect of making it more soluble and so when chemically processed, only the “exposed” pattern will be removed. This leaves gaps in the resist where material can be deposited into thus creating the nanoscale structure. In a negative resist, the opposite happens. Interactions between the electrons and the polymer chains result in cross-linking and a decrease in solubility. Meaning that only the designed pattern remains whilst all other resist material has been removed when the resist is chemically developed. A schematic of the patterning process is shown in figure 3.1.1.

The achievable resolution depends not only on the instrumentation of the EBL system, but on the properties of the resist. This is attributed to the scatter of electrons within the material. As the incident electrons hit the resist, they are elastically and inelastically scattered whilst moving through the material and into the substrate. This scattering generates low-energy secondary electrons (shown in figure 3.1.1). It is these secondary electrons that interact with the resist altering the solubility. The range over which the secondary electrons scatter effects the resolution that can be achieved. Another effect that needs to be accounted for is

that of backscattered electrons. These are electrons that have travelled through the resist into the substrate, causing large angle scattering back into the resist (shown in figure 3.1.1). This results in a low but constant dose into the base of the resist that can be several microns away from the incident beam. This is known as the proximity effect [167]. Secondary electron scattering (also known as forward scattering) and backscattering can both be affected by the energy of the incident beam with higher energy beams produce a smaller spread on the forward scattering electrons.

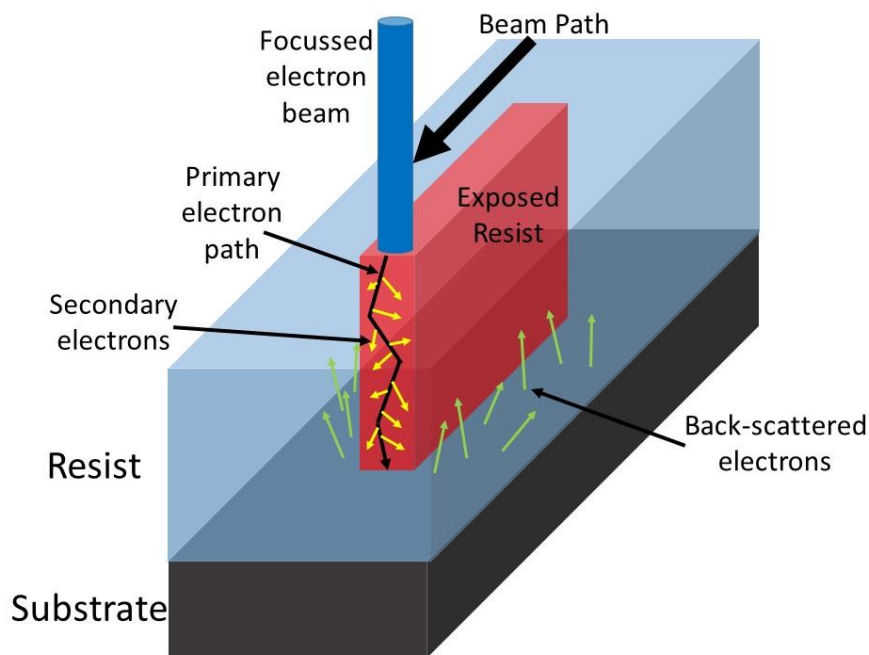


Figure 3.1.1: Schematic of interaction between electron beam and an electrically sensitive resist.

The resist material used is commonly a polymer of some kind. In this thesis, the commonly used polymer poly-methyl-methacrylate (PMMA) has been utilised as the resist material. PMMA is a positive resist material that is capable of resolutions less than 10 nm [168]. As it is a positive resist, the designed pattern will be left as gaps in the material. These need to be filled with the desired material to be used for the nanodevices. The technique used to do this will be discussed in the following section.

3.1.2 Thin Film Deposition

Once a pattern has been created within a resist, there are numerous techniques that can be utilised for thin film deposition. Such methods can be broadly classified into

chemical or physical deposition. Chemical deposition techniques rely on chemical reactions at the substrate surface causing the material to adsorb onto it. Whilst physical deposition methods do not involve chemical reactions. Generally such techniques expose substrates to low-pressure gases of the film material where the gas adsorbs onto the substrate surface. This is known as physical vapour deposition. Other methods create the vapour using intense laser pulses (pulsed laser deposition) or ablation of a solid target using a plasma (sputtering). One of the most simple methods is to heat the material until it evaporates, known as thermal evaporation. Different techniques have various positives and negatives as they result in varying crystallinity, porosity, adhesion, grain size, composition amongst other variables[169]. The method chosen is a balance of cost effectiveness against the desired film requirements. In this thesis, thermal evaporation is the deposition method of choice.

As alluded to earlier, thermal evaporation is a simple method of heating a material until it begins to evaporate. The setup used in this thesis was a custom homemade thermal evaporation chamber the schematics of which are shown in figure 3.1.2. The material is placed in a crucible towards the bottom of an evaporation chamber with the substrate suspended some distance above it. The chamber is pumped down to a vacuum of $\sim 10^{-8}$ mbar before the evaporation process starts. The high vacuum is required to avoid contamination of the film as it is deposited and due to the mean free path of the evaporated material needing to be large enough to reach the target. This is necessary as the sample is placed approximately 0.5m above the crucible and it is desired that the evaporated material reaches the target whilst minimising interactions with the nitrogen and oxygen molecules along the journey. The crucible is heated by applying a current, this allows control of the deposition rate once the material begins to evaporate. A quartz crystal monitor is used near the target substrate to track the film thickness and the deposition rate during the process. A shutter is used between the substrate and the evaporation source so that the amount of deposited material on the substrate can be accurately controlled. Whilst the shutter is open, the deposition rate is kept steady while the material is deposited onto the substrate. The shutter is then closed when the desired film thickness is achieved. The typical deposition rate is approximately 0.2 \AA/s at a pressure of approximately 10^{-6} mbar. This low rate combined with the low base pressure results in the ability to deposit good quality films [170].

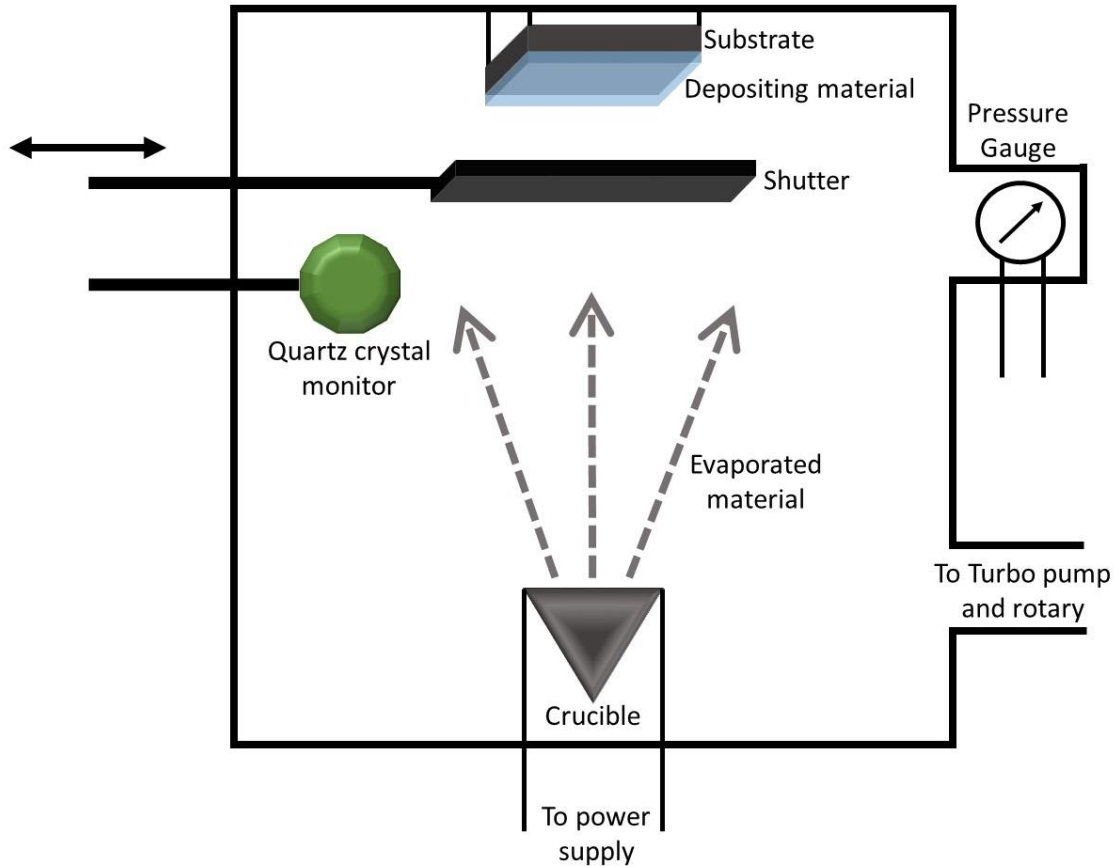


Figure 3.1.2: Schematic of an evaporation chamber

The low pressure in the chamber allows the material to move with almost no collisions and so it can travel in straight lines directly away from the source. This means that this method is extremely directionally dependent. The direction not being perfectly aligned with the substrate can lead to shadowing effects in the resulting sample. These can cause problems during any subsequent phases to remove the remaining resist.

3.1.3 AFM nanomachining

Once the nanowires are created, nanotrenches are created using AFM tip-based nanolithography. All AFM operations in this thesis were conducted using the XE-100 AFM model from Park Systems. The AFM instrumentation can be seen in figure 3.1.3. As part of the setup, the AFM itself is situated on top of an active anti-vibration table (model TS 150 from Table Stable Ltd) whilst the whole system is located inside a full acoustic enclosure. This AFM system contains three piezoelectric actuators. Individual X and Y actuators control the sample stage to a submicron resolution in the x-y plane, whilst a Z actuators is used to define the vertical displacement of the AFM probe along the z axis. To control the system, the Park Systems XEP software is

used for general scanning and characterisation using the AFM, whilst the XEL software is utilised for machining operations.

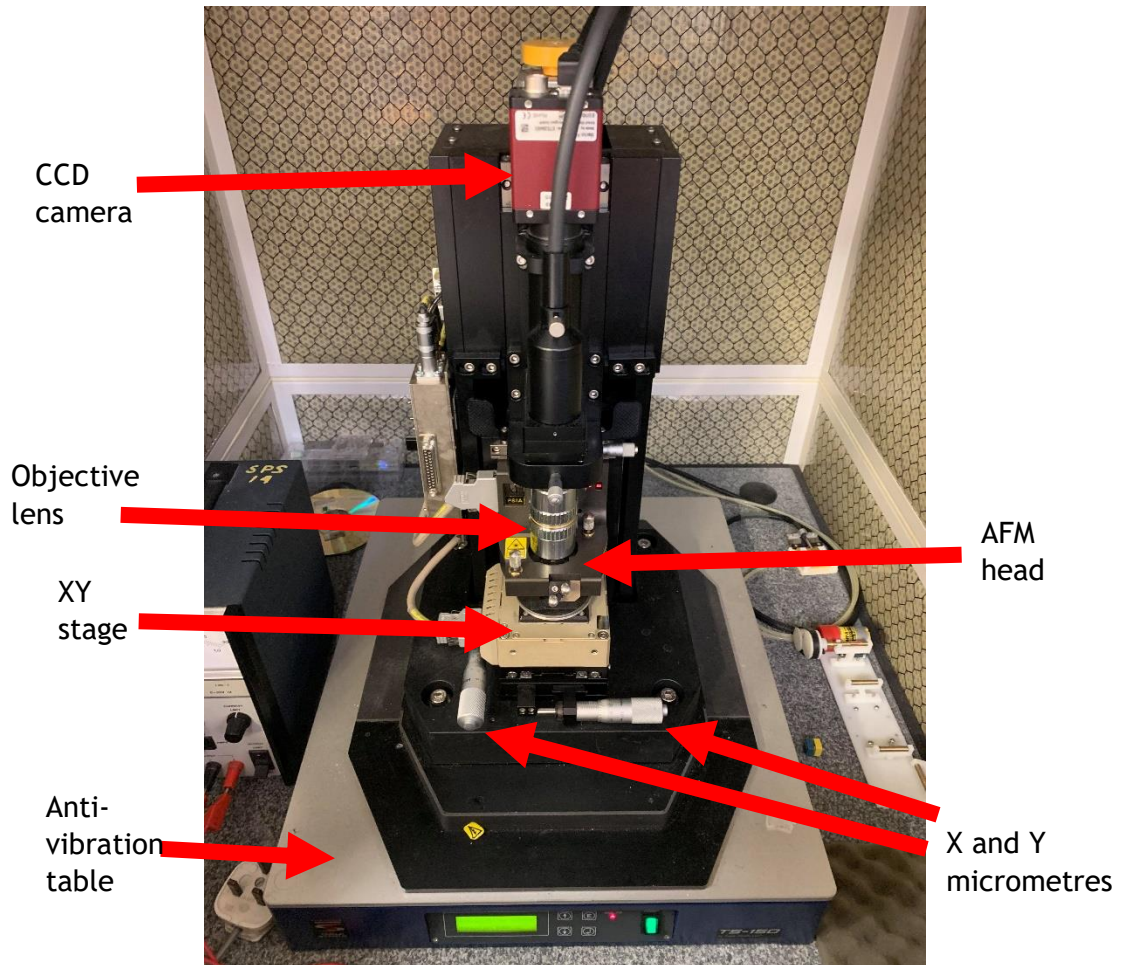


Figure 3.1.3: Photo of the AFM system used in this study.

The details as to how AFM tip-based nanomachining works has been discussed in sections 1.2 and 2.2. In order to vary the size of the desired features, a knowledge of the applied load and to ability to change its magnitude is required. In order to accurately monitor the interaction force between the tip and the sample, calibration of both the optical lever sensitivity and the cantilever's spring constant is required. The spring constant is determined using the Sader method [171]. The normal sensitivity calibration is done by fitting a slope to the force-distance curve obtained whilst pressing the probe tip against a hard surface. The hard surface in this case being fused silica. This calibration is based on Hooke's law. Figure 3.1.4 shows a schematic of the optical lever technique for detecting deformations of the AFM cantilever. A laser spot is focused onto the free end of the cantilever and reflects to the PSPD. The vertical position of the reflected laser spot is monitored

and maintained by the feedback loop producing an output commonly referred to as the V_{A-B} signal.

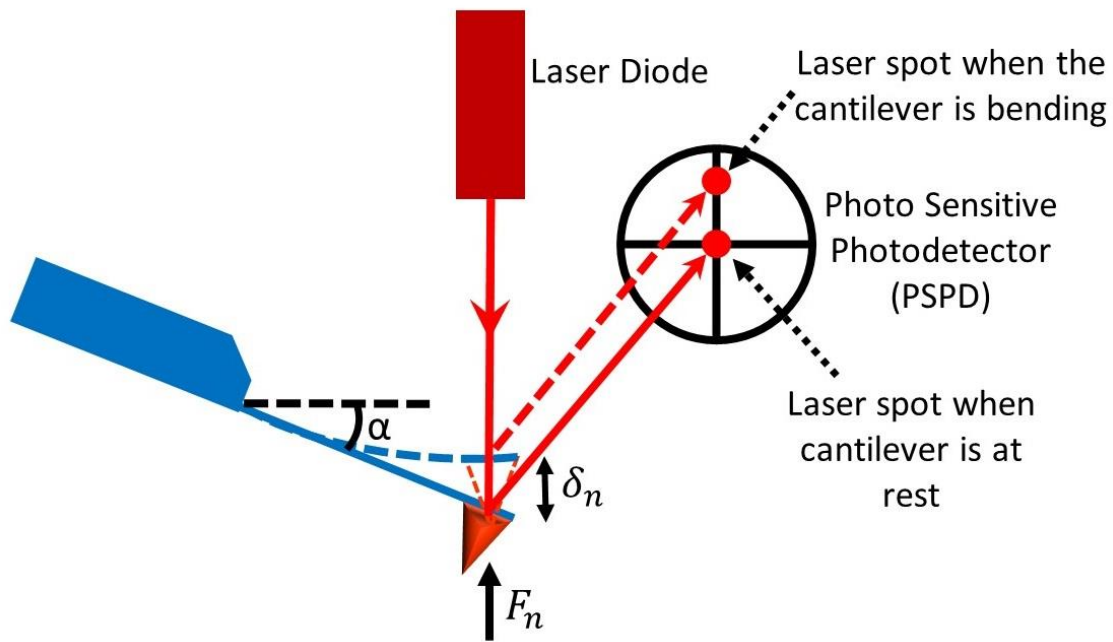


Figure 3.1.4: Schematic of optical lever technique for detecting deformation of the AFM cantilever

Pressing the tip onto a surface generates a normal force, F_n . This force depends on the normal spring constant, k of the cantilever and is related by Hooke's law [60]:

$$F_n = k \cdot \delta_n \quad (3.1)$$

Where δ_n is the vertical deflection at the free end of the cantilever. It follows that if the vertical deflection can be assessed, then the normal force can be established. This is the method generally employed in practice to evaluate the deflection and depends on the knowledge that the output, V_{A-B} and the normal sensitivity of the PSPD, S_n are related by:

$$F_n = k \cdot S_n \cdot V_{A-B} \quad (3.2)$$

It is equation 4.2 that is used to calculate S_n when fitting a slope to the force-distance curve as the linear function $\delta_n = f(V_{A-B})$.

It is worth noting that whilst these calibrations provide values for F_n that are defined and implemented using the software, it is very difficult to know the exact force being applied. This is due to the lack of knowledge of the exact amount of contact between the tip and the surface. Sharper tips will have smaller contact areas when compared to tips with wider radii. However, during use the tips will

wear and so the contact area changes. With this in mind, the numbers provided by the software from the resulting calibration still have value. They are useful when applying relative forces as well as for giving a reference point as to the magnitude scales of such forces.

Machining in earlier experiments in this study were conducted using a three-sided pyramidal diamond tip (model ND-DTIRS) with a nominal spring constant of 35 N/m. Later experiments employed a four-sided pyramidal diamond tip (model ND-DYCRS from Advanced Diamond Technologies) with a nominal spring constant of 35 N/m. Initial trial and error experiments revealed that a minimum load of 1 μN was required to initiate the formation of a trench.

In practice the general procedure of generating nanotrenches is as follows. An initial scan of the region is conducted in contact mode using the XEP software. Without moving the sample, the resulting image is uploaded to the XEL software. XEL allows the user to draw the desired scratches on top of the image to allow for high accuracy of nanotrench placement. Each scratch is defined using a number of parameters including applied force and scratch speed. Once the pattern is designed, the software is allowed to run and the scratches are conducted.

In order to obtain accurate images of the generated nanotrenches, different types of probes were used. Throughout this study the created nanotrenches have been scanned using non-contact mode probes (model NSG30 from NT-MDT) and contact mode probes (model CSG30 from NT-MDT).

3.1.4 Fabrication process chain

The overall fabrication process will be described in this section. A schematic outlining the key steps is shown in figure 3.1.5. Initially a polished SiO_2 coated silicon substrate is cleaned with solvents. The SiO_2 layer is a deliberate oxide measuring approximately 100 nm thick. The substrate is then spin-coated with 950k PMMA accelerating up to 3000 RPM. Once this is completed, it is immediately baked at 180°C on a hot plate to smoothen the resist and to drive off the solvent.

At this stage the sample is loaded into the EBL system to apply the desired pattern via exposure. Once exposed, the sample is placed in a 3:1 solution of IPA:MIBK to develop the exposed regions. It is then rinsed in isopropanol to remove any remaining resist within the desired pattern and any developer. The pattern is now exposed within the resist at this point. To aid material adhesion to the substrate surface, a further cleaning stage of plasma ashing is conducted. A plasma of oxygen

is applied to the surface. Within this process the O₂ reacts with any remaining organic compounds within the resist converting them into water vapour and carbon oxide gases. This procedure is conducted in a 10W powered plasma for 3 minutes in a pressure measuring 0.6 mbar.

Next, the permalloy is deposited onto the sample via thermal evaporation, as discussed in section 3.1.2. The permalloy used in this study was a 99.99% pure sample of Ni₈₁Fe₁₉ with pieces measuring 3-6 mm placed into the crucible. The pressure within the evaporation chamber is initially reduced to 10⁻⁸ mbar and the material is deposited onto the surface at an approximate rate of 0.2 Å/s at 10⁻⁶ mbar. Once the deposition is conducted, the sample is allowed to cool then removed from the evaporation chamber and placed in Acetone for 12 hours in order to remove the remaining resist. Finally the sample is placed in an ultra-sonic bath, combining this with multiple Acetone rinses to remove all remaining resist and unwanted materials. The sample is now ready to be measured and machined.

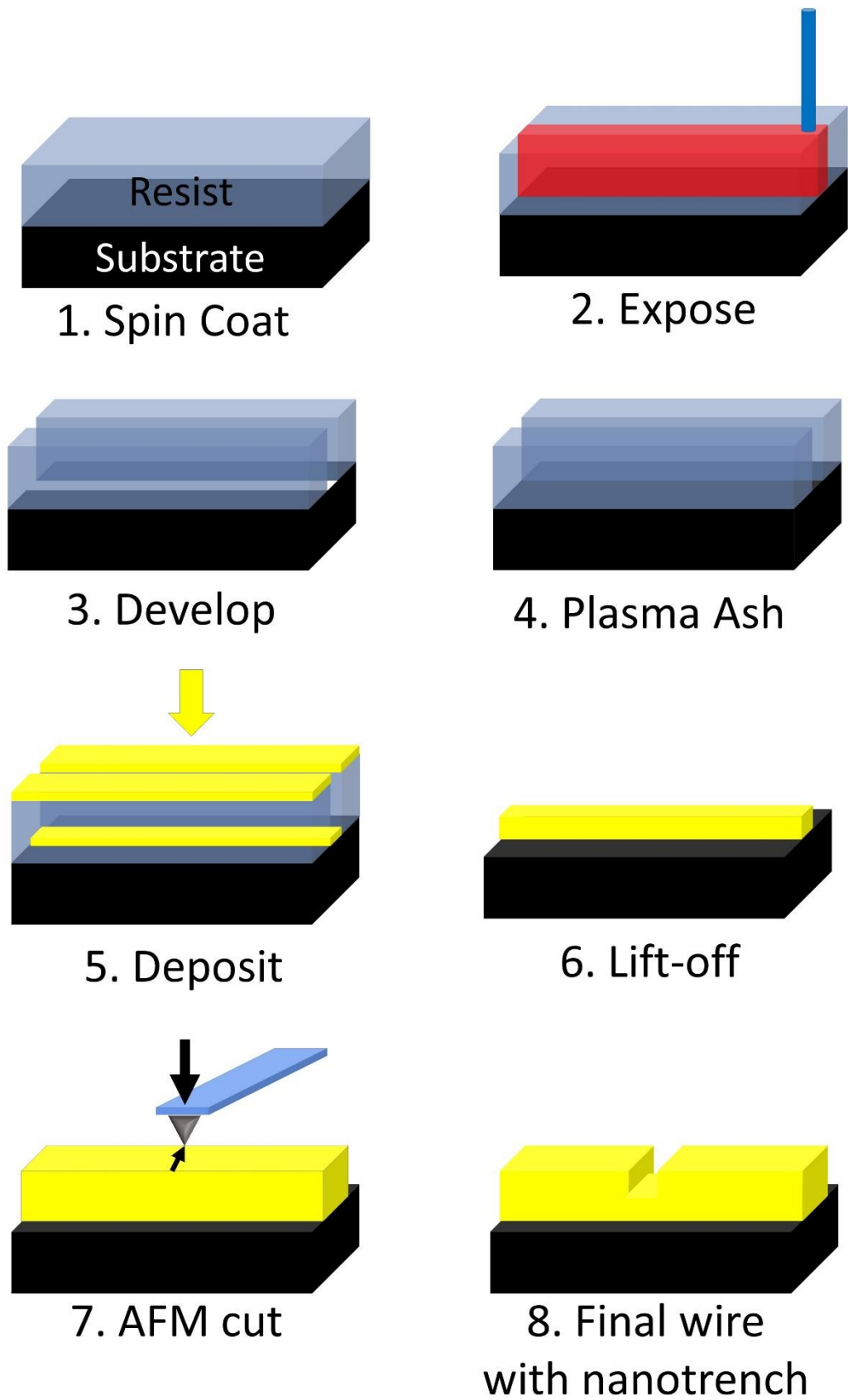


Figure 3.1.5: Schematic of process chain used in sample fabrication

3.1.5 Permalloy

Permalloy is a ferromagnetic alloy made up of nickel and iron, typically in a ratio of approximate 80-20. It is chosen for this study due to some of the properties it possesses. It has a very high magnetic permeability, a low coercivity and near zero magnetostriction.[172] Magnetostriction can cause problems at such small scales due to the material dimensions varying depending on its magnetic structure. Permalloy also possesses negligible magneto-crystalline anisotropy and so the magnetisation is unlikely to be affected by the crystalline structure. Finally permalloy has a significant response to anisotropic magnetoresistance, allowing larger and clearer signals to be observed during AMR measurements[173].

3.2 Sample Characterisation

This section consists of discussions focused on each of the experimental techniques used for sample characterisation. Scanning electron microscopy is used along with AFM for imaging the nanowires. Anisotropic magnetoresistance (AMR) measurements have been used to detect the presence and propagation of DWs. During numerous trips to the Advanced Light Source (ALS) facility in Berkeley, California, full-field soft x-ray microscopy was utilised to image the DW pinning and propagation within machined nanowires.

3.2.1 Scanning Electron Microscopy

Along with AFM, Scanning electron microscopy (SEM) has been used in this thesis to image the fabricated samples. SEM is a high-resolution imaging technique that is capable of resolutions in the order of nanometres. In this method electrons accelerated towards and focused at the surface of a sample. The electrons interact with the sample causing them to scatter elastically, resulting in high energy back scattered electrons, or inelastically giving low energy secondary electrons [174]. Electrons can be identified by their energy. Secondary electrons are considered those with energies ≤ 50 eV whilst back-scattered electrons will have energies more than 50 % of the incident beam energy [175]. Either of these sets of electrons can be used for imaging purposes, each having their own characteristics and advantages. Back-scattered electrons have higher energy, they are able to escape the sample from much further depths, in the order of microns. This enables the observer to probe the sample significantly below the surface. The back-scattering probability also depends on the atomic number and so effects the contrast of the images. This

gives a degree of chemical contrast giving information on the atomic density of the sample.

Secondary electrons are the source of the most common imaging method within SEM systems. Contrasting to the high energy back-scattered electrons, secondary electrons are only able to penetrate shallow distances into the sample surface (typically 2-10 nm for metals [175]). Secondary electrons can be created either as the incident electrons enter the surface, or as back-scattered electrons are leaving the surface. These are defined as two separate groups of secondary electrons, SE1 and SE2 respectively. SE1 electrons are emitted within a narrow area around the incident beam, providing a high-resolution surface-sensitive signal. SE2 electrons are the result of back-scattering electrons attempting to leave the surface and so are emitted from a much wider region of the surface. This leads to a lower resolution signal.

The SEM system used in this thesis is the XB 1540 model from Carl Zeiss, an image of which is shown in figure 3.2.1. This system has the ability to image samples using an inLens detector and a SE2 detector. The inLens detector is the most common method used to detect secondary electrons and is placed within the line of the incident beam. With its positioning it detects the higher energy secondary electrons and so usually produces better images. The SE2 detector is situated on the wall of the SEM chamber at an angle with the sample. Due to this positioning, it is less efficient in its collection of the secondary electrons.

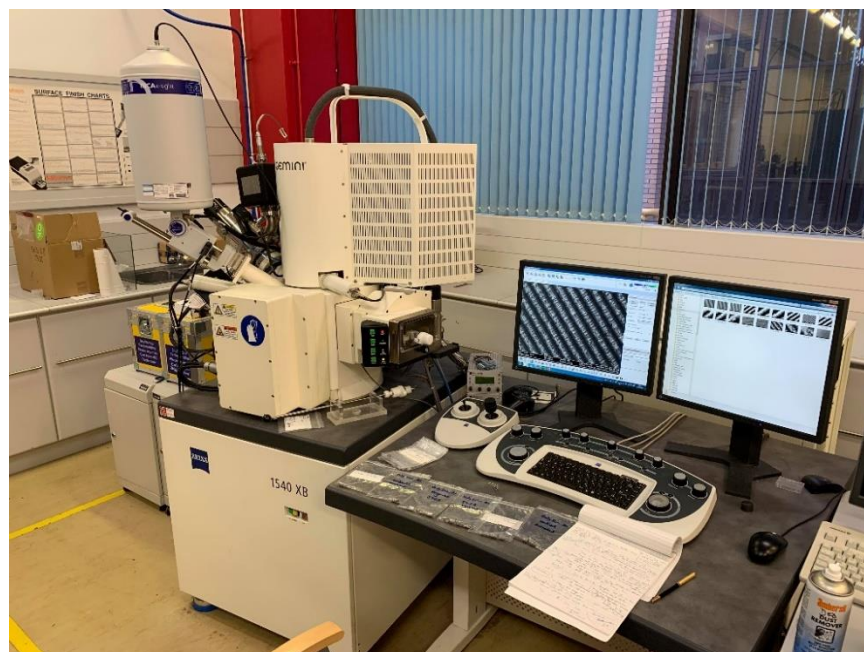


Figure 3.2.1: Photo of SEM system used in this thesis

3.2.2 Magneto-transport measurements

In this thesis, anisotropic magnetoresistance (AMR) measurement is one of two key methods used to detect the presence of DWs and find the corresponding depinning fields. AMR is an interesting property of ferromagnetic materials where the electrical resistance of the material has a dependence on the relative angle between its magnetisation direction and the direction of the current flowing through it. The phenomenon was discovered by Lord Kelvin in a paper published in 1856 focused on nickel and iron [176].

AMR is caused by a combination of the magnetisation interactions with the electron orbits. If the magnetisation becomes aligned with the current path, the probability of current-carrying electrons being scattered increases. This acts to obstruct the current flow. This then causes the resistance of the material to vary such that it is a maximum when the magnetisation vector is parallel with the current vector.

In general, the resistance of a sample depends on the material resistivity along with its geometry. The equation to calculate the resistance of a sample is given by:

$$R = \frac{\rho L}{A} \quad (4.1)$$

Here ρ is the material resistivity while L is the length of the current path and A is the cross-sectional area the current passes through. It is the resistivity that is affected by AMR. It has been found that the resistivity has a \cos^2 dependence on the relative angle. The relationship is given by:

$$\rho(\theta) = \rho_{para} + \delta\rho \cos^2 \theta \quad (4.2)$$

Where ρ_{para} is the resistivity when the magnetisation and current vectors are parallel, $\delta\rho$ is the maximum change in resistance that is observe when the two are perpendicular to one another, and θ is the relative angle between the two. θ is more clearly defined in figure 4.2.2. As the relationship is \cos^2 in nature, it is seen that the material resistivity is the same when the magnetisation and current is aligned parallel and anti-parallel with one another.

Following on from this relationship, an example of experimental data taken from a 20 nm thick permalloy thin film can be seen in figure 3.2.3. A bell-shaped curve can be seen where the magnetisation coherently rotates as the applied field increases in magnitude. The coercive field of the sample is taken to be at the peak of the curve. Note that two distinct curves are seen. Each of these correspond to the thin film reversing magnetisation in one of two directions, i.e. the blue curve corresponds to

the applied field increased from the negative direction through to the positive whilst the red curve shows the applied field going in the opposite direction. The coercive field for this film thickness is shown to be approximately 5 Oe.

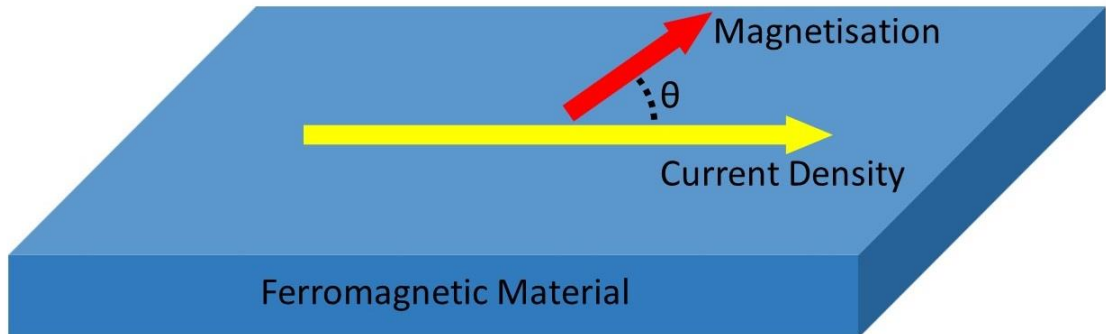


Figure 3.2.2: Diagram displaying defining the relative angle between the magnetisation and current vectors, θ

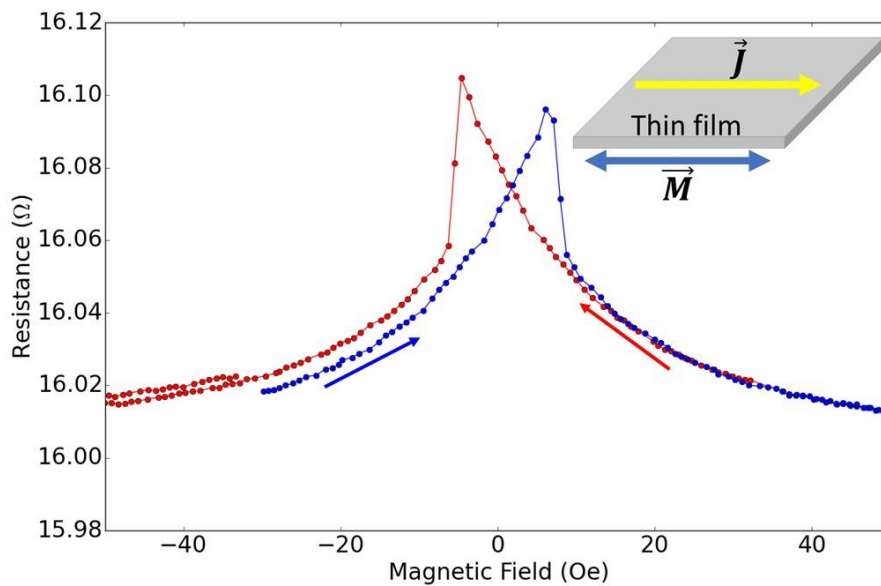


Figure 3.2.3: AMR data for 20 nm thick permalloy thin film. Blue curve shows data from negative to positive fields, red shows the reverse procedure. Blue and red arrows help guide the eye of the direction the magnetisation is changing. Insert demonstrates the thin film with the directions of current and magnetisation.

In the case of nanowires, the same theory is applied, however the data will look different. These differences are attributed to the reversal process varying between a thin film and a nanowire of reduced dimensions. The competition between energy terms (as discussed in section 1.1.4) means that the magnetisation is not able to coherently rotate as it does in a thin film. The competing energies lead to shape

anisotropy in the nanowire. This leads to the magnetic easy axis pointing along the length of the nanowire. Due to the inability for the magnetisation to coherently rotate, magnetisation switching may only occur via domain growth. An example of AMR data for a 20 nm thick, 200 nm wide permalloy nanowire is shown in figure 3.2.4. This data is taken by setting a small fixed current through the nanowire and applying the external magnetic field along the same axis as the current direction. It is seen that the resistance is the same value when the nanowire is magnetised parallel or anti-parallel to the current. During the reversal process, the resistance is seen to reduce with the presence of a DW that causes a magnetisation configuration such that there are some areas of the nanowire where the current is not parallel or antiparallel to the magnetisation direction. If the DW becomes trapped at some pinning site the magnetisation will remain reduced. The DW then propagates over a very small applied field window and very short time scales (approximately nanoseconds). This gives a sharp increase in resistance in the AMR data. This is the field that is taken to be the depinning field.

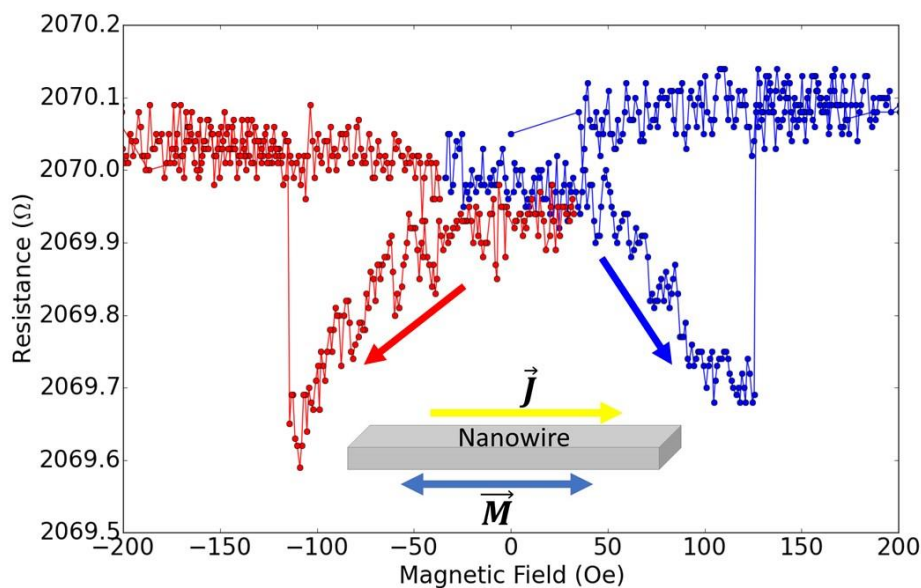


Figure 3.2.4: AMR data for a 20 nm thick, 200 nm wide permalloy nanowire. Blue curve shows data from negative to positive fields, red shows the reverse procedure. Blue and red arrows help guide the eye of the direction the magnetisation is changing. Insert demonstrates the nanowire with the directions of current and magnetisation.

In order to make these measurements, the sample needed to be designed such that a current could be passed through the nanowire and such that the resistance of the

wire alone could be measured. Figure 3.2.5 shows an example of a device used in this study. It is designed such that the ends of the central nanowire are connected to much wider channels of permalloy known as “pads”. These pads extend out towards the edge of the silicon wafer piece (known as the chip) and increase in size in order to make wiring up to the conventional macroscale gold wires easier to achieve. At the outer edges of these pads gold wires are attached to the pads using silver paint. The silver paint acts as a highly conductive bond between the permalloy and the gold wires. These wires are then connected to the measuring devices and provides a measurable path through the sample. These connections are tested using two and four terminal measurements. Assuming that the measured resistances are suitably low, the sample is placed at the centre of an electromagnet such that the applied field direction is parallel to the long axis of the nanowires.

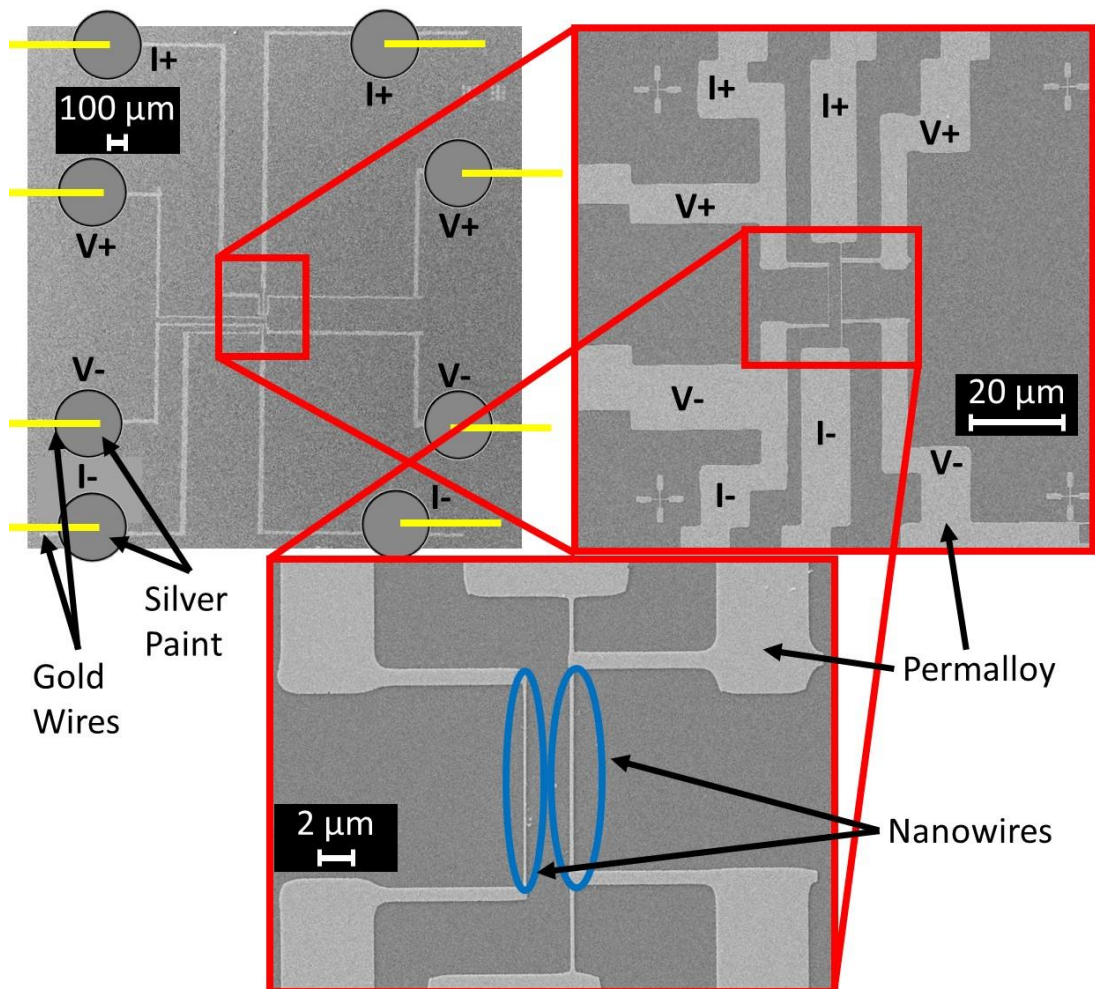


Figure 3.2.5: SEM images of an example device. Displaying the larger permalloy pads used to connect to gold wires via silver paint for electrical measurements. The sets of four terminals are shown with annotations of V+, V-, I+ and I-. Lighter grey regions represent permalloy structures.

Two and four terminal measurements refer to the physical number of connections used to measure to the sample. Two terminal measurements use a single pair of wires to carry the current through the sample whilst simultaneously detecting the voltage. During two terminal measurements, the resistance is measured over the entire current pathway including the gold wires, silver paint, pads and the nanowire itself.

In order to localise the voltage and therefore the resistance measurements, four terminal measurements are utilised. When using four terminal measurements, one pair of wires is used to pass the current whilst the other pair detect a voltage. The pathways connected to the wires used to detect the voltage are often known as the “voltage probes”. The placement of these probes allows the resistance to be measured only between their connections. Leading to more localised data relating to the nanowire as opposed to the whole current path as done with two terminal measurements. Figure 3.2.6 shows an SEM image of a fabricated nanowire with the location of the voltage probes. Positioning the probes as such allows data to be taken of the nanowire with little to no additional information coming from the pads or macroscale gold wires.

The experimental set-up used in this study used a simple copper wound electromagnet capable of fields up to 0.75T. This is powered by a DC electrical supply that is used to control the field values. A Lakeshore AC 370 resistance bridge was used to conduct sensitive magneto-transport measurements [177]. For these measurements a low excitation frequency of 13.7 Hz is used in order to avoid the mains frequency and capacitive effects. To measure the applied magnetic field during experiments, a three axis Lakeshore Hall probe is used. The probe is positioned as close to the sample as possible between the poles of the electromagnet to measure the applied field as accurately as possible.

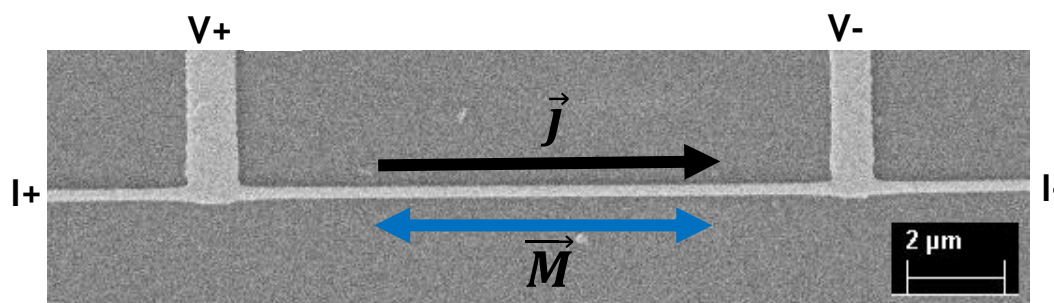


Figure 3.2.6: SEM image of a permalloy nanowire found in figure 3.2.5, demonstrating the four terminal set-up used for AMR measurements

3.2.3 Full-Field Soft X-ray Microscopy

As part of this study, a new set of samples were fabricated and taken to the Advanced Light Source (ALS) facility in Berkeley, California. The experiments were conducted using beamline 6.1.2 which utilises magnetic full-field transmission soft x-ray microscopy (MTXM). MTXM is a technique in which x-ray radiation is passed through a ferromagnetic sample in order to image the magnetisation direction capable of spatial resolutions better than 10 nm [178].

The phenomena that are utilised in this technique are various dichroism effects [179]. In this incidence, the primary phenomenon used for ferromagnetic materials is x-ray magnetic circular dichroism (XMCD) [180]. XMCD can in a way be considered as the x-ray counterpart to the magneto-optical Kerr and Faraday effects, although the mechanism for contrast is of course quite different. In this instance, circularly polarised x-rays interact with the magnetic moments of the material causing a helicity dependent absorption of the x-rays. This originates from the absorption cross-section of the material having a dependence on the relative orientations of the x-ray helicity projection onto the magnetisation direction.

The XMCD effect occurs predominantly in the vicinity of the L_2 and L_3 absorption edges in 3d transition metals such as Fe, Co and Ni when using soft x-rays. The magneto-dichroic signals at each of these edges are approximately the same in magnitude, however they have the opposite signs. It is seen that the size of the effect is proportional to the direction of the magnetisation. Experimentally, XMCD contrast can be achieved by three methods. First of which focuses on modulating the circular polarisation of the x-rays (left and right) whilst keeping the magnetisation constant. Alternatively, the polarisation remains fixed whilst reversing the magnetisation direction via the application of an external field. Finally the reverse spin-orbit coupling of the L_2 and L_3 absorption lines can be utilised for fixed polarisation and magnetisation. Using the second of these methods, images can be taken of the sample with a varying external magnetic field, then compared to one another in order to observe any magnetic switching behaviour [179], [181].

Despite x-rays being discovered in 1885, true x-ray microscopy was not possible until the mid-1980s due to the lack of appropriate x-ray optics. X-rays interact weakly with matter and so refractive indices relating to soft x-rays are extremely close to 1, conventional lenses or mirrors cannot be used in an x-ray microscope. It was found in the 1980s that Fresnel zone plates (FZP) could be used as diffractive optics to build such a microscope [179]. An FZP is a circular grating with a radially increasing

line density. Using FZPs to create an x-ray microscope enables the beam to be focused such that spatial resolutions better than 10 nm can be achieved [178].

The Center of X-ray Optics (CXRO) has operated the full-field, soft transmission x-ray microscope XM-1 at the ALS since 1994. It consists of an optical design similar to that of a conventional microscope that utilises visible light, with a few modifications for handling x-rays. A full schematic of the set-up is shown in figure 3.2.9 with full details of the instrumentation found at [182].

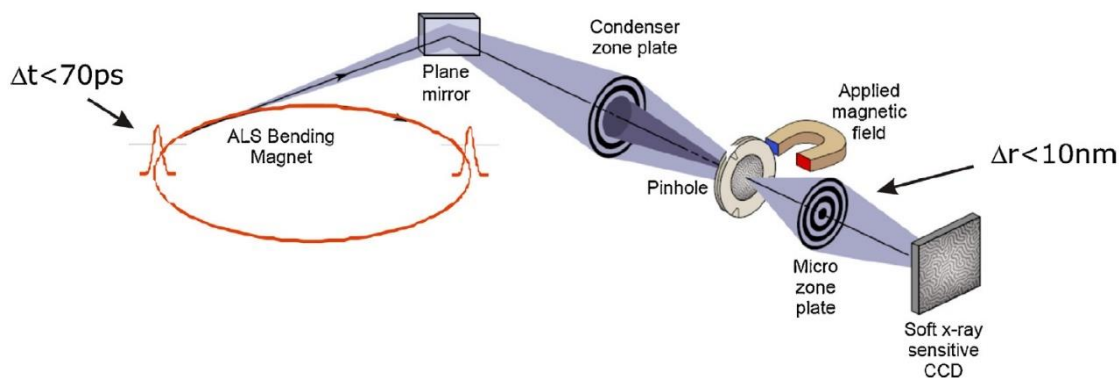


Figure 3.2.6: Schematics of the optical setup of the full field soft X-ray transmission microscope XM-1 located at beamline 6.1.2 at the ALS. Taken from [183].

The key components of the system are as follows. The light source of the system is the third generation x-ray synchrotron found at the ALS. The beam is then redirected using a plane mirror towards the first of two FZPs used in the set-up. The first acts as a condenser lens and combined monochromator and illuminating optic, this is known as the CZP. This is combined with a pinhole close to the specimen, within which an aperture is used in order to select the x-ray polarisation. An external electromagnet is positioned around the sample in order to externally apply magnetic fields in situ. A second FZP is placed near the focal length downstream from the sample. This acts as the high resolution objective lens and is known as the micro zone plate (MZP). Finally a two-dimensional x-ray sensitive charge coupled device (CCD) is positioned such that it can detect the transmitted x-rays.

In order to use this experimental set-up, the samples must be placed on a x-ray transparent substrate. This method requires magnetisation along the plane of the beam. As permalloy nanowires possess in-plane magnetisation, the sample is mounted at an angle of approximately 30° to provide a magnetic component along

the plane of the beam. In this study, the samples were created on a Si_3N_4 membrane approximately 100 nm in thickness.

During hysteresis loops, images were obtained at each applied field. In order to observe magnetisation switching and the presence of DWs clearly further image processing was needed. Within the images, changes in intensity represent changes in magnetisation. To enhance the contrast between images, one image would be divided by another using imaging software. This division of images gave a baseline background colour with changes in magnetisation highlighted by bright or dark regions, depending on the direction of magnetisation switching. These divided images are used to observe DW structures by studying the edges of the regions where the magnetisation had switched.

3.3 Micromagnetic Simulations

Throughout this thesis a number of micromagnetic simulations have been conducted. Some of these investigations have been self-contained pieces of work whilst others have been done to support and explains experimental observations. All of the simulations conducted in this thesis have been done so using the Object Orientated MicroMagnetic Framework (OOMMF) software package (V 1.2b0)[184]. OOMMF is a freely available micromagnetic software package where 3-dimensional micromagnetic problems are broken down into parallelepiped cells of equal size. The size of the cells is defined by the user and are usually very small. In this thesis the largest allocated cell size is chosen to be $5 \times 5 \times 5 \text{ nm}^3$, due to the exchange length. Keeping the cell size smaller than this ensures that the interactions are exchange dominated within the volume, leading to uniform magnetisation. Each cell possesses a uniform magnetisation that is equal to the saturation magnetisation, M_S of the material.

The OOMMF package numerically solves the Landau-Lifshitz (LL) equation, see equation 1.26, for the system of interacting cells. In this context, each cell is considered to be a uniformly magnetised “macrospin”. Within the LL equation, the effective field, H_{eff} experienced by each cell is calculated using $\partial\varepsilon/\partial\mathbf{M}$, here the ε in this case is analogous to equation 1.10. In these calculations, the exchange energy is only considered between a cell and its six nearest neighbours. The demagnetising energy is found using equation 1.16 where the uniform cell magnetisation interacts with a demagnetising field created by diverging magnetisation resulting from the overall geometry. As the LL equation is an ordinary differential equation, it may be solved using either an Euler or Runge-Kutta method. As the computational methods

used contains a means of error determination, there is no perceptible discrepancy in accuracy between the two methods. All simulations carried out within this thesis utilise the Euler method.

Using the Euler method means that a time evolving solution is used to calculate the end states of the micromagnetic configurations. Such a method is important when a particular minimisation path, such as under the stimulus of an applied field, directly influences the end configuration. In the cases presented in this thesis, only the quasi-static energy minimum is required. The energy minimum is found when $\partial M/\partial t$ reduced below a predetermined threshold, set to 0.01 degrees per nanosecond in this study. In order to speed up simulation time for these studies, the damping is increased to an artificially high value of 0.5. Due to this, whilst the energy minimum is found, the path calculated to achieve the final configuration cannot be trusted as an accurate description of the system evolution.

The material of focus in this thesis is permalloy. The material parameters used for all simulations can be found in table 3.1.

Table 3.1: Material parameters of permalloy used in OOMMF simulations

Parameter	Value
Saturation Magnetisation (M_s)	$8 \times 10^5 \text{ A/m}$
Exchange Constant (A)	$1.3 \times 10^{-11} \text{ J/m}$
Anisotropy Constant (K)	0 J/m^3

4. Computational Study of the shape influence on pinning strength of vertical nanotrenches

This chapter presents the computational portion of the study. First the initial simulations conducted will be discussed. These involved setting up an artificial DW in the centre of an unmodified nanowire and allowing it to relax in order to observe the resulting DW structure. The results of this procedure allow a phase diagram to be created and compared to previous literature.

Following this, vertical nanotrenches are introduced to the structure for first time. Initial simulations are conducted to compare to previous literature in order to gain confidence that the created model is a reliable one.

Once these results are established, the main computational study is discussed. This focuses on testing the effects of the nanotrench size and shape on the pinning strength of the site. This is inspired by the potential use of AFM tip-based nanomachining to create vertical pinning sites in magnetic nanowires. Due to the shape of the AFM tip, the generated pinning sites will be nanotrenches that are triangular in shape. Therefore it is necessary to understand the effects that the shape of the nanotrench will have on the way it interacts with DWs. The investigations carried out include how DWs of varying chirality and form interact with various nanotrenches. In particular how varying the depth and length of the nanotrench affect it's pinning strength. These comparisons are made between square, triangular and trapezoidal nanotrenches.

4.1 Initial prototype model - Phase diagram

The first steps for this section of the study was to build the computational model. The software package used to do this is OOMMF as discussed in section 3.3. Once the software package had been chosen, a suitable approach needed to be decided upon. In previous literature, a phase diagram has been created to observe when particular DW structure occur for which nanowire dimensions [24], this was discussed in further detail in section 1.1.7. In order to test out model, a corresponding phase diagram was created in order to test if it compared. Producing similar results gives an increased confidence that the model has been constructed correctly.

In order to test the model against the phase diagram produced by Nakatani and co-workers [24] the same parameters had to be used. These are listed in table 3.1 with α set to 0.02. The nanowires are created such that the length was at least 10 times

longer than their width. This is done so in order to avoid any edge effects from the wire ends influencing the DW as it relaxes. The system is initially set up such that there are two domains orientated head-to-head with the boundary in the centre along the length of the wire. This boundary represents a complete 180° spin rotation between neighbouring cells. This means that initially there is no region between the two domains where the magnetisation is orientated away from the positive or negative x-axis. This is demonstrated in figure 4.1.1.

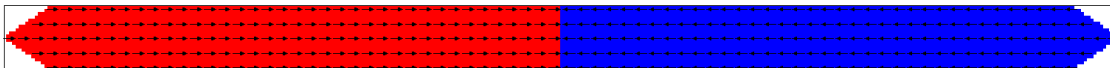


Figure 4.1.1: Initial magnetic state of nanowire before relaxation for creation of phase diagram

This initial state is allowed to relax. This means that the system is allowed to progress in time using an Euler method as discussed in chapter 3.3 without the influence of an external magnetic field. The simulations stop running once a particular threshold is met. In this case, the relaxation stops once dM/dt drops below 0.001 degrees per nanosecond. Once the DW is relaxed and stops progressing, the DW type was noted and plotted against the nanowire width and thickness. This plot is shown in figure 4.1.2.

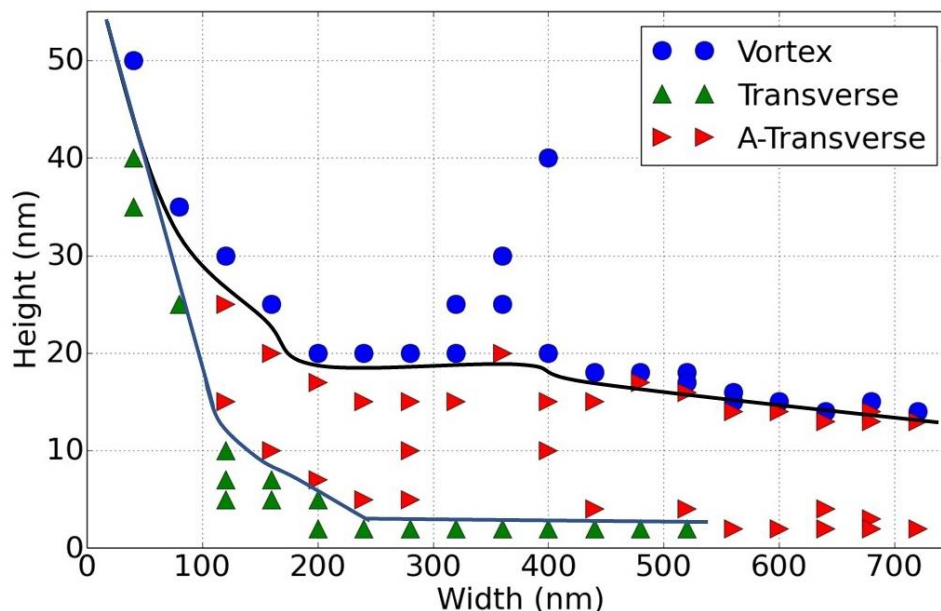


Figure 4.1.2: Phase diagram of domain wall type for varying nanowire dimensions. Blue line is to help guide the eye to the approximate boundary between transverse and asymmetric-transverse DWs. Black line is to help guide the eye to the approximate boundary between asymmetric-transverse and vortex DWs.

Comparing figure 4.1.2 with the plot found in the study by Nakatani and co-workers[24] in figure 1.1.11, it can be seen that the dimensions where transverse DWs occur generally agree with one another. It is also seen that at larger dimensions vortex DWs occur with the overall boundary between the two appears to be decreasing by smaller amounts as the width increases. The key difference between this created phase diagram and the one produced by Nakatani *et al.* found in[24] is the boundary between these two regions. There is a region in both phase diagrams where asymmetric transverse DWs occur, however this region is much wider in the figure produced as part of this study. The boundary between transverse and asymmetric transverse DWs compares well with the previous study. Whilst the upper boundary is found to be at larger wire thicknesses.

There are some possible explanations for these differences. These regard the specific simulation procedures in order to create the data points. One difference could be the initial magnetic state of the simulation. In the paper by Nakatani *et al.*, all three DW structures were placed within each nanowire size and the energies of each configuration compared. This was very different to the procedure in this thesis. In this study, the initial configuration consists of two opposing domains are artificially placed with a straight boundary between them. The system was left to relax under zero applied field to form the DW structure. This procedure requires the artificial DW to undergo phase transitions as the magnetic configuration changed to relax into a particular shape. This provides a possible explanation as to why the ATDW region is larger in this study, existing within thicker nanowires. As discussed in section 1.1.7, the first and second order phase transitions allow TDWs to occur as metastable states in the VDW region[23], [24].

Another explanation could regard the region of the nanowire considered in the simulation. In the previous study, it is described that the simulations are conducted as a moving calculation centred on the DW as it is allowed to move, with the calculation width limited to 2 μm . This means that the nanowire effectively has no ends to it as the appropriately boundary conditions are utilised. The DW motion may influence the DW configuration as it allows metastable configurations to relax. This differs from the simulations in this study as a fixed size nanowire, with the length chosen such that the edge effects from the nanowire ends should not interfere with the DW formation. The DWs in these simulations also naturally do not move any significant distance as the initial magnetic configuration is set such that one side is not stronger than the other, pushing the DW towards one end. Note the cell sizes

used during the production of the phase diagram were set to match those used in the Nakatani *et al.* study[24], i.e. $4 \times 4 \times h \text{ nm}^3$ where h in this instance is the thickness of the nanowire.

These differences in comparison should not provide any significant issues when performing other simulations. This phase diagram is only to provide some guidance as to which DW types to expect for given nanowire dimensions. The simulations in this study are used for qualitative comparison and so the exact values found are not so important, only the relative values to other results. Regarding the computational model used to produce this phase diagram, there will also be another key difference to other simulations conducted. In this case, the damping coefficient was set to match the material parameters of permalloy ($\alpha=0.02$). All simulations conducted beyond this point are done so with $\alpha=0.5$ as is commonly done to quicken computation speeds.

4.2 Inserting nanotrench into computational model

Once the simple magnetic nanowire model was verified comparing it to previous literature, the next step was to create an artificial pinning site. This was done by setting a volume of the simulation space with the material parameters of a vacuum. For the purposes of this study, this is placed across the width of the nanowire and cuts into the material such that it reduces the thickness. This feature is located in the centre along the nanowire's length. This is done as reported by [123] and is shown in figure 4.2.1. The nanowire used in this study was 100 nm wide, 10 nm thick and 2 μm long. The schematics of the square nanotrench are shown in figure 4.2.1.

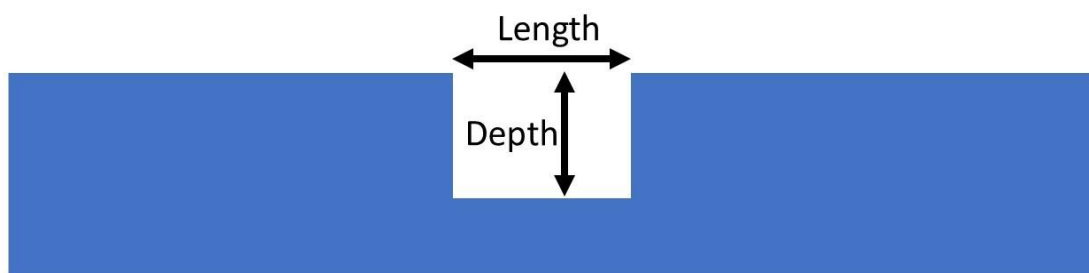


Figure 4.2.1: Cross-sectional view of a square nanotrench used in simulations.

The magnetisation within the material is initially set similarly to the plain nanowire case, as in figure 4.2.2. With the nanotrench in place, the head-to-head DW is artificially created such that it will form beneath the nanotrench. This is done so simply to reduce simulation time while the DW would form and then move into the nanotrench. This is a similar approach to that done by Narayanapillai and Yang

[123]. As done previously, the system is allowed to relax in order to allow either a transverse or vortex DW to form. Once the system reaches equilibrium, an external magnetic field is applied along the length of the wire. As the field increases, the DW is pushed away from the nanotrench. Once the field becomes strong enough, the DW will “depin” and move away from the nanotrench, propagating along the length of the nanowire until the wire is uniformly magnetised in the direction of the applied field. The field at which this propagation occurs is noted and called the depinning field.

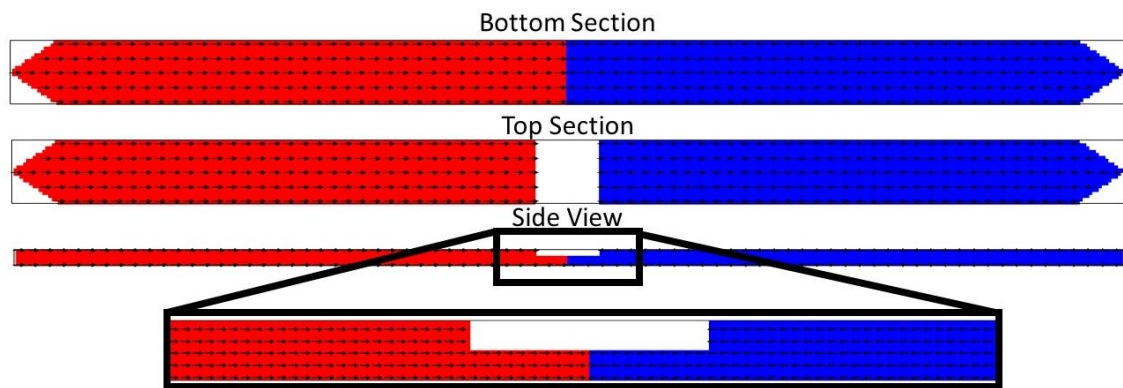


Figure 4.2.2: Initial simulation set-up for nanotrench

In order to test the computational model that has been created, data was taken using a nanowire size and nanotrench dimensions matching those used in study conducted by Narayanapillai and Yang[123] . These results were used to verify the validity of the created model before moving on to further experiments. The results of this test are shown in figure 4.2.3.

The results shown in figure 4.2.3 are very close to those produced by Narayanapillai and Yang [123]. The trends in all cases appear to match with the values also appearing to be very close. This gives increased confidence in the results created by the computational model.

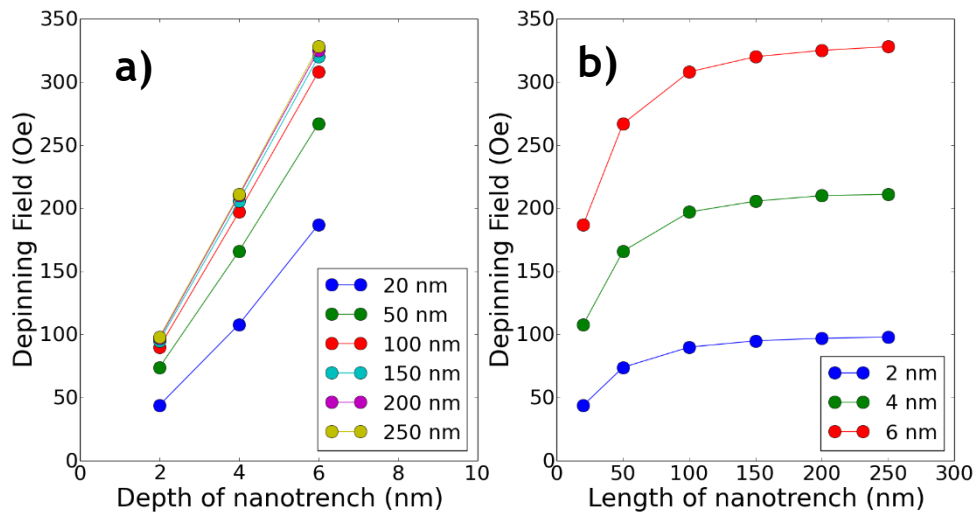


Figure 4.2.3: Results of 100 nm wide 10 nm thick nanowire with a cell size of 5 nm x 5 nm x 2 nm. a) Depinning field against depth of nanotrench for various nanotrench lengths. b) Depinning field against length of nanotrench for various nanotrench depths. Lines are to guide the eye.

4.3 Pinning domain walls with square and triangular vertical nanotrenches

Once it was demonstrated that the computational model created provided results that agreed with previous studies, it was time to move on to further investigations. First square nanotrenches were created and studied before moving onto triangular nanotrenches. Triangular nanotrenches were chosen to approximate those that would be created in practice via AFM tip-based nanomachining.

4.3.1 Square Nanotrench

In this study, nanotrenches are studied for three different size nanowires. A nanowire measuring 100 nm wide and 25 nm thick was investigated. This size nanowire was found to produce transverse DWs. In these simulations, the cell size used was $5 \times 5 \times 2.5 \text{ nm}^3$. The z dimension of the cell was chosen to be 2.5 nm as it is 10% of the nanowire thickness. This allows us to probe the nanotrench depth from 10% through to 90% of the nanowire thickness. This allows a relatively large range of depths to be studied without compromising computational time greatly by creating many vertical rows and so many more cells.

Simulations were conducted with nanotrenches ranging in size from 2.5 to 22.5 nm in depth and 10 to 200 nm in length. The depinning field was noted and all results are plotted in figures 4.3.1 and 4.3.2.

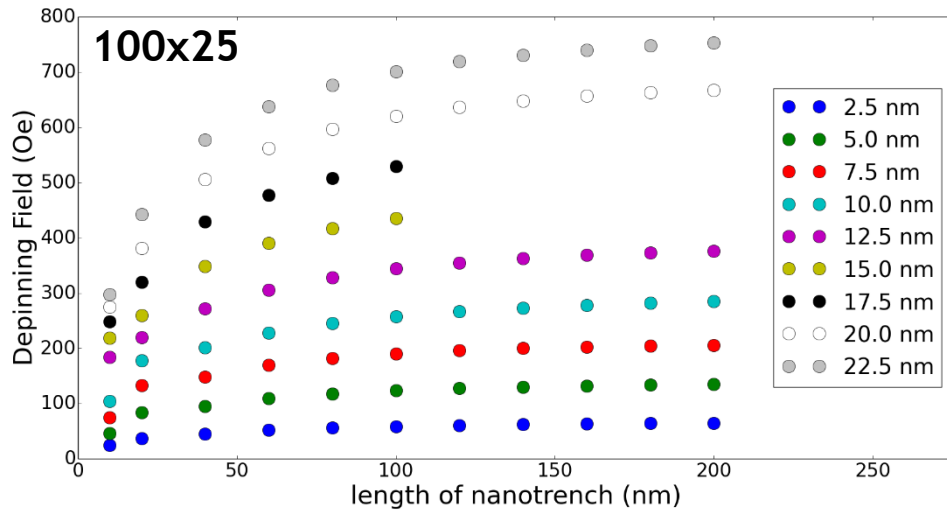


Figure 4.3.1: Square nanotrenches in 100 nm wide, 25 nm thick nanowire - Plot of depinning field against nanotrench length (nm) for various nanotrench depths.

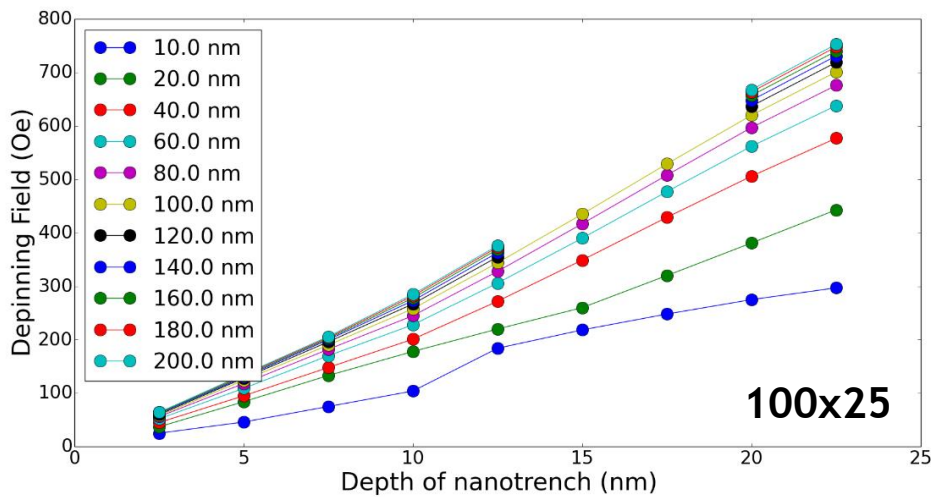


Figure 4.3.2: Square nanotrenches in 100 nm wide, 25 nm thick nanowire - Plot of depinning field against nanotrench depth (nm) for various nanotrench lengths. Lines are to guide the eye.

Figure 4.3.1 shows the depinning strength as it varies with the length of the nanotrench. As seen previously the trends show an initial increase in depinning strength before saturating between 100 and 150 nm. Then further increase in nanotrench length appears to have relatively little effect in the sites pinning strength. Figure 4.3.2 demonstrates the same data set but now comparing the depinning field against nanotrench depth. Again the trends agree with what have been observed previously, that the nanotrench depth appears to have a much

greater influence over the site's pinning strength. This relationship appears to be approximately linear in all cases. As the effects are greater, it is easier to compare the range in which the nanotrench's pinning strength varies with size. For this size nanowire, we see a depinning field range of 25 to 753 Oe.

To further understand the depinning process, observations of the nanowire energy were made. Figure 4.3.3a shows the total energy of the nanowire along with the individual energy contributions from the exchange, demagnetisation, anisotropy and Zeeman effects. Figure 4.3.3b shows the approximate position of the DW for reference. It is seen in figure 4.3.3a that as the applied field increases, this has the effect of increasing the Zeeman energy contribution, this becomes the dominant contribution influencing the total energy. It is shown that the anisotropy energy is always 0 J, this is expected as permalloy has negligible anisotropy effects. Therefore the key energy contributions that will be focused on throughout this chapter are the exchange and demagnetisation energies.

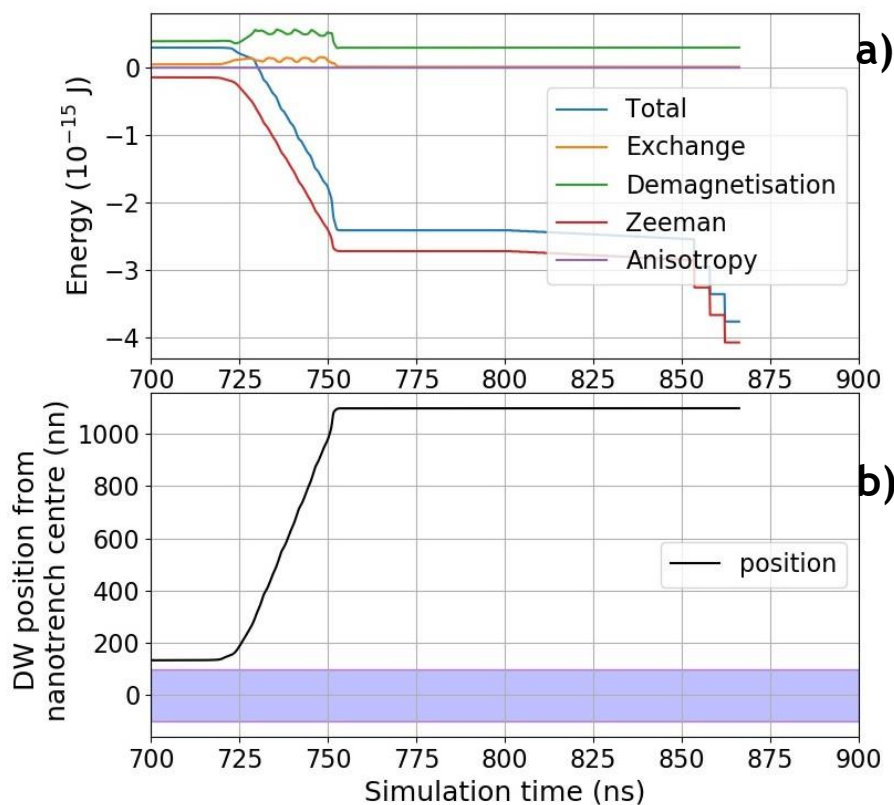


Figure 4.3.3: a) Plot of energy contributions over simulated time, b) Plot of approximate DW position for reference with plot in a). Blue shaded region represents the location of the nanotrench. Plots made for a 100 nm wide, 25 nm thick nanowire containing a 20 nm deep, 200 nm long square nanotrench. The figure focuses on the simulated time over which the DW depins and propagates through the nanowire.

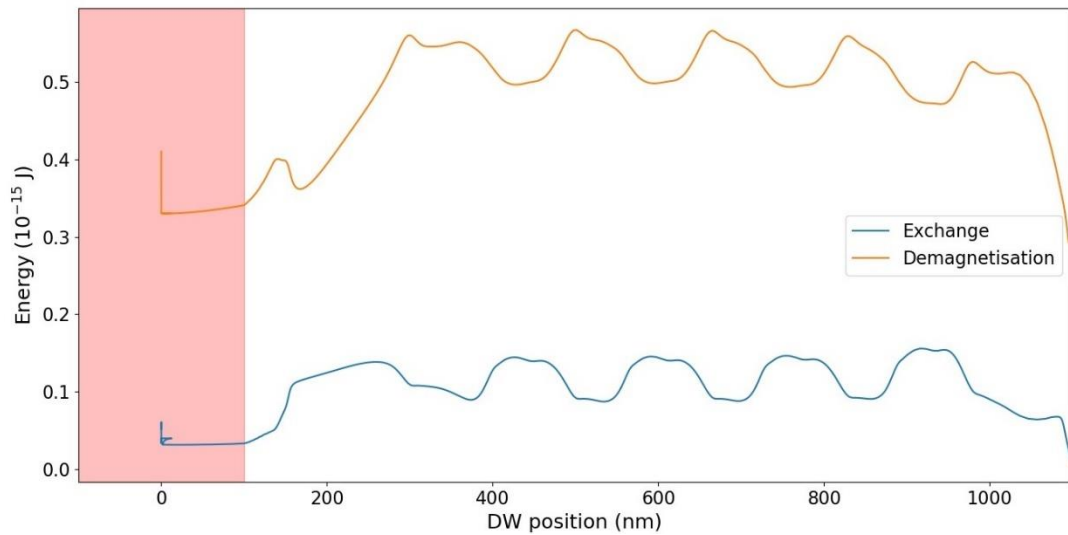


Figure 4.3.4: Energy plot of the exchange and demagnetisation energies for a 100 nm wide, 25 nm thick nanowire containing a 20 nm deep, 200 nm long square nanotrench. The red shaded region represents the location of the nanotrench.

Whilst the dimensions of this nanowire are located within the transverse DW region of the phase diagram, it is closer to the boundary. The next nanowire to be studied was 50 nm wide and 10 nm thick. This smaller nanowire allows the study of the effects of the relative size of the pinning site on the resulting pinning strength. The nanotrench was varied in size from 10 to 190 nm in length in steps of 20 nm, and 1 to 9 nm in depth in steps of 2 nm. The results of these can be found in figures 4.3.5 and 4.3.6.

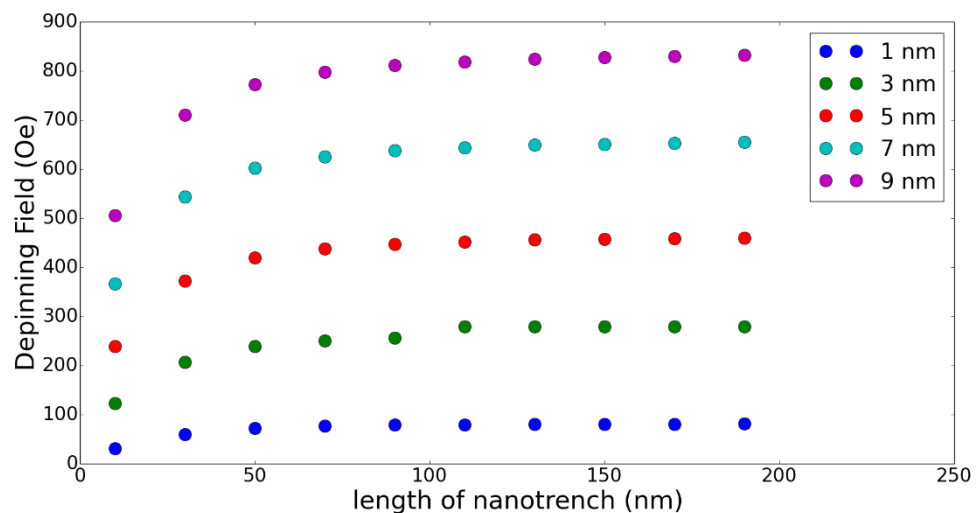


Figure 4.3.5: Square nanotrenches in 50 nm wide, 10 nm thick nanowire - Plot of depinning field against nanotrench width (nm) for various nanotrench depths.

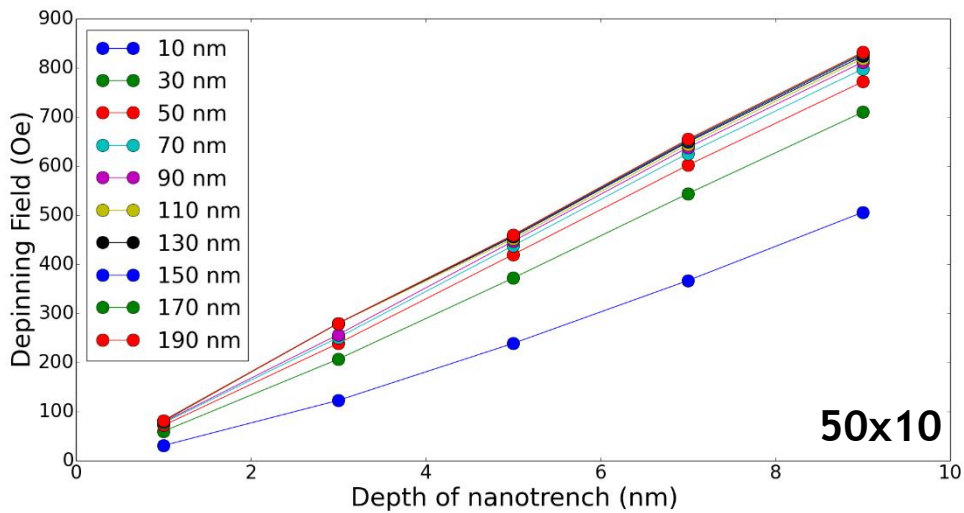


Figure 4.3.6: Square nanotrenches in 50 nm wide, 10 nm thick nanowire - Plot of depinning field against nanotrench depth (nm) for various nanotrench widths. Lines are to guide the eye.

As seen in figure 4.3.5, the overall trends of depinning field against nanotrench length are very similar to that of the 100 nm x 25 nm nanowire. The only difference between the two shows that there is a larger variation in the pinning strengths. All depths show saturation between 100 and 150 nm once again, however there are larger gaps between each series of data points. This is reinforced when observing the results against nanotrench depth in figure 4.3.6. Once again, all the trends agree with those found in the 100 nm x 25 nm nanowire with them all being approximately linear. The smallest nanotrench size requires a larger applied field in order to depin the DW when compared with the smallest nanotrench simulated in the 100 nm x 25 nm nanowire. The relative change in depinning fields with respect to nanotrench depth appears to be similar in both nanowire cases with the absolute values being higher in the smaller wire with a range spanning 31 to 832 Oe.

As done with the 100 nm wide, 25 nm thick nanowire case, energy plots are shown in figure 4.3.7. It is clear to see the energy profiles are similar to those found in the 100 nm wide, 25 nm thick nanowire case. The nanotrench is shown to act as a potential well, with the transverse DW remaining at the same energy within the nanotrench as it moves towards the edge. This is the case regardless of how long the nanotrench is. Once exiting the nanotrench, the DW energies increase to a set value, before the energies reduce on DW annihilation at the end of the nanowire. This is in agreement with the results found by Goolaup *et al.*[105] where the rectangular notch maintained its pinning strength with increased width.

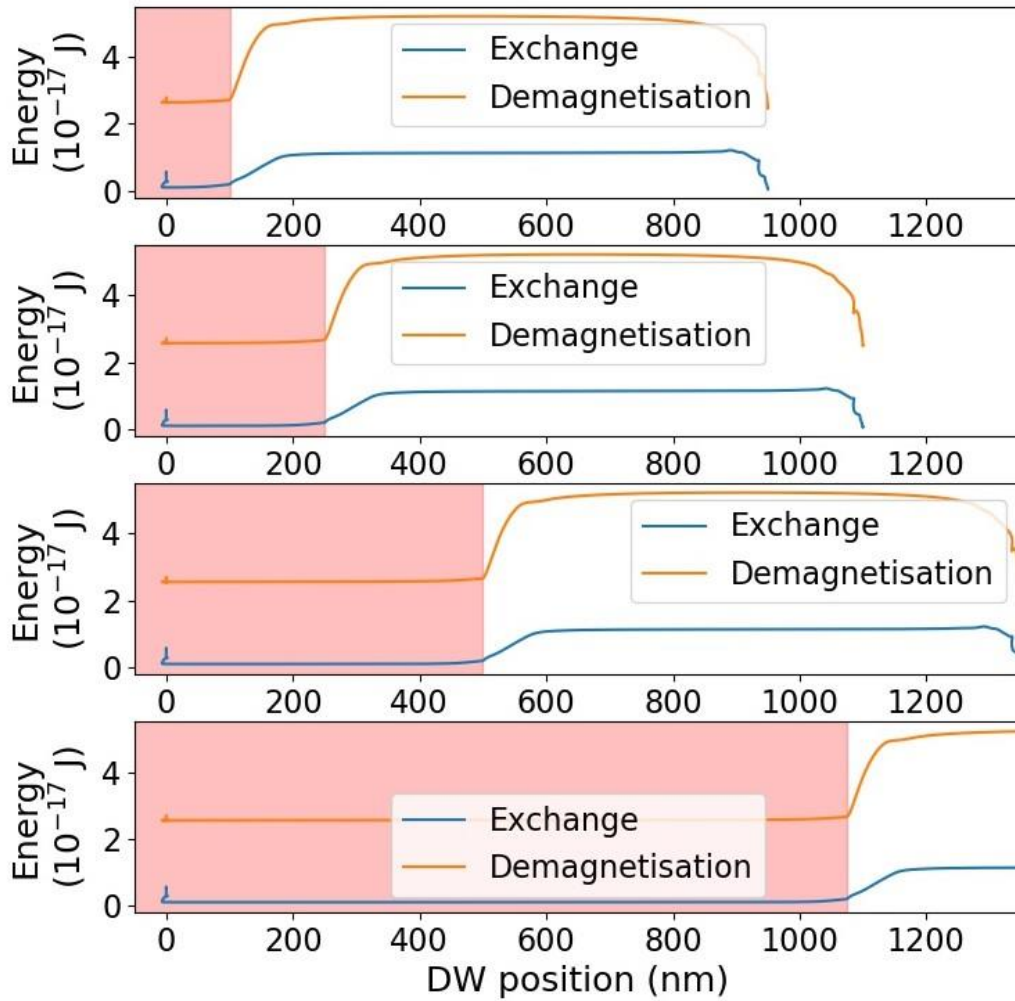


Figure 4.3.7: Energy plots showing exchange and demagnetisation energy against DW position. Plots for a 50 nm wide, 10 nm thick nanowire containing; a) 9 nm deep, 200 nm long square nanotrench. b) 9 nm deep, 500 nm long square nanotrench. c) 9 nm deep, 1000 nm long square nanotrench. and d) 9 nm deep, 2150 nm long square nanotrench. Red shaded regioned represent location of nanotrench.

The final size nanowire that will be used in this study measures 200 nm wide and 50 nm thick. This was chosen to be much larger than the other two as at this size vortex DWs are stable in an unpatterned wire. This provides the opportunity to observe how vortex DWs interact with the vertically placed nanotrench. The variety allows a comparison of the trends relating to the interactions of the nanotrench with both transverse and vortex DWs. Again the nanotrench was varied in length from 10 to 200 nm whilst the depth of the nanotrench varied from 5 to 45 nm in steps of 10 nm. The results of these simulations are shown in figures 4.3.8 and 4.3.9.

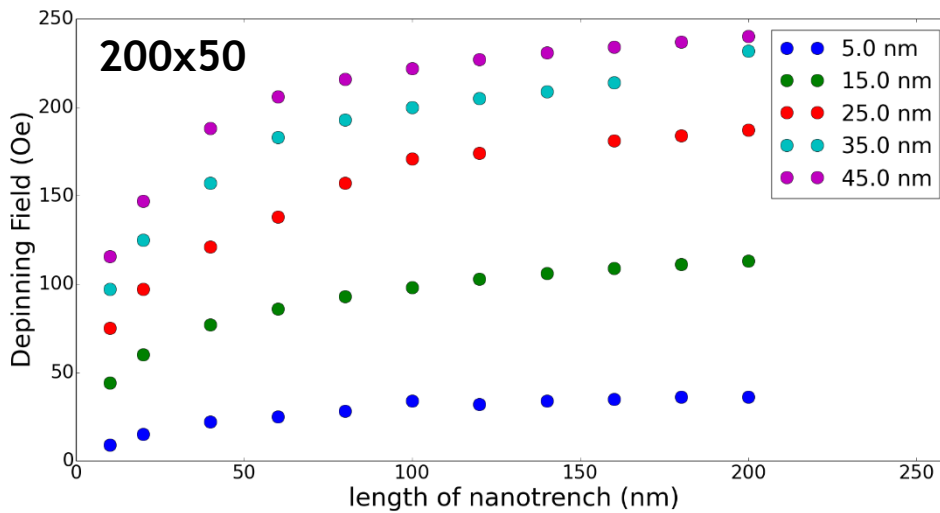


Figure 4.3.8: Square nanotrenches in 200 nm wide, 50 nm thick nanowire - Plot of depinning field against nanotrench width (nm) for various nanotrench depths.

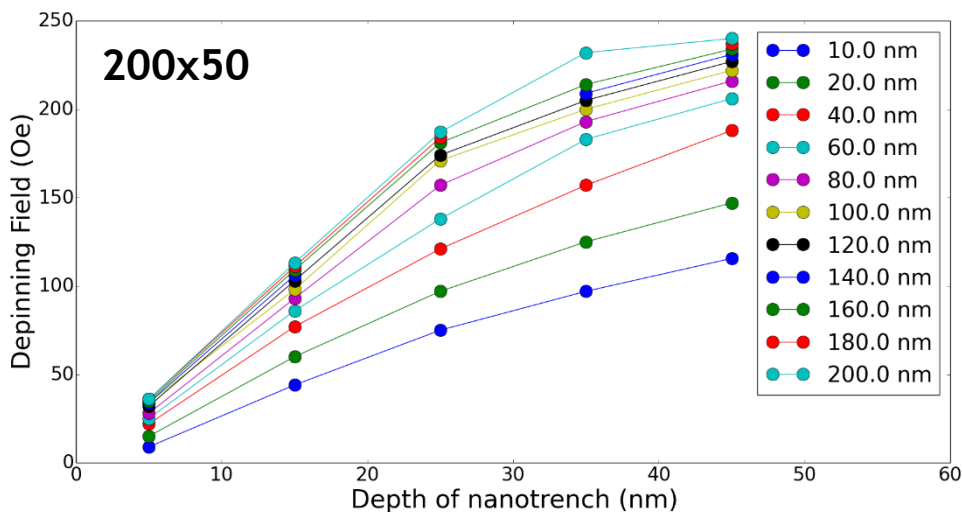


Figure 4.3.9: Square nanotrenches in 200 nm wide, 50 nm thick nanowire - Plot of depinning field against nanotrench depth (nm) for various nanotrench lengths. Lines are to guide the eye.

Figure 4.3.8 shows the plot of depinning field against the length of the nanotrench. Any missing points correspond to simulations where metastable DWs occurred resulting in an artificially high depinning field when compared with the transverse DW results. Similar to the previous cases, the trends appear to show saturation by around 100 nm with the depinning field not increasing much further with further increase in nanotrench length. It is also key to note that there is a much narrower range of depinning fields as the DWs are pinned much more weakly with the

strongest field required to depin the DW being 240 Oe. The relationship between depinning field and depth of nanotrench however does differ slightly from the previous two cases. In the previous cases with transverse DWs, there was an approximately linear relationship between depinning field and the depth of the nanotrench. In the case of vortex DWs in the larger nanowire, the depinning fields do not continue to increase at a linear rate. These curved trends become more apparent the longer the nanotrench becomes. The trend takes the appearance that the pinning strength goes towards saturation at a shallower depth of the nanotrench.

A possible explanation for the reduction in depinning fields may not be related to the nanotrench itself, but more to do with the nanowire structure. Previous studies discussed in section 2.1.3 discovered that the size of the nanowire often held more influence over depinning fields than any pinning sites[36], [103], [104]. In particular, the change in injection/depinning fields varied over a large range once the nanowire width was reduced below 400 nm. This is relevant to the study in this thesis. The widths of the three nanowires studied are 50 nm, 100 nm and 200 nm, all of which are below the 400 nm threshold. Therefore it is likely that the depinning field strength differences between nanowires are influenced heavily by the change in nanowire dimensions as opposed to only the DW structures.

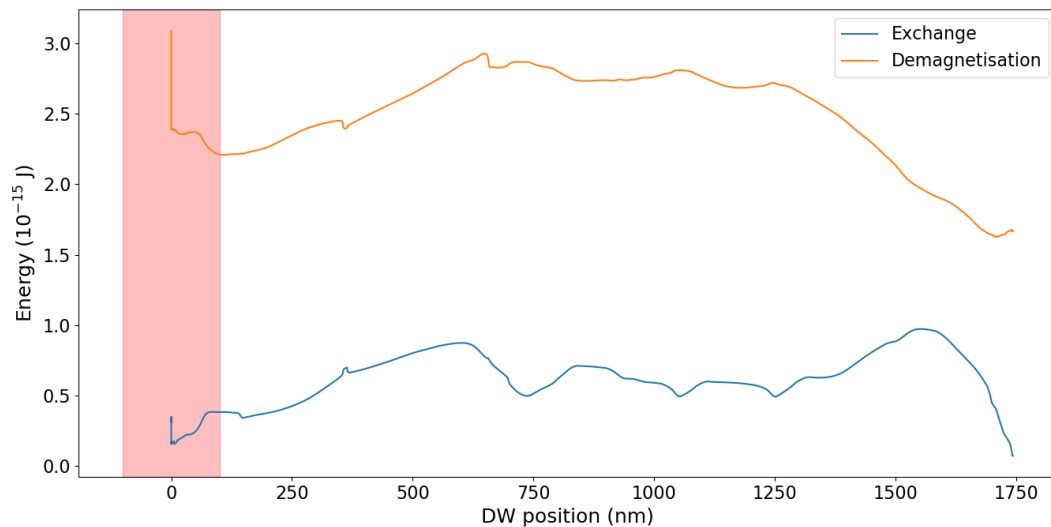


Figure 4.3.10: Energy plot of the exchange and demagnetisation energies for a 200 nm wide, 50 nm thick nanowire containing a 35 nm deep, 200 nm long square nanotrench. The red shaded region represents the location of the nanotrench.

Figure 4.3.10 shows the energy plot for the 200 nm wide, 50 nm thick nanowire containing a 35 nm deep, 200 nm long nanotrench. The energy behaviour is different to those of the previous plots. In this case, the DW is shown to reduce its energy within the nanotrench as it moves toward the edge. This indicates the DW has a

preference to stay at the edge of the nanotrench as opposed to within it. This result suggests the vortex DW obtained in scenario interacts with the nanotrench such that its potential energy profile is that of a potential barrier. Again, this result is consistent to previous studies [123].

This shows a clear difference in interactions with the vertical nanotrench for both DW types. One possible explanation of explaining this difference could relate to the magnetic structure of the DWs themselves. More specifically how the chirality of the DWs could provide an explanation. Within the transverse DW, the vast majority of the magnetization of the wall itself lies purely in the x-y plane of the nanowire. It is reasonable to assume that any geometrical variations in the nanowire relating to the x-y plane would have relatively larger interactions with the DW than variations in the z dimension. This is reinforced by the discovery in previous studies showing that a transverse DW depins from a lateral notch at different applied fields depending on its chirality i.e. whether its core points towards or away from the notch [35], [75], [96]-[98], [185]. Therefore a vertical nanotrench should theoretically eliminate this effect in the case of transverse DWs. However, when considering a vortex DW, there is a much more significant magnetic contribution in the z direction. This is where the core of the vortex DW points in the positive or negative z direction. This would respond to a change in the z geometry much more than any contributions found in a transverse DW.

A further example of this comes simply by relaxing the DW beneath the nanotrench. When the DW relaxes and forms a transverse DW, the DW stays beneath the reduced region and moves towards the centre of the nanotrench. However, if a vortex DW is formed, it has a tendency to move toward the edge of the nanotrench such that the vortex core is in contact with the edge. This is where the DW remains until it is eventually depinned via the application of an external field. This is behaviour that was previously found and discussed by Narayanpillai and Yang [123]. With the DW already at the edge of the nanotrench before an external field is applied, it is understandable that the length of the nanotrench would have less of an impact on its pinning strength than the transverse case that prefers to remain beneath the nanotrench.

The way in which each DW type interacts with the nanotrench can be thought of in terms of the potential energy profile produced by the pinning site. As seen in previous studies [35], [98] lateral notches can have the potential energy profile of a potential well, potential barrier or a combination of both. In the case of the

transverse DW, its tendency to remain beneath the nanotrench implies that the pinning site acts as a potential well. So the externally applied field is required to give the DW enough energy to escape the well and propagate through the rest of the nanowire. As the vortex DW pushes itself towards the edge of the nanotrench, this implies that the pinning site acts as a potential barrier. However, as the DW remains attached to the nanotrench until an appropriate applied field is reached, this could imply that either side of the potential energy barrier there are in fact smaller potential wells. This would be a case similar to that found in [35].

A relatively simple way to test how the DW types interact differently with the nanotrench is to conduct the same simulation multiple times whilst only changing the DW chirality. In order to produce transverse DWs, the 50 nm wide, 10 nm thick nanowire was used with a 100 nm long, 5 nm deep nanotrench. The simulation was set-up such that the chirality of the resulting DW would be as desired. Transverse DW chirality was chosen by initially creating a small region between the opposing domains with the magnetisation in the positive or negative y direction as desired. For vortex walls, the boundary between domains was angled at 45 degrees beneath the nanotrench in order to create clockwise or anti-clockwise DWs. The in or out chirality was dictated by adding a positive or negative z component to the magnetisation beneath the nanotrench. There are four cases considered for the transverse DW, these are combinations of head-to-head (HtH) and tail-to-tail (TtT) DWs where in each case the core can point in the positive or negative y direction (known as “up” and “down” chiralities). Similarly, the 200 nm wide, 50 nm thick nanowire is used to produce vortex DWs with a 100 nm long, 25 nm deep nanotrench. There are eight chiralities tested in total for vortex DWs. These are made up of all the combinations of HtH or TtT, clockwise or anti-clockwise and if the core is facing in the positive or negative z direction (“in” or “out”). The results of this chirality test are found in table 4.1. All results shown are the results of single simulations for each scenario using a cell size of $5 \times 5 \times 1 \text{ nm}^3$.

Table 4.1: Results of Chirality test for square nanotrench. Transverse DWs produced in 50 nm wide, 10 nm thick nanowire. Vortex DWs produced in 200 nm wide, 50 nm thick nanowire. Depinning fields given in Oe.

	Transverse		Vortex			
			Clockwise		Anti-clockwise	
	Up	Down	In	Out	In	Out
HtH	450	450	164	171	171	171
TtT	450	450	171	171	171	164

The results in table 4.1 show that there does not appear to be any chirality influence on the pinning strength of the transverse DW. The depinning field in all four cases is the same. This reinforced the idea that the lack of magnetic contribution in the z direction eliminates any bias in DW interactions depending on the chirality. The spatially symmetry on the potential landscape is an expected result when comparing to results of a symmetrical neck showing chirality independent results[105].

In the case of the vortex DW, there is a difference between particular chiralities. The difference found however is not completely as expected. Using the theory that the core direction could be the key component in how the DW interacts with a vertical pinning site, it would be expected that there would be a difference in depinning field when comparing the “in” and “out” pairs. This was expected as the asymmetry in the potential landscape comes in the z component in the case of a vertical nanotrench. The results show that it is not as simple as that as the TtT-clockwise pair show the same depinning field, as does the HtH-anti-clockwise pair. Comparisons can be made between the sets of results where the HtH-clockwise-In combination shows the same lowered depinning field as the TtT-anti-clockwise-Out combination. This shows that the chirality of the vortex DW does have an influence over the pinning strength of the site, however much further investigations would be needed to fully understand these differences.

4.3.2 Triangular nanotrench

In this section the study moves on from the more common square shaped nanotrenches by introducing a vertical triangular nanotrench. A schematic example of a triangular nanotrench is shown in figure 4.3.11. The depth of the nanotrench is defined as the deepest point into the nanowire. This is designed to be placed in the centre of the feature, such that along the x-axis the nanotrench is symmetrical. The length of the nanotrench refers to the distance where material is removed from the surface of the nanowire. The cross-section of the nanotrench has the appearance of

a isosceles triangle, with the deepest point in the centre of the length. This is displayed in figure 4.3.11.

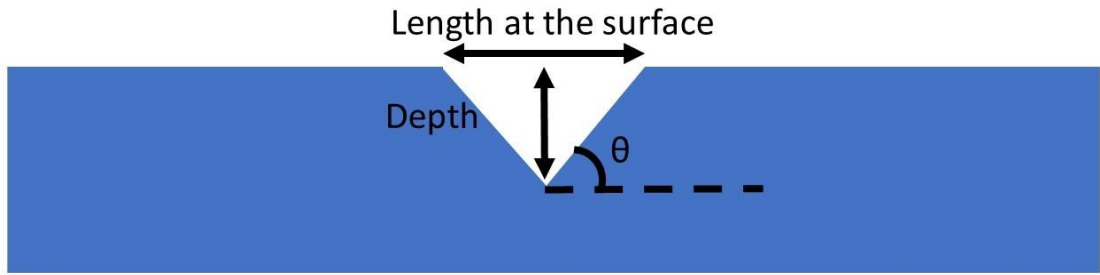


Figure 4.3.11: Cross-sectional schematic of a triangular nanotrench

For this study triangular nanotrenches have been simulated in the three different size nanowires. The dimensions of each nanowire match those used in the previous section studying square nanotrenches (100 nm x 25 nm, 50 nm x 10 nm and 200 nm x 50 nm). The size of the nanotrenches created are similar in size to the square ones studied in the previous section. This allows for direct comparison of pinning strengths and overall trends. The first results to be discussed relate to the 100 nm wide, 25 nm thick nanowire. The depth of the nanotrench is varied from 2.5 nm to 22.5 nm in steps of 2.5 nm whilst the length at the surface is varied from 10 nm to 200 nm in steps of 10 nm. These results are shown in figures 4.3.12 and 4.3.13.

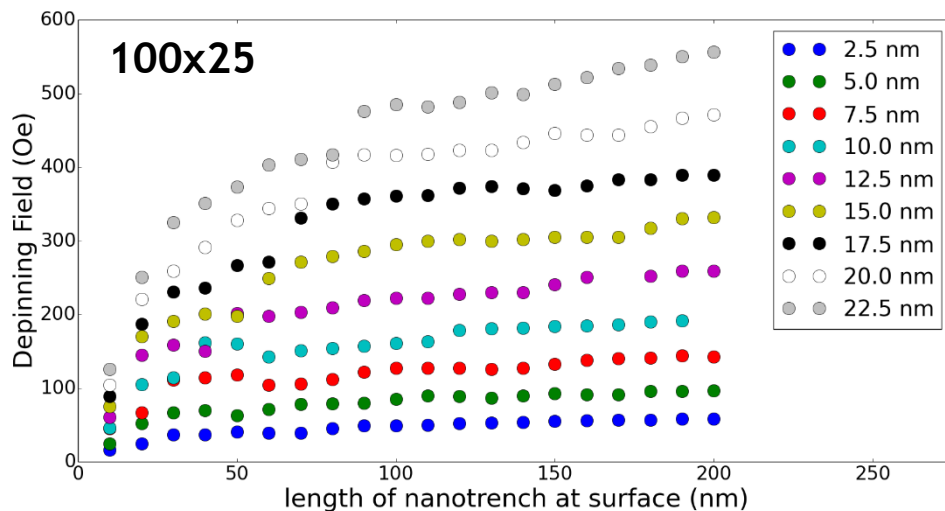


Figure 4.3.12: Triangular nanotrenches in 100 nm wide, 25 nm thick nanowire - Plot of depinning field against nanotrench length at the surface (nm) for various nanotrench depths.

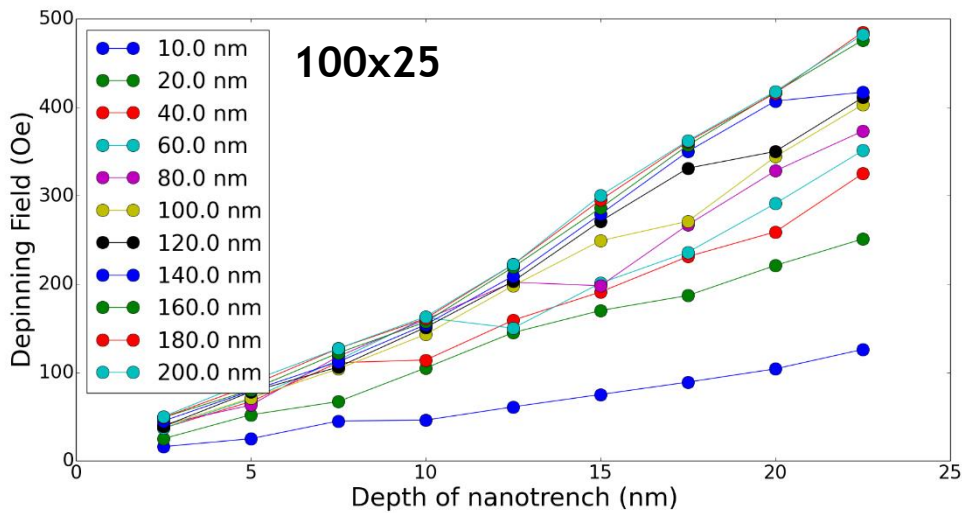


Figure 4.3.13: Triangular nanotrenches in 100 nm wide, 25 nm thick nanowire - Plot of depinning field against nanotrench depth (nm) for various nanotrench lengths.

Lines are to guide the eye.

Figure 4.3.12 contains the plot of depinning field against the length at the nanowire surface for triangular nanotrenches. The general trends are very similar to that found in the square nanotrench case. In all cases the depinning field increases and then saturates at around 100 nm in length. The same can be said when plotting against depth as found in figure 4.3.13. The trends are approximately linear at all depths, as found in the square nanotrench case.

It is worth noting the volatility of the data, especially noticeable in figure 4.3.12. The noise in the curves are particularly noticeable in the region of shorter nanotrench lengths. This is most likely due to the finite cell nature of the simulations. The nanowire is split up into cuboidal cells, this makes it not possible to code the model such that the slopes of the nanotrench are perfectly straight. As such, the models tested here are an approximation of a triangular notch. How accurate these approximations are dependent on the size of the cells used. Smaller dimensions used allows a more accurate approximation of a triangular cross-section. Following this logic, theoretically, a smaller cell size should result in a smoother trend when plotting the data. In order to test this, a particularly noisy row of data was selected from figure 4.3.12. Further simulations were carried out on the same size nanotrenches, but using smaller cell sizes in the x and z dimensions. The y dimension was not adjusted as the nanotrench cross-section occurs in the x-z plane, therefore the y component of the cell size will not affect the shape of the

nanotrench. Figure 4.3.14 shows the results for the x cell size fixed at 5 nm, 2.5 nm and 1 nm, whilst 4.3.15 compares the z dimension at 2.5 nm and 1 nm.

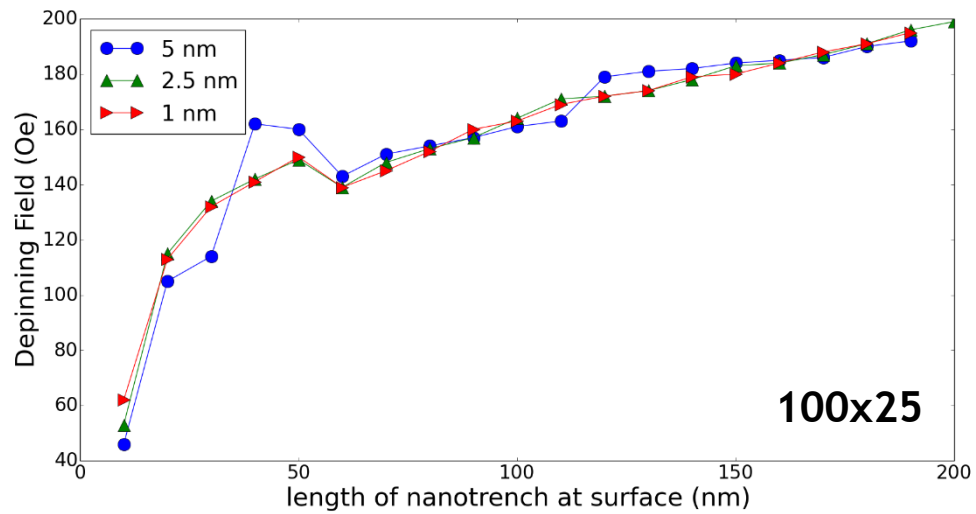


Figure 4.3.14: Plot of depinning field against length at the surface for triangular nanotrenches for different x cell sizes. Results found for 10 nm deep nanotrench in a 100 nm wide, 25 nm thick nanowire.

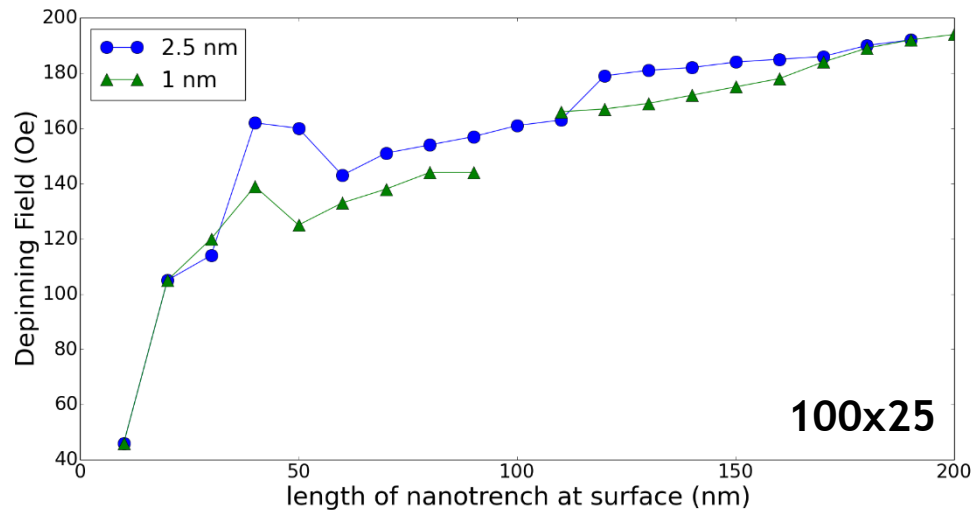


Figure 4.3.15: Plot of depinning field against length at the surface for triangular nanotrenches for different z cell sizes. Results found for 10 nm deep nanotrench in a 100 nm wide, 25 nm thick nanowire.

In both figures it can be seen that the trend becomes smoother with a smaller cell size. This is the case when both the x and z dimensions are reduced. Ideally the smaller sizes would be used for all simulations. However, the reduction in cell size increases the number of cells in the model which causes the computational time to

increase significantly. For the purposes of this study, the overall trend is of importance whilst the exact values found are not.

An energy plot for the 100 nm wide, 25 nm thick nanowire is shown in figure 4.3.16 for the case of a 17.5 nm deep, 200 nm long triangular nanotrench. The general shape of the energies is similar to that of the square nanotrench case. However, it is seen that whilst in the square case the energies stayed constant whilst within the nanotrench, in the triangular case the energies steadily increase. The increase in energy is not a significant amount when compared to the following increase upon exiting the nanotrench, but it is more than in the square case.

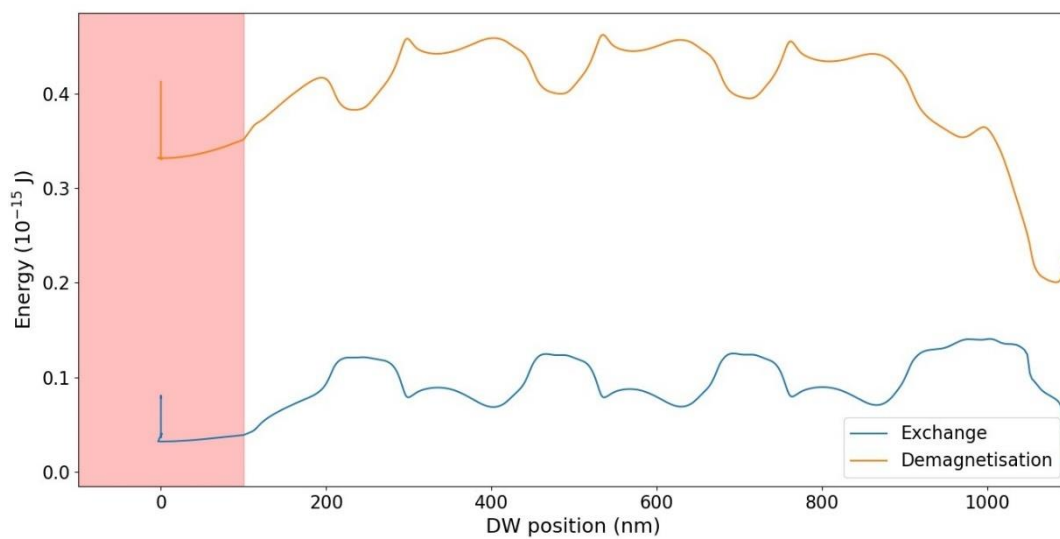


Figure 4.3.16: Energy plot of the exchange and demagnetisation energies for a 100 nm wide, 25 nm thick nanowire containing a 17.5 nm deep, 200 nm long triangular nanotrench. The red shaded region represents the location of the nanotrench.

Triangular nanotrenches were simulated in a 50 nm wide, 10 nm thick nanowire. The dimensions of the nanotrench were varied with depths of 1 nm to 9 nm in steps of 2 nm, whilst the length at the surface was varies initially from 10 nm to 190 nm in steps of 20 nm. Due to the trend that started forming, the range of lengths was later extended to 10 nm to 490 nm in 20 nm steps. The results of these simulations are shown in figures 4.3.17 and 4.3.18.

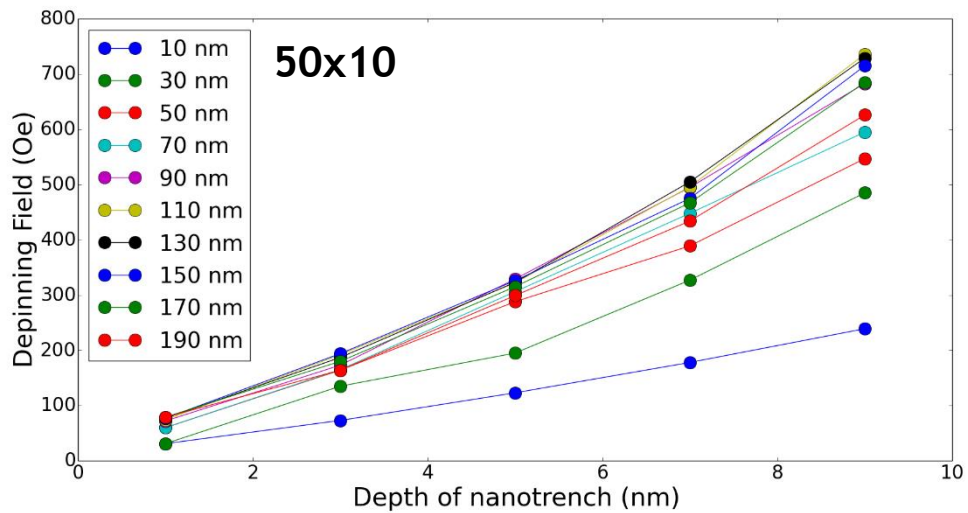


Figure 4.3.17: Triangular nanotrenches in 50 nm wide, 10 nm thick nanowire - Plot of depinning field against nanotrench depth (nm) for various nanotrench lengths. Lines are to guide the eye.

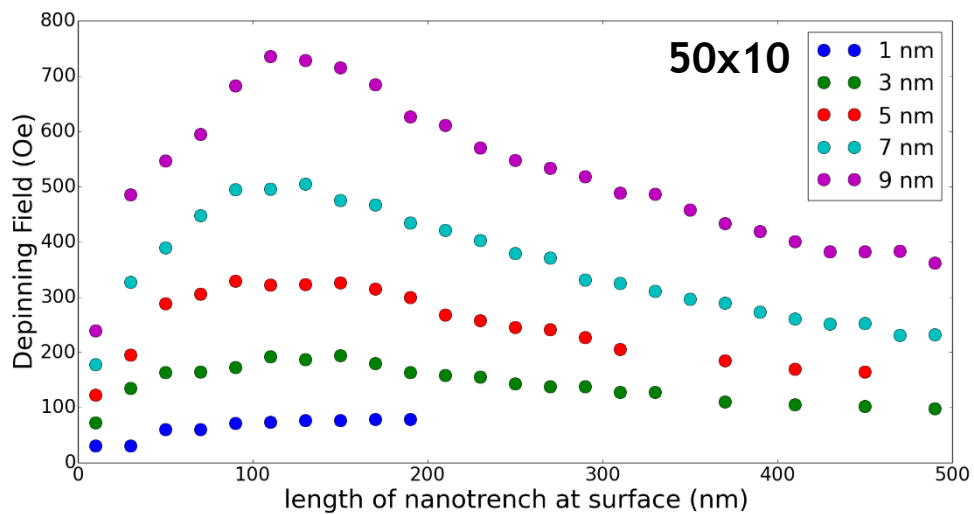


Figure 4.3.18: Triangular nanotrenches in 50 nm wide, 10 nm thick nanowire - Plot of depinning field against nanotrench length at the surface (nm) for various nanotrench depths.

The relationship between the depinning field and nanotrench depth are shown in figure 4.3.17. These results show very similar approximately linear relationships for all nanotrench lengths. However, there appears to be very different results when considering depinning field against nanotrench length. Figure 4.3.18 shows the depinning field initially increases with nanotrench length, up until 100-150 nm. When the length increases beyond this range, the depinning field begins to reduce.

This reduction in depinning field continues up until the end of the range tested of 490 nm.

In an attempt to understand what occurs energetically during this increase and then decrease in pinning strength, energy plots were made for multiple nanotrench lengths for the same depth. Figure 4.3.19 contains plots for the 50 nm wide, 10 nm thick nanowire containing 9 nm deep triangular nanotrenches, with lengths of 50 nm, 110 nm and 310 nm. These data points were chosen as they represent points of lengths less than the peak value, approximately at peak value and a wider value with a weaker depinning field. However, observing figure 4.3.19 shows little variation between the three cases. All show slight increases in energies whilst within the nanotrench, steadily increasing towards the edge. Then increasing significantly once propagating beyond the nanotrench. It is worth noting that the amount of energy increase from the centre to the edge of the nanotrench does increase as the nanotrench length increases.

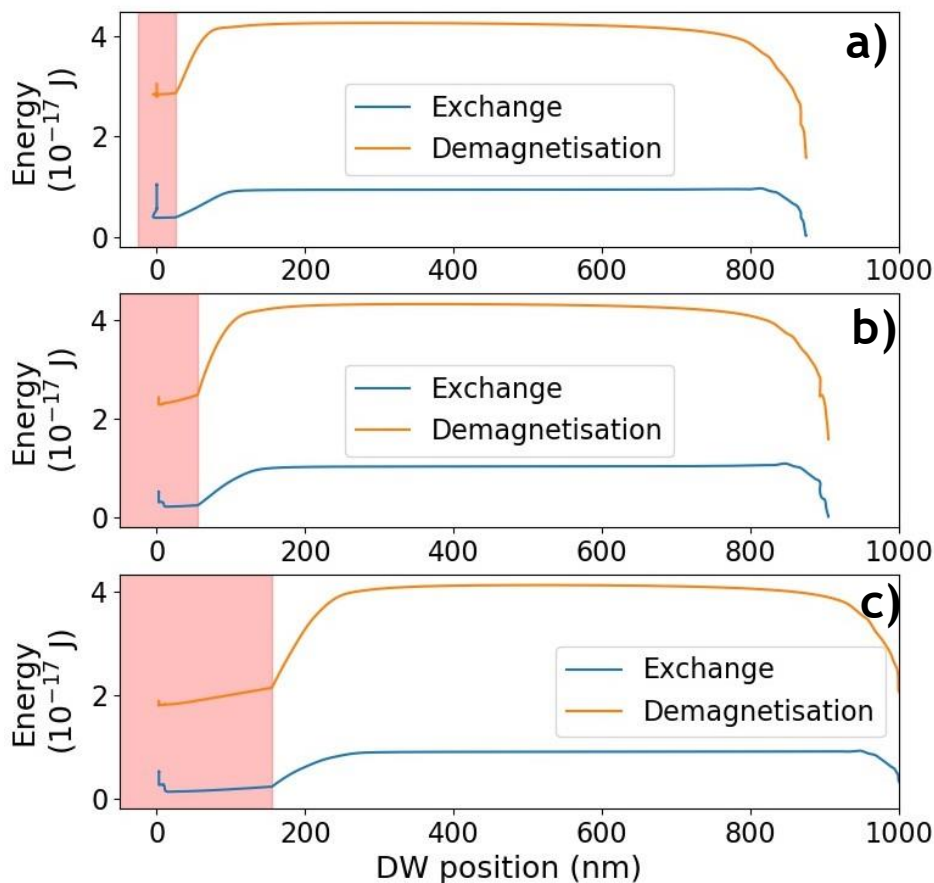


Figure 4.3.19: Energy plots of the exchange and demagnetisation energies for a 50 nm wide, 10 nm thick nanowire containing; a) a 9 nm deep, 50 nm long triangular nanotrench. b) a 9 nm deep, 110 nm long triangular nanotrench. c) a 9 nm deep, 310 nm long triangular nanotrench. The red shaded region represents the location of the nanotrench.

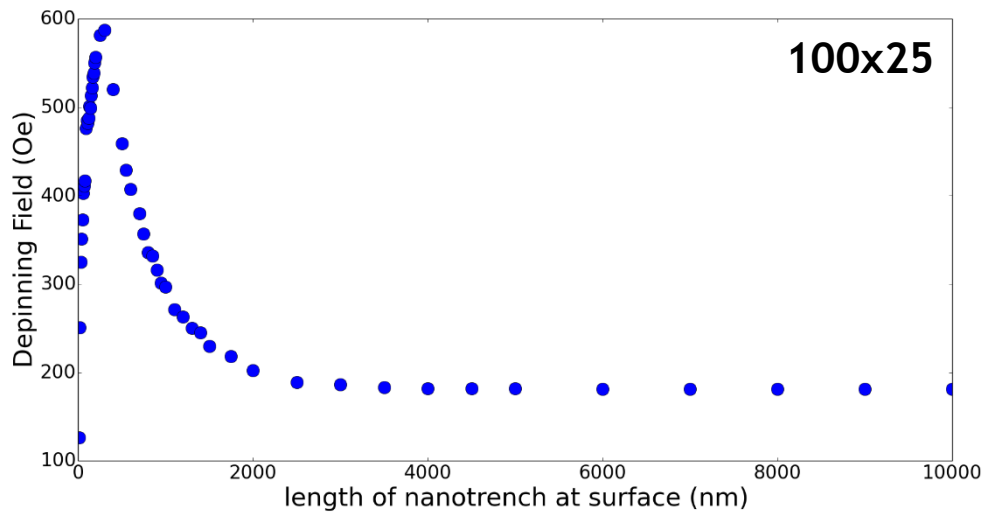


Figure 4.3.20: Results of 22.5 nm deep triangular nanotrenches in 100 nm wide, 25 nm thick nanowire.

The results found in figure 4.3.20 show the depinning field increasing until a length of approximately 300 nm. As the length is increased beyond this point, the depinning field starts decreasing. The field appears to continue to decrease quickly before settling at around 181 Oe for lengths larger than 3 μm .

Again energy plots are made for nanotrench lengths corresponding to various points of the curve found in figure 4.3.20. These are shown in figure 4.3.21. In all four cases, the overall trends look similar to those in figure 4.3.19 for the 50 nm wide, 10 nm thick nanowire case. The energies steadily increase towards the nanotrench edge, before increasing significantly upon propagation. In this instance, the two shortest nanotrenches, 100 nm and 300 nm long, show fluctuations in the energy as the DW leaves the nanotrench. Before reaching peak values, both cases reduce in energy after an initial increase. This is not the case in the 1000 nm and 4000 nm long nanotrenches where the depinning fields are weaker. It is unclear as to whether this feature in the energy plots is related to the pinning strength or not.

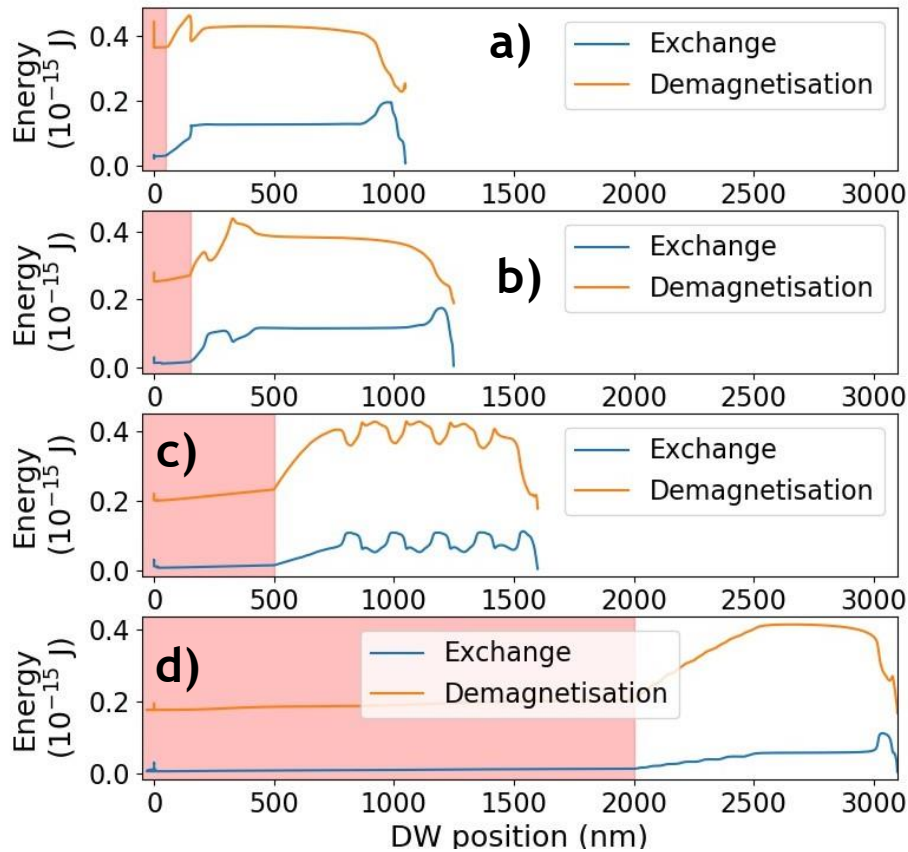


Figure 4.3.21: Energy plots of the exchange and demagnetisation energies for a 100 nm wide, 25 nm thick nanowire containing; a) a 22.5 nm deep, 100 nm long triangular nanotrench. b) a 22.5 nm deep, 300 nm long triangular nanotrench. c) a 22.5 nm deep, 1000 nm long triangular nanotrench. d) a 22.5 nm deep, 4000 nm long triangular nanotrench. The red shaded region represents the location of the nanotrench.

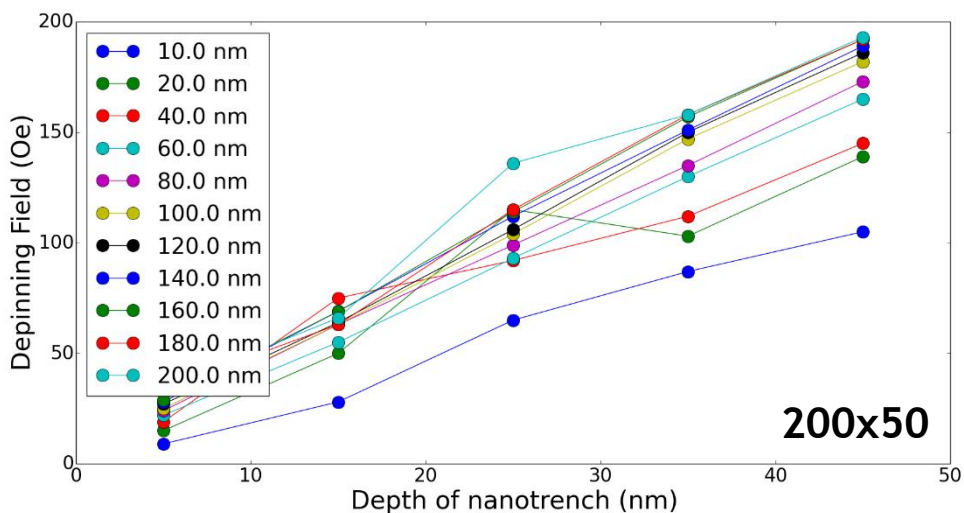


Figure 4.3.22: Triangular nanotrenches in 200 nm wide, 50 nm thick nanowire - Plot of depinning field against nanotrench depth (nm) for various nanotrench lengths.

Lines are to guide the eye.

As in the square nanotrench case, a larger 200 nm wide 50 nm thick wire was used to investigate the interactions between triangular nanotrenches with vortex DWs. The results for depinning field against nanotrench depth are shown in figure 4.3.22. Here it is seen that the general relationship between pinning strength and depth is approximately linear as found in previous cases. This relationship is found at least up to a nanotrench width of 200 nm at the surface.

Figure 4.3.23 shows the results of the depinning field against the length of the nanotrench at the surface of the wire. It is clear that the trends in this plot are very different to those seen previously. At smaller lengths, the general trends are similar to the transverse wall cases, an initial increase followed by a saturation. Then at around 300-400 nm in length, the depinning field begins to increase significantly, before saturating once more. Then beyond a length of around 900 nm, the depinning fields begin to reduce and continue to do so up to the 5000 nm cut off point in the plot. This is a very unexpected trend that required further investigation.

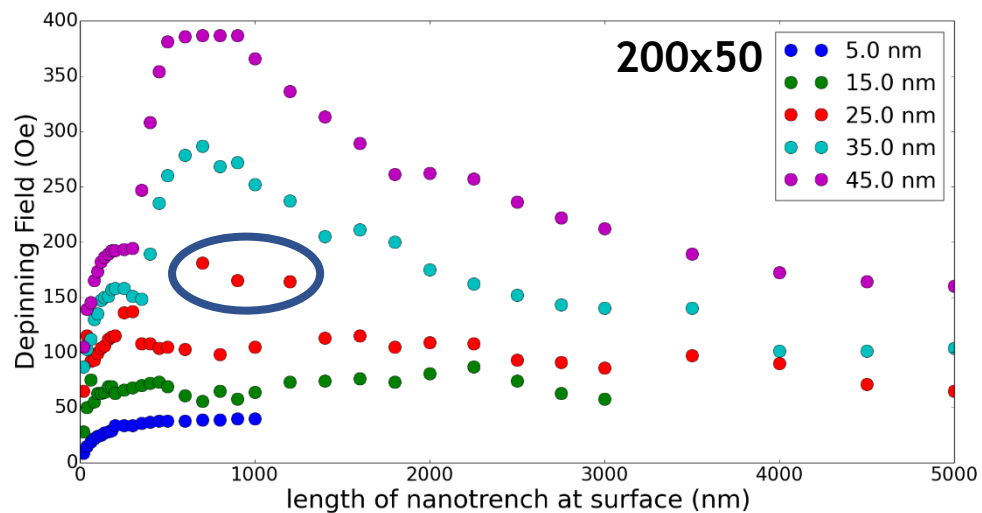


Figure 4.3.23: Triangular nanotrenches in 200 nm wide, 50 nm thick nanowire - Plot of depinning field against nanotrench length at the surface (nm) for various nanotrench depths. Data points within the blue circle indicate instances where metastable asymmetric transverse DWs are present.

Within figure 4.3.23, it can be seen that these unusual trends only occur for the two largest nanotrench depths. It is worth noting that the shallowest nanotrench was not simulated for as many data points as deeper ones. This was due to a 5 nm deep nanotrench only being 1 cell deep. Therefore the actual simulated nanotrench was square. Increasing the nanotrench length further would not have provided any further information. The two shallowest depths continue to demonstrate a similar

trend to the transverse wall case. The depinning field initially increases, then becomes saturated, before gradually decreasing in value as the length continues to increase. The 25 nm deep trend shows a trend that is almost a combination of both cases. The overall trend matches those of the two shallowest cases, whilst there are some data points amongst the trend that stand out. These are highlighted within the circle in figure 4.3.23.

The answer to the differences in depinning field was found when observing the DW structure during the simulations. Whilst in most cases throughout the 25 nm trend vortex DWs formed, the simulations corresponding to the outliers showed a form of asymmetric transverse wall. This metastable asymmetric transverse wall is demonstrated in figure 4.3.24. In the instances where this DW occurs, the corresponding depinning field increases significantly. When assessing the simulated results for the 35 nm and 45 nm deep trends, it was found that similar DWs were forming early in the simulations. Thus causing the depinning fields to drastically increase.

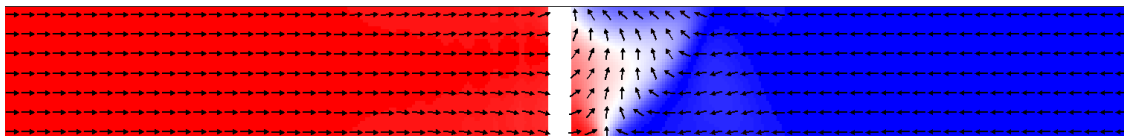


Figure 4.3.24: Example of asymmetric transverse DW occurring beneath a 45 nm deep, 700 nm long triangular nanotrench in a 200 nm wide, 50 nm thick nanowire.

To give a possible explanation for this, it is required to reconsider the phase diagram produced and discussed in section 4.1. When material is removed from the nanowire via the introduction of a nanotrench, the effective size of the nanowire in that region is reduced. In this case the width of the wire remains the same and only the thickness is altered. Taking the 200 nm wide slice out of the phase diagram data, it is seen that transverse DWs occur for thicknesses below 7 nm, asymmetric transverse DWs occurs in the region 7-17 nm whilst vortex DWs occur for thicknesses of 20 nm or more. For the 25 nm deep nanotrench, the remaining thickness of material is also 25 nm. Whilst this is in the phase diagram region for vortex DWs, it is starting to get close to the phase boundary between vortex and A-TW. This may explain why most cases do provide vortex DWs, but a few cases show this metastable DW instead.

For the deepest two nanotrenches, 35 nm and 45 nm deep, this leaves only 15 nm and 5 nm of permalloy nanowire below the nanotrench respectively. These fall

below the boundary between asymmetric transverse and vortex DWs. This depth does only refer to the centre of the nanotrench, and so does not provide an extended region of the nanowire where there are reduced dimensions. This could provide an explanation as to why vortex DWs still occur for the smaller nanotrench lengths. Once the length of the nanotrench increases sufficiently enough, the gradient of the slope reduces, and so the region of effective reduced dimensions becomes extended. At a shallow enough gradient, the effective local region may become long enough such that the DW whilst forming “sees” a smaller nanowire, thus creating these metastable asymmetric transverse DWs.

These metastable DWs cannot be used in analysis relating specifically to vortex DWs, but it is reasonable to still include the data points as they occur. However analysing the data in relation to vortex DWs cannot be done as vortex DWs have not occurred. The region of smaller lengths below 350 nm can be used in consideration of vortex DWs. As experimental nanotrenches generated in chapter 5 are generally smaller than this boundary, it is reasonable for any further analysis to focus on this region when considering the larger 200 nm wide, 50 nm thick nanowire.

To investigate further, energy plots were made for various nanotrench lengths, corresponding to key portions of the trends found in figure 4.3.23. The nanotrenches included in this figure are all 35 nm deep and 200 nm, 700 nm and 2000 nm long. This corresponds to a vortex DW, a metastable DW at the peak of depinning fields, and a further metastable DW with a weaker depinning field. Clues about the DW structure are found in figure 4.3.23. Figure 4.3.23a shows energy plots very similar to what was observed in the square nanotrench case with a vortex DW. The energies decrease as the DW moves from the centre to the edge of the nanotrench, implying the pinning site acts as a potential energy barrier. However, in figure 4.3.23b the energy plot looks like a hybrid between the two DWs. Within the nanotrench the energy slightly increases as it moves toward the edge. However, upon exiting the nanotrench, the energy drops in value before steadily increasing whilst propagating through the nanowire. This feature is more consistent with a vortex DW. From observing the energy profile, it appears that a metastable DW state closer to a transverse DW is formed within the nanotrench and moves towards the edge. Then once the slope of the nanotrench reaches enough height, the DW changes its structure to transform into a vortex DW which is energetically favourable in a nanowire measuring 200 nm wide and 50 nm thick. As the nanotrench length is drastically increased to 2000 nm, the energy profile looks much closer to a

transverse DW case in figure 4.3.23c. There is a steady increase in energy as the DW moves towards the nanotrench edge. The only unusual feature found in this trend is that the DW appears to temporarily start moving back towards the centre of the nanotrench, before continuing to the edge. This apparent reversal in DW motion may be attributed to the DW changing its configuration whilst moving through the nanotrench, however the profile beyond that point does not resemble a vortex DW case.

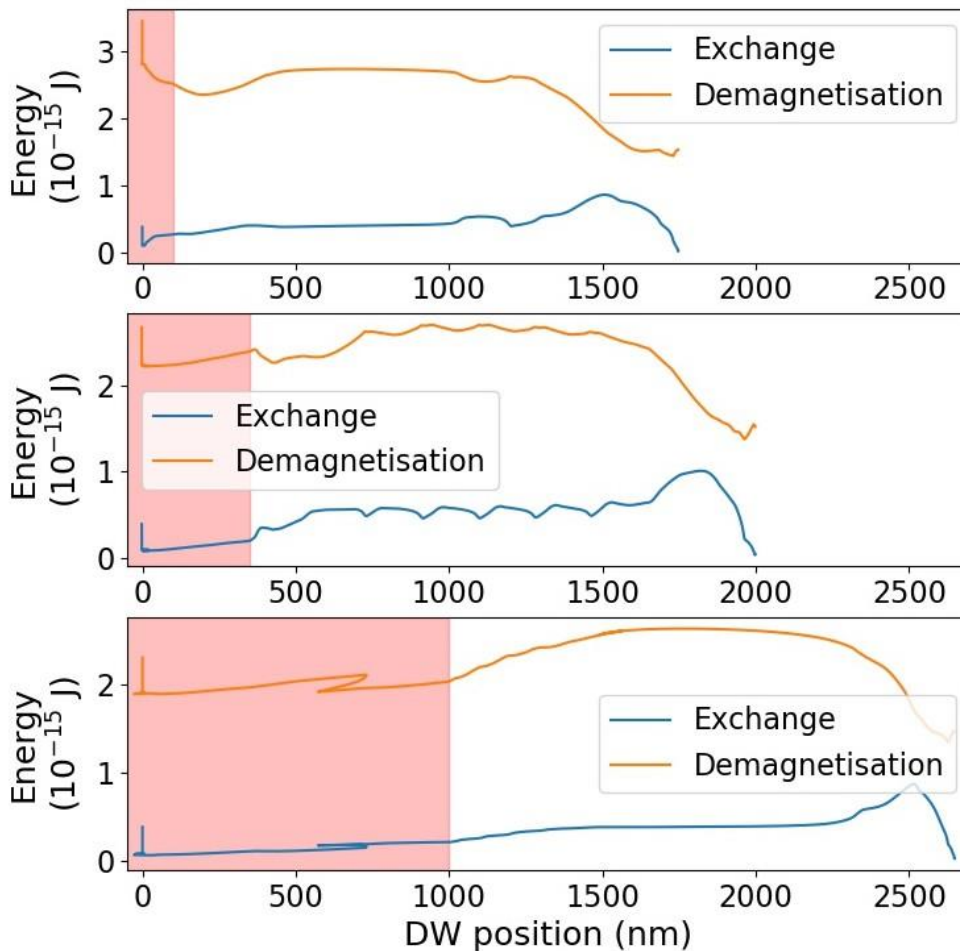


Figure 4.3.25: Energy plots of the exchange and demagnetisation energies for a 200 nm wide, 50 nm thick nanowire containing; a) a 35 nm deep, 200 nm long triangular nanotrench. b) a 35 nm deep, 700 nm long triangular nanotrench. c) a 35 nm deep, 2000 nm long triangular nanotrench. The red shaded region represents the location of the nanotrench.

As done in the case of square nanotrenches, simulations were conducted to assess the effects of the DW chirality on the pinning strength. Again a 50 nm wide, 10 nm thick nanowire was used with a 5 nm deep, 100 nm long triangular nanotrench for transverse DWs. In the case for vortex DWs a 200 nm wide, 50 nm thick nanowire was used, however two nanotrenches were tested. Both cases have a depth of 25

nm, whilst the lengths used are 100 nm and 200 nm. The same chiralities were tested as in the previous square nanotrench case. The results of these simulations are shown in table 4.2.

Table 4.2: Results of Chirality test for a triangular nanotrench. Transverse DWs produced in 50 nm wide, 10 nm thick nanowire. Vortex DWs produced in 200 nm wide, 50 nm thick nanowire. In the vortex cases, the first values correspond to the 100 nm long nanotrench whilst the second are the results of the 200 nm long nanotrench. Depinning fields given in Oe.

	Transverse		Vortex			
			Clockwise		Anti-clockwise	
	Up	Down	In	Out	In	Out
HtH	327	327	99/115	99/115	98/109	98/108
TtT	327	327	98/115	98/108	108/108	99/108

The transverse DW cases show the same results as in the square case. Regardless of the chirality, the depinning field is the same for this nanotrench. This reinforces the theory that the pinning strengths of vertical nanotrenches are not chirality dependent regarding transverse DWs.

The vortex DW cases is not what was expected. From the previous discussion regarding vortex DW chirality, it would be expected to see a form of dependency between the “in” and “out” cases. However, there is no perceivable trend that can be seen in the results. In order to check this, chiralities are tested for two nanotrench sizes. The shorter nanotrench case only provides a very small depinning field difference of 1 Oe in most cases whilst only one case gives a field 10 Oe more than the others. In the longer case a larger 7 Oe difference is observed, however all of the anti-clockwise cases are grouped close together. There is difference in field values for the clockwise cases, however only the “clockwise out” result is different and is similar in value to the anti-clockwise results. These results show no clear trends and so no definitive conclusions can be made for vortex DW chirality dependency on pinning strength.

4.3.3 Comparison between square and triangular nanotrenches

The previous two sections have presented and discussed results concerning square and triangular nanotrenches separately. In this section all sets of results are directly compared for both cases and any key differences are discussed.

Figure 4.3.26 shows the direct comparison for transverse DWs in a 100 nm wide 25 nm thick nanowire. The overall trends per nanotrench depth are very similar in both

cases. In all trends, the depinning fields increase initially with nanotrench length up to around 100-150 nm. Beyond this point, the depinning fields continue to increase but by much smaller increments as the length increases. The key difference in this case regards the values of the depinning fields. The y-axis in both cases are fixed to the same range for easier comparison. It is clear to see that the square nanotrench cases provide stronger pinning sites when comparing nanotrenches of the same depth. In all cases, the square counterpart requires a larger field in order to depin the DW then the triangular nanotrench.

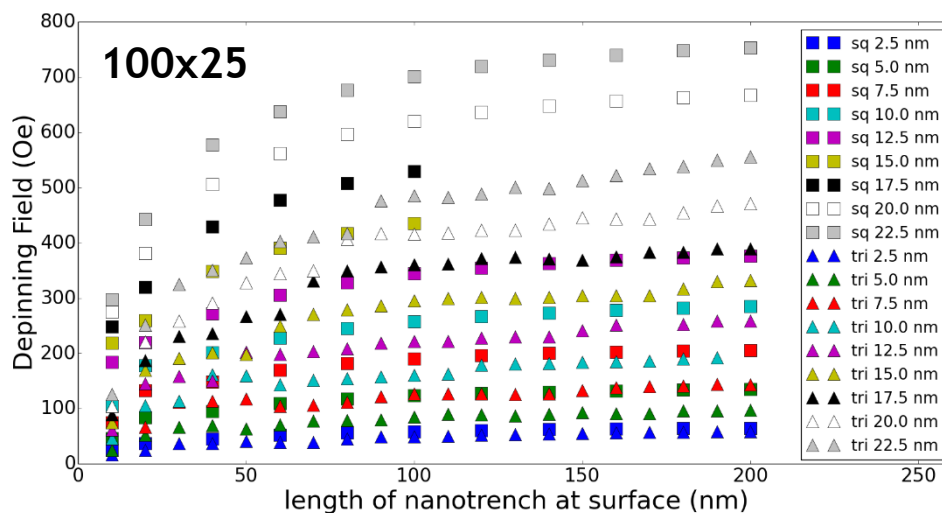


Figure 4.3.26: Depinning field against length of nanotrench for various nanotrench depths for transverse DWs found in a 100 nm wide, 25 nm thick nanowire - Square markers indicate square nanotrench. Triangle markers indicate triangular nanotrench. Markers of the same colour represent nanotrenches of the same depth.

Figure 4.3.27 shows the same comparison as in figure 4.3.26 but for the 50 nm wide, 10 nm thick nanowire. At smaller nanotrench lengths a similar trend is found as in the previous case, the depinning field increases quickly with size before this rate decreases drastically by approximately 100 nm. However, whilst the square nanotrench depinning fields continue to increase very slowly with length, the triangular nanotrenches show a reduction in pinning strength as the nanotrench becomes longer. This shows a key difference in trends for the same nanotrench depth. This gives an initial indication that the shape of the nanotrench influences how DWs will interact with it. It is also worth noting that the triangular depinning fields are always smaller than the square counterparts as in the previous case.

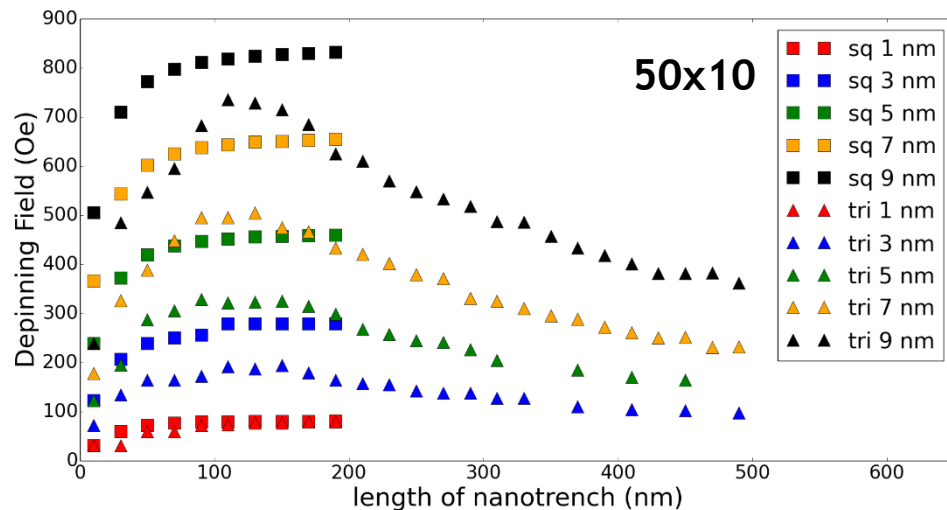


Figure 4.3.27: Depinning field against length of nanotrench for various nanotrench depths for transverse DWs found in a 50 nm wide, 10 nm thick nanowire - Square markers indicate square nanotrench. Triangle markers indicate triangular nanotrench. Markers of the same colour represent nanotrenches of the same depth.

Finally figure 4.3.28 displays results regarding vortex DWs in a 200 nm wide, 50 nm thick nanowire. When considering the shorter lengths region in the triangular case, it is clear that the trends between the square and triangular cases are very similar. As in the other nanowires, the triangular nanotrenches do not pin as strongly as the square counterparts, but the overall shape of the trends match closely. This plot only shows the shortest nanotrench lengths. The datasets at larger lengths are effected by the presence of metastable DWs. However the 15 nm deep and 25 nm deep nanotrench sets do show depinning fields begin to gradually decrease with increased length.

Whilst these comparisons give an indication of any differences in pinning strength between the square and triangular nanotrenches, it does not give a complete picture. Comparing the lengths of each nanotrench for a given depth is not an equal comparison to make. This concerns the fact that the length quoted for the triangular nanotrenches is the length at the nanowire surface. Therefore the total amount of material removed from the nanowire will be half of the volume of a square nanotrench of the same length. In order to probe this further, figures 4.3.29, 4.3.30 and 4.3.31 show the depinning fields for all three nanowires plotted against the cross-sectional area of the nanotrench. This makes direct comparisons much easier with regards to removing the same amount of material to create a pinning site.

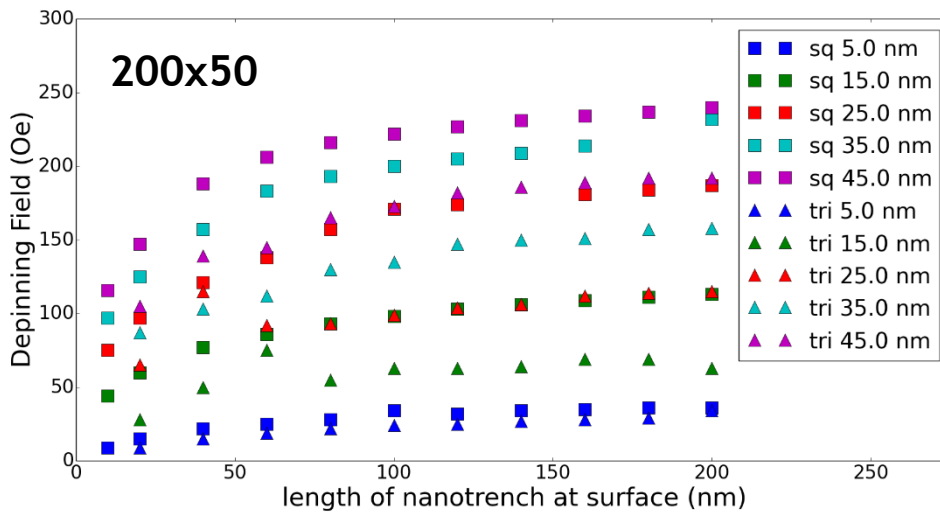


Figure 4.3.28: Depinning field against length of nanotrench for various nanotrench depths for vortex DWs found in a 200 nm wide, 50 nm thick nanowire - Square markers indicate square nanotrench. Triangle markers indicate triangular nanotrench. Markers of the same colour represent nanotrenches of the same depth.

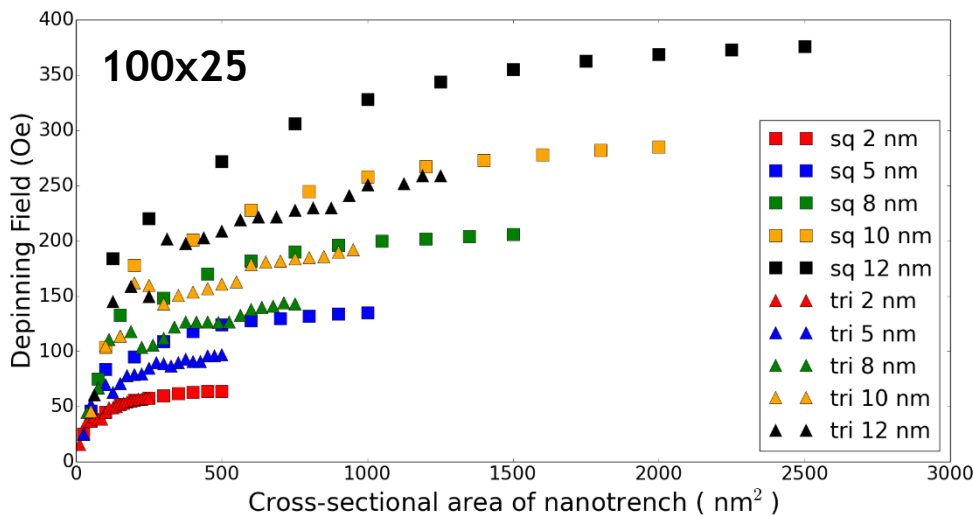


Figure 4.3.29: Cross-sectional area comparison of nanotrenches in a 100 nm wide, 25 nm thick nanowire. Square nanotrenches represented by \square with triangular nanotrenches are represented by Δ . Trends of the same colour correspond to nanotrenches of the same depth.

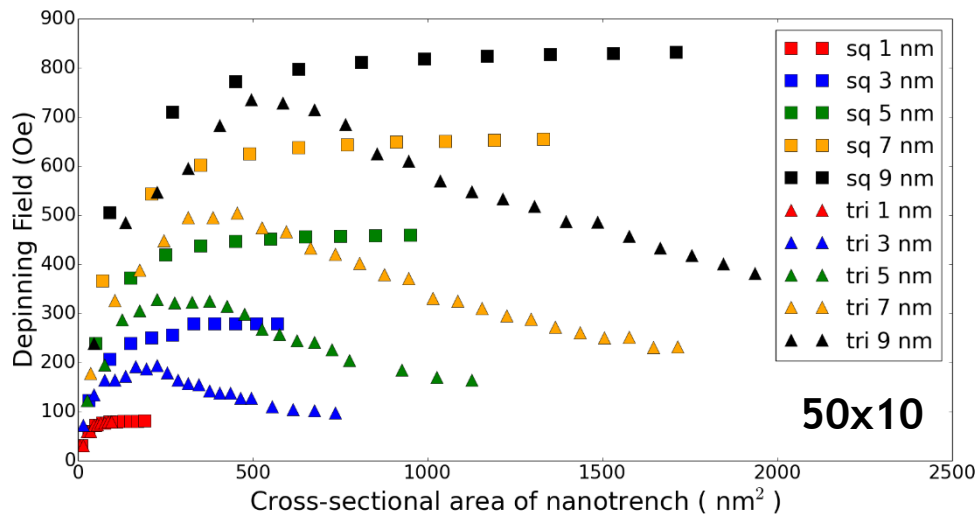


Figure 4.3.30: Cross-sectional area comparison of nanotrenches in a 50 nm wide, 10 nm thick nanowire. Square nanotrenches represented by \square with triangular nanotrenches are represented by Δ . Trends of the same colour correspond to nanotrenches of the same depth.

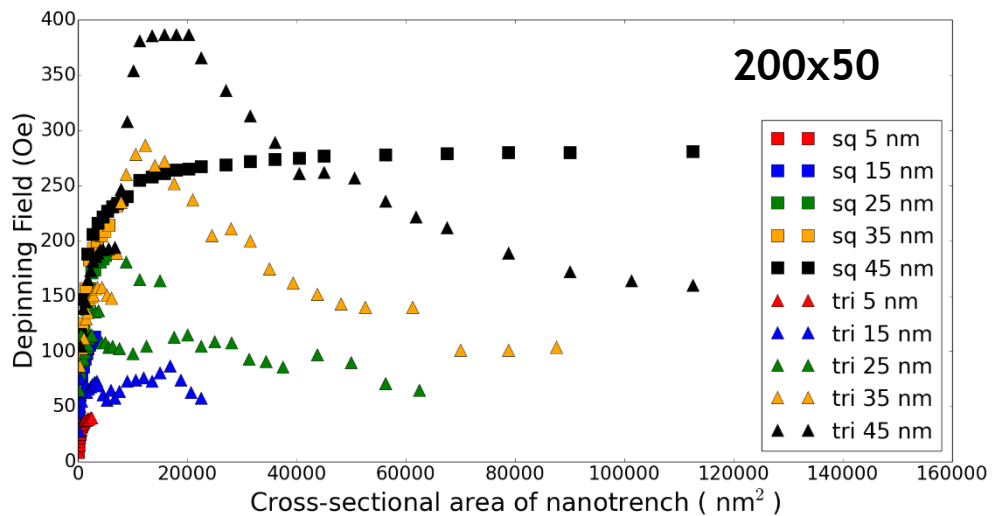


Figure 4.3.31: Cross-sectional area comparison of nanotrenches in a 200 nm wide, 50 nm thick nanowire. Square nanotrenches represented by \square with triangular nanotrenches are represented by Δ . Trends of the same colour correspond to nanotrenches of the same depth.

The general trends shown in figures 4.3.29, 4.3.30 and 4.3.31 match those found when comparing depinning fields against the nanotrench length. In most cases it is shown that the depinning fields for triangular nanotrenches are lower than square nanotrenches of the same volume. The exceptions to this are found in figure 4.3.31

were the asymmetric transverse DWs result in significantly higher depinning fields, leads to the false result that the triangular cases pin more strongly than the square counterparts. This is an unfair comparison due to the presence of different DW structures. Although, even with the presence of asymmetric transverse DWs, at larger nanotrench lengths and so larger cross-sectional areas, the depinning field still reduces below the those in the square case. These results indicate that the shape of the material removed has a larger influence on a site's pinning strength than purely its volume.

To assess the important factors of pinning site shape, it is key to consider the geometry of a nanowire from the point of view of a DW. As the DW propagates through the nanowire along the x-axis, variations in the y-z plane contribute to trapping a DW. In previously studied lateral notches, it is the y-dimension that is altered by either increasing or decreasing it. In this study, vertical nanotrenches are considered and so it is the z-dimension that it altered. In the case of a square nanotrench, as a DW moves along the wire, it experiences a sudden step-change in the z-dimension at a given x co-ordinate. In the case of a triangular nanotrench, there is not a sudden change, more that the z-dimension of the nanowire gradually decreases as the DW moves along the x-axis. This gradual change as opposed to a sudden step-change alters the potential energy landscape of the pinning site.

4.3.4 Angular dependence of triangular nanotrenches

With the gradual change in the z-dimension, another variable that can be considered for analysis is the gradient of the nanotrench walls. This is not something that is a factor when considering a square nanotrench. In this section, the data previously presented will be re-assessed by plotting the depinning field against the angle between the nanotrench wall and the x-axis. This means that a vertical wall as in the square nanotrench case will be considered an angle of 90° whilst very wide relatively shallow nanotrenches will have walls with small angles. The schematic demonstrating this is shown in figure 4.3.11.

The results for the three nanowires used in this study are shown in figures 4.3.32, 4.3.33, 4.3.34, 4.3.35. It is worth noting that for that the trends found in these figures required data to be obtained for small angles. With the depths of the nanotrenches tested, the length at the surface of the nanowire had to be made relatively very large to probe angles below 10° . Whilst this does not represent any pinning site that would realistically be created in practice, it was important to

include these data points to fully understand the relationship between the wall gradient and the pinning strength.

Figures 4.3.32 and 4.3.33 show data taken for the 100 nm wide, 25 nm thick nanowire plotted against angle. In this plot, nanotrenches were only simulated up to a surface length of 200 nm. This does not result in very small angles for the deepest nanotrenches as only half of this length contributes to the angle of the nanotrench wall. Only considering this data, it appears that the depinning field continues to increase as the angle of the nanotrench wall decreases. However, figure 4.3.32 shows data for a 22.5 nm deep nanotrench, but for surface lengths up to an extreme value of 10 μm . This allows angles as small as 0.26° to be simulated. It is seen that the depinning field begins to fall quickly as the angle is decreased further. The field values drop from 587 Oe at 8.5° to 189 Oe by 1.0° and levelling at 181 Oe for smaller angles. This indicates that reducing the wire dimensions still acts as a pinning site despite the change in thickness being very small when compared with the nanotrench length. However, as the strength of the site is heavily reduced, in practice thermal fluctuations could overcome the pinning site rendering it not viable to act as an artificial pinning site. As discussed previously, this is not a realistic scenario to occur as the nanotrench length to reduce the angle sufficiently is at least $2.5 \mu\text{m}$ whilst only reaching a depth of 45 nm at its centre.

Due to the OOMMF software using cuboidal cells to construct the nanowire, the sloped sides of the nanotrench are in fact an approximation as discussed previously. As a test of the accuracy, the 8° case in figure 4.3.25 was considered. The cell size in these simulations was $5 \times 5 \times 2.5 \text{ nm}^3$. The dimensions of the nanotrench in this instance was 300 nm long and 22.5 nm deep. When calculating the angle, only half of the length is used and so the effective length becomes 150 nm. In terms of cells, this makes the slope consist of 30 cells along the length and 9 cells deep. To assess the angle row to row, the number of cells creating the step change needs to be considered. The base of the nanotrench always consists of at least 1 cell either side of the centre. So over the top 8 rows, 29 cells need to be covered. This on average makes the average cells per row to be 3.625. As these cells cannot be split, it leaves the step change to be either 3 or 4 cells change per row. This gives the dimensions of the step change to be either 15 nm long and 2.5 nm deep, or 20 nm long and 2.5 nm deep. These dimensions lead to angles of 9.46° and 7.12° respectively. This leads to a reasonably good approximation of the shape and angle in the triangular nanotrench case.

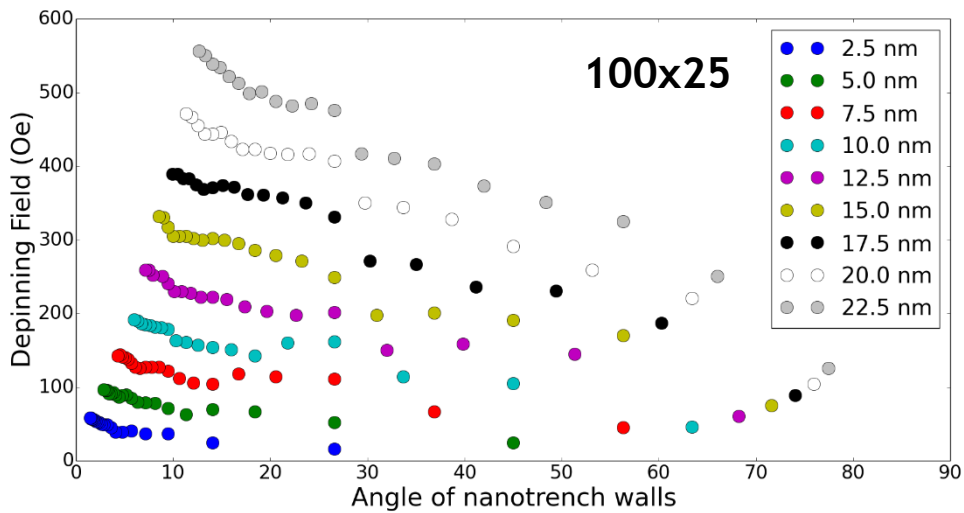


Figure 4.3.32: Triangular nanotrenches in 100 nm wide, 25 nm thick nanowire - Plot of depinning field against angle of nanotrench wall for various nanotrench depths.

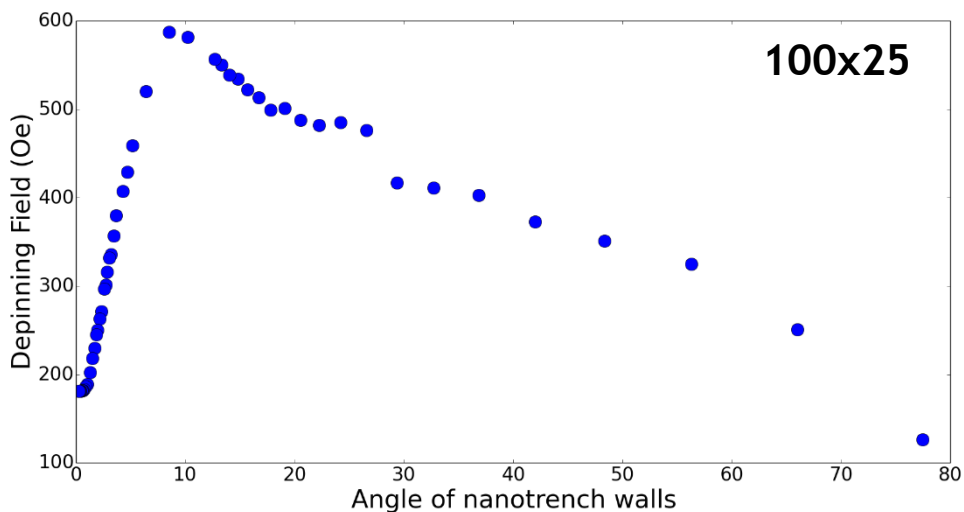


Figure 4.3.33: Plot of depinning field against nanotrench length at the surface (nm) for a 22.5 nm deep triangular nanotrench in a 100 nm wide, 25 nm thick nanowire.

The trend found in figure 4.3.34 is replicated in the other two nanowires simulated. The smallest angles are not reached in these plots as in figure 4.2.33, but the overall trend is still shown. In the 50 nm wide, 10 nm thick nanowire the depinning field drops from 736 Oe at 9.3° to 362 Oe by 2.1° for the deepest 9 nm depth simulated.

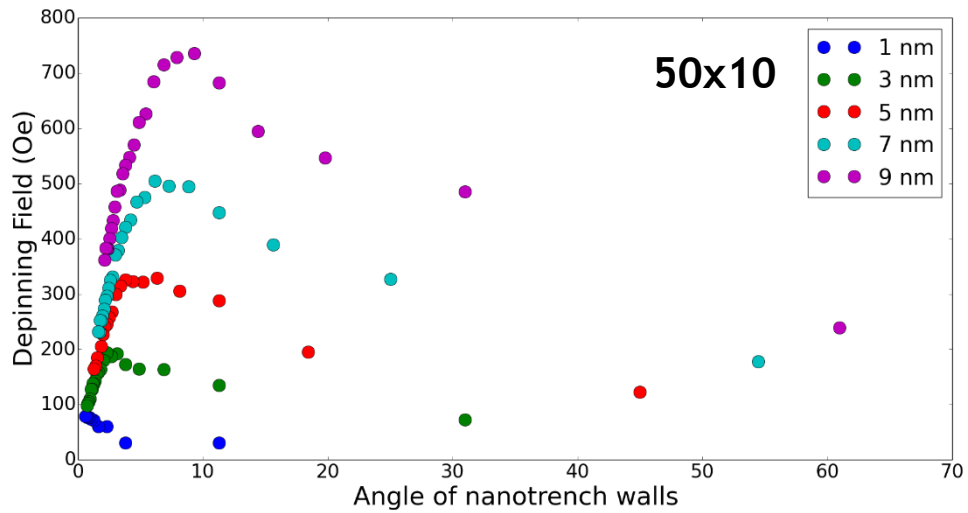


Figure 4.3.34: Triangular nanotrenches in 50 nm wide, 10 nm thick nanowire - Plot of depinning field against angle of nanotrench wall for various nanotrench depths.

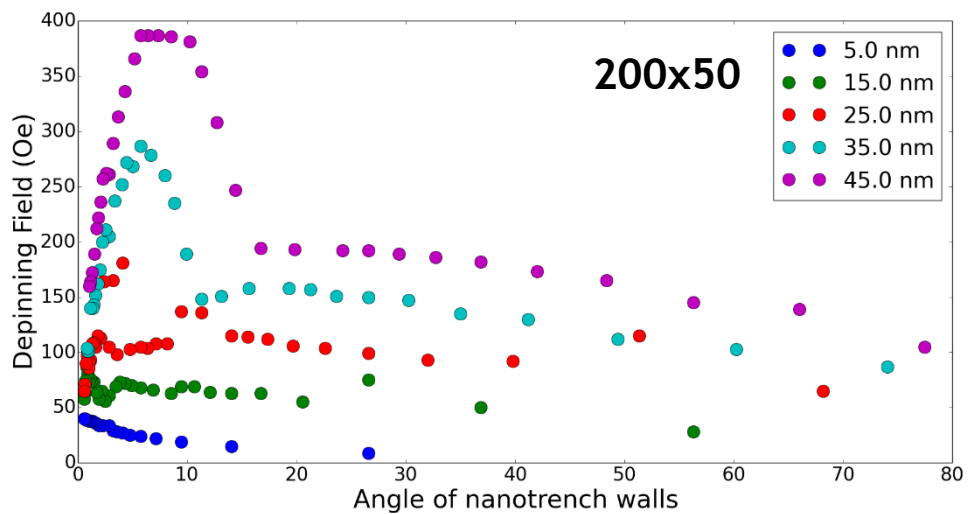


Figure 4.3.35: Triangular nanotrenches in 200 nm wide, 50 nm thick nanowire - Plot of depinning field against angle of nanotrench wall for various nanotrench depths.

The results are affected by the occurrence of the asymmetric transverse DWs discussed earlier in section 4.3.3. Due to this it is not possible to give an accurate angular dependence for vortex DWs. The shallower trends do show the depinning field to decrease at smaller angles, but the overall shape of the trend does appear to be different. For the deeper cases, the trends become similar to those observed in the transverse DW results at the smaller angles, corresponding to longer nanotrenches.

A possible explanation for the decrease in pinning strength regards how the wall gradient affects the potential energy profile of the nanotrench. As discussed previously, the section of the nanowire where the nanotrench is located can act as a potential well, barrier or a combination of the two [35], [98]. It is found, in this study and previous[123], that in the transverse DW case, the nanotrench acts as a well, whilst it is a barrier for vortex DWs. As the triangular nanotrench still pins DWs, it still acts as a well/barrier. Introducing gradual changes in the nanowire dimensions alters the shape of such wells or barriers. The depth or height reduction could be explained as there is less volume where the nanowire becomes its narrowest. A square nanotrench reduces the nanowire to the smallest size across its length, whereas a triangular nanotrench only cuts the material to that size at the centre. This would make it easier for a DW to escape the deepest part of the trap, implying a reduction in depth/height of the potential well/barrier.

Such a theory would provide an explanation for the overall reduced pinning strength when compared with a square nanotrench, but it does not necessarily address the reducing depinning fields despite removing more material in the case of extremely long triangular nanotrenches. As the size of the nanowire changes gradually in these cases, the width of the potential well/barrier becomes much wider spatially. This would alter the spatial energy gradient such that it requires a smaller change in energy for the DW to move a larger distance further into or across the well/barrier. This would make it easier for the DW to propagate along the wire with a weaker applied field. This agrees with the relationship between force and potential energy. With potential energy varying spatially, the required force is $F(x) = -dU/dx$ where U is the potential energy. This makes the required force equal to the spatial gradient of the potential energy. In the triangular nanotrench case, the depth/height of the potential well/barrier does not change as the physical depth is the same. However, widening the nanotrench increases the range of which such depth/heights vary, thus reducing the gradient. This corresponds to a reduction in the amount of force needed to move the DW by applying an external field. These results also show agreement with Goolaup *et al.*[105] despite that study focusing on lateral notches.

To assess the data further, slices of the dataset can be taken for nanotrenches where the walls are at the same angle for different depths. This is comparable to plotting against length for various depths in the square case. Figure 4.3.36 shows the plotted data relating to the 100 nm wide, 25 nm thick nanowire.

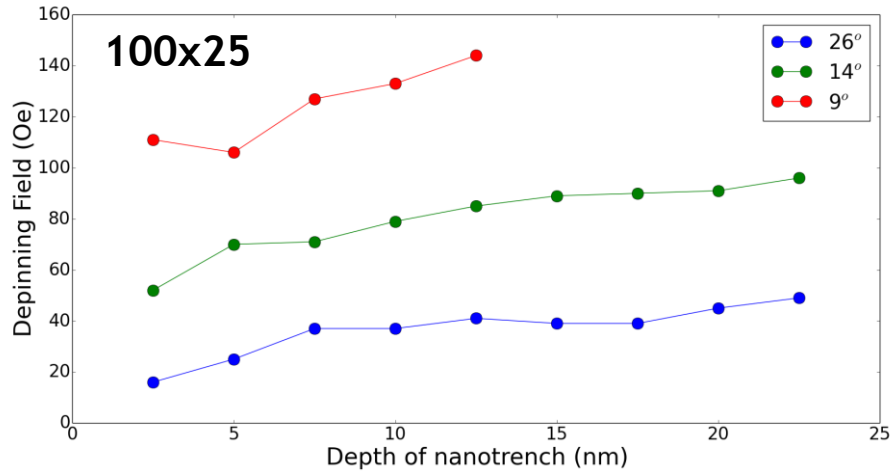


Figure 4.3.36: Triangular nanotrenches in 100 nm wide, 25 nm thick nanowire - Plot of depinning field against depth of nanotrench wall for various nanotrench wall angles. Lines are to guide the eye.

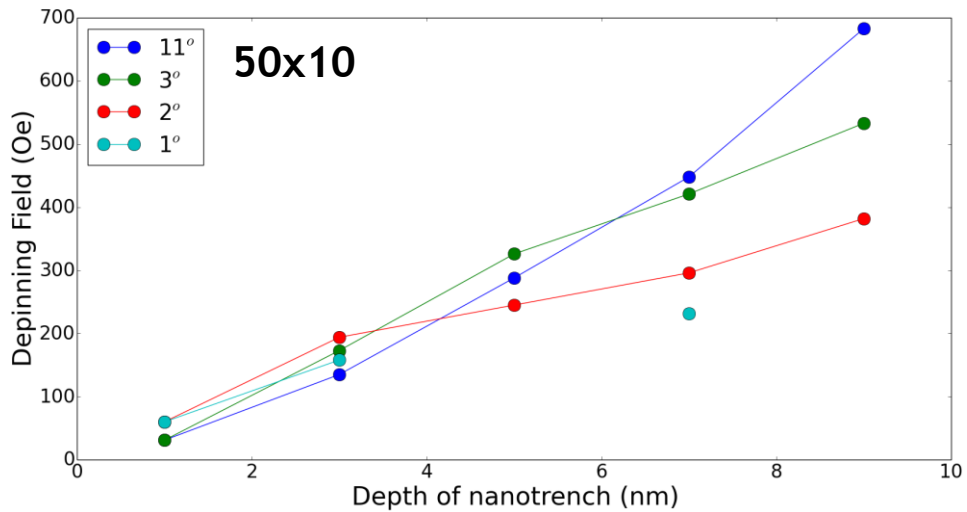


Figure 4.3.37: Triangular nanotrenches in 50 nm wide, 10 nm thick nanowire - Plot of depinning field against depth of nanotrench wall for various nanotrench wall angles. Lines are to guide the eye.

When plotted in this way, the data more resembles the plots produced when comparing depinning fields to the depth for fixed lengths. In this case the fields increase with a reduction in angle. However, for this nanowire, the main dataset did not extend into the region where the depinning field began to reduce with an increase in length. Therefore the smaller angles in this case correspond to the larger nanotrenches and so the depinning field is likely to be larger purely due to more

material being removed. Figure 4.3.37 shows the same data plot for the 50 nm wide, 10 nm thick nanowire.

In this case the trends are still approximately linear and so are comparable to the depinning field against depth cases. In figure 4.3.37, it can be seen that the gradient of these trends reduce as the angle is decreased. At smaller nanotrench depths, there is little difference in the depinning fields. As the depth increases, this range grows and the smallest values are attributed to the smallest angles. This result gives a further indication that creating a triangular nanotrench with flatter gradient walls will pin DWs weaker than those with steeper walls.

Figure 4.3.38 contains the results relating to vortex DWs in the 200 nm wide, 50 nm thick nanowire. In the case of the 27° gradient, the trend agrees with the previous results as it shows an approximately linear increase in depinning field with the depth of the nanotrench. The rate of increase is smaller than those found in the smaller nanowires, but this also agrees with the previous results when considering nanotrenches of the same length and varying the depth. For the shallower 14° dataset, the results are much more inconclusive. This is most likely affected by the issue regarding the presence of asymmetric transverse DWs.

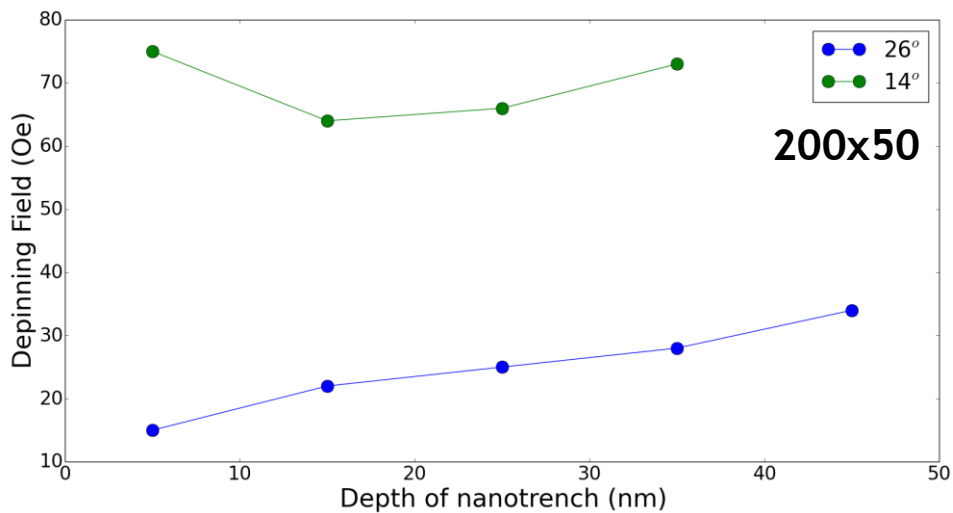


Figure 4.3.38: Triangular nanotrenches in 200 nm wide, 50 nm thick nanowire - Plot of depinning field against depth of nanotrench wall for various nanotrench wall angles. Lines are to guide the eye.

4.3.5 Trapezoidal nanotrench

Trends observed so far when discussing wall angle have shown smaller depinning fields at larger angles, however this is not a true reflection of how larger wall angles

affect a site's pinning strength. This is due to the fact that these larger angles represent very narrow nanotrenches where there is only a small amount of material removed from the nanowire. In particular, it corresponds to the region where the nanotrench length is below 100 nm and so the depinning fields can change drastically with a change in size.

In order to neutralise this issue and create a more representative trend for wall angles, a trapezoidal nanotrench was introduced. The basic idea is to start with a square nanotrench that is large enough that increasing its length will not cause a significant difference in the depinning field. From this starting point, the nanotrench will be expanded by only changing the angle of the sidewalls whilst keeping the same central region. As only increasing the amount of material removed as a square nanotrench does not make any significant changes to the depinning field, any changes observed should be a result of the angle of the sidewalls. A schematic of this is shown in figure 4.3.39.

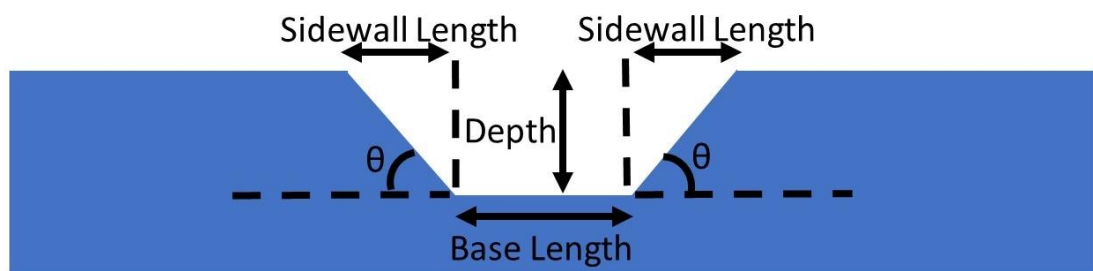


Figure 4.3.39: Schematic demonstrating dimensions associated with a trapezoidal nanotrench

Simulations have been conducted for the 50 nm wide, 10 nm thick nanowire (corresponding to transverse DWs) and the 200 nm wide, 50 nm thick nanowire (corresponding to vortex DWs). In the transverse DW case, the initial nanotrench used a base length of 150 nm long and was 9 nm deep. The deepest possible case was used in order to allow data points corresponding to larger angles. The length of the nanotrench at the nanowire surface is increased in order to reduce the wall angle. As this involves removing more material from the nanowire, an equivalent dataset has been produced by using a square nanotrench and increasing the length such that approximately the same total material has been removed. This allows comparisons to be made on the shape of the nanotrench rather than any other factors. The results of this study are shown in figures 4.3.40 and 4.3.41.

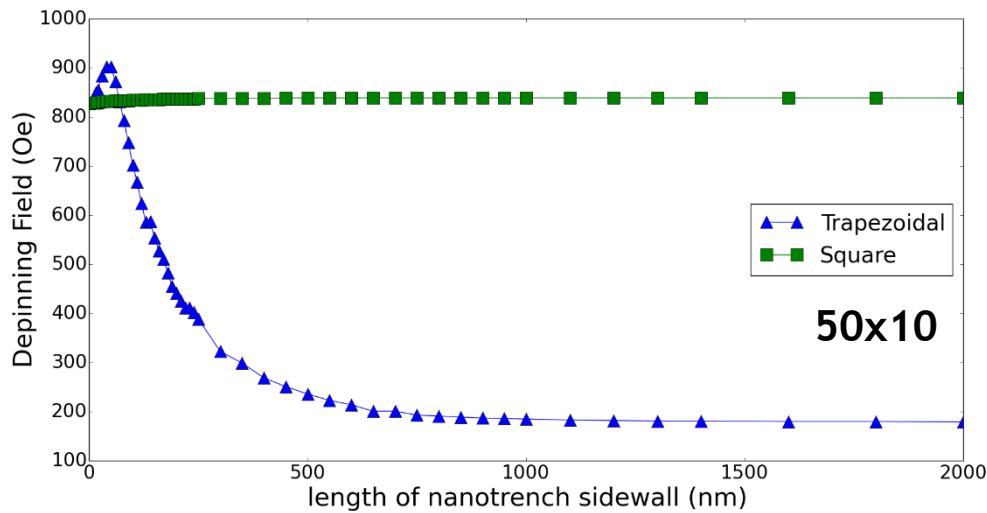


Figure 4.3.40: Trapezoidal nanotrench in a 50 nm wide, 10 nm thick nanowire. Central section of the nanotrench measures 150 nm long, 9 nm deep. This is the 0 nm length data point in both cases - Depinning field against length of nanotrench sidewall. Lines are to guide the eye.

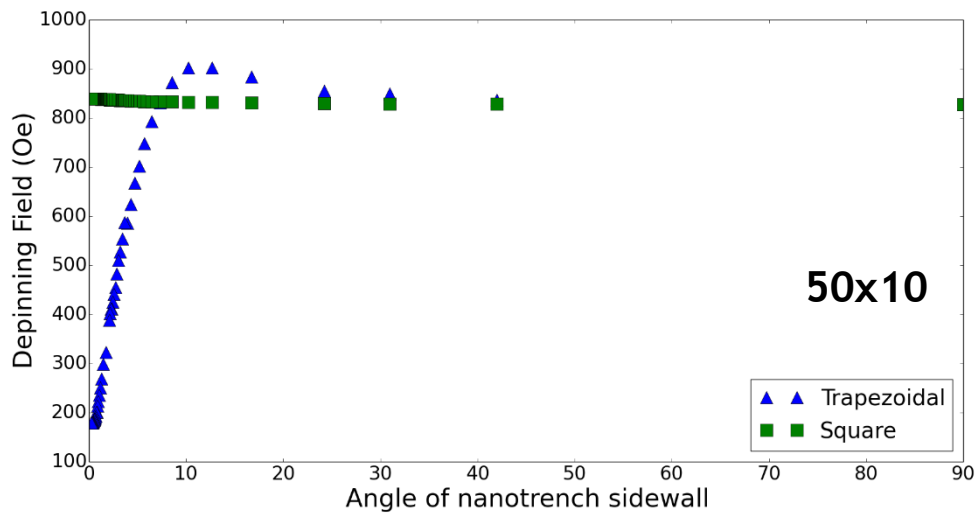


Figure 4.3.41: Trapezoidal nanotrench in a 50 nm wide, 10 nm thick nanowire. Central section of the nanotrench measures 150 nm long, 9 nm deep. This is the 0 nm length data point in both cases - Depinning field against angle of nanotrench sidewall.

As shown in figure 4.3.40, despite increasing the length of the square nanotrench, the depinning field does not increase much further. The case when introducing sloped sidewalls is very different. Interestingly the depinning field initially increases as the sloped walls are added to the central nanotrench. This peaks at a wall length

of 50 nm and an angle of 10° . The depinning fields then begin to quickly reduce as the length is increased, returning to the initial value somewhere between 70 and 80 nm in length. The reduction in depinning field appears to follow a sharp decrease before settling at a value of around 200 Oe by 700 nm and an angle of 0.74° . The pinning strength does continue to decrease as the nanotrench is increased in size, but the change in depinning fields is relatively very small for a much larger change in length. Figure 4.3.41 demonstrated the relationship between the depinning fields and sidewall angle. This plot is in agreement with what was found in the initial triangular nanotrench case displayed in figure 4.3.33. The key angle for this size nanowire appears to be in the region of 10° . In both plots, this is the peak angle at which the nanotrench pins the DW strongest. Angles shallower than this create a weaker pinning site.

Energy plots are made for the trapezoidal nanotrench, these are found in figure 4.3.42. It is seen that the transverse DWs behave the same as beneath a regular square nanotrench whilst beneath the trapezoidal base. Once the DW leaves the base, the energies begin to increase throughout the slope of the trapezium. The trends shown are not distinctly different from those observed in the previous square and triangular nanotrench cases. As such, the plots do not provide any clear answer as to the explanation of why the depinning fields reduce with increased slope width.

In order to test vortex DWs, a relatively longer but shallower initial nanotrench had to be used. This was to ensure that the DW initialising beneath the nanotrench would form a vortex DW and not a transverse DW. The starting nanotrench measured at 500 nm long, 30 nm deep in a 200 nm wide, 50 nm thick nanowire. The results are shown in figure 4.3.43.

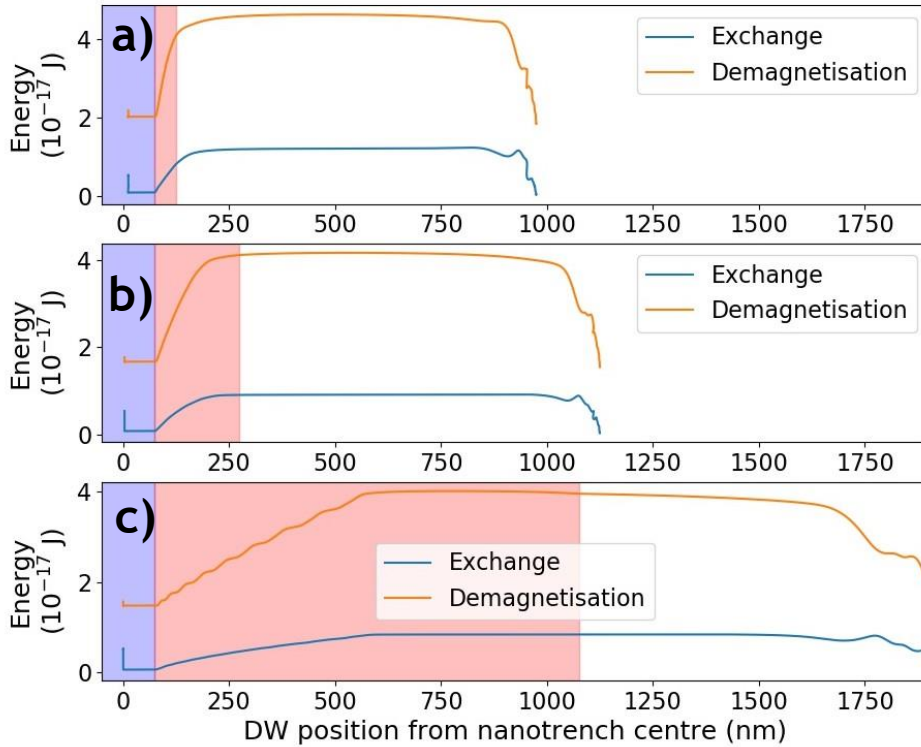


Figure 4.3.42: Energy plots showing exchange and demagnetisation energies for DW position in a a) 50 nm wide, 10 thick nanowire containing; a) trapezoidal nanotrench, 9 nm deep with a central length of 150 nm and a slope length of 50nm. b) trapezoidal nanotrench, 9 nm deep with a central length of 150 nm and a slope length of 200nm. c) trapezoidal nanotrench, 9 nm deep with a central length of 150 nm and a slope length of 1000nm. Blue shaded regions represent location of trapezoidal base, whilst red regions represent location of trapezoidal slopes.

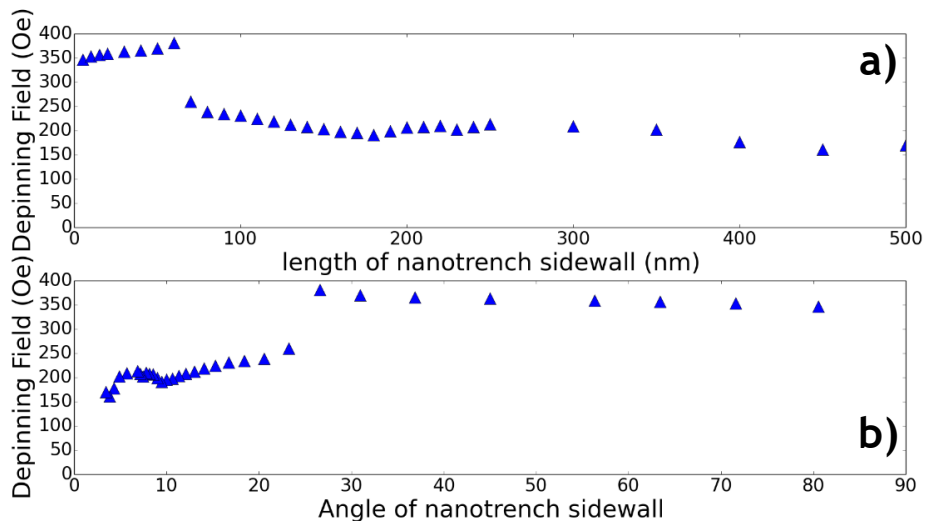


Figure 4.3.43: Trapezoidal nanotrench in a 200 nm wide, 50 nm thick nanowire. Central section of the nanotrench measures 500 nm long, 30 nm deep. a) Depinning field against length of nanotrench sidewall. b) Depinning field against angle of nanotrench sidewall.

As opposed to the triangular nanotrench case, all of the data points presented in figure 4.3.43 are representative of vortex DWs. The trend found in the vortex case is very different to the transverse case. Initially there is a small increase in the depinning field, up to a sidewall length of 60 nm and an angle of 27°. This is a similar length but much larger angle than in the transverse case. Once the sidewall is extended beyond this point, the depinning field drops very suddenly by approximately 31%. Further increase in the sidewall length and reduction in the angle leads to a diminishing pinning strength, however the relationship is gradual and not extreme as in the transverse case. As the depinning fields reduce there is a slight increase and another peak between 9° and 6° before appearing to suddenly reduce at smaller angles. To achieve smaller angles, the length of the nanotrench must be increased significantly. This causes the simulation time to be increased significantly. Due to this, data points relating to smaller angles were not obtained.

This difference in the two trends are possibly due to the fundamental differences in DW structure, in particular regarding the z component. The core of the vortex DW may interact with the gradual change in the z dimension of the nanowire, remaining pinned more strongly than a transverse DW with minimal contributions to the z direction.

Finally energy plots were made for the vortex DW trapezoidal nanotrench case. These are shown in figure 4.3.44. The slope sizes were chosen to represent key features found in the trend. A 20 nm slope was chosen to represent a small slope case, the 60 nm slope is the final data point before the depinning field suddenly drops. The 70 nm slope is the first data point after the drop in depinning field, whilst 200 nm and 500 nm slopes are used to observe the continued reduction in depinning field. Unfortunately all of the energy plots found in figure 4.3.44 look very similar to one another. Therefore they do not provide any further information on why or how the sudden drop in depinning fields occurs and reduces with increased slope.

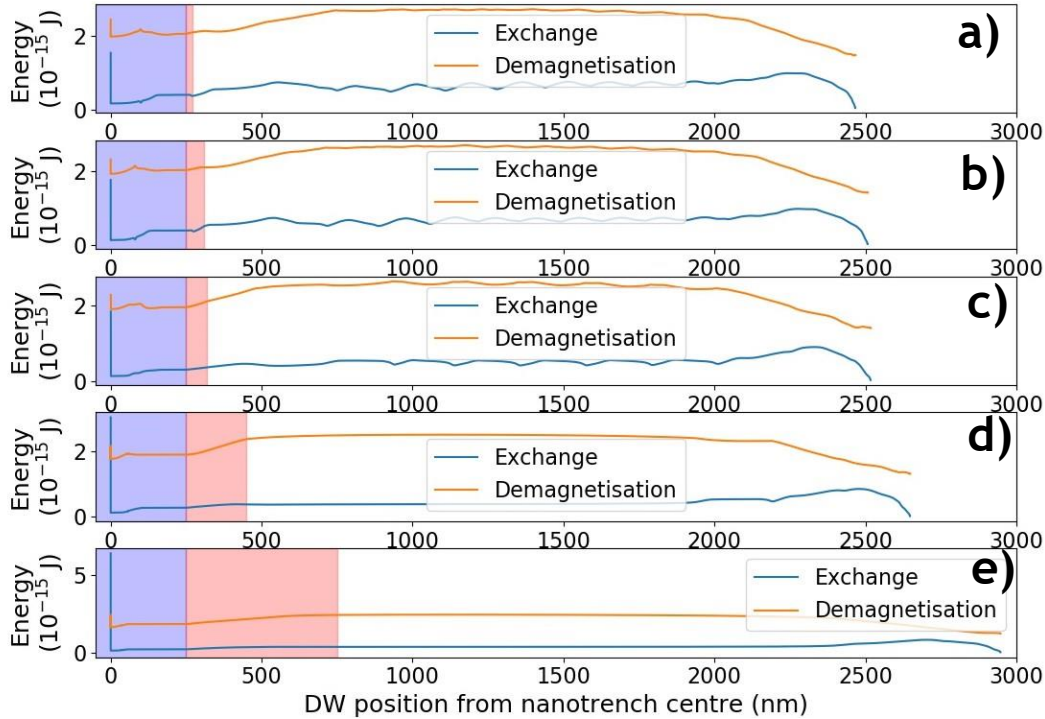


Figure 4.3.44: Energy plots showing exchange and demagnetisation energies for DW position in a 200 nm wide, 50 thick nanowire containing; a) trapezoidal nanotrench, 30 nm deep with a central length of 500 nm and a slope length of 20nm. b) trapezoidal nanotrench, 30 nm deep with a central length of 500 nm and a slope length of 60nm. c) trapezoidal nanotrench, 30 nm deep with a central length of 500 nm and a slope length of 70nm. d) trapezoidal nanotrench, 30 nm deep with a central length of 500 nm and a slope length of 200nm. e) trapezoidal nanotrench, 30 nm deep with a central length of 500 nm and a slope length of 500nm. Blue shaded regions represent location of trapezoidal base, whilst red regions represent location of trapezoidal slopes.

4.4 Summary

To conclude this chapter, this section will provide a brief summary of the key results found in this part of the study.

The first section consisted of building the computational model by starting with a standard nanowire with the material properties matching permalloy. A phase diagram was produced using this model in order to assess the expected DW structure for given nanowire dimensions.

Following this, a vertical nanotrench was included within the wire. Data points were produced for depinning fields of a square nanotrench in a 100 nm wide and 10 nm thick nanowire and compared with [123]. The results were similar verifying the model created.

Once the computational model was established, a study was conducted comparing square nanotrenches with triangular nanotrenches of similar dimensions. Three nanowire sizes were used, two of which producing transverse DWs whilst a larger wire was utilised for vortex DWs. In all cases it was found that triangular nanotrenches pinned DWs weaker than square nanotrenches of similar dimensions.

It was found that the pinning strength for transverse DWs were chirality independent for both square and triangular vertical nanotrenches. Results for vortex DWs indicated a chirality dependence, however no clear relationship could be concluded.

In all cases, the pinning strength increased approximately linearly with nanotrench depth for constant lengths. There was a difference in results between square and triangular nanotrenches when varying the nanotrench length for fixed depths. For transverse DWs, square nanotrenches show an initial increase in depinning field before saturating and no longer increasing as the site length is increased. In the triangular nanotrench case it was found that the pinning strength weakens with increased length following an initial increase. Further analysis showed an apparent angular dependence where the pinning strength begins to significantly decrease when nanotrench walls form angles less than 10° to the x-y plane. This was also shown when a trapezoidal nanotrench was created.

Results produced with the largest 200 nm wide, 50 nm thick nanowire were interrupted by the presence of asymmetric transverse DWs occurring in triangular nanotrench cases. Data points relating to vortex DWs indicate an increase followed by a reduction in pinning strength with nanotrench length, however the rate of reduction is much lower than the transverse DW case. The use of trapezoidal nanotrenches show an angular dependence where the pinning strength reduces sharply as the angle reduces below 30° .

5. Implementing AFM nano-machining for magnetic domain wall pinning

In this chapter, the experimental aspects of the study are reported. First, initial experiments that focussed on modifying permalloy thin films using AFM nanomachining are presented. Next, attempts to machine vertical nanotrenches in permalloy nanowires via this process are described together with measurements conducted to assess how successful these were for pinning DWs. This particular work was completed to address the specific knowledge gap of whether AFM tip-based nanomachining could be used to produce vertical features for the pinning of DWs. An important experimental objective was to aim to vary the size of such nanotrenches in order to provide experimental confirmation that the pinning strength of such features increase with size. Finally, this chapter concludes by reporting the machining of more complex features in permalloy nanowires with the view of opening further explorations of AFM tip-based nanomachining to control the motion of DWs in magnetic nanowires.

5.1 Initial experiments: AFM machining of a permalloy thin film

The first step in the experimental part of the study was to conduct initial experiments on permalloy thin films which had similar thickness to the nanowires that were to be fabricated subsequently. This initial study was realised to gain the necessary practical experience in using the AFM system for tip-based nanomachining, along with the complementary objective of assessing which cutting direction would be most suitable for creating vertical nanotrenches. In particular, three cutting directions were considered namely up, down and horizontal as illustrated within figures 5.1.1, 5.1.2 and 5.1.3. These first set of experiments were implemented with a three-sided AFM tip as the nanoscale cutting tool. The thickness of the films was also chosen such that scratches could be conducted with varying values of the normal force. It was anticipated that the results obtained could act as a guide for controlling the nanotrench depths in the nanowires during subsequent experiments.

In order to assess the optimal cutting direction for the three-sided AFM tip, scratches were machined along 10 μm straight lines. During this study, a 10 nm thick permalloy thin film deposited onto a SiO_2 substrate was used. For each cutting direction, six grooves were created by increasing the number of consecutive 5 μN scratches for a groove, ranging from one to six. AFM images displaying 1 μm long sections of the resulting grooves are reported in figure 5.1.1, 5.1.2 and 5.1.3.

Assessing the error on the applied force values was difficult due to variations in the calibration process along with the tip wearing over time. This changes the amount of contact the tip makes with the surface. Throughout this study the error on the applied forces was estimated to be between 3% and 8%.

Figure 5.1.1 shows the resulting grooves from cutting in the “backward” direction. In this configuration, the grooves are being ploughed using a flat surface in the scratching direction. The images show clean cuts in the grooves themselves with small variations along the depth and the sidewalls are smooth. Residual pile-ups are formed on both sides of the grooves. However, such pile-ups are considerably larger on one side compared to the other. As there is no clear reason as to why this would happen, these results imply that the flat cutting surface was not positioned at exactly 90° to the cutting direction. The small angle would provide a preferable direction for the removed material to move to, thus creating larger pile-up on one particular side.

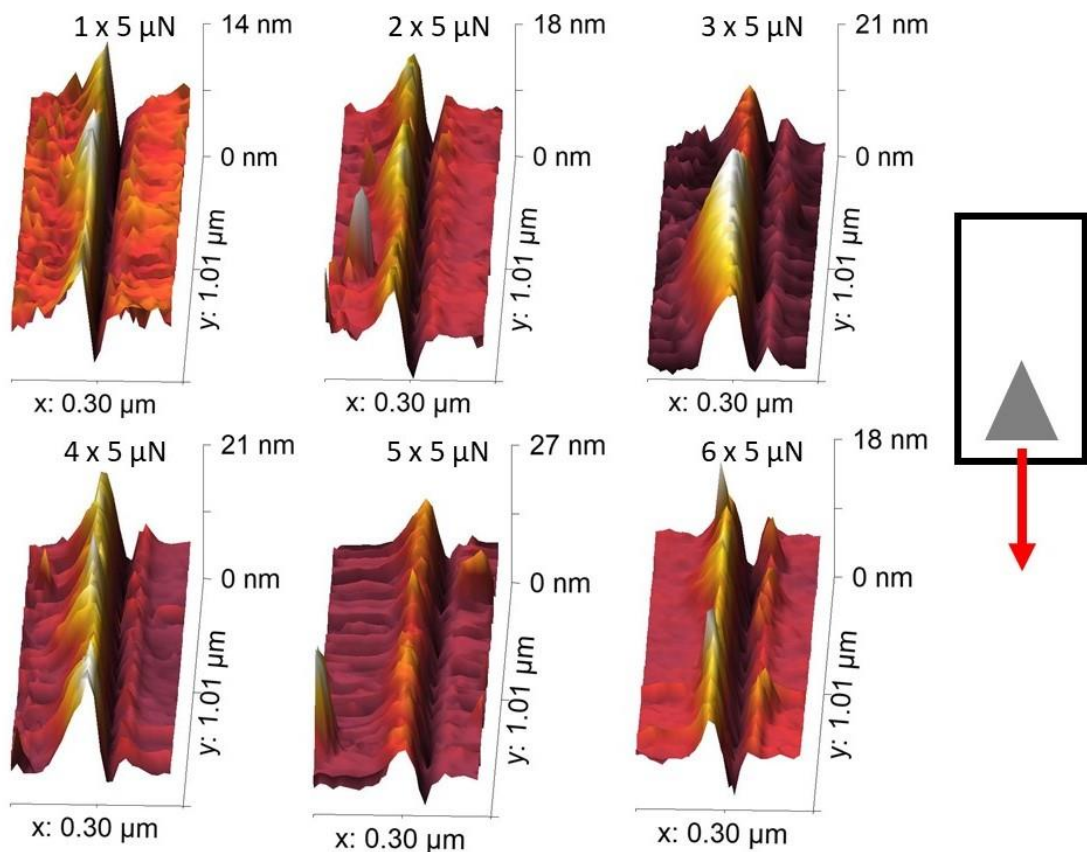


Figure 5.1.1: AFM images showing 1 μm long sections of grooves scratched in the “backward” direction implementing various quantities of 5 μN scratches on a 10 nm thick permalloy thin film..

In figure 5.1.2, results from machining in the “forward” direction are considered. In this case, two faces of the tip are in continuous in contact with the material in the cutting direction with the edge between the two faces located in the centre of the groove. Studying the AFM images of the grooves showed that whilst some of the grooves generated in this way were observed to be smooth, others showed variations in the depth and considerable fluctuations along the walls. Overall, this direction proved to be of relatively lower quality cutting when compared with the “backward” direction. The formation of pile-up is also a more important issue in this case. This can be explained by the fact that, given the tip-material geometric configuration in this case, the tip pushes the material to either side of the groove and so only displaces much of the material via plastic deformation as opposed to cutting and completely removing material via the formation of a chip. This results in very large pile-ups on both sides of the grooves.

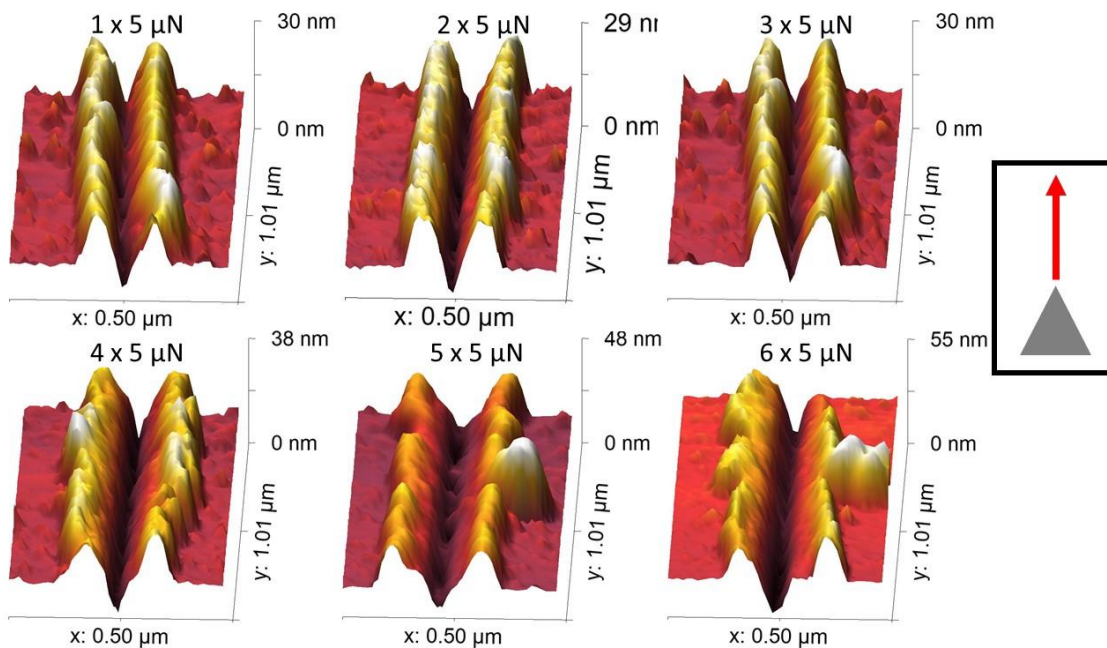


Figure 5.1.2: AFM images showing 1 μm sections of grooves created scratching in the “forward” direction implementing various quantities of 5 μN scratches on a 10 nm thick permalloy thin film..

The final case considered was when cutting in the “upward” direction. The resulting grooves are found in figure 5.1.3. In this configuration, there is one primary side of the tip in contact with the material as it is cutting. However, in contrast to the “backward” case, this time this face is at an angle to the cutting direction. This creates a sharper focal point between two of the tip faces at one edge of the tip width relative to the cutting direction. This acts to cut into the material and so

removes much of it, then pushing and displacing the remaining material to the opposite side. The resulting grooves have smooth sidewalls, and in most cases, consistent depths. Pile-up still occurred but it was relatively small when compared to that in the “backward” case on one side, whilst creating little-to-no pile-up on the other side. The reduction in overall pile-up is due to the tip cutting into the material and removing it via chip formation as opposed plastically deforming the permalloy.

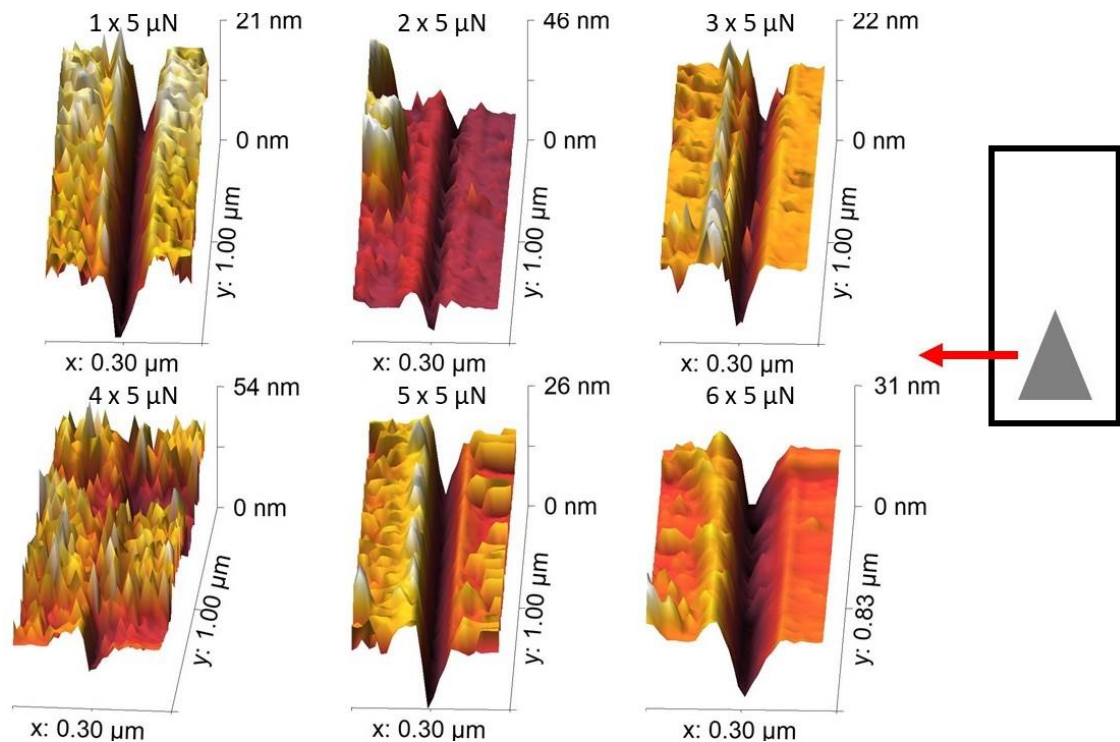


Figure 5.1.3: AFM images showing 1 μm sections of grooves created scratching in the “upward” direction implementing various quantities of 5 μN scratches on a 10 nm thick permalloy thin film..

In order to compare directly the resulting pile-up for all cutting directions, figure 5.1.4 displays plots for the average height of the material left on either side of the groove. The locations “right” and “left” correspond to the sides relative to the cutting direction. The observation of these plots confirms what has been previously described. The “forward” direction produced equal amounts of pile-up on both sides of the groove in the majority of cases. The height of these pile-ups is also larger than any values measured with the “backward” and “upward” directions. Some similarities are noted between the “backward” and “upward” directions in the sense that there is often significantly more pile-up on one side than the other. This is somewhat surprising in the case of the “backward” direction as there is no

immediately distinctive reason why this should be the case given that the cutting face is flat. Indeed, this is expected if the cutting face is not completely perpendicular to the direction of motion as more material should be pushed towards one side compared to the other. It is also clear that the “upward” direction produces the least volume of pile-up. In particular, there are very small amounts of pile-up found along the “left” side of the groove and whilst there is still pile-up on the “right” side, its height is less than for any other “forward” or “backward” cases. This indicates that the horizontal cutting direction produces the cleanest grooves by completely removing more of the material as opposed to plastically displacing it on the surface of the film.

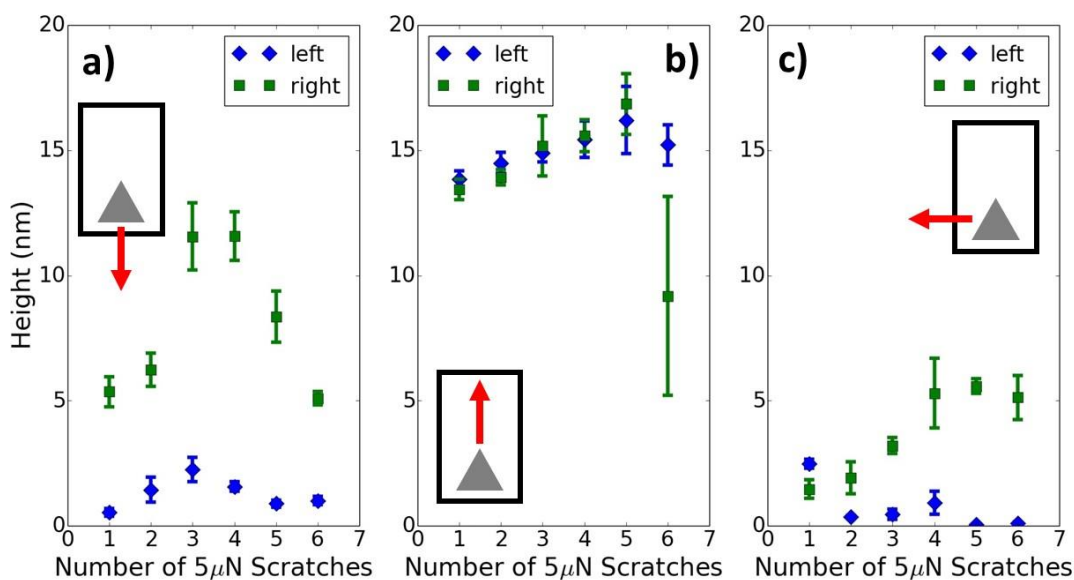


Figure 5.1.4: Plots displaying the height of pile-up formed on either side of the grooves generated using a) “backward”, b) “forward” and c) “upward” cutting directions implementing various quantities of $5\ \mu\text{N}$ scratches on a $10\ \text{nm}$ thick permalloy thin film. Errorbars represent the standard deviation from multiple measurements.

Another analysis that can be made when comparing the cutting directions is to assess the depth and width of the resulting grooves. These plots are found in figure 5.1.5. It is worth remembering that the film thickness was approximately $10\ \text{nm}$ and so any depth measured beyond this value implies that the tip started to cut into the substrate. This means that interpreting depths beyond $10\ \text{nm}$ does not bare any relation to the behaviour of the permalloy properties when cutting it. This is not

considered an issue for this section of the study because the depth and width are considered to bear less significance in choosing which cutting direction should be used in comparison with the quality of the cut discussed earlier. Besides, once a cutting direction has been established, the size of the features can be controlled by varying the applied force. Figure 5.1.5 shows that, generally, the “upward” cutting direction provided the deepest and widest grooves. The “forward” direction resulted in grooves of size close to the horizontal case, whilst grooves cut along the “backward” direction were the shallowest and narrowest.

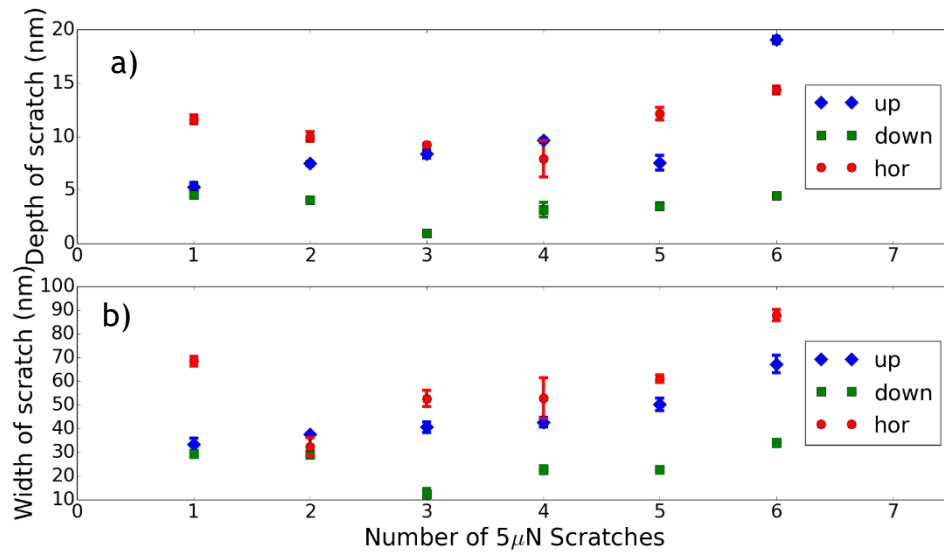


Figure 5.1.5: Plots of average a) depth and b) width of the resulting grooves for “forward”, “backward” and “upward” cutting directions implementing various quantities of 5 μN scratches on a 10 nm thick permalloy thin film. Errorbars represent the standard deviation from multiple measurements.

Once the scratching direction was chosen, the next stage was to investigate the relationship between applied force and size of the resulting grooves. Figure 5.1.6 shows an SEM images of grooves generated by 1, 2, 3 and 4 μN individual scratches. This image was annotated in an attempt to highlight the different grooves. However only the deepest two grooves are clearly visible. AFM scans were conducted on three sections of each groove in order to obtain average measurements of their depth and width; the results of which are shown in figure 5.1.7.

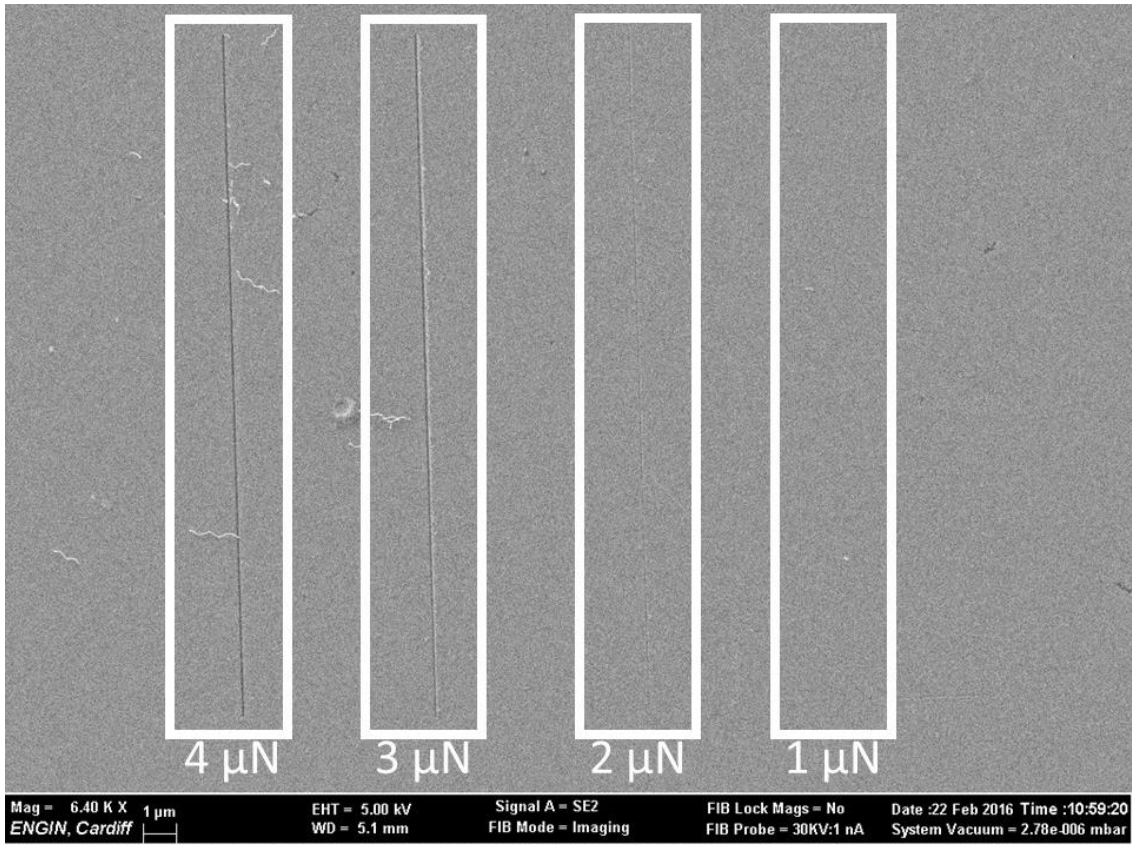


Figure 5.1.6: SEM image of area containing grooves generated by horizontal scratches of varying force.

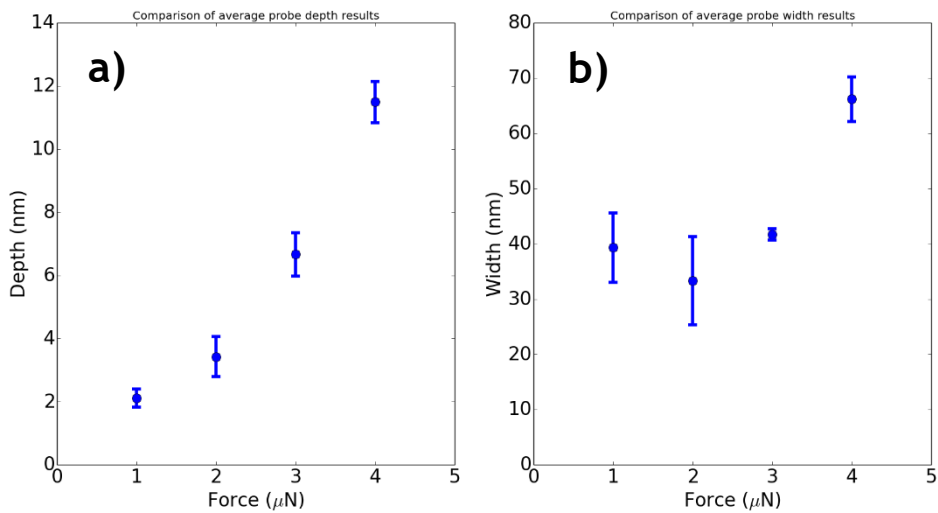


Figure 5.1.7: Plots of a) average depth and b) average width for scratches made in the “upward” direction with various applied forces.

As seen in this figure, a clear relationship is found between the applied force and the depth of the groove. As expected, when the force is increased, the depth

increases. The relationship appears to be higher order than linear. However, the data point when scratching with an applied force of $4 \mu\text{N}$, shows a depth close to 12 nm . This indicates that the permalloy thin film had been completely cut through in this case and that the tip had been cutting into the substrate. Due to this, the data point cannot necessarily be used to deduce a relationship between the applied force and the depth of grooves created in permalloy. When considering the width, it is rather unclear as to whether there any relationship with the applied force can be formulated. The assumption could be made that the width would increase as the tip cuts deeper due to its pyramidal shape but this is not immediately supported by this particular data set.

5.2 Pinning of DWs at a nanotrench on a thin permalloy nanowire

Following the completion of the initial thin film experiments, the next of the study stage was to fabricate devices containing nanowires. These were created using permalloy and designed to probe the nanowires using AMR as discussed in section 3.2.2. An example of the produced devices was shown earlier in figures 3.2.5 and 3.2.6. The first nanowire used in this study measured approximately 685 nm wide and 11.5 nm thick. Figure 5.2.1 shows a line scan representing the average cross-section of the nanowire. An inset image within this plot displays an AFM scan of the nanowire.

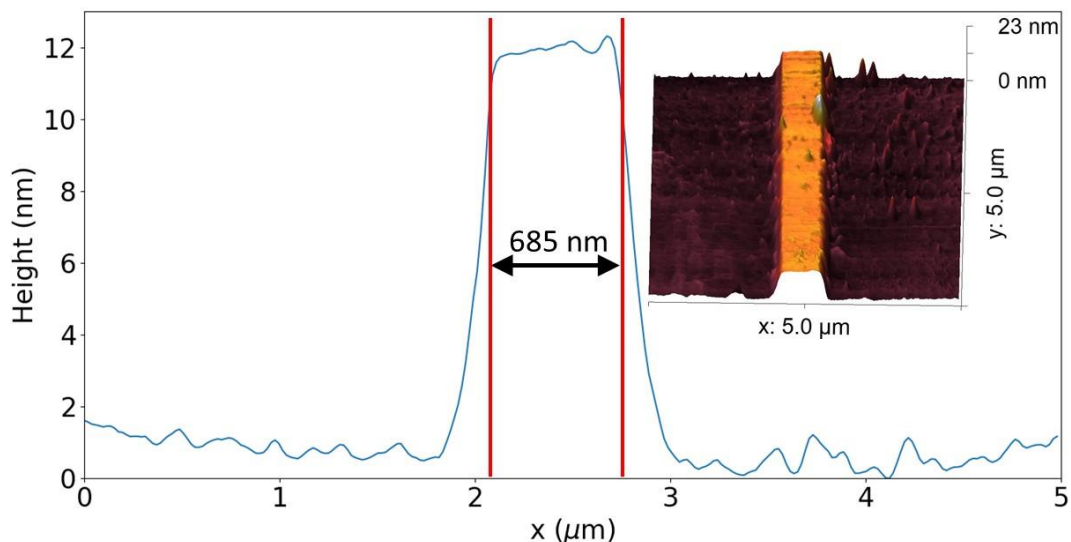


Figure 5.2.1: Linescan of the 685 nm wide, 11.5 nm thick nanowire including an AFM image of the central 5 μm region.

Initial AMR data were taken for the nanowire before any subsequent modifications with AFM nanomachining. In this way, it could be possible to observe how artificially created pinning sites could affect the shape of the AMR data. Examples of this data are displayed in figure 5.2.2, whilst figure 5.2.3 focusses on the more specific regions of the data when the nanowire switches magnetisation. These plots show the resistance of the wire to be approximately 2.2 k Ω . Variations in the resistance is also noted due to changes in the ambient temperature where the experiment was conducted. Based on the analysis of these data, the switching field for the nanowire was found to be 19 ± 1 Oe where the error value was the standard error on the mean of the dataset. This switching field in the absence of a nanotrench can also be considered as the injection field. The injection field is the required magnetic field to create and inject a DW into the nanowire.

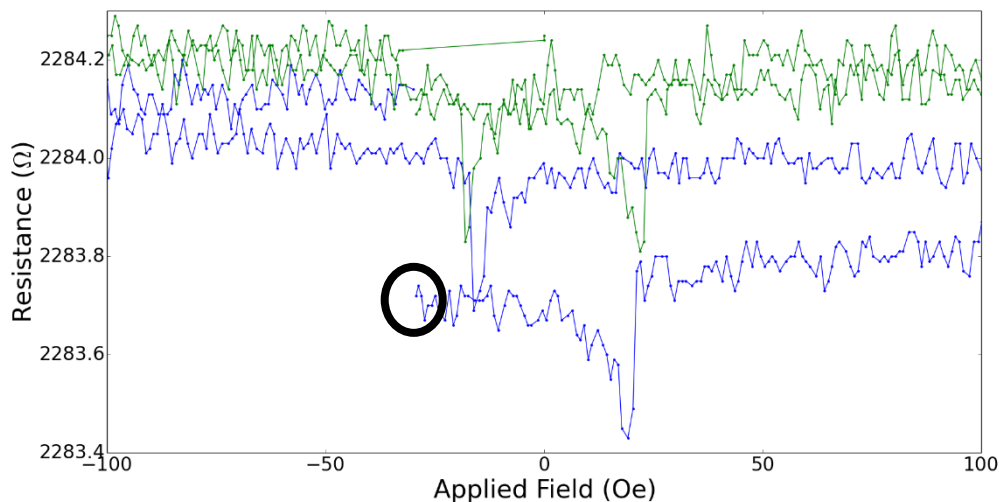


Figure 5.2.2: Example of the raw AMR data for the 685 nm wide, 11.5 nm thick permalloy nanowire before AFM machining. This data contains two hysteresis loops starting in negative fields (shown in the black circle), increasing through 0 field to positive. Trends of different colours represent individual hysteresis loops.

Once these initial measurements had been performed and analysed, the next step was to attempt to create a pinning site using AFM tip-based nanomachining. A “horizontal” AFM scratch was machined across the width of the nanowire with an applied force of 2 μ N. This did succeed in cutting into the nanowire creating a nanotrench across its width. An AFM image of the resulting nanowire is reported in figure 5.2.4. A corresponding linescan of the average profile along the wire is shown in figure 5.2.5 to provide a representation of the cross-sectional profile of the nanotrench.

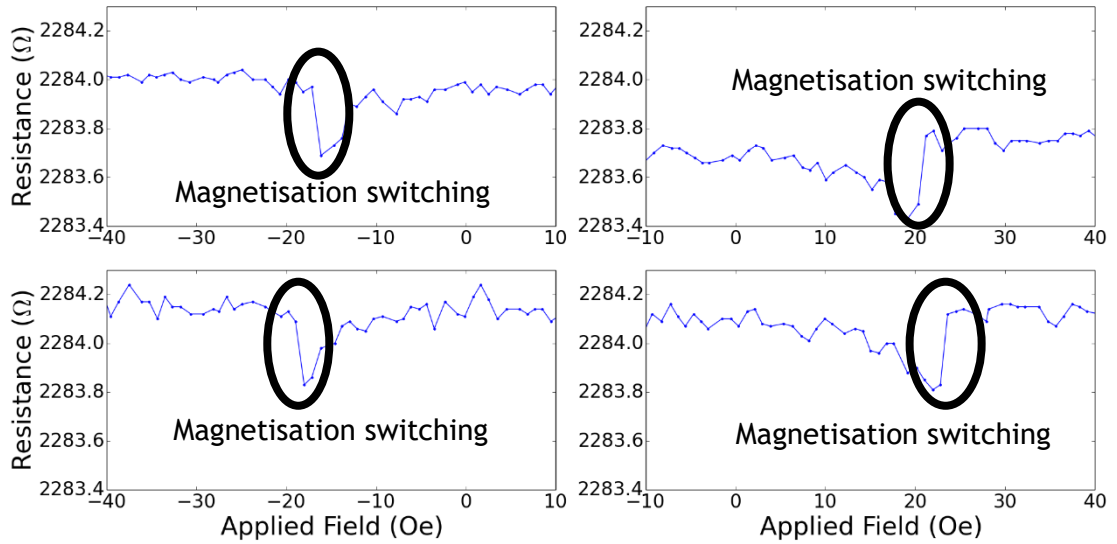


Figure 5.2.3: Examples of the AMR data shown in figure 5.2.2 focusing on when the nanowire switches magnetisation. Left plots show the field transitioning from positive to negative fields. Right plots show the field transitioning from negative to positive fields.

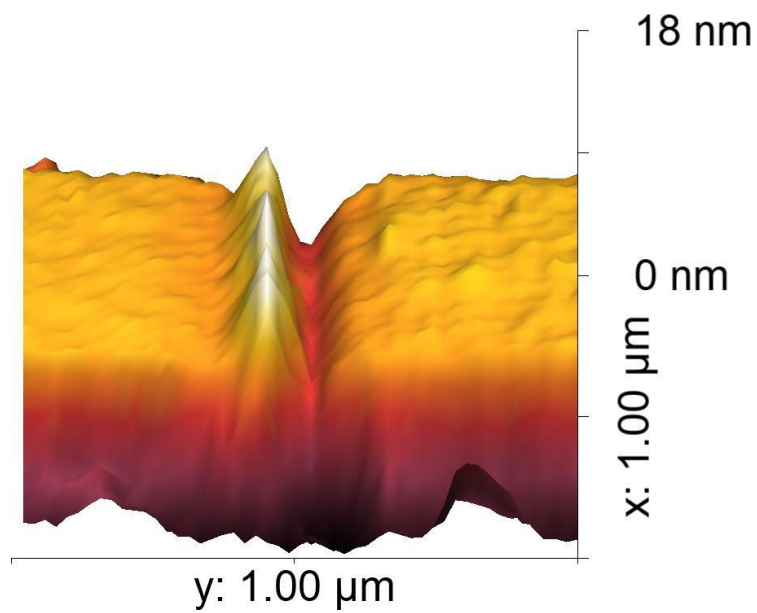


Figure 5.2.4: AFM image of the resulting nanotrench produced by a 2 μN scratch along the width of the 685 nm wide, 11.5 nm thick nanowire.

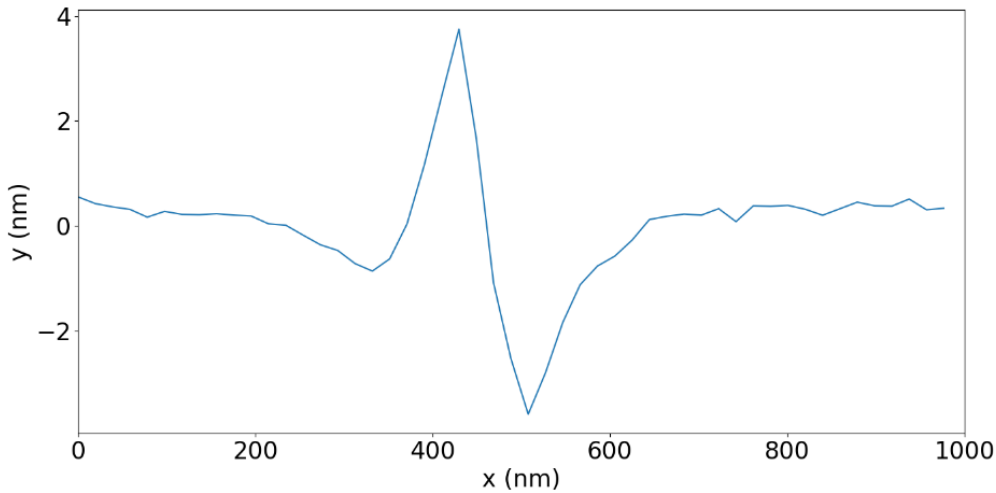


Figure 5.2.5: Average linescan of the profile of the nanotrench generated by a $2\ \mu\text{N}$ scratch along the width of the 685 nm wide, 11.5 nm thick nanowire.

This nanotrench measured had a depth of $3.9 \pm 0.2\ \text{nm}$ and a length of approximately 150 nm. It is also clear to see that material pile-up formed on one side of the nanotrench. This pile-up was approximately 100 nm in length at the surface of the nanowire with a maximum height of approximately 3.3 nm. Further AMR data were taken once the nanotrench was created, an example of which is displayed in figure 5.2.6. These data show an increase in the switching field. As the applied field transitions across 0 field, the resistance of the wire reduces. This represents the presence of a DW within the wire. When the field is increased and the resistance remains below the saturated value, this means that the DW is pinned at the nanotrench. As the field is increased further, the jump in resistance represents the DW being depinned and propagating along the remainder of the wire such that it becomes uniformly magnetised. Following hysteresis loops providing 20 data points, the switching field in this case is found to be $24.9 \pm 0.7\ \text{Oe}$. This represents an increase in switching field of approximately 5.9 Oe. A statistical t test was performed on the two datasets to test whether their means are statistically different. The resulting p value was 0.007. This very small value supports the hypothesis that these means are different distinct values given the datasets.

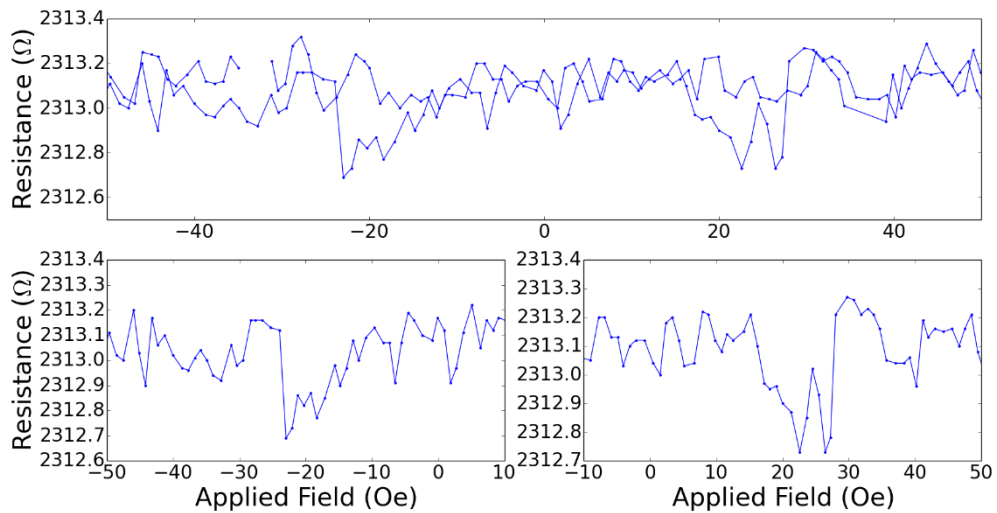


Figure 5.2.6: Example hysteresis loop of AMR data taken for the 685 nm wide, 11.5 nm thick nanowire with a 3.9 nm deep nanotrench.

Once the AMR measurements were analysed for this first nanotrench, another scratch was attempted in the same location in an effort to change the size of the nanotrench and assess the effects on its pinning strength. This time the scratch was conducted with an applied force of 1 μN . This resulted in further modification of the geometry of the nanotrench. An AFM image of this is shown in figure 5.2.7 with the average linescan of the profile given in figure 5.2.8.

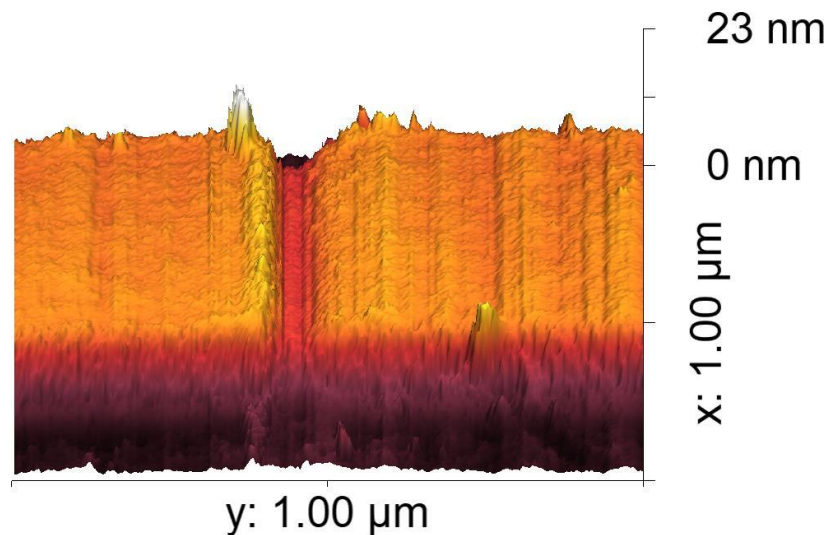


Figure 5.2.7: AFM image of the nanotrench after the second 1 μN scratch along the width of the 685 nm wide, 11.5 nm thick nanowire.

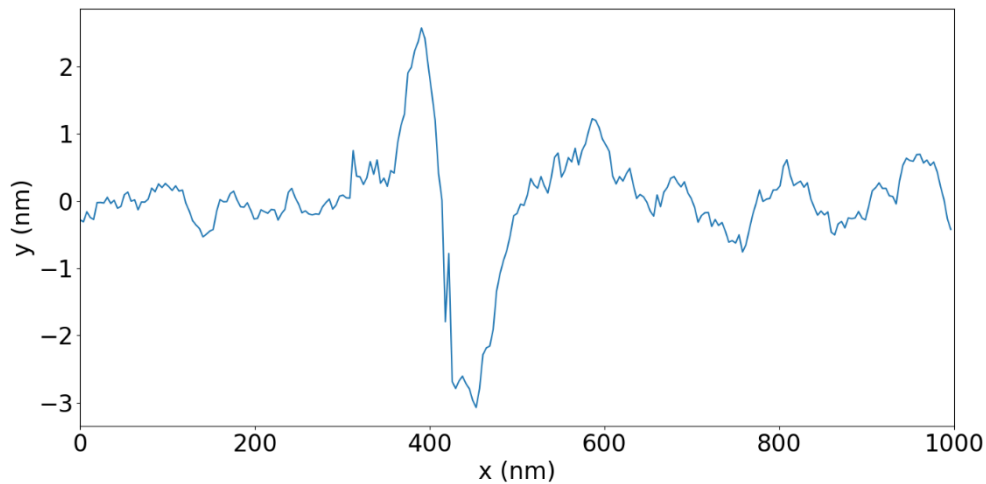


Figure 5.2.8: Average linescan of the profile of the nanotrench after the second 1 μ N scratch along the width of the 685 nm wide, 11.5 nm thick nanowire.

Following this additional 1 μ N scratch, the nanotrench measured 4.5 ± 0.1 nm in depth whilst its length remained approximately 100 nm. It is observed from Figure 5.2.8 that some of the pile-up was removed during the second scratch as its length at the surface reduced to approximately 50 nm whilst its height was 2.5 nm. Again, AMR data were obtained at this stage. An example is shown in figure 5.2.9.

The AMR data is very similar to the previous case. In this case 40 data points were collected and resulted in a slight increase in the switching field to 25.5 ± 0.4 Oe was measured. However, this is a small variation of 0.4 Oe which lies within the standard error of the measurements. While this slight increase in switching field does correspond to the relatively small change in the depth of the nanotrench, the small differences found between the two cases provide insufficient evidence to conclude that the pinning strength of the nanotrench increases with its size. To test this, again a t test was performed on the two datasets. The resulting p value from this test was 0.49. This was a very high p value and so the hypothesis that the means of the two datasets are the same cannot be rejected. This also provides insufficient evidence that the depinning field has increased due to the increase in nanotrench depth.

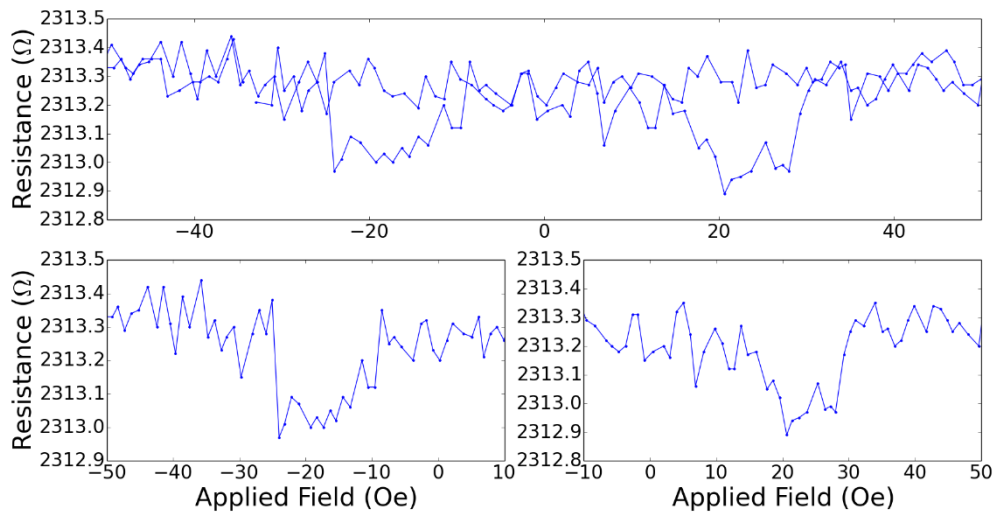


Figure 5.2.9: Example of AMR data taken for the 685 nm wide, 11.5 nm thick nanowire with a 4.46 nm deep nanotrench.

In order to obtain more data points regarding the value of the switching field as a function of the depth of the pinning site, additional attempts were made to increase the size of the nanotrench. A series of scratches were performed in order to try and significantly change its depth. Initially two 1 μN scratches were carried out, followed by 2 μN , 1 μN , two 1.5 μN and another two 1.5 μN scratches. All of these scratches resulted in minimal change in the nanotrench dimensions. Thus, it became apparent that it is more difficult to deform the permalloy plastically as the material thickness between the substrate and the bottom of a nanotrench reduces. Although a different force increment was considered between the machining of the permalloy nanowire and the permalloy thin film, there seems to be a difference in the behaviour of the material in both cases. It is outside the scope of this thesis to analyse this particular phenomenon. However, it is possible that residual compressive stress underneath a nanotrench resulting from a nanomachining operation leads to material hardening. In turn this would increase the range of applied normal force values for which the material only deforms elastically. In addition, numerous reports exist in the literature in which researchers observed an increase in the strength of a material with a decrease in sample size (see for example Greer *et al.* 2005 [186] for a discussion on the topic). In particular, the hypothesis formulated by Greer *et al.* relies on the concept of dislocation starvation. In the case of the nanowires considered in his research, this would mean that dislocations (which are responsible for plastic deformation) reach the nanowire surface before they have had the chance to multiply, hence leading to dislocation starvation and the need for higher

applied stress to nucleate new dislocations in the permalloy material. However, further research would be required to confirm the exact nature of the phenomenon associated with the behaviour of the permalloy material observed here. Indeed it is also possible that the state of initial stress in the permalloy material is quite different between a nanowire and a thin film as a result of the sample fabrication process. In particular, as the permalloy is deposited using thermal evaporation, the substrate and material becomes heated. Once the material is deposited and the process stops, the sample begins to cool down. As the substrate and the device consist of different materials and have different geometries, it is reasonable to assume that they may cool down at different rates which would result in residual thermally-induced stress between in the permalloy.

A series of 3 μN scratches were performed subsequently. As these scratches were conducted, the nanowire ruptured. AFM and SEM images of the broken nanowire are reported in figures 5.2.10 and 5.2.11 respectively. This rupture caused a large section of wire, upwards of 1 μm , to be removed with a region of approximately 630 nm where there is minimal material left on the substrate. At one end of this region, the break is clean and the nanowire remains intact. Beyond this, there is a large region where most of the nanowire material has been removed.

This catastrophic rupture implies that fracture with very limited plastic deformation is the cause of the break, similar to the behaviour of brittle materials.

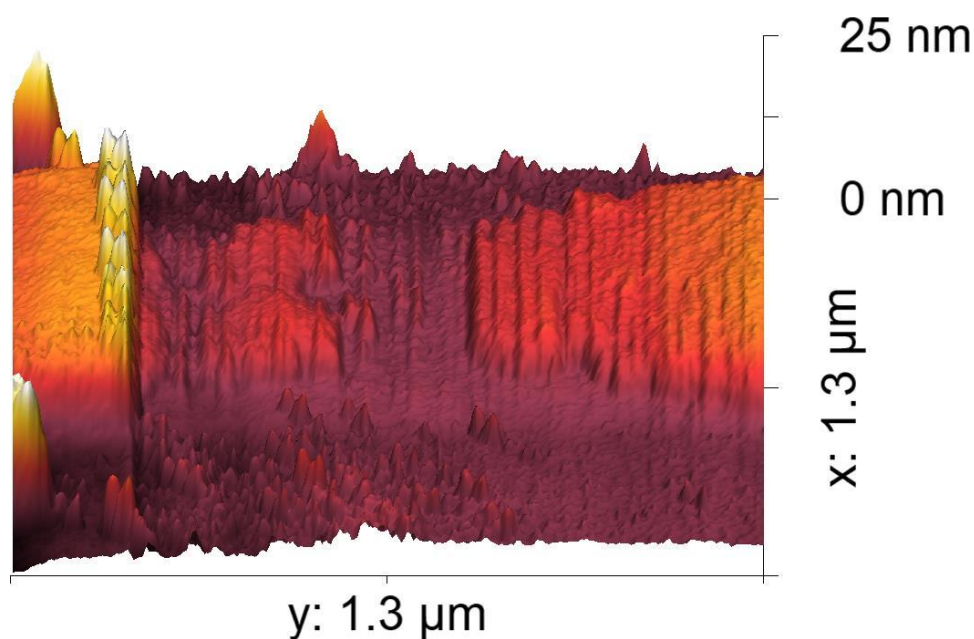


Figure 5.2.10: AFM image of the remaining material from the 685 nm wide, 11.5 nm thick nanowire following rupture.

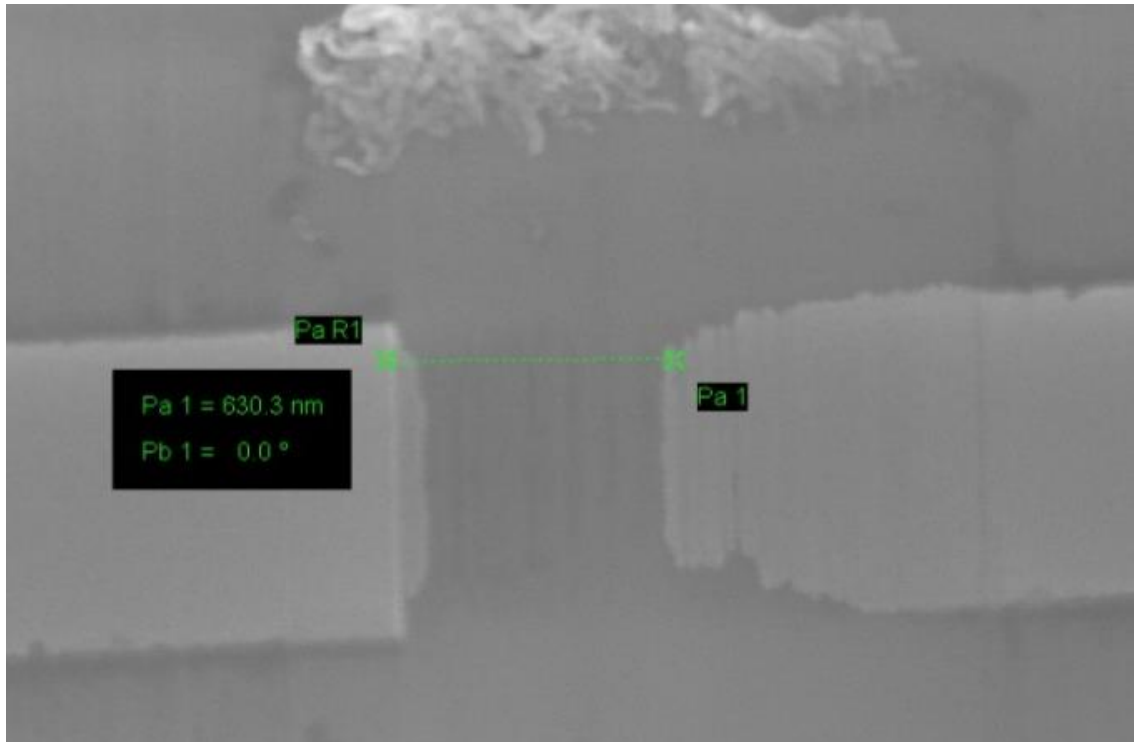


Figure 5.2.11: SEM image of the 685 nm wide, 11.5 nm thick nanowire following rupture.

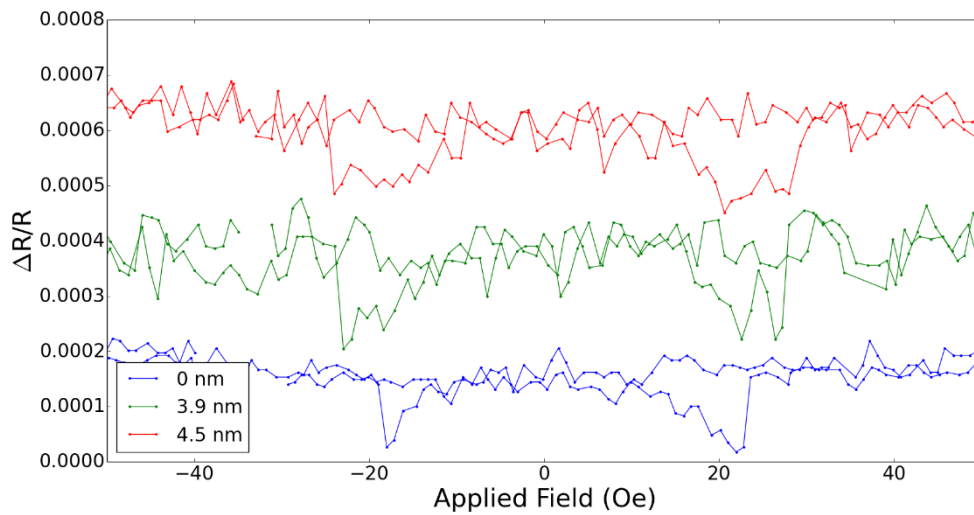


Figure 5.2.12: Examples of AMR data for each step relating to the 685 nm wide, 11.5 nm thick nanowire. The resistance has been converted to arbitrary units, with each dataset offset in order to aid visual comparison.

As the wire ruptured, it was no longer possible to obtain any further data points relating to that specific nanowire. Figure 5.2.12 shows a direct comparison of the AMR data relating to the nanowire at each nanotrench depth. This makes it easier to

clearly see the change in switching field from the initial nanowire to the creation of the nanotrench. There was little change in the AMR data when the nanotrench is deepened. The clear change in switching field once the nanotrench was created indicates that the DW did get pinned at this artificially-created site. This provides experimental evidence that DWs can be pinned at a vertically inserted nanotrench using AFM tip-based nanomachining.

In order to clearly observe the evolution in the pinning strength of the site as a function of its size, a plot of the field at which the DW becomes depinned against the nanotrench depth is displayed in figure 5.2.13. Whilst this plot does show a sequential increase in the depinning field between the two nanotrench depths, this change is considered to be too small to draw a definite conclusion. Also, given that only two data points are available to study the strength of the depinning field against the nanotrench depth, it is not reasonable to infer whether any relationship exists. Thus more data points are required to investigate this aspect further. This particular objective is reported later in section 5.4.

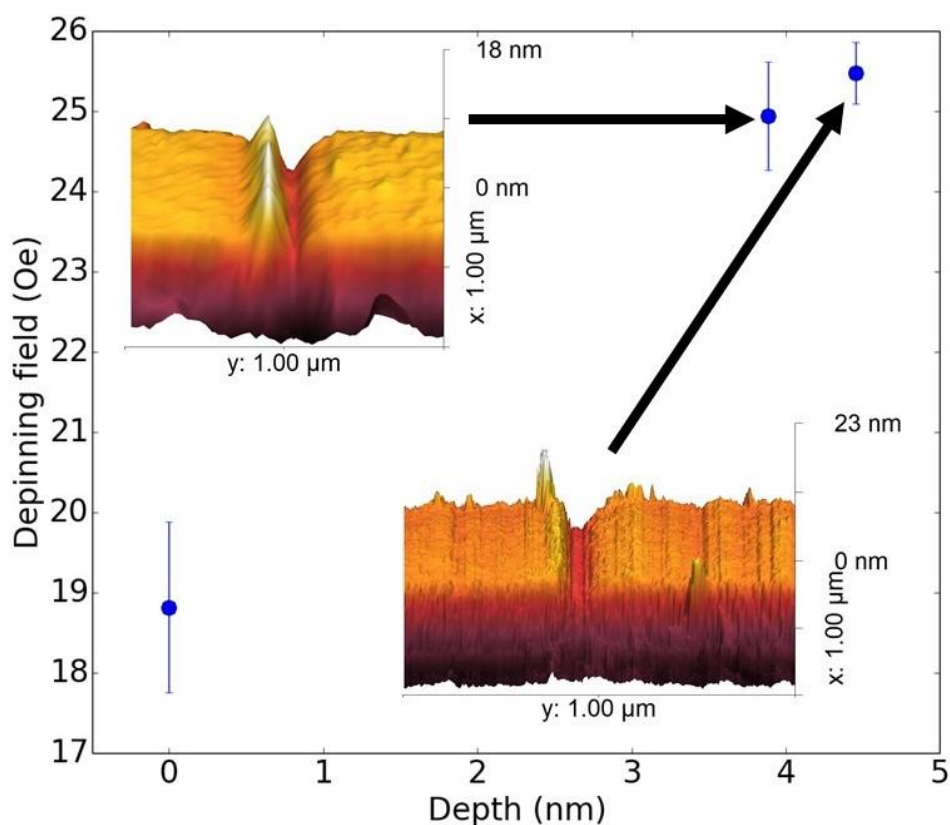


Figure 5.2.13: Plot of depinning field against nanotrench depth for the 685 nm wide, 11.5 nm thick nanowire. Errorbars in this plot represent the standard error on the mean. Data point at 0 nm is actually an injection field but included as a point of reference.

5.3 Pinning of DWs at nanotrenches on thick nanowires

AMR measurements provide a very good indication as to the presence of a DW within the nanowire, but any structural or positional information cannot be obtained using this method. Thus, in an attempt to further confirm that AFM-fabricated nanotrenches are capable of pinning DWs, experiments were conducted at the Advanced Light Source (ALS) facility in Berkeley, California[187]. Magnetic full-field transmission soft x-ray microscopy (MTXM) was used to image the magnetic structure within magnetic nanowire. Nanowires were fabricated for this particular experiment and then nanotrenches were created using AFM tip-based nanomachining for use with the full field soft X-ray transmission microscope.

Three similar sized nanowires were studied. To aid readability, these wires will be called ALS wires A, B and C from this point onwards. The measurements for each of these nanowires can be found in table 5.1. Each of these nanowires had a nanotrench machined on the top surface across their width similarly to the experiment reported in the previous section. The aim was to cut nanotrenches with different depths for each nanowire to try and compare pinning strengths for similar nanowire dimensions. Information of how the nanowires were created and their resulting depths can also be found in table 5.1 AFM images of the three nanotrenches are shown in figure 5.3.1.

Table 5.1.1: Details of experimental ALS nanowires A, B and C

ALS wire	Nanowire width (nm)	Nanowire thickness (nm)	Scratches performed on nanowire	Average depth of nanotrench (nm)
A	435	44.7	2 x 4.5 μ N	25
B	444	42.4	2 x 3 μ N	13
C	427	43.2	2 x 3.5 μ N	17

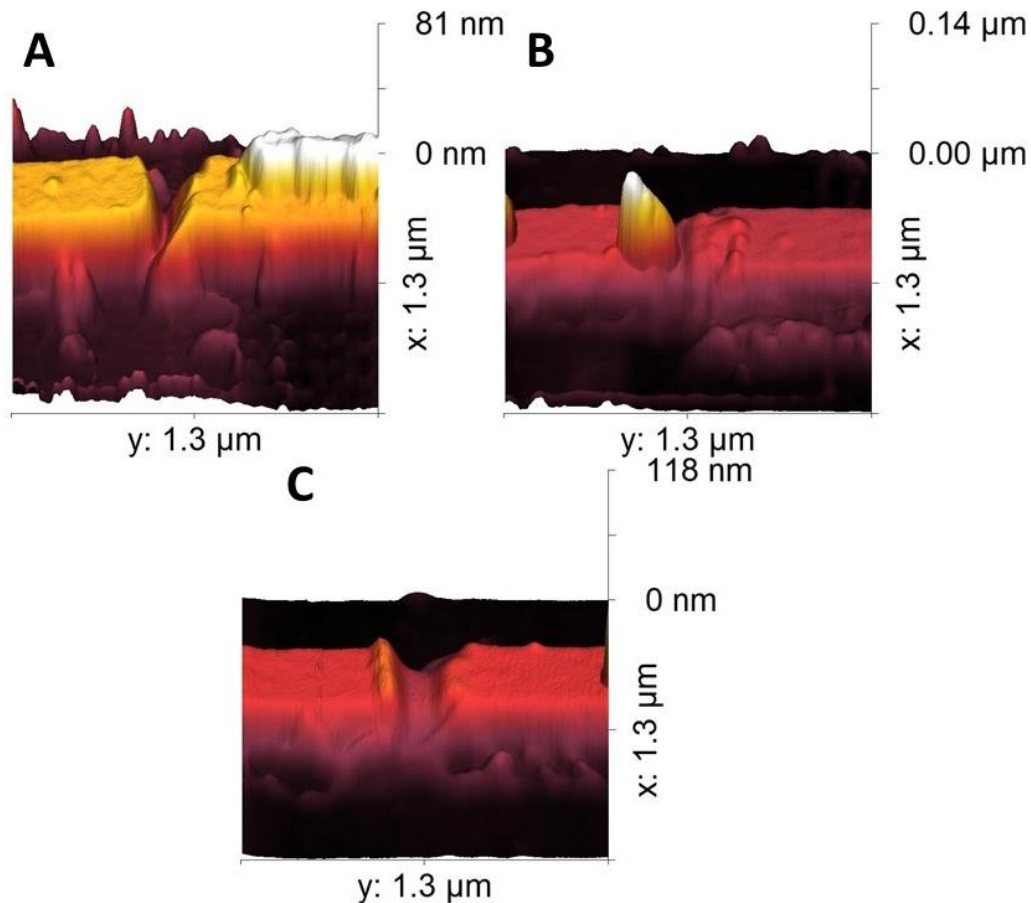


Figure 5.3.1: AFM images of the nanotrenches created in ALS wires A, B and C.

During the experiment at the ALS facility, a magnetic field was applied and changed with images taken of the magnetic configuration at each field. In order to ease the observation of any changes in the magnetic configuration, adjacent images are aligned and divided. This gives a larger contrast in the resulting images where lighter or darker regions represent switches in magnetisation, depending on the direction of the direction change.

The first wire tested was ALS wire A. Figure 5.3.2 contains images showing the nanowire switching magnetisation up to the position of the nanotrench. Note that the CCD camera at the facility contained a series of dead pixels. Whilst efforts were made to avoid this region when producing data, it was not always possible to do so and maintain the best quality. This region of dead pixels is highlighted in figure 5.3.2. In these images, the lightest regions represent magnetisation different from the original configuration. It is also possible to see some of the DW structure in the top and bottom images within figure 5.3.2. Before or beyond the nanotrench a diagonal boundary can be seen between the lighter and background regions, indicating the presence of a vortex DW at the nanotrench. With the applied field

increased further in magnitude, the rest of the nanowire switches magnetisation as the DW propagates beyond the nanotrench. Images showing both halves of the nanowire switching magnetisation are shown in figure 5.3.3. Based on the images obtained for ALS wire A, it was assessed that the DW depinned at applied magnetic fields in the region of 118-136 Oe.

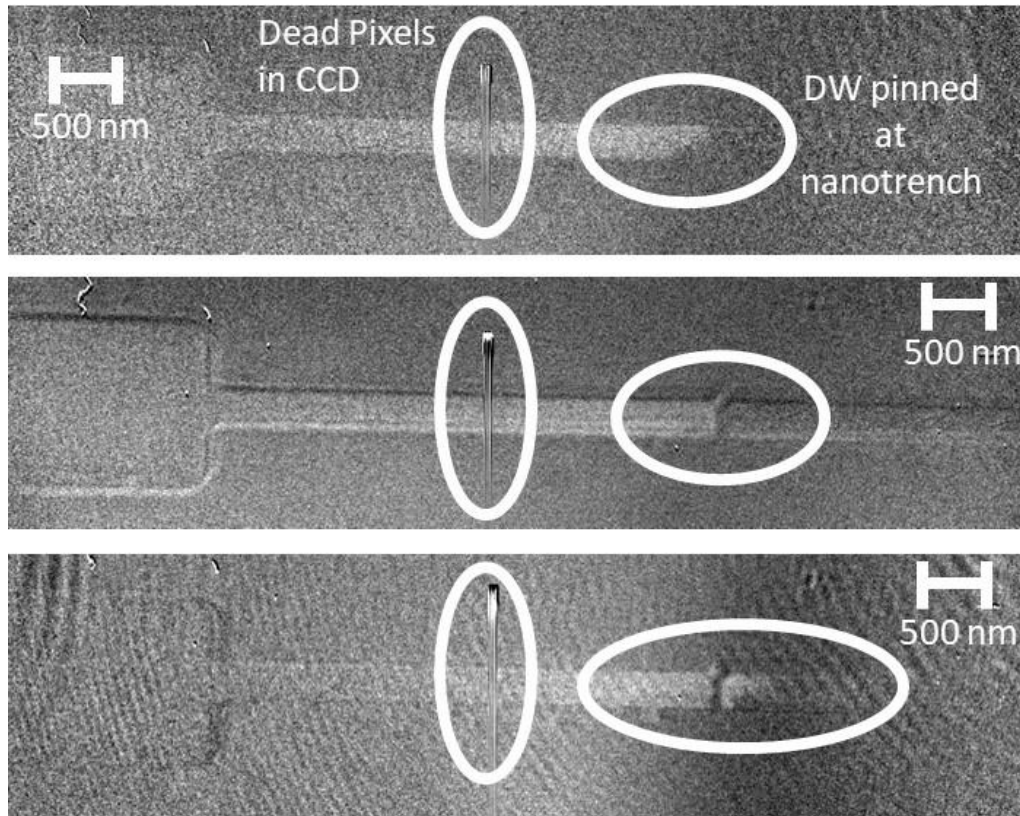


Figure 5.3.2: Top down M-TXM divided images taken at the ALS facility of DWs pinned at the fabricated nanotrench in ALS wire A. Each image shows the DW pinned during independent hysteresis loops.

Similar images are shown in figures 5.3.4 and 5.3.5 for ALS wires B and C respectively. Wire B contains the 13 nm deep trench, the images in figure 5.3.4 shows half of the nanowire switching, before the remainder of the nanowire switches by 110-115 Oe. Whilst less detail is visible regarding the DW structure for this nanowire, it is still clear to see that the DW is pinned at the nanotrench. Figure 5.3.5 shows very similar images for the 17 nm deep nanotrench in ALS wire C. In this case the DW is depinned by magnetic fields in the range 153-171 Oe. Again, the DW structure is not visible, but it is still clear to see both halves of the nanowire switching at distinctly different applied fields. Overall, these data provide further evidence that the DWs are pinned at a nanotrench.

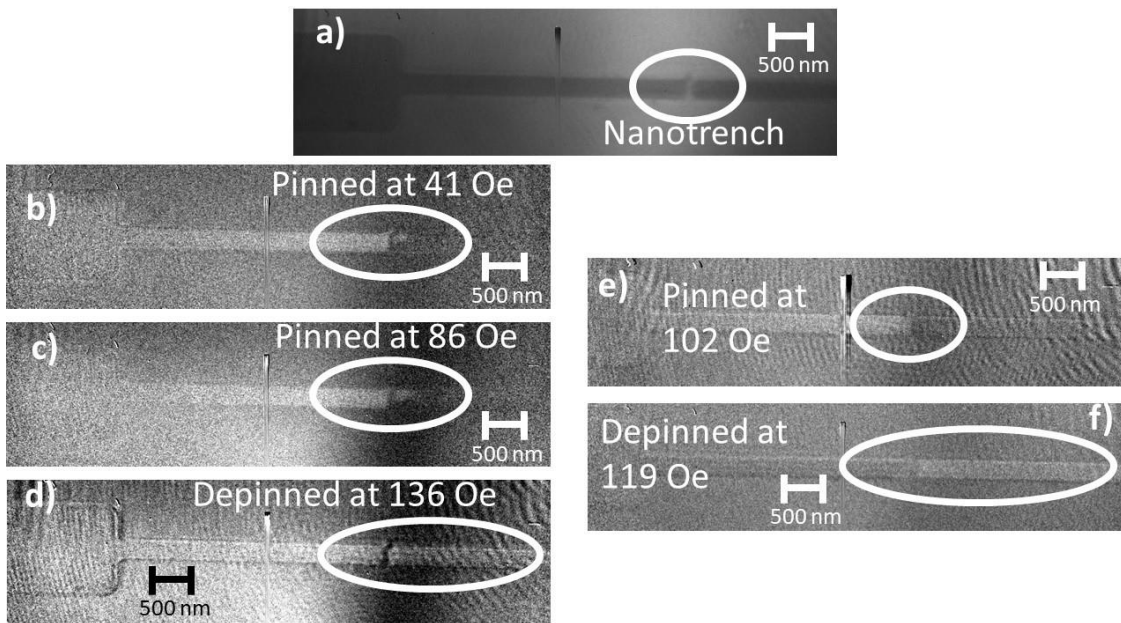


Figure 5.3.3: M-TXM images taken at the ALS facility of DWs pinning and depinning from the fabricated nanotrench in ALS wire A. a) raw unprocessed image to demonstrate nanotrench position. b), c) and d) divided images showing DW pinned and then propagated within a single hysteresis loop. e) and f) divided images showing DW pinned and propagated in a single hysteresis loop.

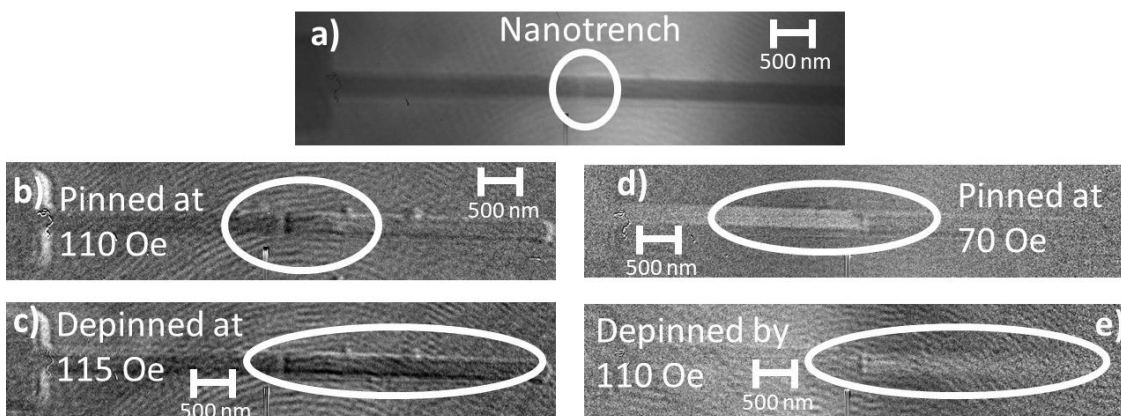


Figure 5.3.4: M-TXM images taken at the ALS facility of DWs pinning and depinning from the fabricated nanotrench in ALS wire B. a) raw unprocessed image to demonstrate nanotrench position. b) and c) divided images showing DW pinned and then propagated within a single hysteresis loop. d) and e) divided images showing DW pinned and propagated in a single hysteresis loop.

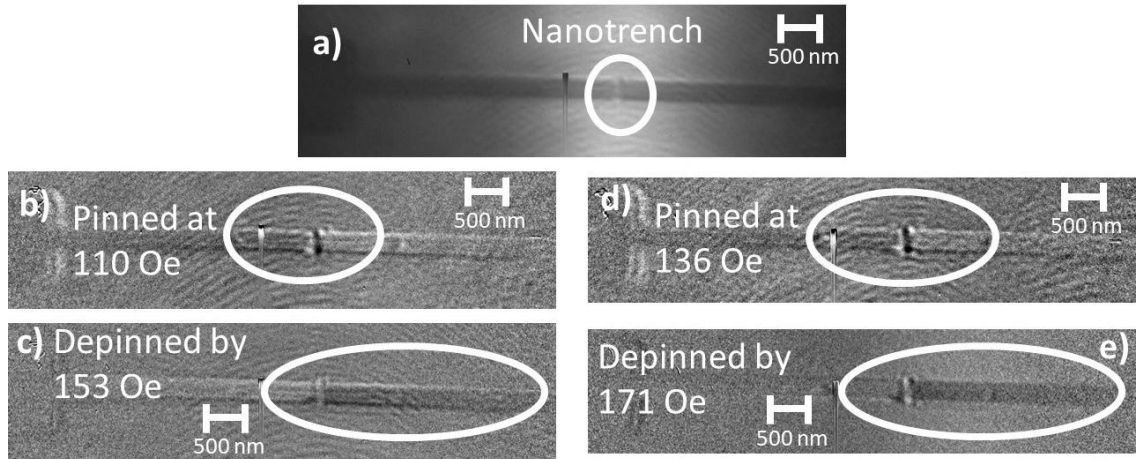


Figure 5.3.5: M-TXM images taken at the ALS facility of DWs pinning and depinning from the fabricated nanotrench in ALS wire C. a) raw unprocessed image to demonstrate nanotrench position. b) and c) divided images showing DW pinned and then propagated within a single hysteresis loop. d) and e) divided images showing DW pinned and propagated in a single hysteresis loop.

All three cases show clear experimental evidence supporting the proposed knowledge gap that DWs can be pinned by a vertically placed nanotrench and that AFM tip-based nanomachining can be used to pin and control the movement of magnetic DWs.

The three wires used in this section of the study were similar in dimensions while they exhibited nanotrenches with different depth. However, it was not possible to obtain sufficient data with small enough field steps in order to provide accurate depinning fields for the nanotrenches. The images shown figures 5.3.3, 5.3.4 and 5.3.4 show DWs depinning at 110-115 Oe, 153-171 Oe and 118-136 Oe for the 13 nm, 17 nm and 25 nm deep nanotrenches respectively. Thus, this clearly provides insufficient evidence to assess any relationship between nanotrench size and the corresponding pinning strength.

In chapter 4 an approximately linear relationship was found between the depinning field and the depth of the nanotrench. There are various reasons as to why these experimental results do not agree with the simulated results. A possible explanation relates to the nanowire dimensions. Whilst the dimensions are similar, they are not identical. As the simulations are carried out at zero temperature, it is unclear how relatively small variations in the nanowire size may affect the depinning fields of nanotrenches in different nanowires. Another possible explanation could relate to any imperfections in any of the nanowires. Whilst the nanowires are similar in size,

other conditions relating to the nanowires may not be. Variations in any possible imperfections may influence how the DW propagates through the wire and interacts with the nanotrench. Other factors relating to DW motion could include slight variations in the material properties, such as grain size, caused during the fabrication process.

In order to accurately assess the relationship between nanotrench dimensions and the pinning strength, ideally multiple sizes would be measured within the same nanowire. This would ensure that all other properties relating to the wire would be the same and the only difference would be the nanotrench itself. This aspect is the focus of the work reported in the next section.

5.4 Influence of the nanotrench depth on the DW pinning strength using thick nanowire

A narrower but significantly thicker nanowire, compared to the experiment reported earlier in section 5.2, was fabricated in an attempt to further investigate the relationship between nanotrench depth and pinning strength. It was decided to increase the thickness significantly as it provided much more material to machine in smaller vertical intervals whilst reducing the risk of cutting completely through and breaking the nanowire. An AFM image of the nanowire are shown in figure 5.4.1. The nanowire measured approximately 320 nm in width and 56 nm in thickness.

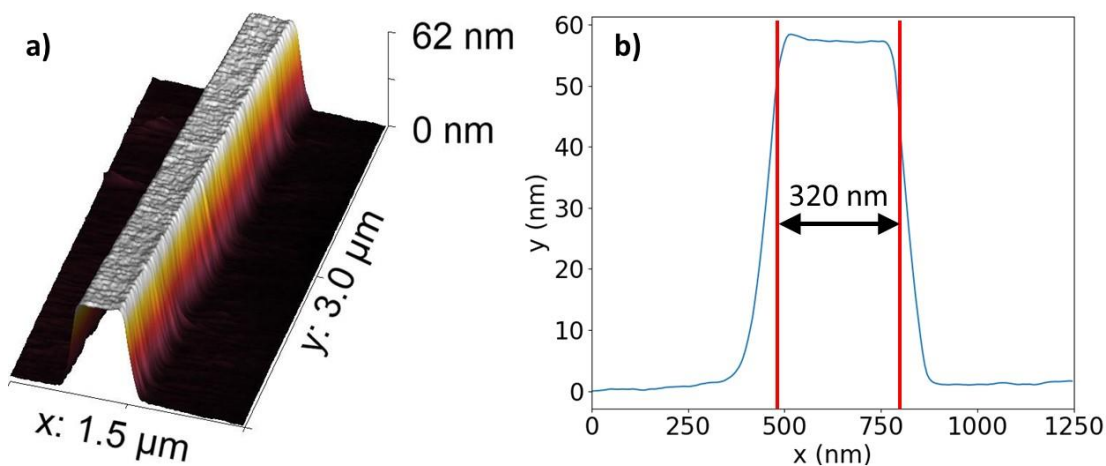


Figure 5.4.1: a) AFM image, b) Linescan showing the cross-section of 320 nm wide, 56 nm thick nanowire.

Experiments were conducted on this nanowire with a similar method to that applied to the 685 nm wide, 11.5 nm thick nanowire presented in section 5.2. AFM images of the resulting nanotrench at each machining stage can be found in figure 5.4.2.

The initial nanotrench was created by a series of scratches. A 4 μN scratch was first performed but resulted in minimal material being displaced. A further 4.5 μN scratch was carried out, but again with no significant nanotrench generated. Finally, three further 4 μN scratches were completed resulting in the first nanotrench found in figure 5.4.2 measuring 18 ± 1 nm deep.

Once the AMR data were recorded, two further 4 μN scratches were subsequently machined. This deepened the nanotrench to a depth of 25 ± 2 nm. Again, once AMR measurements were taken for this depth, a further four 4 μN scratches were implemented along the trench, this time resulting in an average depth of 30 ± 2 nm. At this stage it is clear from fig 5.4.2, that the nanotrench started forming some asymmetry as some material was removed from the nanowire outside of the main nanotrench. This is a factor to consider and will be discussed shortly. It is this asymmetry that contributes to the relatively larger error in the nanotrench depth. The values used are the overall average depth, however it is seen that the nanotrench deepens towards both edges of the nanowire.

At this stage, three further 4 μN scratches were conducted. These scratches were positioned to one edge of the nanotrench in an attempt to reduce the asymmetry created during the previous stage. This resulted in a nanotrench with an average depth of 34 ± 2 nm. However this failed to correct the asymmetry. In order to deepen the nanotrench at this stage, a total of seven 4 μN scratches were completed. This deepened the nanotrench to an average depth of 41 ± 1 nm. During this process, the affected region of the nanowire had also increased to approximately 550 nm in length.

AMR data were also taken for the nanotrench at this higher depth. Unfortunately, the nanowire was destroyed whilst being connected to the AMR set-up at this stage. It is suspected that either a surge of high current or a build-up of static charge occurred causing the central region of the wire to break. An SEM image of the broken nanowire can be found in figure 5.4.3. It is observed that approximately 244 nm of the nanowire, where the nanotrench was located, disappeared. This indicates that the material most likely vaporised due to a high current surge.

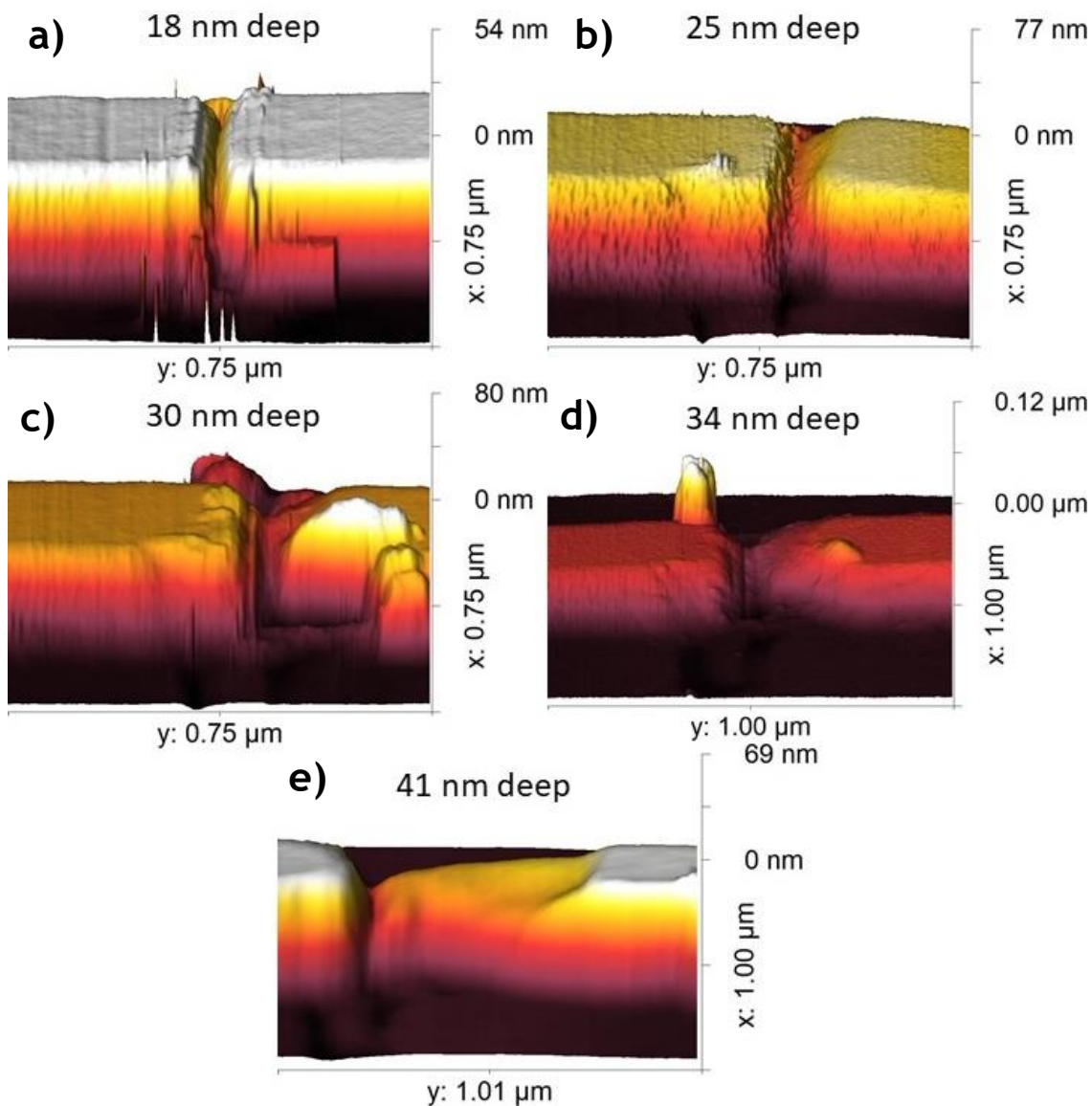


Figure 5.4.2: AFM images of the five distinct nanotrenches measured in the 320 nm wide, 56 nm thick permalloy nanowire. a) shows an 18 nm deep nanotrench resulting from a 4.5 μN and four 4 μN scratches. b) a 25 nm deep nanotrench from a further two 4 μN scratches. c) a 30 nm deep nanotrench from a further four 4 μN scratches. d) a 34 nm deep nanotrench from a further three 4 μN scratches. e) a 41 nm deep nanotrench following a further seven 4 μN scratches.

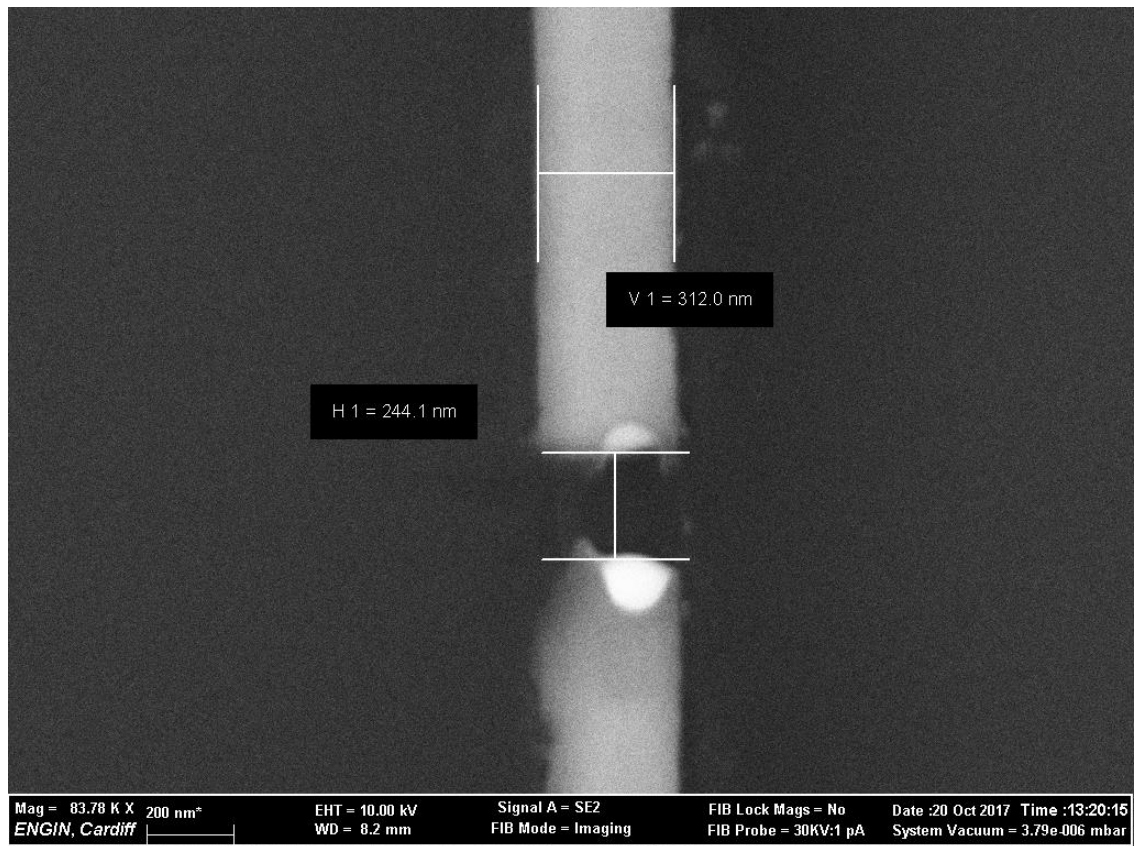


Figure 5.4.3: SEM image of the broken 320 nm wide, 56 nm thick nanowire

Example AMR data for various nanotrenches are shown in figure 5.4.4. These data are presented in arbitrary units and offset to aid visibility for comparison. This figure provides a clear indication that the size of the nanotrench does influence how DWs interact with the site.

The bottom, blue colour, trend represents the nanowire before a nanotrench had been introduced. It is seen that the resistance drops in value at very small fields (around 6 Oe) and remains at a reduced value before jumping back to the uniform resistance value at around 50 Oe. This implies that a DW moved into the region of the nanowire and it pinned at some defect created in the nanowire during the fabrication process. The decrease in resistance is observed in every case, even with the presence of the nanotrench. This indicates the value of the injection field for the nanowire is approximately 6 Oe. That was the value of the applied field that causes a DW to form and be injected into the nanowire. Commonly the resistance would increase around this field value. As the resistance remains reduced until approximately 50 Oe, it indicates the presence of an artefact pre-existing in the nanowire able to pin DWs that remained unaltered throughout the process.

With the introduction of a nanotrench, the AMR data shows a change in behaviour. At the field where the resistance originally increased, showing a total magnetisation switch in the nanowire, the resistance shows a further decrease. This implies that the DW remained within the nanowire, but propagated along it, causing more of the nanowire to become magnetised away from its long axis. At this point it is reasonable to assume that the DW was pinned at the nanotrench. The field at which the resistance suddenly increases in value is taken to be the depinning field. Figure 5.4.4 shows that this jump occurred at increasingly larger fields as the nanotrench depth was increased.

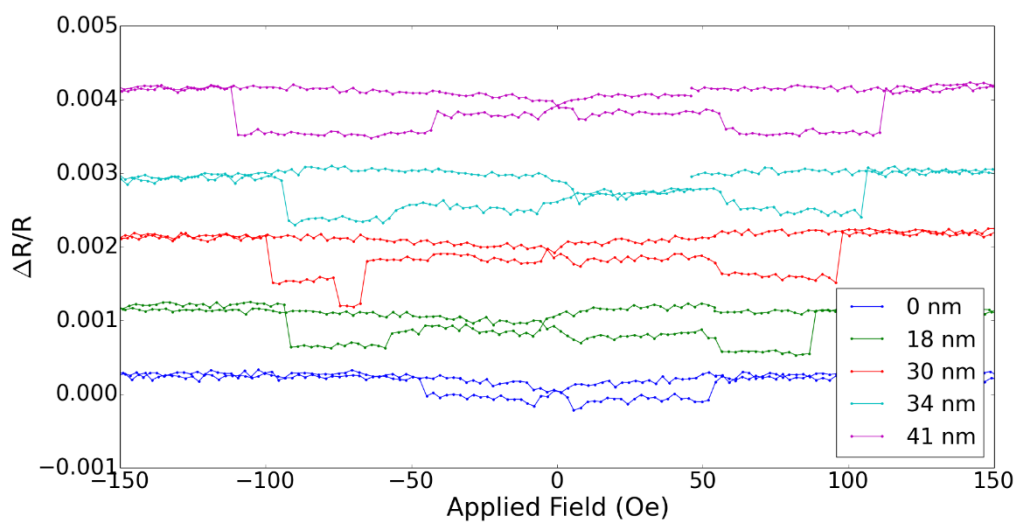


Figure 5.4.4: Examples of AMR data taken for the 320 nm wide, 56 nm thick nanowire for various nanotrench depths.

A summary of the AMR data taken for this nanowire can be found in table 5.2. This table contains the number of data points taken at each nanotrench depth, along with the mean and standard error for the depinning fields.

Table 5.2: Summary of depinning field results for the 320 nm wide, 56 nm thick permalloy nanowire.

Nanotrench depth (nm)	Number of observations	Mean depinning field (Oe)	Standard error of the mean depinning field (Oe)	T test p value to previous nanotrench
0	15	51.8	1.7	
18 ± 1	9	87.7	1.6	2x10 ⁻¹²
25 ± 2	2	90.4	9.0	0.86
30 ± 2	406	94.1	0.4	0.82
34 ± 2	160	98.5	0.4	1x10 ⁻¹¹
41 ± 1	172	113.2	0.2	2x10 ⁻⁷⁸

A plot of the depinning field against nanotrench depth is shown in figure 5.4.5. The simulations performed in chapter 4 suggested that the depth of a nanotrench has larger influence over the pinning strength than its length. Whilst the length of the nanotrench does change as the depth is increased, the depth is the focus of this study. It is seen in figure 5.4.5 that there is a significant increase in the depinning field with the introduction of the nanotrench. All of the subsequent data points show that the depinning field increases as the nanotrench depth does. The four data points found between 18 and 34 nm appear to show an approximately linear relationship. For the final data point (i.e, for the larger depth), the depinning field increased by a relatively larger amount. This could be due to the nanowire being altered beyond the initial nanotrench itself. As previously discussed, a larger asymmetry developed within the nanotrench as the depth increased. An AFM scan of that particular nanotrench also revealed that the nanowire had material removed across a 550 nm region. As this is relatively large compared with the original nanotrench length, it is likely that this relatively important geometric variation also influenced the site pinning strength when compared with previous nanotrench dimensions.

In order to assess how these experimental results compare with the computational model created in chapter 4, simulations were carried out on a nanowire of similar dimensions. One set of simulations were completed with square approximations for the nanotrench geometry whilst another set used triangular simulations in an attempt to observe which would provide a closer match with the experimental results. All simulations were applied on a 320 nm wide, 55 nm thick nanowire with a 5x5x5 nm³ cell size. Figure 5.4.6 contains the plot for all three datasets. As the

nanotrench depth is increased, there is no drastic change in its length. As this is the case, the following simulations were carried out using nanotrenches of constant length. The square nanotrench simulations were all conducted with a nanotrench length of 100 nm, in an attempt to approximately replicate the amount of material removed, whilst the triangular cases had a surface length of 160 nm, similar to the values of the experimental nanotrenches.

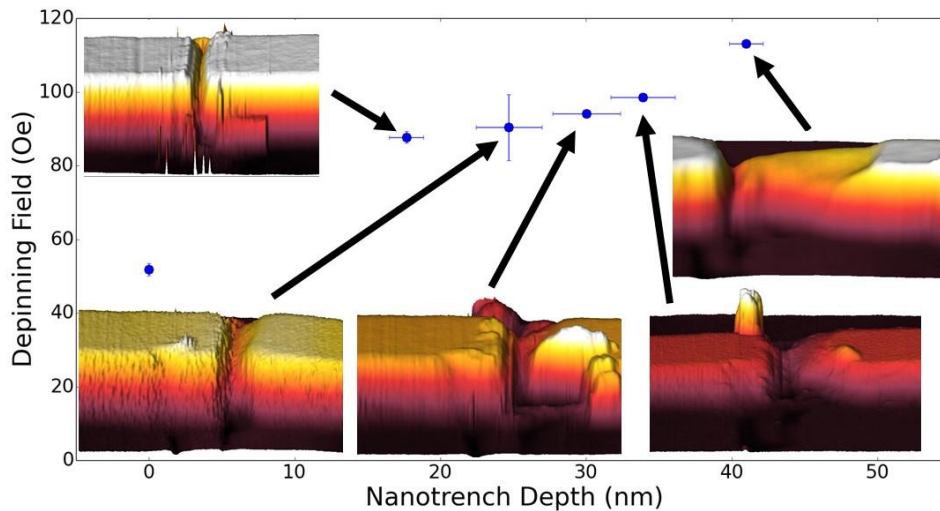


Figure 5.4.5: Plot of depinning field against nanotrench depth for the 320 nm wide, 56 nm thick nanowire. Error bars represent the standard error on the mean. Data point at 0 nm indicates the switching field before the presence of a nanotrench and is included as a reference.

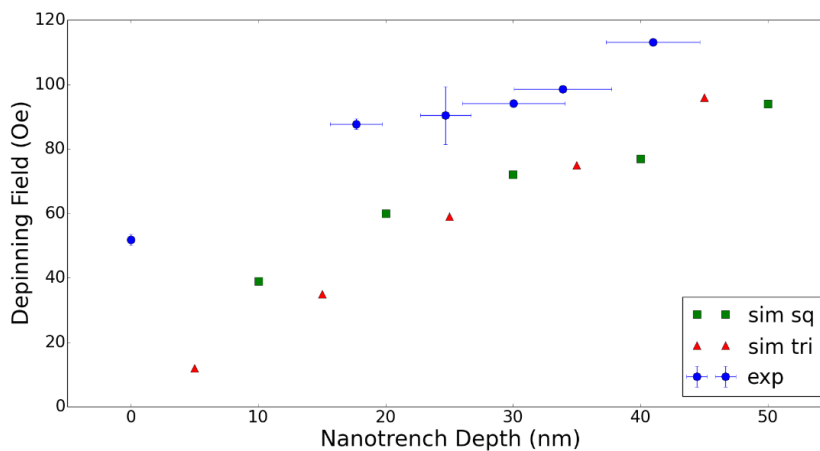


Figure 5.4.6: Experimental and computational results for the 320 nm wide, 56 nm thick nanowire.

The first observation to note from fig 5.4.6 is that the simulation results for both cases always predict lower depinning fields compared to these measured experimentally. It should be said that the experimental and simulated values were not expected to match due to the simulations being conducted at 0K temperature. However, it is normally expected that the values of the experimentally-measured depinning field should be lower than the simulated ones due to thermal fluctuations. The discrepancy observed here may be explained by the fact that the material parameters used in the simulations do not exactly match the actual physical values, and in particular, the damping parameter. In these simulations, a damping coefficient of 0.5 was used in order to speed up simulations whereas the damping coefficient to accurately simulate permalloy is 0.01-0.02 [24]. A previous study by Broomhall and Hayward [188] found that increasing Gilbert damping acted to reduce the stochasticity of DW pinning along. Increasing the damping also had the ability to reduce the strength of depinning fields. This could provide an explanation of how the simulated values for the depinning fields found in this study are lower than those found experimentally. Nevertheless, given that the simulation results are important to observed qualitative trends, the results presented here are still relevant for comparison.

In terms of general trend, the data simulated using the computational models do produce similar results to the experimental dataset. However, whilst the triangular case is designed to more accurately match the experimental nanotrenches, the square simulations appear to produce a more matching trend. In addition, the difference between the simulated and experimental data in the triangular case tended to gradually reduce with the increase in the nanotrench depth to the point where this difference became smaller than that of the rectangular case. In fact, in the square case, the difference between experimental and computational remained approximately constant throughout.

This general agreement observed in terms of trend between the computational model and the experimental data provides evidence to support the finding that deeper nanotrenches pin magnetic DWs more strongly. The experimental trend generally supports simulations suggesting that this relationship is approximately linear, however more datapoints are needed to confirm this.

It is worth noting at this stage that all simulations conducted in this study do not account for the presence of any “pile-up”. This was done as the amount of pile-up that occurs during the creation of a nanotrench is unpredictable and not always

present. The previous study [123] and the computational and experimental results all indicate that the depth of a nanotrench into the nanowire is highly influential on the depinning fields. Therefore to save time on running multiple versions of simulations accounting for different sets of pile-up, it was decided to ignore the presence of pile-up computationally. The analysis of the effect of pile-up on the depinning strength is a subject worthy of study.

5.5 Investigation of an alternative sample design for multiple parallel measurements

With promising results using the 10 nm thick wire and the 56 nm thick nanowire, the study progressed with the aim of obtaining similar datasets for nanowires of varying dimensions in both width and thickness. In an attempt to speed up the experimental process, a new device layout was designed and created. An SEM image of this new design can be found in figure 5.5.1.

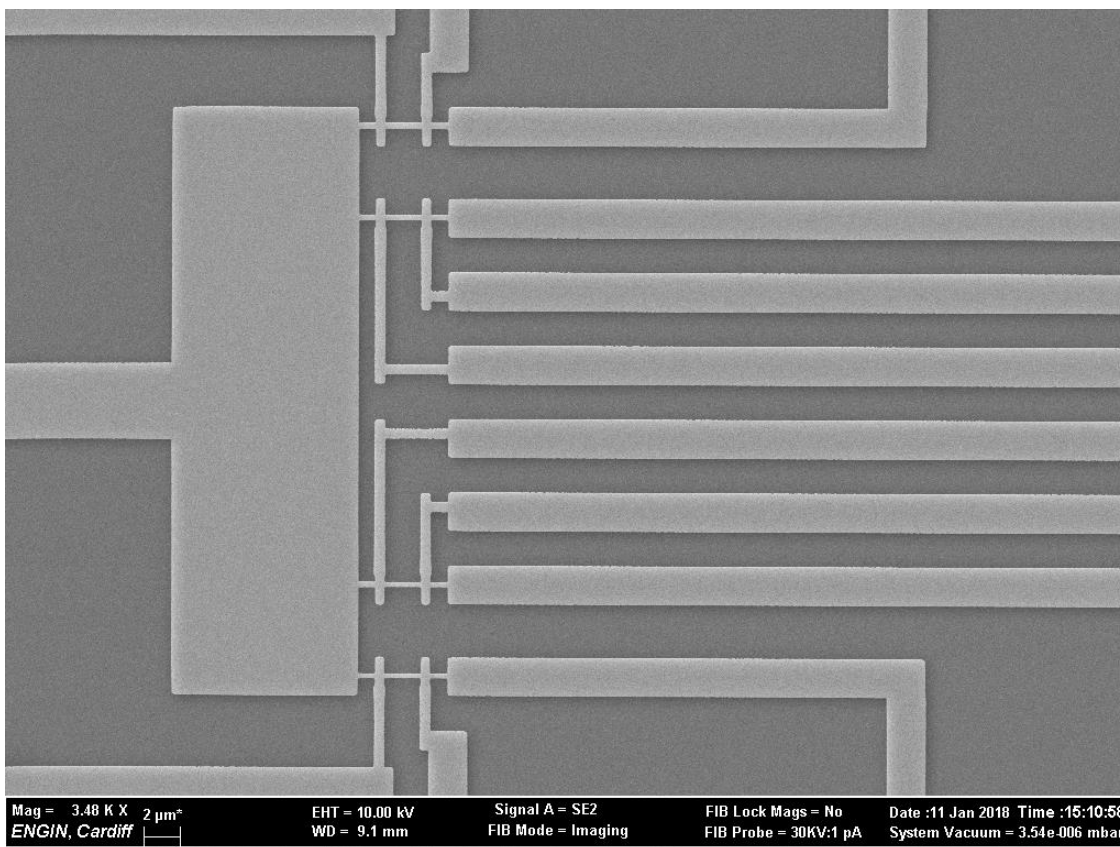


Figure 5.5.1: SEM image of the newer device design.

The motivation for the new design was to reduce the number of electrical contacts required to enable all four nanowires on the chip to be simultaneously connected for AMR measurements. This would need to be achieved whilst leaving enough space for

the AFM probe to reach access surface for machining without having to remove the wire contacts necessary for the AMR set-up. A key change was that, with previous experiments, only one wire at a time was wired and so could be measured in the AMR set-up. The new design would allow all four nanowires to be machined and then measured simultaneously, speeding up the overall experimental process. In order to save space, the device was designed such that there would be one common current input to all four nanowires. This would save three wires needing to be connected, freeing up the space along one edge of the chip. This would leave the space required for the AFM probe to approach and reach the surface. To control the current path through the required nanowire at each stage, three additional wires were designed and connected to each nanowire. These would provide the remaining current path along with the two voltage probes.

The initial sample creation was successful providing a wider range of nanowire widths. SEM images of the four nanowires measured on one chip are shown in figure 5.5.2. The thickness of these nanowires ranged between 53 and 59 nm.

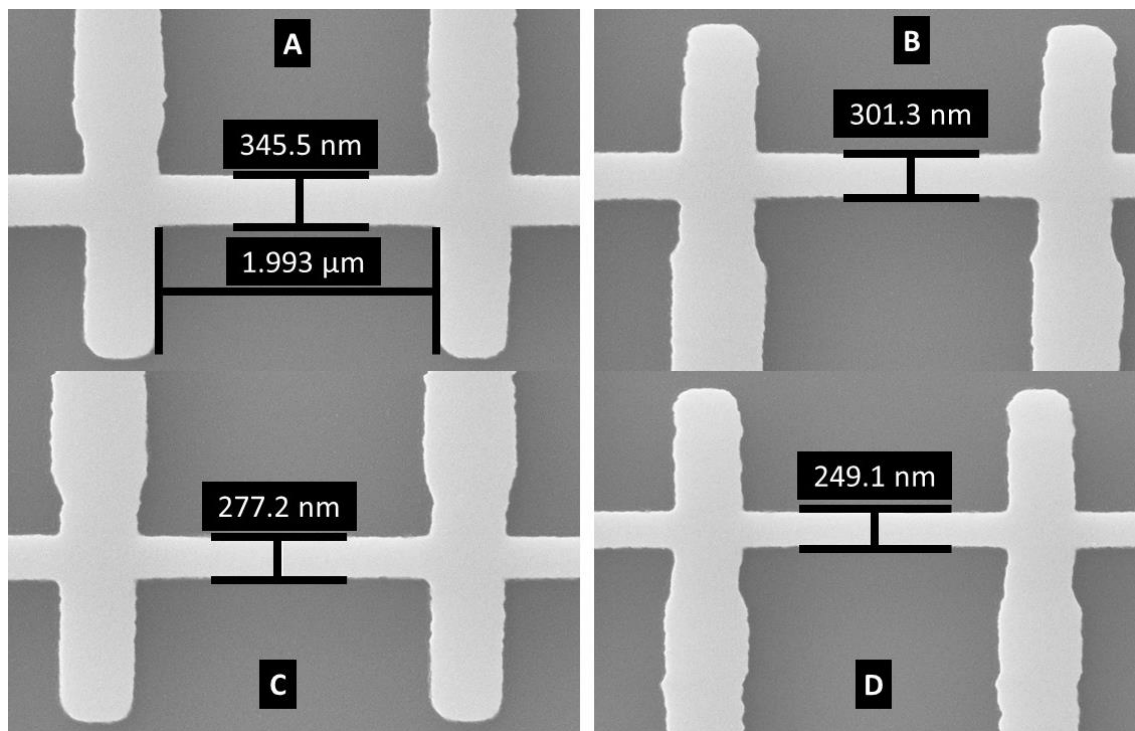


Figure 5.5.2: SEM images of the four nanowires within the new design.

AMR measurements were successfully taken for each of these wires. However, the shape of the data in most cases was very different to previously measured nanowires. Examples of AMR data for each of these nanowires are shown in figures 5.5.3-6.

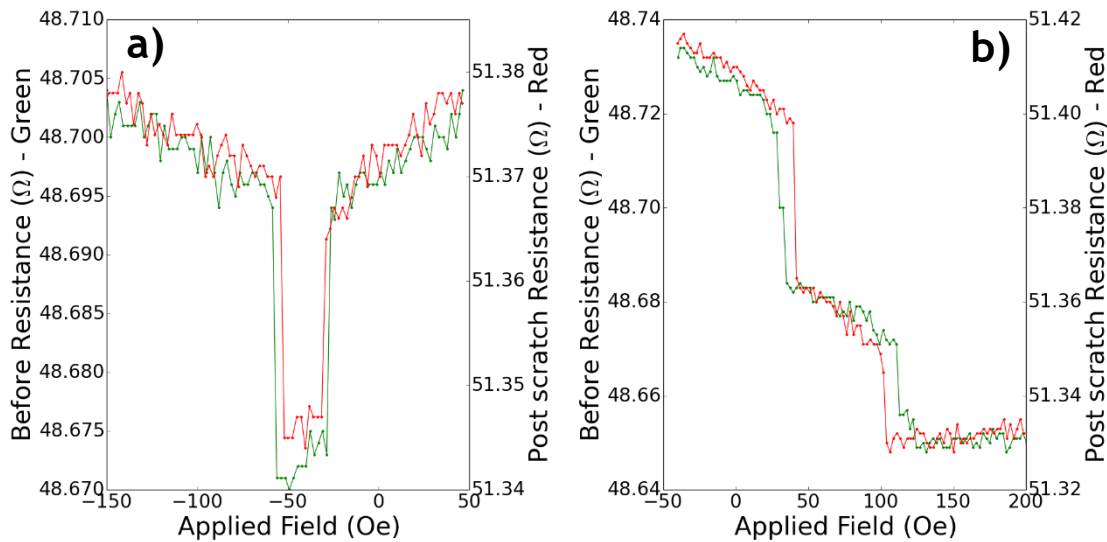


Figure 5.5.3: Example of AMR data for wire A in the new device. a) shows the field passing from positive into negative field values, whilst b) shows the opposite. In both plots, the left y-axis represents the resistance before the introduction of a nanotrench, the right y-axis shows the resistance after.

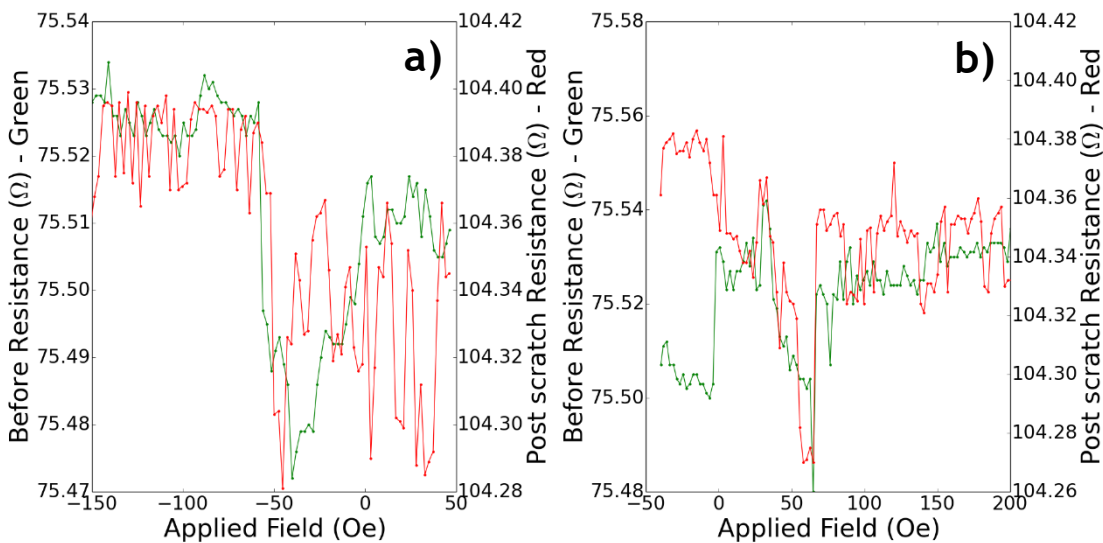


Figure 5.5.4: Example of AMR data for wire B in the new device. a) shows the field passing from positive into negative field values, whilst b) shows the opposite. In both plots, the left y-axis represents the resistance before the introduction of a nanotrench, the right y-axis shows the resistance after.

Data for wire A is shown in figure 5.5.3 and displays a recognisable AMR trend when the field passing through the 0 point in the negative direction, decreasing in value before jumping back to the previous resistance. Whilst increasing it shows a shape very different. The resistance shows an initial drop at low fields before reducing

further. This gives an indication that the voltage probes are not ideally positioned or sized to detect the magnetisation just within the nanowire.

Wire B data is shown in figure 5.5.4, it shows an AMR trend that is similar to what is expected for a nanowire, however it is relatively noisy. Thus, it is difficult to observe the presence of a DW within the nanowire.

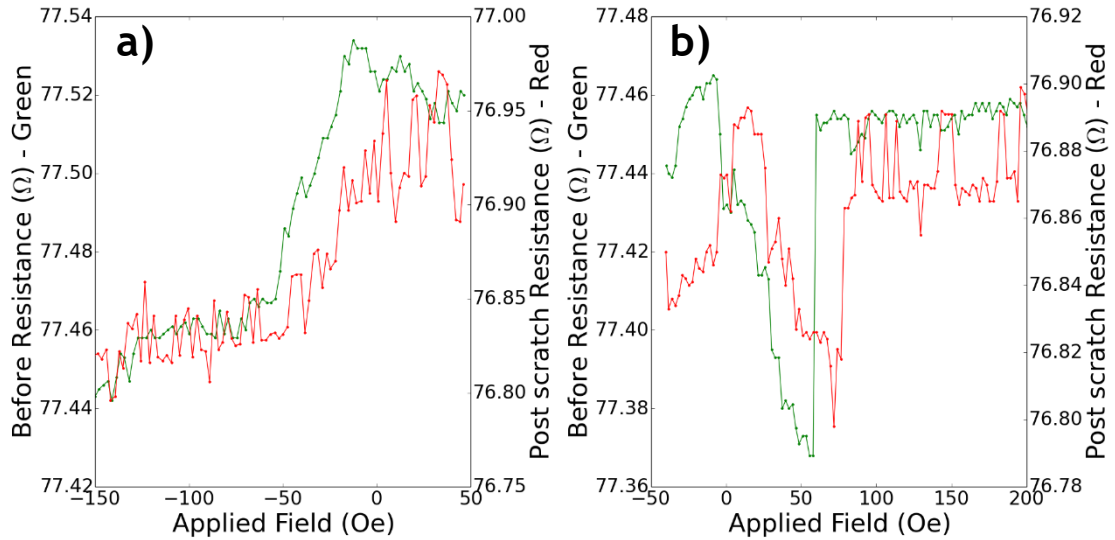


Figure 5.5.5: Example of AMR data for wire C in the new device. a) shows the field passing from positive into negative field values, whilst b) shows the opposite. In both plots, the left y-axis represents the resistance before the introduction of a nanotrench, the right y-axis shows the resistance after.

AMR data relating to wire C is found in figure 5.5.5 and is similar to wire A such that one half of the trend is as expected. As the applied field increases, there is a clear decrease in resistance, followed by a sharp jump at a higher field. The trend beyond this point appears to show the resistance at a steady value. When decreasing the field however, there is a gradual decrease in the resistance which does not increase until the field is applied back in the positive direction.

Finally figure 5.5.6 shows AMR data taken for wire D. This particular dataset is extremely noisy and much more volatile than any of the datasets taken for the other three nanowires. The current was increased for this nanowire in an attempt to reduce the noise, but this was the most it could be reduced by without applying a current that would risk melting the nanowire. Once again, despite the noise, the overall trend of the data is very different to what is expected as the resistance starts low and jumps in value as the field is reduced. In addition to this, the resistance does not return to the value corresponding to uniform magnetisation in

positive fields. When the field is increased, the resistance gradually reduces without increasing in value until passing back through 0 field as in wire C.

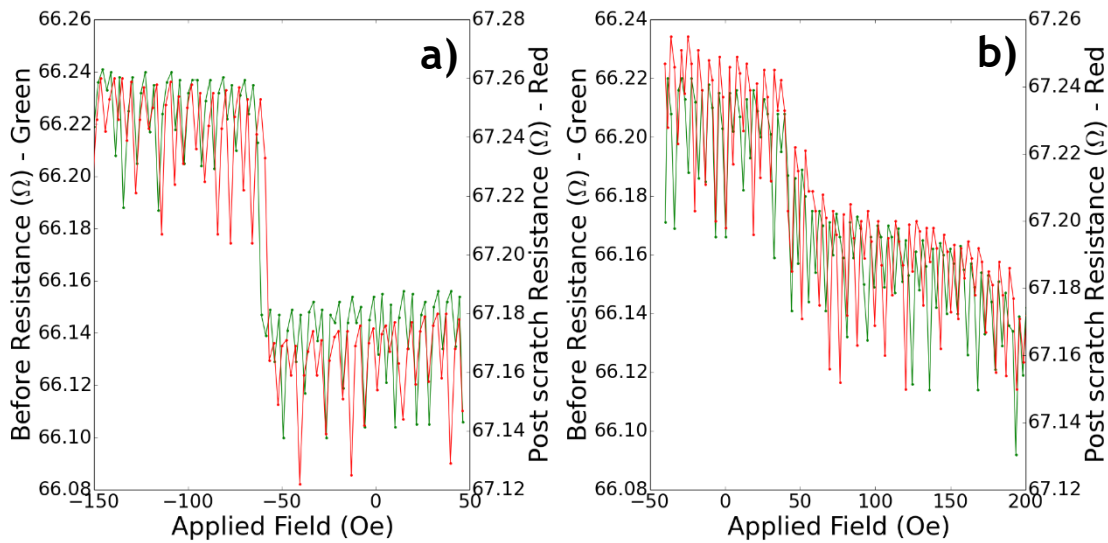


Figure 5.5.6: Example of AMR data for wire D in the new device. a) shows the field passing from positive into negative field values, whilst b) shows the opposite. In both plots, the left y-axis represents the resistance before the introduction of a nanotrench, the right y-axis shows the resistance after.

The overall AMR trends imply key differences within the device design making it more difficult to properly observe the magnetisation behaviour within a nanowire. One difference that may be key from previous devices is with regards the nanowire length. All previous nanowires measured approximately 10 μm or longer in length while the nanowires in this new device measured only 2 μm in between the voltage probes. As the nanowires in this case are relatively very thick, there is a possibility that any DWs occurring in these nanowires are the proposed Landau DWs presented by Nguyen and co-workers[28]. As these DWs are relatively very long, it is possible that they may occur but not be contained within the relatively short nanowire. This may affect the observed trends in the AMR data.

Another possible factor may be the relatively large voltage probe pads. The pads in this instance are larger than those previously used. This factor combined with the decreased nanowire size may cause the voltage probes to act as a thin film within the measured region. As the probes themselves are comparable in size to the nanowires, they may affect the shape of the AMR data as the magnetisation reverses within them. This would make the observation of changes in magnetisation relating only to the nanowire difficult.

Another device was made simultaneously along with this one. The design was identical and located on the same wafer during the fabrication process. Leading to nanowires of similar thickness and widths ranging between 275 - 400 nm. These nanowires were also wired and measured in the AMR set-up. The resulting AMR trends were very similar, including the same equivalent wire D producing extremely noisy datasets. This provided further evidence that there are most likely issues with the new design itself.

Despite these unusual AMR trends, nanotrenches were created in all 4 nanowires on the first chip, in an attempt to observe any differences they would generate in the AMR data. The resulting nanotrenches in each nanowire can be seen in figure 5.5.7. The average depths for the nanotrenches in wires A, B, C and D were approximately 16 nm, 45 nm, 5.5 nm and 16 nm, respectively. The significantly deeper depth for the nanotrench in wire B was not intentional. During the machining process a error occurred within the AFM software. It is believed that this error caused a relative misalignment with the photo-sensitive photo diode (PSPD) within the AFM and so a much larger force was applied during the scratch than intended.

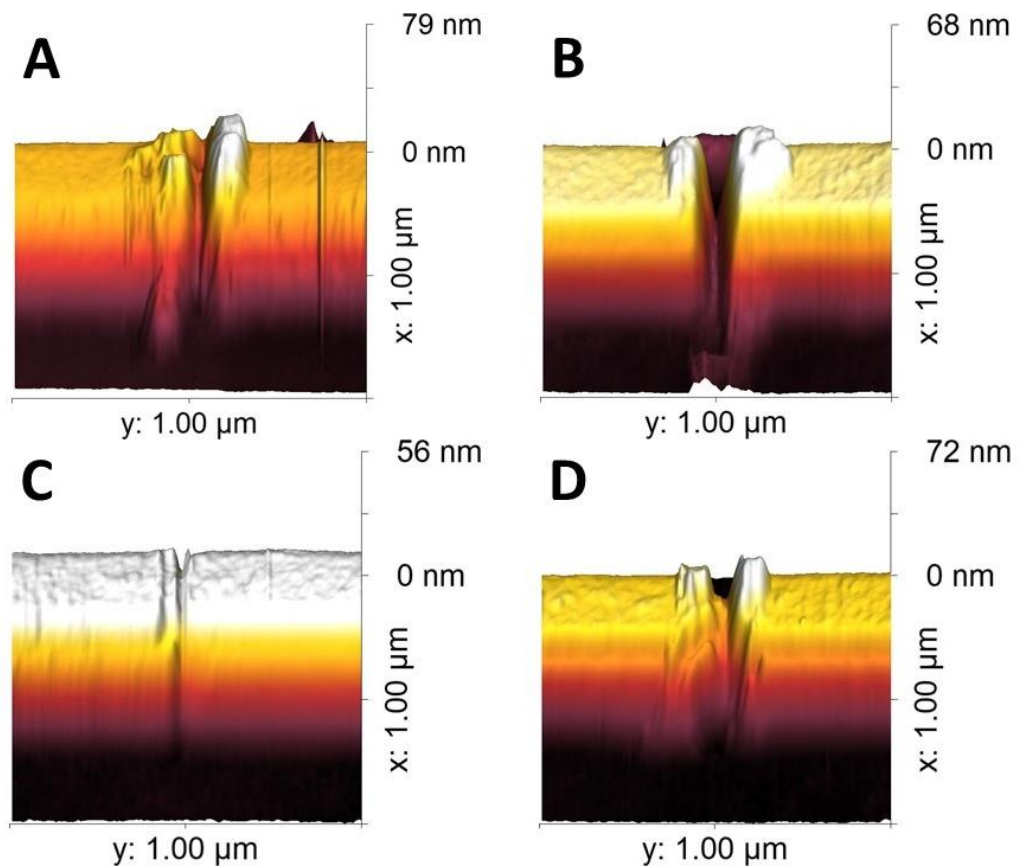


Figure 5.5.7: AFM images of the generated nanotrenches in all four nanowires of the new sample design.

The data taken after these nanotrenches were created are shown in figures 5.5.3-6 represented by the red data lines with the resistances given by the y-axis on the right. The effects of the introduction of a nanotrench varies for each nanowire. In some cases, the field at which some events occur increase in magnitude, as expected. In some cases however, the trend moves towards a smaller absolute field value.

In order to continue the study and provide more data points, the nanotrenches were to be further machined as done previously. However, before this was possible the resistance readings related to wires B and D caused an error reading following a gap in measurements being taken. On further inspection with a microscope, it was found that the central region of wire B was missing, similar to the case with the 320 nm wide, 56 nm thick nanowire. Wire D had also broken but not within the nanowire itself. An AFM image showing wire D following this break is found in figure 5.5.8. It can be seen that the nanowire itself has become deformed whilst the extend region of the nanowire beyond the voltage probe has disappeared. This could have been the result of a static leading to a current surge. It is possible that there may have been some defect or issue with the device design that caused a weakness within this section of the nanowires. This defect may have been the cause of the original noise found in the AMR data for that specific nanowire.

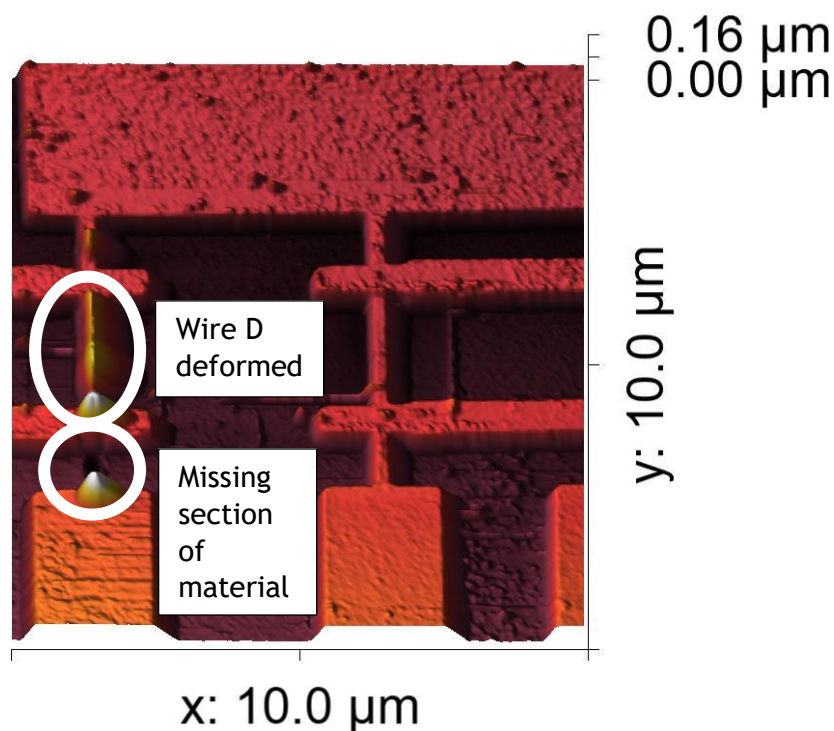


Figure 5.5.8: AFM image of nanowires D (left) and C (right) following wire D breaking.

Following this the nanotrenches in wires A and C were machined further in order to obtain a second data point for each of them. However, on reintroduction to the AMR set-up both remaining nanowires were destroyed. As the previous nanowire had gone through multiple cycles of machining and AMR measurements, it is likely that the relatively easy destruction of the remaining nanowires was related to the sample design.

Along with this sample, a second device with an identical design was created on the same wafer leading to very similar thicknesses. The nanowire widths were patterned such that the widths were very similar to the first sample. The four nanowires on the second sample were measured in the AMR set-up. The resulting AMR trends were very similar to the nanowires on the first sample. Each of the four nanowires showed similar data sets to the counterparts from the first sample. These results support the theory that the differences observed in the AMR data are due to the sample design. These nanowires were scratched and following AMR measurements were made, with similar outcomes to the first instance. Unfortunately at this point the AFM system became faulty and a long delay occurred before it could be repaired. Due to the large time interval between the initial machining and the point at which the AFM was made operational again, it was decided that these nanowires could no longer be used. This was due to the possibility that any results may have been corrupted by any possible oxidation of the sample and accurate nanotrench measurements may no longer be possible. At this point, no further work was completed on this alternative device design.

5.6 Additional AFM nanomachining experiments for the exploration of future studies

In preparation for the experiments to be carried out at the Advanced Light Source facility, numerous nanowires were fabricated. The experiments discussed in section 5.3 involved creating nanotrenches and observing DWs pinned at them. For practical reasons, it was not possible to conduct the ALS experiments with the objective of deepening the nanotrench on the same wire and to observe changes in depinning fields. However, in order to maximise the beamtime available at the ALS facility, AFM nanomachining was used to create more complex features within the nanowires. This was done in an attempt to observe how these features may influence the structure and motion of DWs.

The first of these structures considered related to computational cases where the length as well as the depth was varied. The intention was to create a nanotrench with an extended length. To create such a feature, a series of ten 4 μN scratches were conducted on a nanowire measuring approximately 445 nm wide and 42 nm thick. Each scratch was performed across the width of the nanowire, spaced approximately 50-60 nm apart such that the total length was approximately 500 nm. An AFM image of the resulting feature is shown in figure 5.6.1. The average linescan along the length of the nanowire is shown in figure 5.6.2.

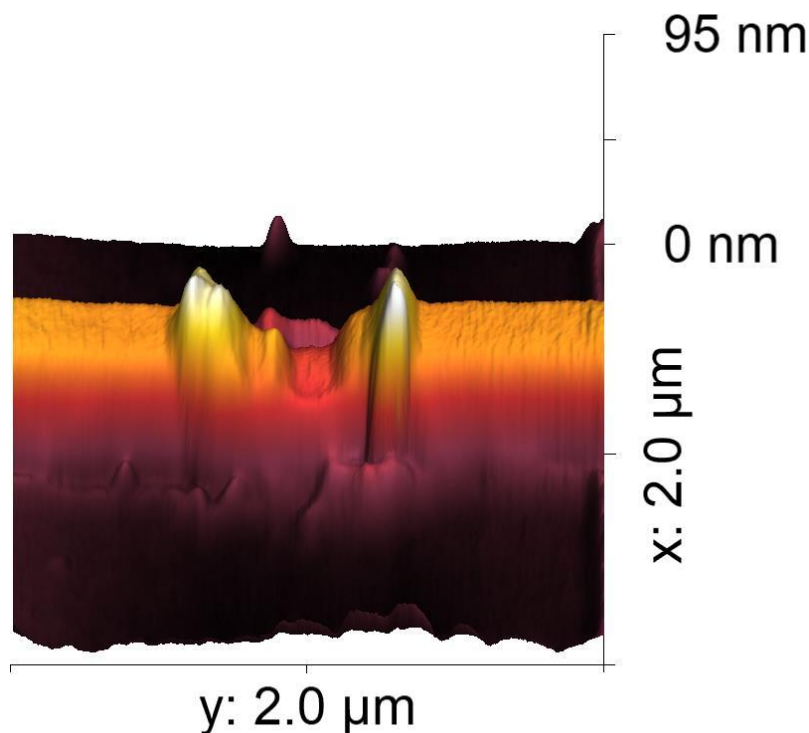


Figure 5.6.1: AFM image of extended nanotrench created in a 445 nm wide, 42 nm thick nanowire.

It is seen that whilst the resulting nanotrench does not span the full 500 nm, its length is significantly larger than those created previously. The deepest region of the nanotrench measured approximately 13 nm below the surface of the nanowire. In previous cases the nanotrench floor was very small as the overall shape approximated a triangle. In this instance the nanotrench floor measured approximately 140 nm in length. As the sidewalls are angled, at the level of the surface of the nanowire, the total length reaches approximately 240 nm. From the AFM image and the average linescan, it is clear to see that there are very large amounts of pile-up located at each end of the extended nanotrench. This may be a factor in any DW interactions.

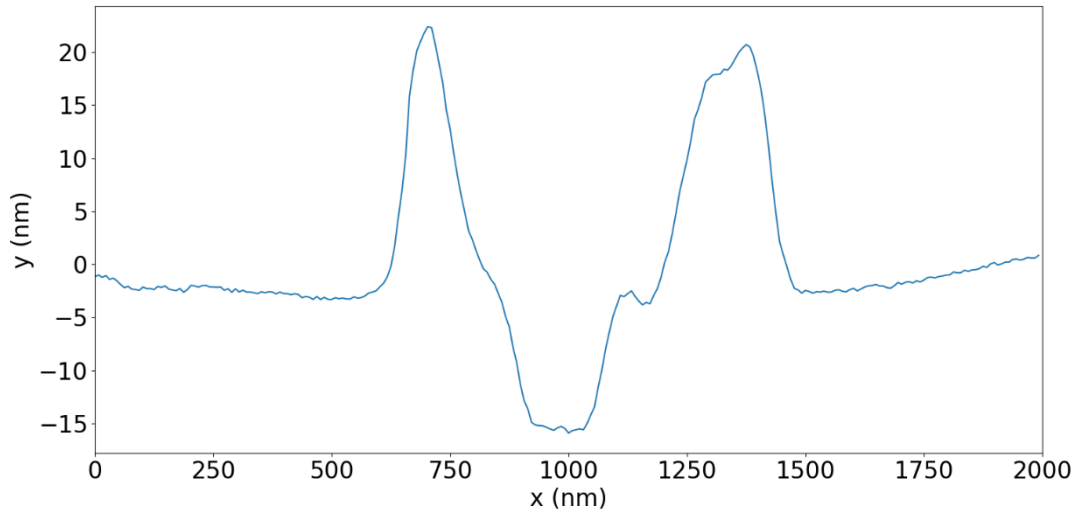


Figure 5.6.2: Average linescan of extended nanotrench created in a 445 nm wide, 42 nm thick nanowire.

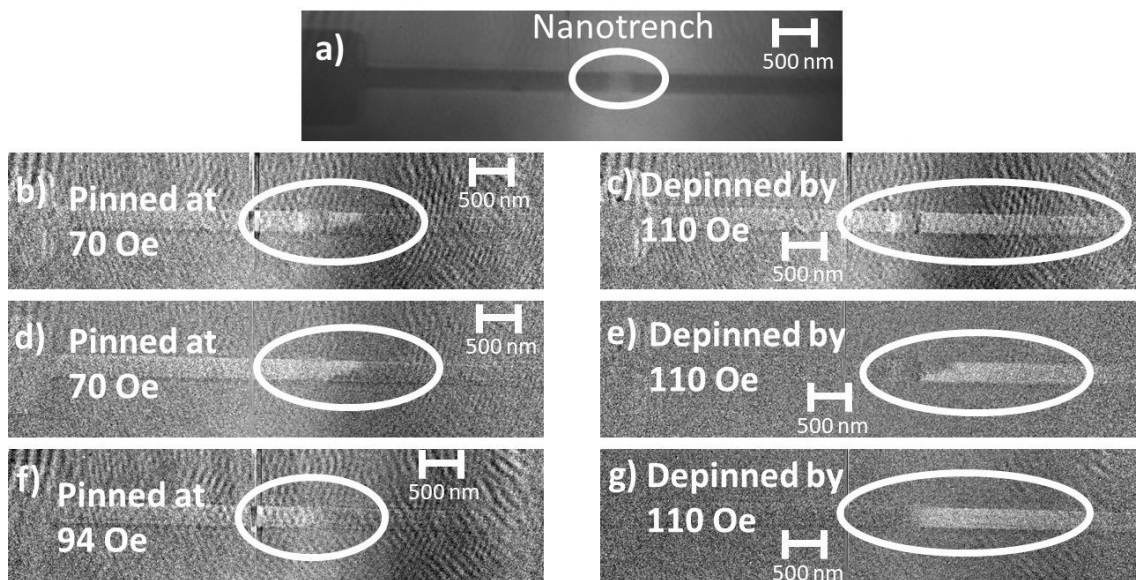


Figure 5.6.3: M-TXM images taken at the ALS facility of DWs pinned at the fabricated extended nanotrench in a 445 nm wide, 42 nm thick nanowire. Each row of images are taken from separate hysteresis loops. a) raw unprocessed image to demonstrate nanotrench position. b) and c), d) and e), f) and g) are pairs of divided images showing DW pinned and then propagated within separate hysteresis loops.

Figure 5.6.3 contains various images displaying DWs pinned at the extended nanotrench on the left and the corresponding images following the DW propagated on the right. In some of the images, it can be seen that the DW pinned at the extended nanotrench becomes extended over a relatively large length. Whilst some DW structure was observed in previous nanowires, the size of the DW appears to be

larger in these images. This gives an indication that this extended nanotrench may pin the DW over a larger range causing the DW itself to stretch across a longer section of the nanowire.

The second experimental feature created was inspired by the resulting asymmetry in the nanotrench created within the 320 nm wide, 56 nm thick nanowire. The intention in this instance was to create an L shape feature imprinted onto the top surface of the nanowire. This was done by creating an initial nanotrench, then removing some material across the nanowires width for an extended region of the wire length from the location of the nanotrench. To generate this feature, an approximately 570 nm wide, 57 nm thick nanowire was used. Initially, four 5 μN scratches were performed to create a standard nanotrench approximately 17 nm deep. Once this was achieved, a series of three 5 μN scratches were performed across the nanowire, from the centre of the nanowire out towards its edge. These sets of scratches were applied similarly to those in the extended nanotrench case. AFM images of the resulting feature can be seen in figure 5.6.4.

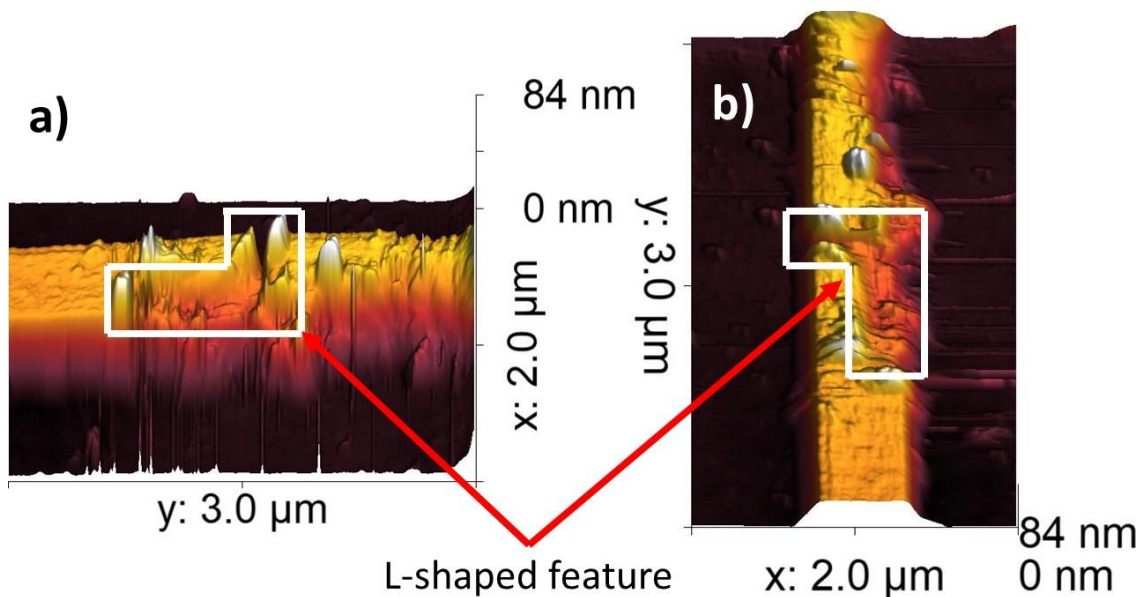


Figure 5.6.4: AFM images a) side-view, b) top-down view of L-shaped feature created within a 570 nm wide, 57 nm thick nanowire. White outlines to guide the eye to the overall shape of the feature.

As figure 5.6.4 shows, an L-shaped feature was achieved. Material was removed creating a lower levelled platform along the nanowire width. A linescan along this region is shown in figure 5.6.5. This platform occurs across approximately 200 nm of the nanowire surface and has a thickness approximately 17 nm less than the rest of

the nanowire. This region of the nanowire spans approximately 800 nm along the nanowire's length.

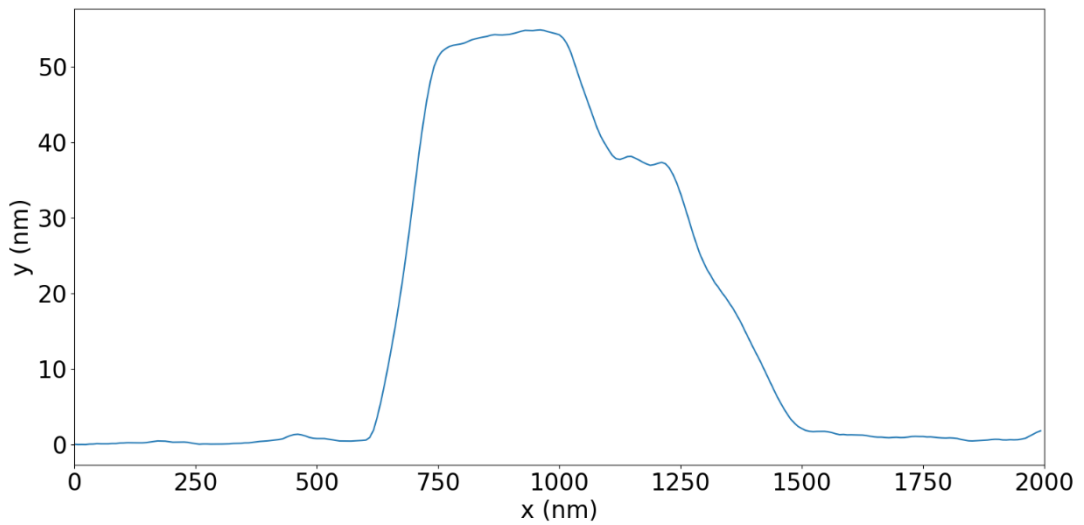


Figure 5.6.5: Plot of linescan across the width of the 570 nm wide, 57 nm thick nanowire displaying the thickness change across the L-shaped nanotrench.

Images taken of the magnetisation of this nanowire at the ALS facility are displayed in figure 5.6.6. In all of the images shown in figure 5.6.6, it can be seen that the DW structure spans at least the length of the created pinning site. An approximate L-shape can be observed at the boundary between the magnetisation directions. This give a possible indication of potential applications of AFM tip-based nanomachining for further control and manipulation of DW movement and structure.

The final nanowire presented in this study does not feature any nanotrenches across the whole width of the nanowire as done previously. The possibility of controlling the DW movement along the nanowire was considered as opposed to only stopping the DW at one site. An idea was proposed that indentations could be created at the edges of the top surface to act as pinning sites along the nanowire length. For this case, an approximately 560 nm wide, 50 nm thick nanowire was used. The design intention was to create indentations on alternating edges of the nanowire spaced along its length. Attempting to achieve this, four sets of five 5 μ N scratches were performed. Each set of scratches began in the centre of the nanowire and moved outwards, to not remove material along the entire width. This was done in four positions, in alternating directions, spaced approximately 500 nm between sets. Figure 5.6.7 shows AFM images of the results.

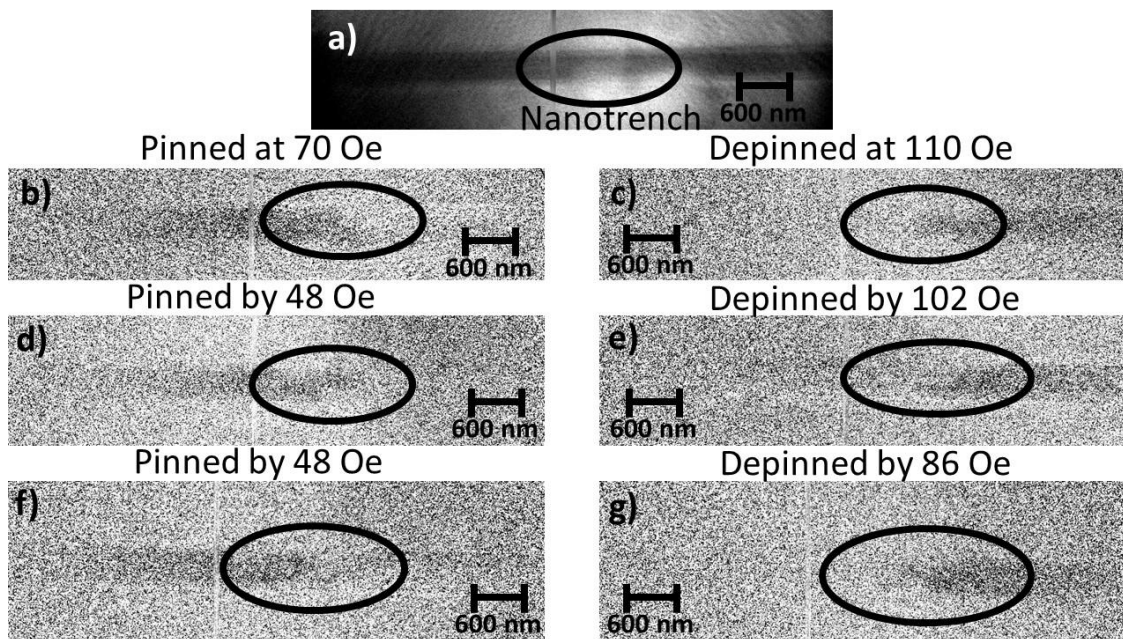


Figure 5.6.6: M-TXM images taken at the ALS facility of DWs pinned at the fabricated L-shaped nanotrench in a 570 nm wide, 57 nm thick nanowire. Each row of images are taken from separate hysteresis loops. a) raw unprocessed image to demonstrate nanotrench position. b) and c), d) and e), f) and g) are pairs of divided images showing DW pinned and then propagated within separate hysteresis loops.

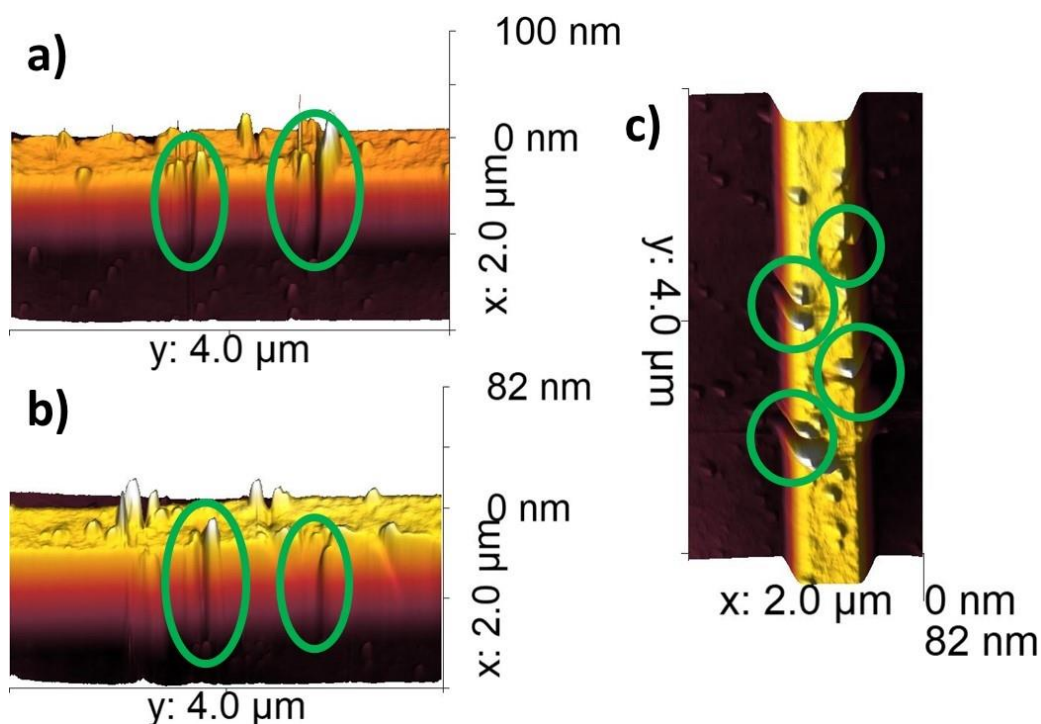


Figure 5.6.7: AFM images showing a) and b) side-views, c) top-down view of the alternating indentations created along a 560 nm wide, 50 nm thick nanowire. The green circles are to guide the eye to highlight the features.

Figure 5.6.7 displays a series of generated indentations along the length of the nanowire. Unfortunately, the resulting features did not match exactly what was intended. In particular, the aim was to create a set of indentations where the thickness would be explicitly reduced by some value as seen in the L-shaped nanotrench. The resulting features however show a more gradual change in thickness at the edge of the nanowire. Whilst this is not what was intended, the features should still act as pinning sites. The indentations varied in width across the wire, the largest feature spanned up to 350 nm of the nanowire width, whilst the others spanned 230 nm, 165 nm and 100 nm. Images were taken at the ALS facility and some of them are reported in figure 5.6.8.

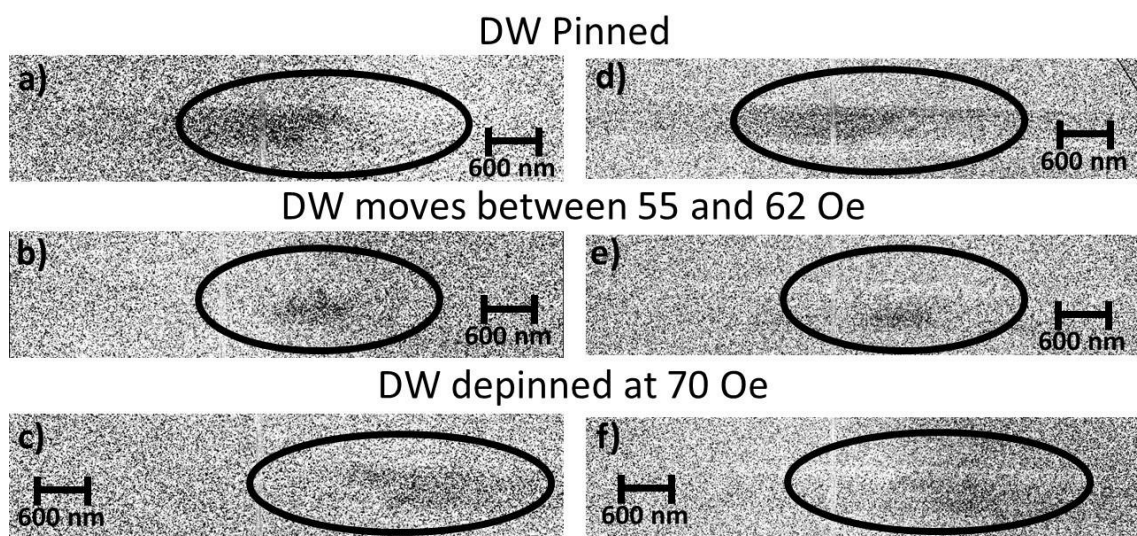


Figure 5.6.8: M-TXM divided images taken at the ALS facility of DWs moving between alternating indentations a 560 nm wide, 50 nm thick nanowire. a), b) and c), d), e) and f) are sets of Images showing DW pinned and then propagated within separate hysteresis loops.

The top row of images shows the presence of a DW at the first indentation. The boundary between magnetisations is angled showing some DW structure. As it is not possible to see the exact location of the indentations in these images, it may be that this boundary is diagonal from the first indentation to the next located on the opposite side of the nanowire.

As the applied field is increased from 55 Oe to 62 Oe, some contrast in the images can be noted. A triangular region of the nanowire switches magnetisation from the previous location of the DW. This indicates that the DW has moved along the nanowire but is still trapped and unable to propagate through to the end. This

movement occurs between the same field steps for multiple hysteresis loops with figure 5.6.8 only demonstrating two examples.

As the applied field is further increased to 70 Oe, the rest of the nanowire switches, indicating the DW has escaped the pinning sites, propagating through to the end. These series of images demonstrate evidence supporting that a set of such indentations may be used to control the movement of a DW along a nanowire.

5.7 Summary

In this section, the key results of the experimental work conducted in chapter 5 will be summarised.

Initial experiments were conducted testing the cutting direction for AFM tip-based nanomachining using a three-sided pyramidal tip. Thin films were used during this test. It was found that the horizontal cutting direction produced the cleanest cut with the least overall pile-up.

AFM tip-based nanomachining was used to create vertical nanotrenches in several permalloy nanowires. AMR measurements were used to detect the presence of DWs and measure the depinning fields for nanotrenches of varying depths. To support these results, magnetic full-field transmission soft x-ray microscopy was used to directly image DWs pinned at the generated nanotrenches in the nanowires. These results support the viability of using AFM tip-based nanomachining to create DW pinning sites.

Further work included the experimental study of a 56 nm thick, 320 nm wide nanowire. Multiple nanotrench depths were measured using AMR. To support these experimental results, simulations were conducted on a nanowire with similar dimensions. These results qualitatively agreed with each other and showed an approximately linear relationship between pinning strength and nanotrench depth.

Two further samples were fabricated with an alternative design with the intention of streamlining the experimental process. AMR measurements were conducted and resulted in trends unlike those observed in previous nanowires. AMR data relating to each of the four wires in each sample gave comparable results. Indicating issues with the sample design. All four nanowires on the same sample broke after one round of machining due to various reasons. Further measurements on the second sample were restricted due to failure in the AFM system.

Three additional nanowires were modified with more complex features in an attempt to observe how DWs interact with them. There were an extended nanotrench, an L-shaped nanotrench and alternating indentations. MTXM was used to observe the DWs pinned at these features.

6. Conclusions and Future work

This chapter concludes the Thesis by discussing to which extent each of the knowledge gaps identified in Chapter 2 were addressed and by presenting the key findings and conclusions reached from the work. Ideas for future investigations to follow on from this study are also suggested.

6.1 Knowledge contributions and key conclusions

Given the recent efforts from the micro and nanomanufacturing research community in developing AFM tip-based nanomachining, there is a drive to find potential applications for the technique. At the same time, studies focussed on the behaviour of magnetic domains in small scale devices have been of interest to researchers due to their potential to be used in various applications such as data storage and memory. A potential obstacle in these applications however relates to the need for the reliable control of the motion and positioning of the boundaries between these domains known as domain walls (DWs).

This study aimed to combine these two fields of research as it was suggested that AFM tip-based nanomachining could be used to artificially create sites that could pin DWs within magnetic nanowires. Based on the analysis of the literature in chapter 2, some knowledge gaps in this area were identified. Each of these are listed below together with a summary of how this study attempted to address them and the key conclusions found.

Knowledge gap: Investigation on the interaction between different types of DWs and the specific geometry of vertical nanotrenches.

- The methodology followed to explore this was to conduct a computational study focusing on the effects of length and depth of different types of vertical nanotrenches on DW pinning strength. This was the specific focus of the work reported in Chapter 4. First nanotrenches were studied that consisted of square walls. The simulated pinning strength values were then compared with those produced for equivalent size triangular nanotrenches. triangular in shape. This particular shape was also considered as it is more akin to features created using AFM tip-based nanomachining. The computational work was conducted on three different nanowire dimensions. More specifically, to investigate transverse DWs, two nanowires were modelled (respectively 50 nm wide, 10 nm thick and 100 nm wide and 25 nm

thick), while a 200 nm wide, 50 nm thick nanowire was employed to study vortex DWs.

- This computational study indicates that the shape, as well as size, of vertically placed nanotrenches does influence the pinning strength. Square and triangular nanotrenches were studied for each of the three nanowire sizes.
- For transverse DWs, it was observed that both square and triangular nanotrenches were chirality independent. The effect of depth on the pinning strength was found to be similar in both cases, increasing approximately linearly with depth. However, there was a difference in effect regarding the nanotrench length. In particular, the influence of the length on the pinning strength was small beyond a value of 100-150 nm in the square nanotrench case. However, the triangular configuration resulted in an initial increase in pinning strength, followed by a reduction as the length of the nanotrench increased further. It was observed that this may be due to an angular dependence. When plotting the depinning field against the angle of the nanotrench wall, it was found that the pinning strength begins to drastically fall for angles below 10°. Regardless of the angular dependency, it was found that the pinning strength of triangular nanotrenches is weaker than their square counterparts, even when the same amount of material is removed.
- In comparison, for vortex DWs, chirality testing resulted in inconclusive outcomes. This was due to various chiralities resulting in varying depinning fields whilst not providing any perceivable trend. The results found for square nanotrenches were similar to those in the transverse DW case. Similarly, it was generally seen that the square nanotrenches pin DWs stronger than the triangular nanotrenches. The relationships found when comparing pinning strength to length and depth of the nanotrench are comparable for the square and triangular shapes. In the triangular nanotrench case, the data was affected by the occurrence of metastable asymmetric transverse walls as opposed to vortex DWs. In the instances where these metastable walls did not occur, there appears to be an initial increase in nanotrench pinning strength before a gradual decrease with increasing size.
- To support the angular dependence on pinning strength, trapezoidal nanotrenches were studied. For transverse DWs, the results compliment the triangular case, with the depinning fields reducing when the angle of the

nanotrench wall reduces below 10° . For the vortex case, a small but gradual increase in pinning strength is seen as the angle reduces to an angle of approximately 27° , at which there is a sudden drop in depinning fields. These values continued to reduce steadily with the reduction in angle. In summary, domain walls can be pinned by vertical nanotrenches. Size and geometry are important factors in the pinning strength of such sites. Generally square nanotrenches pin domain walls stronger than triangular nanotrenches of similar size. Depth of the nanotrench has a greater influence over the pinning strength than the length.

Knowledge gap: Demonstration that AFM tip-based nanomachining can be used to create artificial pinning sites for DWs.

- Following the computational study conducted in Chapter 4, Chapter 5 reported the actual implementation of the AFM tip-based nanomachining technique to create vertical nanotrenches across the width of a number of different ferromagnetic permalloy nanowires. AMR measurements were first utilised to indicate the presence of DWs pinned at such sites. To verify and support the outcomes of the AMR measurements, magnetic full-field transmission soft x-ray microscopy was also employed on multiple nanowires that contained similar nanotrenches cut with an AFM. In this case, DWs were directly imaged to be pinned at such sites. These complementary measurements provided additional evidence that AFM tip-based nanomachining is a technique capable of creating artificial pinning sites for magnetic DWs. In summary, there is experimental evidence supporting the use of AFM tip-based nanomachining to create artificial domain wall pinning sites.

Knowledge gap: Experimental confirmation that vertical features can be used to pin DWs and in particular, that the pinning strength increases with the depth of such features.

- In chapter 5, numerous permalloy nanowires were fabricated and nanotrenches inserted across the width of their top surface via AFM tip-based nanomachining. Some of these nanowires were machined several times with the intention of observing the effects of deepening the nanotrench on the pinning strength. An initial 11.5 nm thick, 685 nm wide nanowire provided

promising preliminary experimental results suggesting that the depth of such nanotrenches increased the pinning strength. This initial outcome was supported by a more successful experiment with a 56 nm thick, 320 nm wide nanowire. In particular, additional data points were obtained, showing a general agreement with the simulation results of Chapter 4 that the increase in depth of a nanotrench results in a higher pinning strength. Further attempts were made to obtain data relating to a range of nanowire dimensions. However, issues with the sample design and the AFM instrument limited the ability to obtain further data.

- In summary, there is experimental evidence showing that domain walls can be pinned using vertically inserted nanotrenches. Furthermore it is shown that the strength of such pinning sites increases as the depth of the nanotrench increases.

This thesis shows that AFM tip-based nano-machining is a viable method of creating artificial pinning sites capable of controlling magnetic domain wall motion. It has also shown computational and experimental evidence that such domain walls are able to be pinned and controlled via the insertion of vertical nanotrenches along the top surfaces of nanowires. Finally it has shown computational evidence that the size and geometries of such nanotrench have an influence over the pinning strength of such sites.

6.2 Further work

Following on from this study, there are various avenues where further research may be conducted.

The first of these relates to obtaining more datasets relating to nanowires of various sizes. This is desirable to gain further understanding of the relationship between size and pinning strength in practice.

Another possible study concerns investigating the material's resistance to AFM tip-based nanomachining. In chapter 5, it was found that scratches made with the same applied force on a nanowire and on a thin film of the same material resulted in the machining of different size features. It was also observed that the nanowire became harder once an initial scratch had been performed.

Brief experiments discussed at the end of chapter 5 raise another possible line of future investigations. In particular, this study has shown that AFM tip-based nanomachining can be used to pin DWs at relatively simple nanotrenches. However,

this can be expanded to add more complex features to nanowires. Such artificially created pinning sites may be used to control the motion of DWs along a nanowire by adding multiple features along its length. An AFM may be used to create vertical trenches or cavities of particular shapes in an attempt to control or alter the structure of any present DWs. The possibilities here are only limited by how such vertical features can be created using AFM tip-based nanomachining.

Finally, the emergence of skyrmion racetrack memory was mentioned at the start of the Thesis, in section 1.1.10. A key issue regarding this technology relates to preventing the skyrmions from moving away from the racetrack centre and annihilating at the walls. In the future, it may be of interest research whether AFM nanomachining can be used to create features that may prevent this from happening. More specifically, it may be reasonable to envisage that scratches may be performed with the intention of creating a track along thin films to avoid skyrmion annihilation.

References

- [1] S. S. P. Parkin, M. Hayashi, and L. Thomas, "Magnetic domain-wall racetrack memory," *Science.*, vol. 320, no. 5873, pp. 190-194, Apr. 2008, doi: 10.1126/science.1145799.
- [2] S. Blundell, *Magnetism in condensed matter*. Oxford: Oxford University Press, 2001.
- [3] C. Tannous and J. Gieraltowski, "The Stoner-Wohlfarth model of Ferromagnetism: Dynamic and Statistical properties," *Eur. J. Phys.*, vol. 29, no. 3, pp. 475-487, 2006.
- [4] P. Weiss, "L 'hypothèse du champ moléculaire et la propriété ferromagnétique," *J. Phys. Theor. Appl.*, vol. 6, no. 1, pp. 661-690, 1907.
- [5] A. Aharoni, *Introduction to the Theory of Ferromagnetism*. Oxford: Clarendon Press, 1996.
- [6] J. M. D. Coey, *Magnetism and Magnetic Materials*. Cambridge: Cambridge University Press, 2012.
- [7] L. Landau and E. Lifshits, "on the Theory of the Dispersion of Magnetic Permeability in Ferromagnetic Bodies," *Collect. Pap. L.D. Landau*, vol. 169, no. 14, pp. 101-114, 1935, doi: 10.1016/B978-0-08-010586-4.50023-7.
- [8] W. F. Brown, "Theory of the approach to magnetic saturation," *Phys. Rev.*, vol. 58, no. 8, pp. 736-743, 1940, doi: 10.1103/PhysRev.58.736.
- [9] G. S. Abo, Y. K. Hong, J. Park, J. Lee, W. Lee, and B. C. Choi, "Definition of magnetic exchange length," *IEEE Trans. Magn.*, vol. 49, no. 8, pp. 4937-4939, 2013, doi: 10.1109/TMAG.2013.2258028.
- [10] L. Néel, L. Néel, and J. Phys, "Anisotropie magnétique superficielle et surstructures d 'orientation," *J. Phys. Radium*, vol. 15, no. 4, pp. 225-239, 1954.
- [11] A. Hubert and R. Schafer, *Magnetic Domains: The Analysis of Magnetic Microstructures*. Springer, 1998.
- [12] G. Bertotti, *Hysteresis in Magnetism*. San Diego, CA: Academic Press, 1998.
- [13] H. Kronmüller, "Mikromagnetische Berechnung der Magnetisierung in der Umgebung unmagnetischer Einschlüsse in Ferromagnetika," *Zeitschrift für Phys.*, vol. 168, no. 5, pp. 478-494, Oct. 1962, doi: 10.1007/BF01378144.
- [14] R. Ploessl, J. N. Chapman, A. M. Thompson, J. Zweck, and H. Hoffmann, "Investigation of the micromagnetic structure of cross-tie walls in permalloy," *J. Appl. Phys.*, vol. 73, no. 5, pp. 2447-2452, 1993, doi: 10.1063/1.353102.
- [15] W. F. Brown, "The fundamental theorem of fine-ferromagnetic-particle theory," *J. Appl. Phys.*, vol. 39, no. 2, pp. 993-994, 1968, doi: 10.1063/1.1656363.
- [16] W. F. Brown, *Micromagnetics*. Interscience, 1963.
- [17] W. F. Brown, "Thermal Fluctuations of a single-domain particle," *Phys. Rev.*, vol. 130, no. 5, pp. 1677-1686, 1963.
- [18] E. C. Stoner and E. P. Wohlfarth, "A mechanism of magnetic hysteresis in

- heterogeneous alloys (Reprinted from Philosophical Transaction Royal Society-London, Vol 240, Pg 599-642, 1948),” *IEEE Trans. Magn.*, vol. 27, no. 4, pp. 3475-3518, 1948, doi: 10.1109/TMAG.1991.1183750.
- [19] C. R. Chang, C. M. Lee, and J. S. Yang, “Magnetization curling reversal for an infinite hollow cylinder,” *Phys. Rev. B*, vol. 50, no. 9, pp. 6461-6464, 1994, doi: 10.1103/PhysRevB.50.6461.
- [20] S. Goolaup, N. Singh, A. O. Adeyeye, V. Ng, and M. B. A. Jalil, “Transition from coherent rotation to curling mode reversal process in ferromagnetic nanowires,” *Eur. Phys. J. B*, vol. 44, no. 2, pp. 259-264, 2005, doi: 10.1140/epjb/e2005-00122-7.
- [21] T. Schrefl, J. Fidler, K. J. Kirk, and J. N. Chapman, “Domain structures and switching mechanisms in patterned magnetic elements,” *J. Magn. Magn. Mater.*, vol. 175, no. 1-2, pp. 193-204, 1997, doi: 10.1016/S0304-8853(97)00156-X.
- [22] K. J. Kirk, J. N. Chapman, and C. D. W. Wilkinson, “Switching fields and magnetostatic interactions of thin film magnetic nanoelements,” *Appl. Phys. Lett.*, vol. 71, no. 4, pp. 539-541, 1997, doi: 10.1063/1.119602.
- [23] A. Thiaville and Y. Nakatani, “Domain-Wall Dynamics in Nanowires and Nanostrips,” in *Spin Dynamics in Confined Magnetic Structures III*, B. Hillebrands and A. Thiaville, Eds. Berlin, Heidelberg: Springer Berlin Heidelberg, 2006, pp. 161-205.
- [24] Y. Nakatani, A. Thiaville, and J. Miltat, “Head-to-head domain walls in soft nano-strips: A refined phase diagram,” *J. Magn. Magn. Mater.*, vol. 290-291 PA, pp. 750-753, 2005, doi: 10.1016/j.jmmm.2004.11.355.
- [25] R. D. McMichael and M. J. Donahue, “Head to head domain wall structures in thin magnetic strips,” *IEEE Trans. Magn.*, vol. 33, no. 5, pp. 4167-4169, 1997, doi: 10.1109/20.619698.
- [26] M. Kläui, “Head-to-head domain walls in magnetic nanostructures,” *J. Phys. Condens. Matter*, vol. 20, no. 31, p. 313001, Jul. 2008, doi: 10.1088/0953-8984/20/31/313001.
- [27] V. Estévez and L. Laurson, “Head-to-head domain wall structures in wide permalloy strips,” *Phys. Rev. B - Condens. Matter Mater. Phys.*, vol. 91, no. 5, p. 054407, 2015, doi: 10.1103/PhysRevB.91.054407.
- [28] V. D. Nguyen, O. Fruchart, S. Pizzini, J. Vogel, J.-C. Toussaint, and N. Rougemaille, “Third type of domain wall in soft magnetic nanostrips,” *Sci. Rep.*, vol. 5, p. 12417, 2015, doi: 10.1038/srep12417.
- [29] M. Jamali, K.-J. Lee, and H. Yang, “Metastable magnetic domain wall dynamics,” *New J. Phys.*, vol. 14, no. 3, p. 33010, 2012, doi: 10.1088/1367-2630/14/3/033010.
- [30] H. D. Bush and R. S. Tebble, “The barkhausen effect,” *Proc. Phys. Soc.*, vol. 60, p. 370, 1948.
- [31] S. Yang, G. S. D. Beach, and J. L. Erskine, “Negative Barkhausen jumps in permalloy thin-film microstructures,” *J. Appl. Phys.*, vol. 100, no. 11, p. 113914, 2006, doi: 10.1063/1.2400513.
- [32] R. Cowburn and J. Ferré, “Domain-wall dynamics, pinning, and nucleation in

- ultrathin epitaxial Fe films,” *Phys. Rev. B - Condens. Matter Mater. Phys.*, vol. 58, no. 17, pp. 11507-11513, 1998, doi: 10.1103/PhysRevB.58.11507.
- [33] K. J. Sixtus and L. Tonks, “Propagation of Large Barkhausen Discontinuities,” *Phys. Rev.*, vol. 37, p. 930, 1931.
- [34] D.-H. H. Kim, S.-B. B. Choe, and S.-C. C. Shin, “Direct Observation of Barkhausen Avalanche in Co Thin Films,” *Phys. Rev. Lett.*, vol. 90, no. 8, p. 87203, Feb. 2003, doi: 10.1103/PhysRevLett.90.087203.
- [35] D. D. Petit, A.-V. V. Jausovec, D. Read, and R. P. Cowburn, “Domain wall pinning and potential landscapes created by constrictions and protrusions in ferromagnetic nanowires,” *J. Appl. Phys.*, vol. 103, no. 11, p. 114307, 2008, doi: 10.1063/1.2936981.
- [36] L. K. Bogart, D. Atkinson, K. O’Shea, D. McGrouther, and S. McVitie, “Dependence of domain wall pinning potential landscapes on domain wall chirality and pinning site geometry in planar nanowires,” *Phys. Rev. B - Condens. Matter Mater. Phys.*, vol. 79, no. 5, p. 054414, 2009, doi: 10.1103/PhysRevB.79.054414.
- [37] M. A. Basith, S. McVitie, D. McGrouther, and J. N. Chapman, “Reproducible domain wall pinning by linear non-topographic features in a ferromagnetic nanowire,” *Appl. Phys. Lett.*, vol. 100, no. 23, 2012, doi: 10.1063/1.4724210.
- [38] B. Bhushan, “Historical evolution of magnetic data storage devices and related conferences,” *Microsyst. Technol.*, vol. 24, no. 11, pp. 4423-4436, 2018, doi: 10.1007/s00542-018-4133-6.
- [39] S. Bhatti, R. Sbiaa, A. Hirohata, H. Ohno, S. Fukami, and S. N. Piramanayagam, “Spintronics based random access memory: a review,” *Mater. Today*, vol. 20, no. 9, pp. 530-548, 2017, doi: 10.1016/j.mattod.2017.07.007.
- [40] G. Grynkewich, J. Åkerman, P. Brown, B. Butcher, R. W. Dave, M. DeHerrera, M. Durlam, B. N. Engel, J. Janesky, S. Pietambaram, N. D. Rizzo, J. M. Slaughter, K. Smith, J. J. Sun, and S. Tehrani, “Nonvolatile Magnetoresistive Random-Access Memory Based on Magnetic Tunnel Junctions,” *MRS Bull.*, vol. 29, no. 11, pp. 818-821, Nov. 2004, doi: 10.1557/mrs2004.234.
- [41] M. Tsoi, R. E. Fontana, and S. S. P. Parkin, “Magnetic domain wall motion triggered by an electric current,” *Appl. Phys. Lett.*, vol. 83, no. 13, pp. 2617-2619, 2003, doi: 10.1063/1.1578165.
- [42] M. Yamanouchi, D. Chiba, F. Matsukura, and H. Ohno, “Current-induced domain-wall switching in a ferromagnetic semiconductor structure,” *Nature*, vol. 428, no. 6982, pp. 539-541, 2004, doi: 10.1038/nature02441.
- [43] A. Yamaguchi, T. Ono, S. Nasu, K. Miyake, K. Mibu, T. Shinjo, and T. S. Akinobu Yamaguchi, Teruo Ono, Saburo Nasu, Kousaku Miyake, Ko Mibu, “Real-Space Observation of Current-Driven Domain Wall Motion in Submicron Magnetic Wires,” *Phys. Rev. Lett.*, vol. 92, no. February, pp. 77201-77205, 2004, doi: 10.1103/PhysRevLett.92.077205.
- [44] G. t. Hooft, “Magnetic monopoles in unified gauge theories,” *Nucl. Physics, Sect. B*, vol. 79, no. 2, pp. 276-284, 1974, doi: 10.1016/0550-3213(74)90486-6.
- [45] A. Neubauer, C. Pfleiderer, B. Binz, A. Rosch, R. Ritz, P. G. Niklowitz, and P.

- Böni, "Topological hall effect in the a phase of MnSi," *Phys. Rev. Lett.*, vol. 102, no. 18, p. 186602, 2009, doi: 10.1103/PhysRevLett.102.186602.
- [46] S. Mühlbauer, "Skyrmion lattice in a chiral magnet" *Science.*, vol. 333, no. 6048, p. 1381, 2011, doi: 10.1126/science.333.6048.1381-b.
- [47] A. Fert, V. Cros, and J. Sampaio, "Skyrmions on the track," *Nat. Nanotechnol.*, vol. 8, no. 3, pp. 152-156, 2013, doi: 10.1038/nnano.2013.29.
- [48] J. Zang, M. Mostovoy, J. H. Han, and N. Nagaosa, "Dynamics of Skyrmion crystals in metallic thin films," *Phys. Rev. Lett.*, vol. 107, no. 13, pp. 1-5, 2011, doi: 10.1103/PhysRevLett.107.136804.
- [49] J. Barker and O. A. Tretiakov, "Static and Dynamical Properties of Antiferromagnetic Skyrmions in the Presence of Applied Current and Temperature," *Phys. Rev. Lett.*, vol. 116, no. 14, pp. 1-5, 2016, doi: 10.1103/PhysRevLett.116.147203.
- [50] X. Zhang, Y. Zhou, and M. Ezawa, "Antiferromagnetic Skyrmion: Stability, Creation and Manipulation," *Sci. Rep.*, vol. 6, pp. 1-8, 2016, doi: 10.1038/srep24795.
- [51] G. Binnig, H. Rohrer, C. Gerber, and E. Weibel, "Surface Studies by Scanning Tunneling Microscopy," *Phys. Rev. Lett.*, vol. 49, no. 1, pp. 57-61, 1982.
- [52] G. Binnig, C. F. Quate, and C. Gerber, "Atomic force microscope," *Phys. Rev. Lett.*, vol. 56, no. 9, pp. 930-934, 1986.
- [53] G. Meyer and N. M. Amer, "Optical-beam-deflection atomic force microscopy: The NaCl (001) surface," *Appl. Phys. Lett.*, vol. 56, no. 21, pp. 2100-2101, 1990, doi: 10.1063/1.102985.
- [54] G. Binnig, C. Gerber, E. Stoll, T. R. Albrecht, and C. F. Quate, "Atomic resolution with atomic force microscope," *Epl*, vol. 3, no. 12, pp. 1281-1286, 1987, doi: 10.1209/0295-5075/3/12/006.
- [55] O. Marti, B. Drake, S. Gould, and P. K. Hansma, "Probing Surfaces With The Atomic Force Microscope," *Scanning Microsc. Technol. Appl.*, vol. 0897, no. November 1988, p. 22, 1988, doi: 10.1117/12.944502.
- [56] A. A. Tseng, A. Notargiacomo, and T. P. Chen, "Nanofabrication by scanning probe microscope lithography: A review," *J. Vac. Sci. Technol. B Microelectron. Nanom. Struct.*, vol. 23, no. 3, pp. 877-894, 2005, doi: 10.1116/1.1926293.
- [57] M. J. Jackson, *Microfabrication and Nanomanufacturing*. Boca Raton, FL: Taylor and Francis, 2006.
- [58] R. W. Carpick and M. Salmeron, "Scratching the surface: Fundamental investigations of tribology with atomic force microscopy," *Chem. Rev.*, vol. 97, no. 4, pp. 1163-1194, 1997, doi: 10.1021/cr960068q.
- [59] F. J. Giessibl, "Advances in atomic force microscopy," *Rev. Mod. Phys.*, vol. 75, no. 3, pp. 949-983, 2003, doi: 10.1103/RevModPhys.75.949.
- [60] H. J. Butt, B. Cappella, and M. Kappl, "Force measurements with the atomic force microscope: Technique, interpretation and applications," *Surf. Sci. Rep.*, vol. 59, no. 1-6, pp. 1-152, 2005, doi: 10.1016/j.surfrep.2005.08.003.
- [61] B. Bhushan and K. J. Kwak, "Noble metal-coated probes sliding at up to 100

mm s⁻¹ against PZT films for AFM probe-based ferroelectric recording technology,” *J. Phys. Condens. Matter*, vol. 20, no. 22, 2008, doi: 10.1088/0953-8984/20/22/225013.

- [62] F. L. Leite and P. S. P. Herrmann, “Application of atomic force spectroscopy (AFS) to studies of adhesion phenomena: A review,” *J. Adhes. Sci. Technol.*, vol. 19, no. 3-5, pp. 365-405, 2005, doi: 10.1163/1568561054352667.
- [63] A. M. Baro and R. G. Reifengerger, *Atomic force microscopy in liquid: Biological Applications*. New Jersey, United States: John Wiley & Sons, 2012.
- [64] B. Bhushan, “Nanotribology and Nanomechanics I: Measurement Techniques and Nanomechanics,” New York, United States: Springer, 2011.
- [65] G. Haugstad, *Atomic force microscopy: understanding basic modes and advanced applications*. New Jersey, United States: John Wiley & Sons, 2012.
- [66] H. Yang, “Atomic Force Microscopy (AFM): Principles, modes of operation and limitations,” *At. Force Microsc. Princ. Modes Oper. Limitations*, no. April 2014, pp. 1-372, 2014.
- [67] Y. Martin, C. C. Williams, and H. K. Wickramasinghe, “Atomic force microscope-force mapping and profiling on a sub 100-Å scale,” *J. Appl. Phys.*, vol. 61, no. 10, pp. 4723-4729, 1987, doi: 10.1063/1.338807.
- [68] Q. Zhong, D. Inniss, K. Kjoller, and V. B. Elings, “Fractured polymer/silica fiber surface studied by tapping mode atomic force microscopy,” *Surf. Sci.*, vol. 290, no. 1-2, pp. L688-L692, Jun. 1993, doi: 10.1016/0039-6028(93)90582-5.
- [69] X. Jin and W. N. Unertl, “Submicrometer modification of polymer surfaces with a surface force microscope,” *Appl. Phys. Lett.*, vol. 61, no. 6, pp. 657-659, 1992, doi: 10.1063/1.107813.
- [70] T. A. Jung, A. Moser, H. J. Hug, D. Brodbeck, R. Hofer, H. R. Hidber, and U. D. Schwarz, “The atomic force microscope used as a powerful tool for machining surfaces,” *Ultramicroscopy*, vol. 42-44, pp. 1446-1451, Jul. 1992, doi: 10.1016/0304-3991(92)90464-U.
- [71] Y. Kim and C. M. Lieber, “Machining oxide thin films with an atomic force microscope: Pattern and object formation on the nanometer scale,” *Science*, vol. 257, no. 5068, pp. 375-377, 1992, doi: 10.1126/science.257.5068.375.
- [72] E. R. Lewis, D. Petit, A. V. Jausovec, L. O’Brien, D. E. Read, H. T. Zeng, and R. P. Cowburn, “Measuring domain wall fidelity lengths using a chirality filter,” *Phys. Rev. Lett.*, vol. 102, no. 5, p. 057209, 2009, doi: 10.1103/PhysRevLett.102.057209.
- [73] A. Beguivin, H. Corte-León, A. Manzin, V. Nabaiei, P. Krzysteczko, H. W. Schumacher, D. Petit, R. P. Cowburn, and O. Kazakova, “Simultaneous magnetoresistance and magneto-optical measurements of domain wall properties in nanodevices,” *J. Appl. Phys.*, vol. 115, no. 17, pp. 6-9, 2014, doi: 10.1063/1.4862377.
- [74] D. Petit, A. V. Jausovec, H. T. Zeng, E. Lewis, L. O’Brien, D. Read, and R. P. Cowburn, “High efficiency domain wall gate in ferromagnetic nanowires,” *Appl. Phys. Lett.*, vol. 93, no. 16, p. 163108, 2008, doi: 10.1063/1.3005586.
- [75] D. Petit, A. V. Jausovec, H. T. Zeng, E. Lewis, L. O’Brien, D. Read, and R. P.

- Cowburn, "Mechanism for domain wall pinning and potential landscape modification by artificially patterned traps in ferromagnetic nanowires," *Phys. Rev. B - Condens. Matter Mater. Phys.*, vol. 79, no. 21, pp. 1-9, 2009, doi: 10.1103/PhysRevB.79.214405.
- [76] K. J. O'Shea, S. McVitie, J. N. Chapman, and J. M. R. Weaver, "Direct observation of changes to domain wall structures in magnetic nanowires of varying width," *Appl. Phys. Lett.*, vol. 93, no. 20, pp. 1-4, 2008, doi: 10.1063/1.3023048.
- [77] H. Corte-León, V. Nabaei, A. Manzin, J. Fletcher, P. Krzysteczko, H. W. Schumacher, and O. Kazakova, "Anisotropic magnetoresistance state space of permalloy nanowires with domain wall pinning geometry.," *Sci. Rep.*, vol. 4, p. 6045, 2014, doi: 10.1038/srep06045.
- [78] H. Corte-Leon, A. Beguivin, P. Krzysteczko, H. W. Schumacher, A. Manzin, R. P. Cowburn, V. Antonov, and O. Kazakova, "Influence of geometry on domain wall dynamics in Permalloy nanodevices," *IEEE Trans. Magn.*, vol. 51, no. 1, pp. 3-6, 2015, doi: 10.1109/TMAG.2014.2356617.
- [79] C. Brownlie, S. McVitie, J. N. Chapman, and C. D. W. Wilkinson, "Lorentz microscopy studies of domain wall trap structures," *J. Appl. Phys.*, vol. 100, no. 3, 2006, doi: 10.1063/1.2227263.
- [80] D. A. Allwood, G. Xiong, and R. P. Cowburn, "Domain wall diodes in ferromagnetic planar nanowires," *Appl. Phys. Lett.*, vol. 85, no. 14, pp. 2848-2850, 2004, doi: 10.1063/1.1802388.
- [81] A. Himeno, S. Kasai, and T. Ono, "Current-driven domain-wall motion in magnetic wires with asymmetric notches," *Appl. Phys. Lett.*, vol. 87, no. 24, p. 243108, 2005, doi: 10.1063/1.2140884.
- [82] A. Himeno, T. Okuno, S. Kasai, T. Ono, S. Nasu, K. Mibu, and T. Shinjo, "Propagation of a magnetic domain wall in magnetic wires with asymmetric notches," *J. Appl. Phys.*, vol. 97, no. 6, pp. 1-4, 2005, doi: 10.1063/1.1861505.
- [83] A. Cao, X. Zhang, Z. Li, Q. Leng, L. Wen, and W. Zhao, "A Christmas-Tree-Like Magnetic Field Sensor Based on Domain Wall Depinning in a Notched Nanowire," *IEEE Magn. Lett.*, vol. 9, pp. 1-4, 2018, doi: 10.1109/LMAG.2018.2854698.
- [84] D. Ozkaya L, R. M. Langford, W. L. Chan, and A. K. Petford-Long, "Effect of Ga implantation on the magnetic properties of permalloy thin films," *J. Appl. Phys.*, vol. 91, no. 12, pp. 9937-9942, 2002, doi: 10.1063/1.1477265.
- [85] S. I. Woods, S. Ingvarsson, J. R. Kirtley, H. F. Hamann, and R. H. Koch, "Local magnetic anisotropy control in NiFe thin films via ion irradiation," *Appl. Phys. Lett.*, vol. 81, no. 7, pp. 1267-1269, 2002, doi: 10.1063/1.1498869.
- [86] A. Vogel, S. Wintz, J. Kimling, M. Bolte, T. Strache, M. Fritzsche, M. Y. Im, P. Fischer, G. Meier, and J. Fassbender, "Domain-wall pinning and depinning at soft spots in magnetic nanowires," *IEEE Trans. Magn.*, vol. 46, no. 6, pp. 1708-1710, 2010, doi: 10.1109/TMAG.2010.2042285.
- [87] A. Vogel, S. Wintz, T. Gerhardt, L. Bocklage, T. Strache, M. Y. Im, P. Fischer, J. Fassbender, J. McCord, and G. Meier, "Field- and current-induced domain-wall motion in permalloy nanowires with magnetic soft spots," *Appl. Phys. Lett.*, vol. 98, no. 20, p. 202501, 2011, doi: 10.1063/1.3590267.

- [88] M. A. Basith, S. McVitie, D. McGrouther, J. N. Chapman, and J. M. R. Weaver, "Direct comparison of domain wall behavior in permalloy nanowires patterned by electron beam lithography and focused ion beam milling," *J. Appl. Phys.*, vol. 110, no. 8, p. 083904, 2011, doi: 10.1063/1.3642966.
- [89] L. O'Brien, D. Petit, H. T. Zeng, E. R. Lewis, J. Sampaio, A. V. Jausovec, D. E. Read, and R. P. Cowburn, "Near-field interaction between domain walls in adjacent permalloy nanowires," *Phys. Rev. Lett.*, vol. 103, no. 7, p. 077206, 2009, doi: 10.1103/PhysRevLett.103.077206.
- [90] H. T. Zeng, D. Petit, L. O'Brien, D. Read, E. R. Lewis, and R. P. Cowburn, "The influence of wire width on the charge distribution of transverse domain walls and their stray field interactions," *J. Magn. Magn. Mater.*, vol. 322, no. 14, pp. 2010-2014, 2010, doi: 10.1016/j.jmmm.2010.01.024.
- [91] L. O'Brien, D. Petit, E. R. Lewis, R. P. Cowburn, D. E. Read, J. Sampaio, H. T. Zeng, and A. V. Jausovec, "Tunable remote pinning of domain walls in magnetic nanowires," *Phys. Rev. Lett.*, vol. 106, no. 8, p. 087204, 2011, doi: 10.1103/PhysRevLett.106.087204.
- [92] L. O'Brien, A. Beguivin, A. Fernandez-Pacheco, D. Petit, D. E. Read, and R. P. Cowburn, "Magnetic domain wall induced, localized nanowire reversal," *Appl. Phys. Lett.*, vol. 101, no. 6, p. 062415, 2012, doi: 10.1063/1.4742746.
- [93] E. R. Lewis, D. Petit, L. O'Brien, H. T. Zeng, D. E. Read, and R. P. Cowburn, "Chirality dependence of nanoscale ferromagnetic NOT gates," *J. Appl. Phys.*, vol. 109, no. 5, p. 053904, 2011, doi: 10.1063/1.3549599.
- [94] C. C. Faulkner, M. D. Cooke, D. A. Allwood, D. Petit, D. Atkinson, and R. P. Cowburn, "Artificial domain wall nanotraps in Ni₈₁Fe₁₉ wires," *J. Appl. Phys.*, vol. 95, no. 11, pp. 6717-6719, 2004, doi: 10.1063/1.1652391.
- [95] M. Hayashi, L. Thomas, C. Rettner, R. Moriya, X. Jiang, and S. S. P. Parkin, "Dependence of current and field driven depinning of domain walls on their structure and chirality in permalloy nanowires," *Phys. Rev. Lett.*, vol. 97, no. 20, p. 207205, 2006, doi: 10.1103/PhysRevLett.97.207205.
- [96] D. Atkinson, D. S. Eastwood, and L. K. Bogart, "Controlling domain wall pinning in planar nanowires by selecting domain wall type and its application in a memory concept," *Appl. Phys. Lett.*, vol. 92, no. 2, p. 022510, 2008, doi: 10.1063/1.2832771.
- [97] S. H. Huang and C. H. Lai, "Domain-wall depinning by controlling its configuration at notch," *Appl. Phys. Lett.*, vol. 95, no. 3, p. 032505, 2009, doi: 10.1063/1.3187530.
- [98] D. Petit, H. T. Zeng, J. Sampaio, E. Lewis, L. O'Brien, A. V. Jausovec, D. Read, R. P. Cowburn, K. J. O'Shea, S. McVitie, and J. N. Chapman, "Magnetic imaging of the pinning mechanism of asymmetric transverse domain walls in ferromagnetic nanowires," *Appl. Phys. Lett.*, vol. 97, no. 23, pp. 2008-2011, 2010, doi: 10.1063/1.3523351.
- [99] H. Yuan and X. Wang, "Vortex-assisted domain wall depinning and propagation in notched nanowires," *Eur. Phys. J. B*, vol. 88, no. 9, p. 214, 2015, doi: 10.1140/epjb/e2015-60421-x.
- [100] Y. Gao, B. You, X. Z. Ruan, M. Y. Liu, H. L. Yang, Q. F. Zhan, Z. Li, N. Lei, W. S. Zhao, D. F. Pan, J. G. Wan, J. Wu, H. Q. Tu, J. Wang, W. Zhang, Y. B. Xu, and J. Du, "Depinning of domain walls in permalloy nanowires with

asymmetric notches,” *Sci. Rep.*, vol. 6, no. 1, p. 32617, 2016, doi: 10.1038/srep32617.

- [101] M.-Y. Im, L. Bocklage, G. Meier, and P. Fischer, “Magnetic soft x-ray microscopy of the domain wall depinning process in permalloy magnetic nanowires,” *J. Phys. Condens. Matter*, vol. 24, no. 2, p. 024203, 2012, doi: 10.1088/0953-8984/24/2/024203.
- [102] H. T. Zeng, D. Read, D. Petit, A. V. Jausovec, L. O’Brien, E. R. Lewis, and R. P. Cowburn, “Combined electrical and magneto-optical measurements of the magnetization reversal process at a domain wall trap,” *Appl. Phys. Lett.*, vol. 94, no. 10, p. 103113, 2009, doi: 10.1063/1.3098359.
- [103] L. K. Bogart, D. S. Eastwood, and D. Atkinson, “The effect of geometrical confinement and chirality on domain wall pinning behavior in planar nanowires,” *J. Appl. Phys.*, vol. 104, no. 3, p. 033904, 2008, doi: 10.1063/1.2961313.
- [104] D. S. Eastwood, L. K. Bogart, and D. Atkinson, “Scaling behaviour of chirality dependent domain wall pinning in planar nanowires,” *Acta Phys. Pol. A*, vol. 118, no. 5, pp. 719-722, 2010, doi: 10.12693/APhysPolA.118.719.
- [105] S. Goolaup, S. C. Low, M. C. Sekhar, and W. S. Lew, “Dependence of pinning on domain wall spin structure and notch geometry,” *J. Phys. Conf. Ser.*, vol. 266, no. 1, p. 012079, 2011, doi: 10.1088/1742-6596/266/1/012079.
- [106] Y. Gao, B. You, H. L. Yang, Q. F. Zhan, Z. Li, N. Lei, W. S. Zhao, J. Wu, H. Q. Tu, J. Wang, L. J. Wei, W. Zhang, Y. B. Xu, and J. Du, “Stochastic domain wall depinning in permalloy nanowires with various types of notches,” *AIP Adv.*, vol. 6, no. 12, p. 125124, 2016, doi: 10.1063/1.4973647.
- [107] Y. Gao, B. You, X. Z. Ruan, M. Y. Liu, H. L. Yang, Q. F. Zhan, Z. Li, N. Lei, W. S. Zhao, D. F. Pan, J. G. Wan, J. Wu, H. Q. Tu, J. Wang, W. Zhang, Y. B. Xu, and J. Du, “Depinning of domain walls in permalloy nanowires with asymmetric notches,” *Sci. Rep.*, vol. 6, no. 1, p. 32617, 2016, doi: 10.1038/srep32617.
- [108] A. Kunz and J. D. Priem, “Dynamic notch pinning fields for domain walls in ferromagnetic nanowires,” *IEEE Trans. Magn.*, vol. 46, no. 6, pp. 1559-1561, 2010, doi: 10.1109/TMAG.2010.2041044.
- [109] T. C. Chen, C. Y. Kuo, A. K. Mishra, B. Das, and J. C. Wu, “Magnetic domain wall motion in notch patterned permalloy nanowire devices,” *Phys. B Condens. Matter*, vol. 476, pp. 161-166, 2015, doi: 10.1016/j.physb.2015.04.004.
- [110] A. Himeno, T. Ono, S. Nasu, K. Shigeto, K. Mibu, K. Shinjo, S. Kasai, and T. Ono, “Dynamics of a magnetic domain wall in magnetic wires with an artificial neck,” *J. Appl. Phys.*, vol. 99, no. 8, pp. 8430-8432, 2003, doi: 10.1063/1.1556980.
- [111] A. Himeno, T. Ono, S. Nasu, T. Okuno, K. Mibu, and T. Shinjo, “Propagation velocity measurement of a magnetic domain wall in a submicron magnetic wire,” *J. Magn. Magn. Mater.*, vol. 272-276, pp. 1577-1578, 2004, doi: 10.1016/j.jmmm.2003.12.307.
- [112] A. Olziersky, A. Vilà, M. Rubio-Roy, E. Bertran, and J. Fontcuberta, “Magnetic domain wall pinning by focused ion beam milling of permalloy layers,” *Microelectron. Eng.*, vol. 86, no. 4-6, pp. 878-881, 2008, doi:

10.1016/j.mee.2008.12.028.

- [113] A. Ding, I. Will, C. Lu, and Y. Xu, "Vortex domain wall formation in nanowires with twin pinning sites," *IEEE Trans. Magn.*, vol. 48, no. 8, pp. 2304-2306, 2012, doi: 10.1109/TMAG.2012.2191974.
- [114] A. Ding, I. Will, and Y. Xu, "MFM observation of twin pinning sites on NiFe nanowires," *IEEE Trans. Magn.*, vol. 49, no. 4, pp. 1334-1336, 2013, doi: 10.1109/TMAG.2012.2216540.
- [115] C. Kurniawan and D. Djuhana, "Current driven domain wall depinning in notched Permalloy nanowires," *AIP Conf. Proc.*, vol. 1711, no. 1, p. 20001, 2016, doi: 10.1063/1.4941610.
- [116] G. Zahnd, V. T. Pham, A. Marty, M. Jamet, C. Beigné, L. Notin, C. Vergnaud, F. Rortais, L. Vila, and J. P. Attané, "Introduction and pinning of domain walls in 50 nm NiFe constrictions using local and external magnetic fields," *J. Magn. Magn. Mater.*, vol. 406, pp. 166-170, 2016, doi: 10.1016/j.jmmm.2016.01.012.
- [117] C. Wuth, P. Lendecke, and G. Meier, "Temperature-dependent dynamics of stochastic domain-wall depinning in nanowires," *J. Phys. Condens. Matter*, vol. 24, no. 2, p. 024207, 2012, doi: 10.1088/0953-8984/24/2/024207.
- [118] T. J. Hayward, "Intrinsic Nature of Stochastic Domain Wall Pinning Phenomena in Magnetic Nanowire Devices," *Sci. Rep.*, vol. 5, no. 1, p. 13279, 2015, doi: 10.1038/srep13279.
- [119] A. Himeno, T. Okuno, T. Ono, K. Mibu, S. Nasu, and T. Shinjo, "Temperature dependence of depinning fields in submicron magnetic wires with an artificial neck," *J. Magn. Magn. Mater.*, vol. 286, no. SPEC. ISS., pp. 167-170, 2005, doi: 10.1016/j.jmmm.2004.09.023.
- [120] H. Asada, Y. Hyodo, J. Yamasaki, M. Takezawa, and T. Koyanagi, "Micromagnetic study of domain wall-pinning characteristics with step-like thickness change in thin film," *IEEE Trans. Magn.*, vol. 40, no. 4, pp. 2110-2112, 2004, doi: 10.1109/TMAG.2004.832145.
- [121] H. Asada, H. Ii, J. Yamasaki, M. Takezawa, and T. Koyanagi, "Micromagnetic study of domain-wall pinning characteristics with grooves in thin films," *J. Appl. Phys.*, vol. 97, no. 10, p. 10E317, 2005, doi: 10.1063/1.1857652.
- [122] G. Watanabe, S. Koizumi, T. Yamada, Y. Takemura, and J. Shirakashi, "Magnetoresistance of patterned NiFe thin films with structures modified by atomic force microscope nanolithography," *J. Vac. Sci. Technol. B Microelectron. Nanom. Struct.*, vol. 23, no. 6, p. 2390, 2005, doi: 10.1116/1.2122767.
- [123] K. Narayanapillai and H. Yang, "Control of domain wall motion at vertically etched nanotrench in ferromagnetic nanowires," *Appl. Phys. Lett.*, vol. 103, no. 25, pp. 2011-2015, 2013, doi: 10.1063/1.4850415.
- [124] B. A. Gozen and O. B. Ozdoganlar, "A rotating-tip-based mechanical nano-manufacturing process: Nanomilling," *Nanoscale Res. Lett.*, vol. 5, no. 9, pp. 1403-1407, 2010, doi: 10.1007/s11671-010-9653-7.
- [125] L. Li, M. Hirtz, W. Wang, C. Du, H. Fuchs, and L. Chi, "Patterning of polymer electrodes by nanoscratching," *Adv. Mater.*, vol. 22, no. 12, pp. 1374-1378, 2010, doi: 10.1002/adma.200902941.

- [126] C. Martin-Olmos, L. G. Villanueva, P. D. Van Der Wal, A. Llobera, N. F. De Rooij, J. Brugger, and F. Perez-Murano, "Conductivity of SU-8 thin films through atomic force microscopy nano-patterning," *Adv. Funct. Mater.*, vol. 22, no. 7, pp. 1482-1488, 2012, doi: 10.1002/adfm.201102789.
- [127] F. Teixeira, R. Mansano, M. Salvadori, M. Cattani, and I. Brown, "Atomic force microscope nanolithography of polymethylmethacrylate polymer," *Rev. Sci. Instrum.*, vol. 78, p. 53702, 2007, doi: 10.1063/1.2736311.
- [128] L. Zhang and J. Dong, "High-rate tunable ultrasonic force regulated nanomachining lithography with an atomic force microscope," *Nanotechnology*, vol. 23, p. 85303, 2012, doi: 10.1088/0957-4484/23/8/085303.
- [129] A. G. Khurshudov, K. Kato, and H. Koide, "Nano-wear of the diamond AFM probing tip under scratching of silicon, studied by AFM," *Tribol. Lett.*, vol. 2, no. 4, pp. 345-354, Dec. 1996, doi: 10.1007/BF00156907.
- [130] L. Santinacci, T. Djenizian, H. Hildebrand, S. Ecoffey, H. Mokdad, T. Campanella, and P. Schmuki, "Selective palladium electrochemical deposition onto AFM-scratched silicon surfaces," *Electrochim. Acta*, vol. 48, pp. 3123-3130, 2003, doi: 10.1016/S0013-4686(03)00340-2.
- [131] M. Versen, B. Klehn, U. Kunze, D. Reuter, and A. D. Wieck, "Nanoscale devices fabricated by direct machining of GaAs with an atomic force microscope," *Ultramicroscopy*, vol. 82, no. 1, pp. 159-163, 2000, doi: [https://doi.org/10.1016/S0304-3991\(99\)00127-8](https://doi.org/10.1016/S0304-3991(99)00127-8).
- [132] T.-H. Fang and W.-J. Chang, "Effects of AFM-based nanomachining process on aluminum surface," *J. Phys. Chem. Solids*, vol. 64, pp. 913-918, 2003, doi: 10.1016/S0022-3697(02)00436-5.
- [133] T. Sumomogi, T. Endo, K. Kuwahara, and R. Kaneko, "Nanoscale layer removal of metal surfaces by scanning probe microscope scratching," *J. Vac. Sci. Technol. B Microelectron. Nanom. Struct. Process. Meas. Phenom.*, vol. 13, no. 3, pp. 1257-1260, 1995, doi: 10.1116/1.588247.
- [134] Y. Yan, T. Sun, Y. Liang, and S. Dong, "Investigation on AFM-based micro/nano-CNC machining system," *Int. J. Mach. Tools Manuf.*, vol. 47, pp. 1651-1659, 2007, doi: 10.1016/j.ijmactools.2007.01.008.
- [135] G. Lu, X. Zhou, H. Li, Z. Yin, B. Li, L. Huang, F. Boey, and H. Zhang, "Nanolithography of single-layer graphene oxide films by atomic force microscopy," *Langmuir*, vol. 26, no. 9, pp. 6164-6166, 2010, doi: 10.1021/la101077t.
- [136] L. Santinacci, T. Djenizian, and P. Schmuki, "Atomic Force Microscopy-Induced Nanopatterning of Si(100) Surfaces," *J. Electrochem. Soc.*, vol. 148, no. 9, pp. 640-646, 2001, doi: 10.1149/1.1389341.
- [137] X. Zhao and B. Bhushan, "Material removal mechanisms of single-crystal silicon on nanoscale and at ultralow loads.," *Wear*, vol. 223, no. 1, pp. 66-78., 1998.
- [138] M. Firtel, G. Henderson, and I. Sokolov, "Nanosurgery: observation of peptidoglycan strands in *Lactobacillus helveticus* cell walls," *Ultramicroscopy*, vol. 101, no. 2-4, pp. 105-109, 2004, doi: 10.1016/j.ultramic.2004.05.009.
- [139] B. W. Muir, A. Fairbrother, T. R. Gengenbach, F. Rovere, M. A. Abdo, K. M.

- McLean, and P. G. Hartley, "Scanning probe nanolithography and protein patterning of low-fouling plasma polymer multilayer films," *Adv. Mater.*, vol. 18, no. 23, pp. 3079-3082, 2006, doi: 10.1002/adma.200600343.
- [140] Z. Kato, M. Sakairi, and H. Takahashi, "Fabrication of Grooves on Aluminum Surface with Atomic Force Microscope Probe Processing," *J. Electrochem. Soc.*, vol. 148, pp. C790-C798, 2001, doi: 10.1149/1.1417555.
- [141] H. W. Schumacher, B. Kracke, and B. Damaschke, "Modification of thin gold films with a scanning force microscope," *Thin Solid Films*, vol. 264, no. 2, pp. 268-272, 1995, doi: [https://doi.org/10.1016/0040-6090\(95\)05830-3](https://doi.org/10.1016/0040-6090(95)05830-3).
- [142] A. Elkaseer and E. B. Brousseau, "Modelling the surface generation process during AFM probe-based machining: Simulation and experimental validation," *Surf. Topogr. Metrol. Prop.*, vol. 2, no. 2, p. 025001, 2014, doi: 10.1088/2051-672X/2/2/025001.
- [143] E. B. Brousseau, F. Krohs, E. Caillaud, S. Dimov, O. Gibaru, and S. Fatikow, "Development of a novel process chain based on atomic force microscopy scratching for small and medium series production of polymer nanostructured components," *J. Manuf. Sci. Eng. Trans. ASME*, vol. 132, no. 3, pp. 0309011-0309018, 2010, doi: 10.1115/1.4001481.
- [144] S. S. Hassani, "Nanolithography Study Using Scanning Probe Microscope," in *Recent Advances in Nanofabrication Techniques and Applications*, H. R. A. E. - B. Cui, Ed. Rijeka: IntechOpen, 2011, p. Ch. 23.
- [145] S. Hu, A. Hamidi, S. Altmeyer, T. Köster, B. Spangenberg, and H. Kurz, "Fabrication of silicon and metal nanowires and dots using mechanical atomic force lithography," *J. Vac. Sci. Technol. B Microelectron. Nanom. Struct. Process. Meas. Phenom.*, vol. 16, no. 5, pp. 2822-2824, 1998, doi: 10.1116/1.590277.
- [146] X. Jiang, G. Wu, J. Zhou, S. Wang, A. A. Tseng, and Z. Du, "Nanopatterning on silicon surface using atomic force microscopy with diamond-like carbon (DLC)-coated Si probe," *Nanoscale Res. Lett.*, vol. 6, no. 1, p. 518, 2011, doi: 10.1186/1556-276X-6-518.
- [147] A. A. Tseng, "Advancements and challenges in development of atomic force microscopy for nanofabrication," *Nano Today*, vol. 6, no. 5, pp. 493-509, 2011, doi: 10.1016/j.nantod.2011.08.003.
- [148] Y. Yan, Y. Geng, and Z. Hu, "Recent advances in AFM tip-based nanomechanical machining," *Int. J. Mach. Tools Manuf.*, vol. 99, pp. 1-18, 2015, doi: 10.1016/j.ijmachtools.2015.09.004.
- [149] Y. Yan, Y. He, Y. Geng, Z. Hu, and H. Li, "Review on AFM Tip-Based Mechanical Nanomachining: The Influence of the Input Machining Parameters on the Outcomes," *Curr. Nanosci.*, vol. 12, no. 6, pp. 666-675, 2016, doi: 10.2174/1573413712666160527151032.
- [150] D. S. Engstrom, B. Porter, M. Pacios, and H. Bhaskaran, "Additive nanomanufacturing - A review," *J. Mater. Res.*, vol. 29, no. 17, pp. 1792-1816, 2014, doi: 10.1557/jmr.2014.159.
- [151] S. S. Park, M. G. Mostofa, C. I. Park, M. Mehrpouya, and S. Kim, "Vibration assisted nano mechanical machining using AFM probe," *CIRP Ann. - Manuf. Technol.*, vol. 63, pp. 537-540, 2014, doi: 10.1016/j.cirp.2014.03.138.

- [152] Y. Geng, E. B. Brousseau, X. Zhao, M. Gensheimer, and C. R. Bowen, "AFM tip-based nanomachining with increased cutting speed at the tool-workpiece interface," *Precis. Eng.*, vol. 51, no. June 2017, pp. 536-544, 2018, doi: 10.1016/j.precisioneng.2017.10.009.
- [153] H. W. Schumacher, U. F. Keyser, U. Zeitler, R. J. Haug, and K. Eberl, "Controlled mechanical AFM machining of two-dimensional electron systems: Fabrication of a single-electron transistor," *Phys. E Low-Dimensional Syst. Nanostructures*, vol. 6, no. 1, pp. 860-863, 2000, doi: 10.1016/S1386-9477(99)00230-1.
- [154] J. Cortes Rosa, M. Wendel, H. Lorenz, J. P. Kotthaus, M. Thomas, and H. Kroemer, "Direct patterning of surface quantum wells with an atomic force microscope," *Appl. Phys. Lett.*, vol. 73, no. 18, pp. 2684-2686, 1998, doi: 10.1063/1.122553.
- [155] Z. Wang, D. Wang, N. Jiao, S. Tung, and Z. Dong, "A nanochannel system fabricated by MEMS microfabrication and atomic force microscopy," *NEMS 2011 - 6th IEEE Int. Conf. Nano/Micro Eng. Mol. Syst.*, vol. 5, no. February, pp. 372-376, 2011, doi: 10.1109/NEMS.2011.6017370.
- [156] L. Y. Hong and H. N. Lin, "Fabrication of single titanium oxide nanodot ultraviolet sensors by atomic force microscopy nanolithography," *Sensors Actuators, A Phys.*, vol. 232, pp. 94-98, 2015, doi: 10.1016/j.sna.2015.05.013.
- [157] P. Vettiger, G. Cross, M. Despont, U. Drechsler, U. Dürig, B. Gotsmann, W. Häberle, M. A. Lantz, H. E. Rothuizen, R. Stutz, and G. K. Binnig, "The 'millipede'-nanotechnology entering data storage," *IEEE Trans. Nanotechnol.*, vol. 1, no. 1, pp. 39-54, 2002, doi: 10.1109/TNANO.2002.1005425.
- [158] A. a. Tseng, J. Shirakashi, S. Nishimura, K. Miyashita, and A. Notargiacomo, "Scratching properties of nickel-iron thin film and silicon using atomic force microscopy," *J. Appl. Phys.*, vol. 106, no. 4, p. 044314, 2009, doi: 10.1063/1.3197313.
- [159] A. a. Tseng, J. Shirakashi, S. Nishimura, K. Miyashita, and Z. Li, "Nanomachining of permalloy for fabricating nanoscale ferromagnetic structures using atomic force microscopy," *J. Nanosci. Nanotechnol.*, vol. 10, no. 1, pp. 456-466, 2010, doi: <http://dx.doi.org/10.1166/jnn.2010.1797>
- [160] A. A. Tseng, C. F. J. Kuo, S. Jou, S. Nishimura, and J. I. Shirakashi, "Scratch direction and threshold force in nanoscale scratching using atomic force microscopes," *Appl. Surf. Sci.*, vol. 257, no. 22, pp. 9243-9250, 2011, doi: 10.1016/j.apsusc.2011.04.065.
- [161] H. W. Schumacher, D. Ravelosona, F. Cayssol, J. Wunderlich, C. Chappert, V. Mathet, A. Thiaville, J. P. Jamet, J. Ferré, and R. J. Haug, "Propagation of a magnetic domain wall in the presence of AFM fabricated defects," *IEEE Trans. Magn.*, vol. 37, no. 4 I, pp. 2331-2333, 2001, doi: 10.1109/20.951163.
- [162] H. W. Schumacher, D. Ravelosona, F. Cayssol, J. Wunderlich, C. Chappert, V. Mathet, A. Thiaville, J. P. Jamet, J. Ferré, and R. J. Haug, "Control of the magnetic domain wall propagation in Pt/Co/Pt ultra thin films using direct mechanical AFM lithography," *J. Magn. Magn. Mater.*, vol. 240, no. 1-3, pp. 53-56, 2002, doi: 10.1016/S0304-8853(01)00727-2.

- [163] S. Franssila, *Introduction to Microfabrication*. West Sussex: Wiley, 2004.
- [164] J. van Schoot, K. van Ingen Schenau, C. Valentin, and S. Migura, "EUV lithography scanner for sub-8nm resolution," in *Extreme Ultraviolet (EUV) Lithography VI*, 2015, vol. 9422, pp. 449-460, doi: 10.1117/12.2087502.
- [165] A. A. Tseng, K. Chen, C. D. Chen, and K. J. Ma, "Electron beam lithography in nanoscale fabrication: Recent development," *IEEE Trans. Electron. Packag. Manuf.*, vol. 26, no. 2, pp. 141-149, 2003, doi: 10.1109/TEPM.2003.817714.
- [166] A. N. Broers, A. C. F. Hoole, and J. M. Ryan, "Electron Beam lithography-Resolution Limits," *Microelectron. Eng.*, vol. 32, no. 1-4, pp. 131-142, Sep. 1996, doi: 10.1016/0167-9317(95)00368-1.
- [167] M. A. Mohammad, M. Muhammad, S. K. Dew, and M. Stepanova, "Fundamentals of Electron Beam Exposure and Development," in *Nanofabrication: Techniques and Principles*, M. Stepanova and S. Dew, Eds. Vienna: Springer Vienna, 2012, pp. 11-41.
- [168] M. Khoury and D. K. Ferry, "Effect of molecular weight on poly(methyl methacrylate) resolution," *J. Vac. Sci. Technol. B Microelectron. Nanom. Struct. Process. Meas. Phenom.*, vol. 14, no. 1, pp. 75-79, 1996, doi: 10.1116/1.588437.
- [169] O. O. Abegunde, E. T. Akinlabi, O. P. Oladijo, S. Akinlabi, and A. U. Ude, "Overview of thin film deposition techniques," *AIMS Mater. Sci.*, vol. 6, no. 2, pp. 174-199, 2019, doi: 10.3934/MATERSCI.2019.2.174.
- [170] A. J. Newell, W. Williams, and D. J. Dunlop, "A generalization of the demagnetizing tensor for nonuniform magnetization," *J. Geophys. Res.*, vol. 98, no. B6, pp. 9551-9555, 1993.
- [171] J. E. Sader, J. W. M. Chon, and P. Mulvaney, "Calibration of rectangular atomic force microscope cantilevers," *Rev. Sci. Instrum.*, vol. 70, no. 10, pp. 3967-3969, 1999, doi: 10.1063/1.1150021.
- [172] H. D. Arnold and G. W. Elmen, "Permalloy, A New Magnetic Material of Very High Permeability," *Bell Syst. Tech. J.*, vol. 2, no. 3, pp. 101-111, 1923, doi: 10.1002/j.1538-7305.1923.tb03595.x.
- [173] J. C. Mallinson, "CHAPTER 4 - The Anisotropic Magneto-Resistive Effect," in *Electromagnetism*, J. C. B. T.-M.-R. and S. V. H. (Second E. MALLINSON, Ed. San Diego: Academic Press, 2002, pp. 27-38.
- [174] "Scanning Electron Microscopy," in *Microstructural Characterization of Materials*, John Wiley & Sons, Ltd, 2008, pp. 261-331.
- [175] J. Orloff, *Handbook of charged particle optics*. Boca Raton, FL: Taylor and Francis, 2009.
- [176] W. Thomson, "On the Electro-Dynamic Qualities of Metals : Effects of Magnetization on the Electric Conductivity of Nickel and of Iron," *Proceeding R. Soc. London*, vol. 8, pp. 546-550, 1857.
- [177] L. S. Cryotronics, "Model 370 AC Resistance Bridge." [Online]. Available: <http://www.lakeshore.com/products/AC-Resistance-Bridges/Model-370/Pages/Overview.aspx>. [Accessed: 01-May-2016].
- [178] W. Chao, P. Fischer, T. Tyliczszak, S. Rekawa, E. Anderson, and P. Naulleau, "Real space soft x-ray imaging at 10 nm spatial resolution," *Opt. Express*, vol.

20, no. 9, p. 9777, 2012, doi: 10.1364/oe.20.009777.

- [179] P. Fischer and H. Ohldag, "X-rays and magnetism," *Reports Prog. Phys.*, vol. 78, no. 9, p. 094501, 2015, doi: 10.1088/0034-4885/78/9/094501.
- [180] C. T. Chen, F. Sette, Y. Ma, and S. Modesti, "Soft-x-ray magnetic circular dichroism at the L_{2,3} edges of nickel," *Phys. Rev. B*, vol. 42, no. 11, pp. 7262-7265, 1990, doi: 10.1103/PhysRevB.42.7262.
- [181] C. M. Schneider, "Perspectives in element-specific magnetic domain imaging," *J. Magn. Magn. Mater.*, vol. 156, no. 1-3, pp. 94-98, 1996, doi: 10.1016/0304-8853(95)00802-0.
- [182] P. Fischer, D. H. Kim, W. Chao, J. A. Liddle, E. H. Anderson, and D. T. Attwood, "Soft X-ray microscopy of nanomagnetism," *Mater. Today*, vol. 9, no. 1-2, pp. 26-33, 2006, doi: 10.1016/S1369-7021(05)71335-3.
- [183] P. Fischer, M. Y. Im, C. Baldasseroni, C. Bordel, F. Hellman, J. S. Lee, and C. S. Fadley, "Magnetic imaging with full-field soft X-ray microscopies," *J. Electron Spectros. Relat. Phenomena*, vol. 189, pp. 196-205, 2013, doi: 10.1016/j.elspec.2013.03.012.
- [184] The OOMMF code is available at <http://math.nist.gov/oommf>. [185] M. Hayashi, L. Thomas, Y. B. Bazaliy, C. Rettner, R. Moriya, X. Jiang, and S. S. P. Parkin, "Influence of current on field-driven domain wall motion in permalloy nanowires from time resolved measurements of anisotropic magnetoresistance," *Phys. Rev. Lett.*, vol. 96, no. 19, pp. 25-28, 2006, doi: 10.1103/PhysRevLett.96.197207.
- [186] J. R. Greer, W. C. Oliver, and W. D. Nix, "Size dependence of mechanical properties of gold at the micron scale in the absence of strain gradients," *Acta Mater.*, vol. 53, pp. 1821-1830, 2005, doi: 10.1016/j.actamat.2004.12.031.
- [187] This research used resources of the Advanced Light Source, a DOE Office of Science User Facility under contract no. DE-AC02-05CH11231.
- [188] T. J. Broomhall and T. J. Hayward, "Suppression of Stochastic Domain Wall Pinning Through Control of Gilbert Damping," *Sci. Rep.*, vol. 7, no. 1, p. 17100, 2017, doi: 10.1038/s41598-017-17097-4.